CALIBRATING ARCHEAN AND MIOCENE LARGE IGNEOUS PROVINCE EMPLACEMENT AND GEOLOGIC TIMESCALES WITH HIGH-PRECISION U-PB ZIRCON GEOCHRONOLOGY

JENNIFER JEAN KASBOHM

A DISSERTATION
PRESENTED TO THE FACULTY
OF PRINCETON UNIVERSITY
IN CANDIDACY FOR THE DEGREE
OF DOCTOR OF PHILOSOPHY

RECOMMENDED FOR ACCEPTANCE BY
THE DEPARTMENT OF
GEOSCIENCES

ADVISER: PROFESSOR BLAIR SCHOENE

JUNE 2020

Abstract

In the past decade, methodological advances in the precision and accuracy of geochronology have improved estimates of the timing and duration of large igneous province (LIP) emplacement, mass extinction events, and global climate perturbations, and in general have supported a temporal link between them. In this thesis, I use high-precision U-Pb ID-TIMS zircon geochronology to present new temporal constraints on Earth's oldest and youngest LIPs.

By integrating paleomagnetism and geochronology into a detailed stratigraphic study of two intervals of flood basalt volcanism in the Neoarchean Fortescue Group (Western Australia), I provide temporal constraints on rapid plate motion at 2.7 Ga, and the timing of Earth's oldest documented magnetic field reversal. I then apply U-Pb zircon geochronology to the Miocene Columbia River Basalt Group (Northwest USA), Earth's youngest LIP, and show that it erupted in ~750 ka, 2.4 times faster than previously thought, with its largest formation emplaced in ~500 ka. The new age model provides estimates for a constant eruptive flux through the main phase of volcanism, the timing of Miocene magnetic field reversals during a poorly calibrated interval of the Geomagnetic Polarity Timescale, and stronger temporal evidence for a correlation between the beginning of LIP volcanism and the onset of the Miocene Climate Optimum (MCO), an interval of global warming and elevated atmospheric carbon dioxide.

Age models for the MCO and other paleoclimate events in the sedimentary record are often calibrated by biostratigraphy and magnetostratigraphy rather than absolute geochronology, which may hinder their correlation to high-precision eruptive timelines for LIPs. I present a case study from the Early Miocene Bisciaro Formation (Italy) to show the importance of radiometric calibration of sedimentary records where astronomical tuning is not possible, to address inadequacies in traditional methods of age calibration.

Finally, I review existing high-precision geochronology from 12 LIPs and their corresponding extinction or climate events, to begin to assess if advances in geochronology support a causal relationship between them. Despite much progress, higher precision geochronology of both LIPs and environmental records will be required to further understand how these catastrophic volcanic events have changed the course of our planet’s surface evolution.

Acknowledgments

When I first entered Guyot Hall in October 2008, as a visiting high school student who was curious about geology, I could never have imagined that nearly 12 years later, I would be leaving with a PhD in Geosciences. There are so many people, inside and outside of Guyot, who helped me achieve my goals and are deserving of my thanks:

My advisor Blair Schoene has consistently modeled the pursuit of scientific excellence while caring about his students and colleagues, balancing family life, and always keeping his door open. Blair's intellectual rigor, dedication, humility, sense of humor, even temper, and compassion are qualities I seek to emulate as I advance my career. I am so grateful for his mentorship on the projects presented here, and the extreme patience he has shown me as I struggled to get on the right path. I look forward to many more collaborations in the years ahead!

I thank my other dissertation committee members: Gerta Keller, Danny Sigman, and especially John Higgins, who was the second reader for this thesis and helped guide our interpretations of the paleoclimatic implications of our findings. Co-authors who contributed to the projects presented here are Seth Burgess, Scott Maclennan, David Evans, Ben Weiss, Joshua Murray, and Alessandro Montanari. Steve Reidel, Bart Martin, and Alessandro Montanari assisted with sample acquisition and identification in the CRBG and Italy, and I am grateful that they took the time to share some of their extensive regional expertise with me.

When I returned to Guyot in summer 2009 as a high school intern, Catherine Rose and Nick Swanson-Hysell taught me how fascinating Earth history could be, and modeled the dedication, enthusiasm, and kindness that made me want to go to grad school, before I had even taken my first geology class. It was a privilege to join the Schoene group years later, and I am grateful to all of its members. Mélanie Barboni and Jon Husson got me started in lab; Kyle Samperton and Brenhin Keller were always there when I needed help. Postdocs Mike Eddy and Ayla Pamukcu provided emotional and intellectual support, and much-needed laughter. Sam Gwizd and Disha Okhai kept me motivated to keep going downstairs to crush, and I'm grateful for their friendship. Our most recent additions, Travis Steiner-Leach, Elena Watts, Alyssa Anderson, and Dawid Szymanowski have been true assets to the lab and good friends, and I look forward to seeing all the great things they'll do! Finally, I owe immense gratitude to my classmate Scott Maclennan. I am indebted to Scott for shouldering the entirety of driving us across Australia, as well as taking on far too many lab responsibilities when I couldn't keep up, and never ceasing to be kind and supportive as he did so.

The "second floor" provided a great community of fellow Earth historians, and I am especially grateful to my classmates Alliya Akhtar and Danielle Santiago-Ramos for supporting me through the ups and downs of these seven years. Innumerable lunches with Clara Blättler, Ana-Sofie Ahm, and Liz Lundstrom helped me through each day. I was also privileged to work with a number of Princeton undergrads on my research, and they are acknowledged in the following chapters. A special thank you to Joshua Murray and Alison Campion, who were superlative assistants, collaborators, DJs, field cooks, and friends. I am also grateful to my PWiGS mentor, Jessica Irving, for advice and support through the years, and my mentee Naomi Intrator, for friendship and hospitality!

The support staff in Geosciences has empowered me in every way to pursue my goals. Sheryl Robas was the first Geoscience department member I ever spoke with; she organized my very first visit in 2008, and is now on top of everything I need to submit with my thesis. Dawn Reading has been an incredible assistant; I couldn’t be more grateful for the kindness and patience she showed while booking and expensing all of my field and conference travel, with a caring personal touch. Nora Zelizer was always on call to support us, whether in the department or in the field. Mike Morris and Bob Koenigsmark made sure my samples arrived safely, and that everything in the lapidary worked so that I could process them. Finally, Mary Rose Russo and Georgette Chalker went above and beyond in helping prepare for a remote dissertation defense.

Serving as a Resident Graduate Student in Forbes College helped me feel at home at Princeton, and I am grateful to everyone so invested in building that community and supporting me during my time there, especially Maria Garlock, Michael Hecht, Patrick Caddeau, Maureen Riggi, Jen Paslowski, and my fellow RGS. A special shoutout to Kris Pardo, my sixth year writing buddy who motivated and encouraged me over breakfast each day, and all the best to my former zees and RCAs.

Jackie Small, Sisira Gorthala, Frances Sawyer, Sam Berstler, and Carol Chiodo have gifted me with, combined, 63 years of friendship, and I would not have made it without their love and support. And from the beginning, my family has nurtured my passion for science (“Chris…it’s a gas”), pursuit of excellence (“I can’t believe I’m losing to a pig”), and curiosity about the natural world. Our travels through 34 states, 9 Canadian provinces, and 50 national, state, or provincial parks, as well as hundreds of other interesting sites, planted the seeds of my eventual geology fieldwork, where I brought the same planning and navigating skills I used on our family trips. I am so grateful for their support through my PhD, whether by helping me move apartments, clean my field gear, taking me to dinner or grocery shopping, trying to learn more about geochronology and peer review, and even helping me prep paleomag samples late into the night (thanks, Emily!)

Most importantly, I am grateful to David Suwondo for eight years of love and partnership. One week after we began dating, I left for three months in the field, and he was waiting when I came back. He later waited for me through six more years while I pursued graduate work at Princeton, understanding and supportive of my dating rocks. Not only my personal physician (packing all of my first aid kits for fieldwork), housekeeper, and barista (making all the coffee I needed to write this thesis), David has kept me smiling, supported, motivated, and loved, after taking care of countless others every day in the emergency department, and now serving on the front lines of the coronavirus pandemic. I can’t wait to resume our world travels and share in our wonderful future together. He is the true rock in my life, the most important one I’ll ever date.

Conference Presentations

Published and Presented Abstracts (Talks)

Kasbohm, J., Schoene B., (2018). U-Pb Zircon Ages Correlate the Columbia River Flood Basalt with the Mid-Miocene Climate Optimum. *Goldschmidt Abstracts*.

Kasbohm, J., Schoene, B., (2017). Assessing Causes and Consequences of Columbia River Basalt Volcanism with Zircon Geochronology. *American Geophysical Union Fall Meeting Abstracts*.

Kasbohm, J., Schoene, B., (2016). U-Pb Zircon Geochronology of the Columbia River Basalt. *American Geophysical Union Fall Meeting Abstracts*.

Published and Presented Abstracts (Posters)

Kasbohm, J., Schoene, B. (2019). Assessing Eruptive Tempo of the Columbia River Basalt Group and Recalibrating Miocene Climate Records with Zircon Geochronology. *American Geophysical Union Fall Meeting Abstracts*. ***Outstanding Student Paper Award**

Kasbohm, J., Schoene, B. (2019). Calibrating the Miocene Geomagnetic Polarity Timescale with Zircon Geochronology. *Gordon Research Conference on Geochronology*.

Kasbohm, J., Schoene, B. (2018). Assessing Correlation of Columbia River Flood Basalt Volcanism with the Mid-Miocene Climate Optimum through Zircon Geochronology. *American Geophysical Union Fall Meeting Abstracts*.

Kasbohm, J., Maloof, A., Schoene, B., Weiss, B. (2015). Constraining Rates of Neoarchean Plate Motion through Magnetostratigraphy and High-Precision Geochronology of the Fortescue Group, Pilbara, Western Australia. *American Geophysical Union Fall Meeting Abstracts*.

Kasbohm, J., Maloof, A., Schoene, B. (2015). Volcanostratigraphy and Paleogeography of the Archean Fortescue Group, Pilbara, Western Australia. *Northeastern Geobiology Conference*.

In memory of my grandfathers,

Anthony P. Blose & Martin L. Kasbohm –

I hope I make you proud

Table of Contents

Chapter 1

Introduction and Methods

This chapter is taken from

Kasbohm, J.J., Schoene, B., Burgess, S. (in press). Radiometric constraints on the timing, tempo, and effects of large igneous province emplacement. In: Ernst, R.E., Dickson, A.J., Bekker, A. (eds.), Large Igneous Provinces: A Driver of Global Environmental and Biotic Changes. *AGU Geophysical Monograph 255.*

The observation that Large Igneous Province (LIP) magmatism has in some cases occurred concurrently with mass extinctions (Courtillot & Renne, 2003; Ernst & Youbi, 2017) leads to the question of whether there is a cause-and-effect relationship between them. While various hypotheses exist as to how LIPs lead to catastrophic climate change that can lead to ecosystem collapse and mass extinctions, they generally focus on volatile release from either magma-derived gases or indirectly through heating of organic-, carbonate-, or evaporite-rich sediments (Self et al., 2006; Svensen et al., 2004; Thordarson & Self, 1996). Determining whether any of these mechanisms are important contributors to climate change requires understanding the relative rate of both extrusive and intrusive magmatism, and correlating these with paleoenvironmental records. The only way to directly date the rates of LIP emplacement is through radioisotope geochronology. Furthermore, as LIP lava flows and biological evidence for mass extinctions rarely occur in the same stratigraphic sections, making direct stratigraphic temporal correlation impossible, geochronology is also essential to test the plausibility of causality.

Although a wide range of geochronologic techniques have been applied to dating LIPs, uranium-lead (U-Pb) and argon-argon ($^{40}Ar/^{39}Ar$) geochronometers are the most widely used geochronometers for this application because their parent isotopes are characterized by long half-lives and relatively high concentrations in a variety of mineral phases (Reiners et al., 2017; Renne et al., 1998a). Temporal correlation between some LIPs and mass extinctions were suggested over 30 years ago (McLean, 1985), and this was rapidly tested using $^{40}Ar/^{39}Ar$ geochronology on basalts (Courtillot et al., 1986; Duncan & Pyle, 1988). However, not until the 1990s were $^{40}Ar/^{39}Ar$ and U-Pb geochronology used to demonstrate a temporal coincidence between the Siberian Traps LIP and the end-Permian mass extinction to within ~ 1 Ma (Campbell et al., 1992; Dalrymple et al., 1995; Renne & Basu, 1991; Kamo et al., 2003; Reichow et al., 2002). Attempts to further correlate LIPs and mass extinctions have both capitalized on, and pushed the development of, higher precision geochronology. Because the duration of the hypothesized individual environmental effects of LIPs can vary in timescale from years (cooling associated with sulfate aerosols, acid rain, ozone depletion) to 100 ka (warming associated with CO_2) (Black & Manga, 2017; Wignall, 2001), greater and greater precision is required to test hypotheses relating LIPs to paleoclimate and paleontological records. Geochronological uncertainties > 1 Ma, which were commonplace in datasets from the early efforts to date these events, obscure the relative timing of LIP eruptions versus global change on relevant climatic timescales, and limit assessment of the plausibility of a causal connection. However, the last decade has seen dramatic improvement in the precision and accuracy of dates generated by radiogenic geochronology, such that recently published datasets can begin to compare and resolve relative timing differences between the onset and duration of LIP magmatism and potential downstream environmental effects, such as biotic decline, ecosystem deterioration, global warming and carbon cycling, and sea level change. With methodological advances in U-Pb geochronology, it is now possible to discern an coincidence of events with precision of 10-100 ka, allowing testing of a potential causal connections at the sub-100 kyr level. However, further increases in analytical precision of dates for LIPs and of age models for stratigraphic sections that contain paleoenvironmental records will be required in order to resolve the timing of environmental effects operating on shorter timescales, such as cooling due to SO_2.

Dating methods for Large Igneous Provinces

Most dates for LIPs and their corresponding environmental perturbations are derived from the $^{40}Ar/^{39}Ar$ or U-Pb techniques. Historically, $^{40}Ar/^{39}Ar$ studies have yielded a temporal framework of LIP emplacement at ~1% resolution (e.g., Barry et al., 2013; Kerr et al., 2003; Marzoli et al., 2018; Renne et al., 1995), sufficient to establish a broad correlation, but in excess of that required to resolve the relative timing of LIP emplacement relative to environmental change. This relatively coarse resolution is due to small concentrations of the parent isotope, ^{40}K, found in whole-rock basalt samples or plagioclase separates. U-Pb geochronology can yield higher-precision dates (to better than ±0.1%), but amenable minerals (e.g., zircon, baddeleyite) are not ubiquitous in LIPs. With their particular strengths and shortcomings, both techniques have been crucial to improving understanding of the connection between LIPs and environmental change, and working to better understand that connection has produced methodological breakthroughs in both geochronometers. In this section, we will briefly describe the methodological advances leading to improved accuracy and precision for both techniques, with a stronger focus on U-Pb methods as these have provided the majority of high-precision ages discussed in this review. We follow the definitions of accuracy and precision summarized in Schoene et al. (2013): an accurate date agrees with the actual age of an event within uncertainty, while precision is defined as the reported uncertainties, which may include both random and systematic uncertainties (Renne et al., 1998b; Schoene, 2014).

The accuracy of ^{40}Ar/^{39}Ar dates has increased as methodology evolved from analyzing primarily LIP whole-rock/groundmass samples, to more recent efforts focused on analysis of aliquots of plagioclase or biotite separated from basalts, or sanidines separated from intercalated silicic ashes. These recent studies have also used more careful means to hand-pick plagioclase grains to avoid the effects of weathering, and choosing grains of sufficient size to mitigate effects from ^{39}Ar recoil (Renne et al., 2015). New procedures also treat translucent, inclusion-free grains with an HF solution in an ultrasonic bath to lessen the effect of surface alteration (Sprain et al., 2019). While these efforts aid in improving the accuracy of ^{40}Ar/^{39}Ar dates, increases in analytical precision have resulted from increasing the number of different aliquots from the same sample used to derive a weighted mean plateau age, densely bracketing samples with standards during irradiation (Sprain et al., 2019), and advances in mass spectrometry, including the use of multi-collector mass spectrometers (Jicha et al., 2016). As will be discussed further below, the decades-long effort to reduce uncertainties resulting from neutron fluence monitors that act as age standards in ^{40}Ar/^{39}Ar geochronology (Kuiper et al., 2008; Renne et al., 1998b, 2010, 2011), as well as efforts to better quantify decay constants (Min et al., 2000; Renne et al., 2010, 2011), have also helped to advance the accuracy and precision of dates.

U-Pb geochronology has been applied to three different U-bearing accessory minerals in pursuit of dating LIPs: baddeleyite, perovskite, and zircon. Baddeleyite has proven useful for dating diabase dikes and gabbros as well as hydrothermal contact aureoles (Fraser et al., 2004; Heaman & LeCheminant, 1993; Kamo et al., 1989; Söderland et al., 2103), but can be prone to Pb-loss (e.g., Rioux et al., 2010). Perovskite has also been utilized to date LIPs, but >50% of the Pb in the mineral can be “common” Pb, not derived from radioactive decay, making the accuracy of perovskite dates accordingly sensitive to the chosen isotopic composition of common Pb (Burgess & Bowring, 2015; Kamo et al., 2003). Zircon lacks common Pb, but is rarely saturated and crystallized in LIP basalts. However, it has been dated from coarse-grained intrusions (sills and/or dikes) and thick lava flows (Blackburn et al., 2013; Burgess & Bowring, 2015; Davies et al., 2017; Dunning & Hodych, 1990; Kamo et al., 1996; Krogh et al., 1987; Schoene et al., 2010; Svensen et al., 2009, 2010), and from silicic ashes intercalated with LIP lava stratigraphy (Kasbohm & Schoene, 2018; Schoene et al., 2015a, 2019). U-Pb dates are obtained through secondary ion mass spectrometry (SIMS), laser ablation inductively coupled plasma mass spectrometry (LA-ICPMS), and isotope dilution – thermal ionization mass spectrometry (ID-TIMS). While SIMS and LA-ICPMS techniques are rapid and well-suited to studies requiring high spatial resolution, both of these techniques yield dates with analytical precision on the order of 2-3% (Schoene, 2014). Because LIP emplacement and potentially associated environmental effects occur on timescales between 10-100 ka, here we focus only on U-Pb datasets generated via ID-TIMS, which commonly yields precision on the order of 0.1%.

ID-TIMS has seen a number of methodological advancements that have improved the accuracy and precision of analyses while reducing sample size. Reduction of laboratory blank and improvements in mass spectrometry over decades has enabled routine dating of single zircon grains and even fractions of single grains (e.g., Davis et al., 2003; Krogh, 1973; Michard-Vitrac et al., 1977; Parrish, 1987; Schoene, 2014). A key development allowing for substantial improvement to the accuracy of zircon ages came with the introduction of the chemical abrasion (CA) protocol, which preferentially dissolves portions of zircon grains that have been affected by radiation damage, and thus are more prone to Pb-loss (Mattinson, 2005). The EARTHTIME initiative has pushed for enhanced interlaboratory calibration through the use of the (^{202}Pb-)^{205}Pb-^{233}U-^{235}U tracer solutions (Condon et al., 2015; McLean et al., 2015), as well as a detailed account of uncertainties that factor into each date generated, allowing for comparison with dates derived from other methods (Bowring et al., 2011; McLean et al., 2011; Schmitz & Schoene, 2007).

While improvements in accuracy and precision have allowed geochronologists to better assess the correlation between LIPs and environmental perturbations, these breakthroughs have illuminated further complications inherent in interpreting the accuracy of an unknown quantity: the age of the rock being dated. Once a *date* is obtained, by using mass spectrometry to solve radioactive decay equations for time, geological uncertainty must be addressed at every stage of data interpretation, ultimately yielding an *age*, an interpretation of that date in terms of geological processes (Schoene, 2014). Geological uncertainty may be reflected in macroscopic questions, such as how well the timing of an intrusive unit aligns with its corresponding extrusive unit, or in essential smaller-scale questions of how to deal with complex age populations, when high-precision techniques yield individual dates that do not overlap within analytical uncertainty (Davydov et al., 2010; Keller et al., 2018; Mundil et al., 2004; Ramezani et al., 2007; Schoene et al., 2010).

Interpreting pre-eruptive zircon growth in volcanic ashes provides an instructive example of addressing complex age populations and geological uncertainty in geochronological data. This interpretation is an important consideration, as zircon geochronology of volcanic ashes has yielded most of the age constraints for the environmental perturbations described in this paper, and for some of the constraints on the timing of LIP eruptions (e.g., Burgess et al., 2014; Clyde et al., 2016; Kasbohm & Schoene, 2018; Maclennan et al., 2018). Zircon dates obtained for dikes and sills are understandably more reproducible because zircon saturates very late during crystallization of mafic magmas. However, detecting age dispersion among single crystals is not unique to U-Pb zircon geochronology; high-precision ^{40}Ar/^{39}Ar studies utilizing multi-collector mass spectrometry are beginning to resolve complex age populations of single sanidine crystals (Andersen et al., 2017), and the ramifications of these new datasets have yet to be teased out. Below, we discuss how this geological uncertainty has been addressed in zircon geochronology in the past decade, as it has not yet been routinely dealt with in the ^{40}Ar/^{39}Ar community.

Many of the studies presented here use weighted means of several individual zircon dates to provide an age for an ashbed, yielding lower uncertainty than that obtained for individual measurements. Calculating a mean square of weighted deviates (MSWD), with an expected value of 1, can assess how well analytical uncertainty explains the observed dispersion of dates about the mean (Wendt & Carl, 1991). However, a weighted mean should be used when the analytical uncertainty of the data corresponds to the actual error. Given evidence for protracted zircon crystallization and incorporation of xenocrysts and antecrysts in magma chambers, ~100 ka or even 1 Ma before an ash is deposited (Charlier & Zellmer, 2000; Ramezani et al., 2007; Schmitt, 2011; Schoene et al., 2010), a weighted mean age may under-represent the geologic uncertainty in the age of an ash. An alternative approach using the youngest zircon dated in a population as the age of the rock may be more tenable, as one may assume this youngest crystal most closely approximates the timing of eruption (Kasbohm & Schoene, 2018; Schoene et al., 2010). This approach minimizes age bias from pre-eruptive crystallization, though it assumes the youngest zircon in the rock was sampled, and yields a lower-precision age than a weighted mean approach. Its accuracy may be assessed by observing whether or not the youngest zircon ages young upward in a comprehensively dated stratigraphic section. Some U-Pb studies utilize a combination of these approaches, by presenting the weighted mean age of the youngest few grains of the sample, which overlap within analytical uncertainty (Day et al., 2015; Kasbohm & Schoene, 2018; Meyers et al., 2012; Du Vivier et al., 2015). Importantly, unless high-precision single analyses are obtained by the method, either U-Pb or ^{40}Ar/^{39}Ar, geologic scatter cannot be recognized and accuracy cannot be assessed to better than the approximate precision of a single analysis.

While geological uncertainty can complicate interpretation of geochronological data, geological or stratigraphic constraints have been used to improve the accuracy and precision of geochronology through statistical modeling. Bayesian statistical models have been used in combination with high-precision data to evaluate eruptive ages for samples based on the timing of crystallization of individual zircon grains leading up to eruption (Keller et al., 2018; Schoene et al., 2019). Additionally, several studies incorporate Markov Chain Monte Carlo sampling of numerous samples taken from a single stratigraphic sequence, inspired by the practices of the radiocarbon community (Buck et al., 1991; Haslett & Parnell, 2008). Stratigraphic position has been leveraged to refine the precision of groups of zircon ages using this technique (Guex et al., 2012; Keller et al., 2018; Meyers et al., 2012; Schoene et al., 2015, 2019; De Vleeschouwer & Parnell, 2014). The combination of using high-precision dates and robust statistical models can test for whether age interpretations of individual ashbeds themselves are permissible.

Although accuracy and precision have improved in recent decades for U-Pb and ^{40}Ar/^{39}Ar geochronology, systematic uncertainties remain in radioactive decay constants, isotope tracer composition for U-Pb analysis, and ages of fluence monitors used in ^{40}Ar/^{39}Ar geochronology. Indeed, an early observation that U-Pb and ^{40}Ar/^{39}Ar ages for the Siberian Traps were offset at the ~1% level considering analytical uncertainty alone led to greater efforts to report and propagate systematic uncertainties for both methods (Renne et al., 1998b; Schoene et al., 2006). This offset has largely been attributed to inaccuracy in the ^{40}K decay constants (Renne et al., 2010). Although the ^{238}U and ^{235}U decay constants are among the best characterized in geochronology, with 0.11% and 0.14% uncertainty, respectively (Jaffey et al., 1971), these estimates derive from a single set of measurements, leaving open the possibility that inaccuracies in one or both U decay constants may exist (Parsons-Davis et al., 2018; Schoene et al., 2006).

Perhaps the most important remaining source of systematic uncertainty for Cenozoic samples is the adopted age of neutron fluence monitors used in ^{40}Ar/^{39}Ar geochronology. These monitors, also known as reference materials or standards, are natural minerals whose prescribed ages directly influence the calculated ages of samples. A typical monitor used is the Fish Canyon Sanidine, for which most ^{40}Ar/^{39}Ar labs have adopted the age of either 28.201 or 28.294 Ma (Kuiper et al., 2008; Renne et al., 2010, 2011). However, the U-Pb date for zircons from the Fish Canyon tuff from which the sanidine is derived is 28.196 ± 0.038 Ma (youngest zircon from (Wotzlaw et al., 2013)), agreeing better with the younger Fish Canyon sanidine age estimate of Kuiper et al. (2008). Studies working to intercalibrate U-Pb, astrochronology, and ^{40}Ar/^{39}Ar geochronology have shown improved concordance of U-Pb with ^{40}Ar/^{39}Ar ages when using the 28.201 Ma age for the Fish Canyon Sanidine (Kuiper et al., 2008; Meyers et al., 2012). This source of uncertainty affects the ability to compare U-Pb to ^{40}Ar/^{39}Ar dates as well as discern the existence of pre-eruptive zircon crystallization, but is irrelevant for comparing dates within the ^{40}Ar/^{39}Ar system, if the same age, standard, and decay constants are used.

The following studies were undertaken to better understand the timing and tempo of LIP emplacement in the Archean (Chapter 2) and Miocene (Chapters 3 & 4), and to recalibrate the timescales that provide age models for their corresponding climate events (Chapters 3-5). In Chapter 6, I provide a review of high-precision geochronology of 12 pairs of LIPs and environmental events, which reveals new insights into the temporal dynamics of LIP emplacement, while highlighting future challenges for the field that must be resolved to better understand the effects of LIPs on the Earth system.

REFERENCES

Andersen, N. L., Jicha, B. R., Singer, B. S., & Hildreth, W. (2017). Incremental heating of Bishop Tuff sanidine reveals preeruptive radiogenic Ar and rapid remobilization from cold storage. *Proceedings of the National Academy of Sciences of the United States of America*, *114*(47), 12407–12412. https://doi.org/10.1073/pnas.1709581114

Barry, T. L., Kelley, S. P., Camp, V. E., Self, S., Jarboe, N. A., & Duncan, R. A. (2013). Eruption chronology of the Columbia River Basalt Group. *Geological Society of America Special Paper*, *497*, 45–66. https://doi.org/10.1130/2013.2497(02).

Black, B. A., & Manga, M. (2017). Volatiles and the tempo of flood basalt magmatism. *Earth and Planetary Science Letters*, *458*, 130–140. https://doi.org/10.1016/J.EPSL.2016.09.035

Blackburn, T. J., Olsen, P. E., Bowring, S. A., McLean, N. M., Kent, D. V., Puffer, J. H., et al. (2013). Zircon U-Pb geochronology links the end-Triassic extinction with the Central Atlantic magmatic Province. *Science*. https://doi.org/10.1126/science.1234204

Bowring, J. F., McLean, N. M., & Bowring, S. A. (2011). Engineering cyber infrastructure for U-Pb geochronology: Tripoli and U-Pb-Redux. *Geochemistry, Geophysics, Geosystems*, *12*(6). https://doi.org/10.1029/2010GC003479

Buck, C. E., Kenworthy, J. B., Litton, C. D., & Smith, A. F. M. (1991). Combining archaeological and radiocarbon information: a Bayesian approach to calibration. *Antiquity*, *65*(249), 808–821. https://doi.org/10.1017/S0003598X00080534

Burgess, S. D., & Bowring, S. A. (2015). High-precision geochronology confirms voluminous magmatism before, during, and after Earth's most severe extinction. *Science Advances*, *1*(7), e1500470–e1500470. https://doi.org/10.1126/sciadv.1500470

Burgess, S. D., Bowring, S. A., & Shen, S. (2014). High-precision timeline for Earth's most severe extinction. *Proceedings of the National Academy of Sciences of the United States of America*, *111*(9), 3316–21. https://doi.org/10.1073/pnas.1317692111

Campbell, I. H., Czamanske, G. K., Fedorenko, V. A., Hill, R. I., & Stepanov, V. (1992). Synchronism of the Siberian Traps and the Permian-Triassic Boundary. *Science*, *258*(5089), 1760–3. https://doi.org/10.1126/science.258.5089.1760

Charlier, B., & Zellmer, G. (2000). Some remarks on U-Th mineral ages from igneous rocks with prolonged cystallisation histories. *Earth and Planetary Science Letters*, *183*(3–4), 457–469. https://doi.org/10.1016/S0012-821X(00)00298-3

Clyde, W. C., Ramezani, J., Johnson, K. R., Bowring, S. A., & Jones, M. M. (2016). Direct high-precision U–Pb geochronology of the end-Cretaceous extinction and calibration of Paleocene astronomical timescales. *Earth and Planetary Science Letters*, *452*, 272–280. https://doi.org/10.1016/j.epsl.2016.07.041

Condon, D. J., Schoene, B., McLean, N. M., Bowring, S. A., & Parrish, R. R. (2015). Metrology and traceability of U-Pb isotope dilution geochronology (EARTHTIME Tracer Calibration Part I). *Geochimica et Cosmochimica Acta*, *164*, 464–480. https://doi.org/10.1016/j.gca.2015.05.026

Courtillot, V. E., & Renne, P. R. (2003). On the ages of flood basalt events. *Comptes Rendus - Geoscience*, *335*(1), 113–140. https://doi.org/10.1016/S1631-0713(03)00006-3

Courtillot, V. E., Besse, J., Vandamme, D., Montigny, R., Jaeger, J.-J., & Cappetta, H. (1986). Deccan flood basalts at the Cretaceous/Tertiary boundary? *Earth and Planetary Science Letters*, *80*(3–4), 361–374. https://doi.org/http://dx.doi.org/10.1016/0012-821X(86)90118-4

Dalrymple, G. B., Czamanske, G. K., Fedorenko, V. A., Simonov, O. N., Lanphere, M. A., & Likhachev, A. P. (1995). A reconnaissance ^{40}Ar^{39}Ar geochronologic study of ore-bearing and related rocks, Siberian Russia. *Geochimica et Cosmochimica Acta*, *59*(10), 2071–2083. https://doi.org/10.1016/0016-7037(95)00127-1

Davies, J. H. F. L., Marzoli, A., Bertrand, H., Youbi, N., Ernesto, M., & Schaltegger, U. (2017). End-Triassic mass extinction started by intrusive CAMP activity. *Nature Communications*, *8*, 15596. https://doi.org/10.1038/ncomms15596

Davis, D. W., Krogh, T. E., & Williams, I. S. (2003). Historical development of zircon geochronology. *Reviews in Mineralogy and Geochemistry*, *53*(1), 145–181. https://doi.org/10.2113/0530145

Davydov, V. I., Crowley, J. L., Schmitz, M. D., & Poletaev, V. I. (2010). High-precision

U-Pb zircon age calibration of the global Carboniferous time scale and Milankovitch band cyclicity in the Donets Basin, eastern Ukraine. *Geochemistry, Geophysics, Geosystems*, *11*(2). https://doi.org/10.1029/2009GC002736

Day, M. O., Ramezani, J., Bowring, S. A., Sadler, P. M., Erwin, D. H., Abdala, F., & Rubidge, B. S. (2015). When and how did the terrestrial mid-Permian mass extinction occur? Evidence from the tetrapod record of the Karoo Basin, South Africa. *Proceedings of the Royal Society B: Biological Sciences*. https://doi.org/10.1098/rspb.2015.0834

Duncan, R. A., & Pyle, D. G. (1988). Rapid eruption of the Deccan flood basalts at the Cretaceous/Tertiary boundary. *Nature*, *333*(6176), 841–843. Retrieved from http://dx.doi.org/10.1038/333841a0

Dunning, G. R., & Hodych, J. P. (1990). U/Pb zircon and baddeleyite ages for the Palisades and Gettysburg sills of the northeastern United States: implications for the age of the Triassic/Jurassic boundary. *Geology*, *18*(8), 795–798. https://doi.org/10.1130/0091-7613(1990)018<0795:UPZABA>2.3.CO;2

Ernst, R. E., & Youbi, N. (2017). How Large Igneous Provinces affect global climate, sometimes cause mass extinctions, and represent natural markers in the geological record. *Palaeogeography, Palaeoclimatology, Palaeoecology*, *478*, 30–52. https://doi.org/10.1016/j.palaeo.2017.03.014

Fraser, G. L., Pattison, D. R. M., & Heaman, L. M. (2004). Age of the Ballachulish and Glencoe Igneous Complexes (Scottish Highlands), and paragenesis of zircon, monazite and baddeleyite in the Ballachulish Aureole. *Journal of the Geological Society*, *161*(3), 447–462. https://doi.org/10.1144/0016-764903-018

Guex, J., Schoene, B., Bartolini, A., Spangenberg, J. E., Schaltegger, U., O'Dogherty, L., et al. (2012). Geochronological constraints on post-extinction recovery of the ammonoids and carbon cycle perturbations during the Early Jurassic. *Palaeogeography, Palaeoclimatology, Palaeoecology*, *346–347*(0), 1–11.

Haslett, J., & Parnell, A. C. (2008). A simple monotone process with application to radiocarbon-dated depth chronologies. *Journal of the Royal Statistical Society. Series C: Applied Statistics*, *57*(4), 399–418. https://doi.org/10.1111/j.1467-9876.2008.00623.x

Heaman, L. M., & LeCheminant, A. N. (1993). Paragenesis and U-Pb systematics of baddeleyite (ZrO2). *Chemical Geology*, *110*(1–3), 95–126. https://doi.org/10.1016/0009-2541(93)90249-I

Jaffey, A. H., Flynn, K. F., Glendenin, L. E., Bentley, W. C., & Essling, A. M. (1971). Precision measurement of half-lives and specific activities of ^{235}U and ^{238}U. *Physical Review C*, *4*(5), 1889–1906. https://doi.org/10.1103/PhysRevC.4.1889

Jicha, B. R., Singer, B. S., & Sobol, P. (2016). Re-evaluation of the ages of ^{40}Ar/^{39}Ar sanidine standards and supereruptions in the western U.S. using a Noblesse multi-collector mass spectrometer. *Chemical Geology*, *431*, 54–66. https://doi.org/10.1016/J.CHEMGEO.2016.03.024

Kamo, S. L., Gower, C. F., & Krogh, T. E. (1989). Birthdate for the lapetus Ocean? A precise U-Pb zircon and baddeleyite age for the Long Range dikes, southeast Labrador. *Geology*, *17*(7), 602. https://doi.org/10.1130/0091-7613(1989)017<0602:BFTLOA>2.3.CO;2

Kamo, S. L., Czamanske, G. K., & Krogh, T. E. (1996). A minimum U-Pb age for

Siberian flood-basalt volcanism. *Geochimica et Cosmochimica Acta*, *60*(18), 3505–3511. https://doi.org/10.1016/0016-7037(96)00173-1

Kamo, S. L., Czamanske, G. K., Amelin, Y., Fedorenko, V. A., Davis, D. W., & Trofimov, V. R. (2003). Rapid eruption of Siberian flood-volcanic rocks and evidence for coincidence with the Permian-Triassic boundary and mass extinction at 251 Ma. *Earth and Planetary Science Letters*, *214*(1–2), 75–91. https://doi.org/10.1016/S0012-821X(03)00347-9

Kasbohm, J. J., & Schoene, B. (2018). Rapid eruption of the Columbia River flood basalt and correlation with the mid-Miocene climate optimum. *Science Advances*, *4*(9), 1–8. https://doi.org/10.1126/sciadv.aat8223

Keller, C. B., Schoene, B., & Samperton, K. M. (2018). A stochastic sampling approach to zircon eruption age interpretation. *Geochemical Perspectives Letters*, 31–35. https://doi.org/10.7185/geochemlet.1826

Kerr, A. C., White, R. V., Thompson, P. M. E., Tarney, J., & Saunders, A. D. (2003). No Oceanic plateau - No caribbean plate? The seminal role of an oceanic plateau in Caribbean plate evolution. *AAPG Memoir*, (79), 23–26.

Krogh, T. E. (1973). A low-contamination method for hydrothermal decomposition of zircon and extraction of U and Pb for isotopic age determinations. *Geochimica et Cosmochimica Acta*, *37*(3), 485–494. https://doi.org/10.1016/0016-7037(73)90213-5

Krogh, T. E., Corfu, F., Davis, D. W., Dunning, G. R., Heaman, L. M., Kamo, S. L., et al. (1987). Precise U–Pb isotopic ages of diabase dykes and mafic to ultramafic rocks using trace amounts of baddeleyite and zircon. In H. C. Halls & W. F. Fahrig (Eds.), *Mafic Dike Swarms* (Vol. 34, pp. 147–152). Geological Association of Canada, Special Paper.

Kuiper, K. F., Deino, A. L., Hilgen, F. J., Krijgsman, W., Renne, P. R., & Wijbrans, J. R. (2008). Synchronizing rock clocks of earth history. *Science*, *320*(5875), 500–504. https://doi.org/10.1126/science.1154339

Maclennan, S., Park, Y., Swanson-Hysell, N., Maloof, A. C., Schoene, B., Gebreslassie, M., et al. (2018). The arc of the Snowball: U-Pb dates constrain the Islay anomaly and the initiation of the Sturtian glaciation. *Geology*. https://doi.org/10.1130/G40171.1

Marzoli, A., Callegaro, S., Dal Corso, J., Davies, J. H. F. L., Chiaradia, M., Youbi, N., et al. (2018). The Central Atlantic Magmatic Province (CAMP): a review. In *The Late Triassic World* (pp. 91–125). Springer.

Mattinson, J. M. (2005). Zircon U-Pb chemical abrasion (“CA-TIMS”) method: Combined annealing and multi-step partial dissolution analysis for improved precision and accuracy of zircon ages. *Chemical Geology*, *220*(1–2), 47–66. https://doi.org/10.1016/j.chemgeo.2005.03.011

McLean, D. M. (1985). Deccan Traps mantle degassing in the terminal Cretaceous marine extinctions. *Cretaceous Research*, *6*(3), 235–259.

McLean, N. M., Bowring, J. F., & Bowring, S. A. (2011). An algorithm for U-Pb isotope dilution data reduction and uncertainty propagation. *Geochemistry, Geophysics, Geosystems*, *12*(6). https://doi.org/10.1029/2010GC003478

McLean, N. M., Condon, D. J., Schoene, B., & Bowring, S. A. (2015). Evaluating uncertainties in the calibration of isotopic reference materials and multi-element isotopic tracers (EARTHTIME Tracer Calibration Part II). *Geochimica et*

Cosmochimica Acta, *164*, 481–501. https://doi.org/10.1016/j.gca.2015.02.040

Meyers, S. R., Siewert, S. E., Singer, B. S., Sageman, B. B., Condon, D. J., Obradovich, J. D., et al. (2012). Intercalibration of radioisotopic and astrochronologic time scales for the Cenomanian-Turonian boundary interval, Western Interior Basin, USA. *Geology*, *40*(1), 7–10. https://doi.org/10.1130/G32261.1

Michard-Vitrac, A., Lancelot, J., Allègre, C. J., & Moorbath, S. (1977). U-Pb ages on single zircons from the Early Precambrian rocks of West Greenland and the Minnesota River Valley. *Earth and Planetary Science Letters*, *35*(3), 449–453. https://doi.org/10.1016/0012-821X(77)90077-2

Min, K., Mundil, R., Renne, P. R., & Ludwig, K. R. (2000). A test for systematic errors in ^{40}Ar/^{39}Ar geochronology through comparison with U-Pb analysis of a 1.1 Ga rhyolite. *Geochim. Cosmochim. Acta*, *64*, 73–98. https://doi.org/10.1016/S0016-7037(99)00204-5

Mundil, R., Ludwig, K. R., Metcalfe, I., & Renne, P. R. (2004). Age and timing of the Permian mass extinctions: U/Pb dating of closed-system zircons. *Science*. https://doi.org/10.1126/science.1101012

Parrish, R. R. (1987). An improved micro-capsule for zircon dissolution in U□Pb geochronology. *Chemical Geology: Isotope Geoscience Section*, *66*(1–2), 99–102. https://doi.org/10.1016/0168-9622(87)90032-7

Parsons-Davis, T., Wimpenny, J., Keller, C. B., Thomas, K., Samperton, K. M., Renne, P. R., et al. (2018). New measurement of the ^{238}U decay constant with inductively coupled plasma mass spectrometry. *Journal of Radioanalytical and Nuclear Chemistry*, *318*(1), 711–721. https://doi.org/10.1007/s10967-018-6148-y

Ramezani, J., Schmitz, M. D., Davydov, V. I., Bowring, S. A., Snyder, W. S., & Northrup, C. J. (2007). High-precision U-Pb zircon age constraints on the Carboniferous-Permian boundary in the southern Urals stratotype. *Earth and Planetary Science Letters*, *256*(1–2), 244–257. https://doi.org/10.1016/j.epsl.2007.01.032

Reichow, M. K., Saunders, A. D., White, R. V., Pringle, M. S., Al'Mukhamedov, A. I., Medvedev, A. I., & Kirda, N. P. (2002). 40Ar/39Ar dates from the West Siberian Basin: Siberian flood basalt province doubled. *Science*, *296*(5574), 1846–1849. https://doi.org/10.1126/science.1071671

Reiners, P. W., Carlson, R. W., Renne, P. R., Cooper, K. M., Granger, D. E., McLean, N. M., & Schoene, B. (2017). *Geochronology and thermochronology*. *Geochronology and Thermochronology*. https://doi.org/10.1002/9781118455876

Renne, P. R., & Basu, A. R. (1991). Rapid Eruption of the Siberian Traps Flood Basalts at the Permo-Triassic Boundary. *Science*, *253*(5016), 176–179. https://doi.org/10.1126/science.253.5016.176

Renne, P. R., Zichao, Z., Richards, M. A., Black, M. T., & Basu, A. R. (1995). Synchrony and causal relations between Permian-Triassic boundary crises and siberian flood volcanism. *Science*. https://doi.org/10.1126/science.269.5229.1413

Renne, P. R., Karner, D. B., & Ludwig, K. R. (1998a). Absolute ages aren't exactly. *Science*, *282*, 1840–1841. https://doi.org/10.1126/science.282.5395.1840

Renne, P. R., Swisher, C. C., Deino, A. L., Karner, D. B., Owens, T. L., & DePaolo, D. J. (1998b). Intercalibration of standards, absolute ages and uncertainties in 40Ar/39Ar dating. *Chemical Geology*, *145*(1–2), 117–152. https://doi.org/10.1016/S0009-

2541(97)00159-9

Renne, P. R., Mundil, R., Balco, G., Min, K., & Ludwig, K. R. (2010). Joint determination of ^{40}K decay constants and ^{40}Ar/^{40}K for the Fish Canyon sanidine standard, and improved accuracy for ^{40}Ar/^{39}Ar geochronology. *Geochimica et Cosmochimica Acta*, *74*(18), 5349–5367. https://doi.org/10.1016/j.gca.2010.06.017

Renne, P. R., Balco, G., Ludwig, K. R., Mundil, R., & Min, K. (2011). Response to the comment by WH Schwarz et al. on "Joint determination of ^{40}K decay constants and ^{40}Ar*/^{40}K for the Fish Canyon sanidine standard, and improved accuracy for ^{40}Ar/^{39}Ar geochronology" by P. *Geochimica et Cosmochimica Acta*, *75*(17), 5097–5100. https://doi.org/10.1016/j.gca.2011.06.021

Renne, P. R., Sprain, C. J., Richards, M. A., Self, S., Vanderkluysen, L., & Pande, K. (2015). State shift in Deccan volcanism at the Cretaceous-Paleogene boundary, possibly induced by impact. *Science*. https://doi.org/10.1126/science.aac7549

Rioux, M., Bowring, S. A., Dudás, F., & Hanson, R. (2010). Characterizing the U-Pb systematics of baddeleyite through chemical abrasion: Application of multi-step digestion methods to baddeleyite geochronology. *Contributions to Mineralogy and Petrology*, *160*(5), 777–801. https://doi.org/10.1007/s00410-010-0507-1

Schmitt, A. K. (2011). Uranium Series Accessory Crystal Dating of Magmatic Processes. *Annual Review of Earth and Planetary Sciences*, *39*(1), 321–349. https://doi.org/10.1146/annurev-earth-040610-133330

Schmitz, M. D., & Schoene, B. (2007). Derivation of isotope ratios, errors, and error correlations for U-Pb geochronology using ^{205}Pb-^{235}U-(^{233}U)-spiked isotope dilution thermal ionization mass spectrometric data. *Geochemistry, Geophysics, Geosystems*, *8*(8). https://doi.org/10.1029/2006GC001492

Schoene, B. (2014). U-Th-Pb Geochronology. *Treatise on Geochemistry: Second Edition*, *4*, 341–378. https://doi.org/10.1016/B978-0-08-095975-7.00310-7

Schoene, B., Crowley, J. L., Condon, D. J., Schmitz, M. D., & Bowring, S. A. (2006). Reassessing the uranium decay constants for geochronology using ID-TIMS U-Pb data. *Geochimica et Cosmochimica Acta*, *70*(2), 426–445. https://doi.org/10.1016/j.gca.2005.09.007

Schoene, B., Guex, J., Bartolini, A., Schaltegger, U., & Blackburn, T. J. (2010). Correlating the end-Triassic mass extinction and flood basalt volcanism at the 100 ka level. *Geology*, *38*(5), 387–390. https://doi.org/10.1130/G30683.1

Schoene, B., Condon, D. J., Morgan, L. E., & McLean, N. M. (2013). Precision and Accuracy in Geochronology. *Elements*, *9*(1), 19–24. https://doi.org/10.2113/gselements.9.1.19

Schoene, B., Samperton, K. M., Eddy, M. P., Keller, G., Adatte, T., Bowring, S. A., et al. (2015). U-Pb geochronology of the Deccan Traps and relation to the end-Cretaceous mass extinction. *Science*, *347*(6218), 182–184. https://doi.org/10.1126/science.aaa0118

Schoene, B., Eddy, M. P., Samperton, K. M., Keller, C. B., Keller, G., Adatte, T., & Khadri, S. F. R. (2019). U-Pb constraints on pulsed eruption of the Deccan Traps across the end-Cretaceous mass extinction. *Science*, *363*(6429), 862–866. https://doi.org/10.1126/science.aau2422

Self, S., Widdowson, M., Thordarson, T., & Jay, A. E. (2006). Volatile fluxes during flood basalt eruptions and potential effects on the global environment: A Deccan perspective. *Earth and Planetary Science Letters*, *248*(1–2), 517–531. https://doi.org/10.1016/j.epsl.2006.05.041

Sprain, C. J., Renne, P. R., Vanderkluysen, L., Pande, K., Self, S., & Mittal, T. (2019). The eruptive tempo of Deccan volcanism in relation to the Cretaceous-Paleogene boundary. *Science*, *363*(6429), 866–870. https://doi.org/10.1126/science.aav1446

Svensen, H. H., Planke, S., Malthe-Sørenssen, A., Jamtveit, B., Myklebust, R., Eidem, T. R., & Rey, S. S. (2004). Release of methane from a volcanic basin as a mechanism for initial Eocene global warming. *Nature*, *429*(6991), 542. https://doi.org/10.1038/nature02566

Svensen, H. H., Planke, S., Polozov, A. G., Schmidbauer, N., Corfu, F., Podladchikov, Y. Y., & Jamtveit, B. (2009). Siberian gas venting and the end-Permian environmental crisis. *Earth and Planetary Science Letters*, *277*(3–4), 490–500. https://doi.org/10.1016/j.epsl.2008.11.015

Svensen, H. H., Planke, S., & Corfu, F. (2010). Zircon dating ties NE Atlantic sill emplacement to initial Eocene global warming. *Journal of the Geological Society*, *167*(3), 433–436. https://doi.org/10.1144/0016-76492009-125

Thordarson, T., & Self, S. (1996). Sulfur, chlorine and fluorine degassing and atmospheric loading by the Roza eruption, Columbia River Basalt Group, Washington, USA. *Journal of Volcanology and Geothermal Research*, *74*(1–2), 49–73. https://doi.org/10.1016/S0377-0273(96)00054-6

Du Vivier, A. D. C., Selby, D., Condon, D. J., Takashima, R., & Nishi, H. (2015). Pacific 187Os/188Os isotope chemistry and U-Pb geochronology: Synchroneity of global Os isotope change across OAE 2. *Earth and Planetary Science Letters*. https://doi.org/10.1016/j.epsl.2015.07.020

De Vleeschouwer, D., & Parnell, A. C. (2014). Reducing time-scale uncertainty for the Devonian by integrating astrochronology and Bayesian statistics. *Geology*, *42*(6), 491–494. https://doi.org/10.1130/G35618.1

Wendt, I., & Carl, C. (1991). The statistical distribution of the mean squared weighted deviation. *Chemical Geology: Isotope Geoscience Section*, *86*(4), 275–285. https://doi.org/10.1016/0168-9622(91)90010-T

Wignall, P. B. (2001). Large igneous provinces and mass extinctions. *Earth Science Reviews*, *53*(1–2), 1–33. https://doi.org/10.1016/S0012-8252(00)00037-4

Wotzlaw, J.-F., Schaltegger, U., Frick, D. A., Dungan, M. A., Gerdes, A., & Günther, D. (2013). Tracking the evolution of large-volume silicic magma reservoirs from assembly to supereruption. *Geology*, *41*(8), 867–870. https://doi.org/10.1130/G34366.1

Chapter 2

Paleogeography and high-precision geochronology of the Fortescue Group, Pilbara, Western Australia

This chapter will be submitted to a journal with the following authors:

Kasbohm, J.J., Schoene, B., Maclennan, S.A., Evans, D.A.D., Weiss, B.P.

ABSTRACT

While rates of Phanerozoic plate movements and magnetic field reversals have been well studied, little is known about such phenomena on early Earth. The 2.7 Ga Fortescue Group on the Pilbara craton in Western Australia has been recognized as a well-preserved sequence of Archean rift volcanics thought to derive from a flood basalt, and may have been moving rapidly at two different intervals in its depositional history. We present the results of a magnetostratigraphic study integrated with high-precision U-Pb ID-TIMS geochronology to quantify rates of plate motion and provide a continuous time series for changes in Pilbara paleogeography during these two rapid intervals. We resolve a minimum continental drift rate of 68±24 cm/a during the craton's largest geographic displacement, which exceeds both background and modern rates of plate motion. We provide a new high-precision U-Pb zircon age of 2721.23±0.88 Ma for the Tumbiana

Formation stromatolite colony, which developed as the Pilbara craton drifted from 48±9.1° to 31±9.5° paleolatitude. Although the Fortescue Group has been considered an early prototype of large igneous provinces, it presents significant differences from its Phanerozoic counterparts and would not fit the definition of a large igneous province.

INTRODUCTION

The acceptance of plate tectonics irreversibly changed the way geoscientists understand Earth's mantle dynamics and lithospheric movements. However, a point of contention in the study of Earth history is whether tectonic processes were operating during the Archean (Hamilton, 1998; De Wit, 1998), and if so, whether they were fundamentally different from those of the present. Did a hotter Earth allow for more vigorous convection and rapid plate motion (Davies, 1992), or were tectonics slowed by dehydration and thickening of the mantle lithosphere (Korenaga, 2003)?

A paleomagnetic study integrated with high-precision geochronological data has the potential to quantify rates of plate motion during the Archean. Collecting both paleomagnetic and geochronological samples within a detailed stratigraphic context may provide a continuous time series for changes in paleogeography, and removes the need for regional correlation. Continental flood basalts are ideal targets for this type of study because basalt is a faithful paleomagnetic recorder that retains a record of paleohorizontal, and is erupted in a layered stratigraphic manner. The 2.7 Ga Fortescue Group of the Pilbara craton in Western Australia (Figure 1a) has been recognized as one

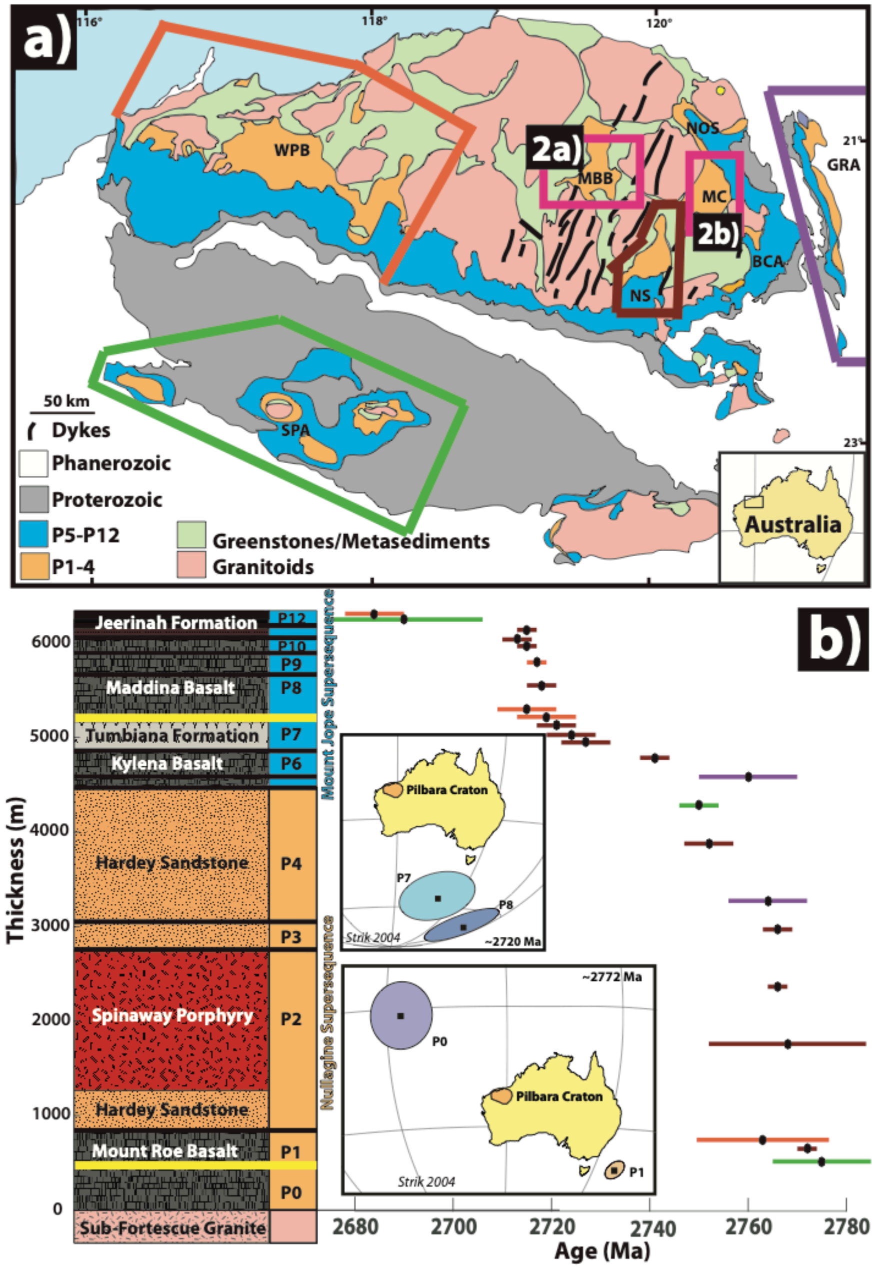

Figure 1. Geologic Context of the Fortescue Group. The areal extent of the Fortescue Group is shown in part **(a)** (after Blake et al., 2004), with different abbreviations for different regions: WPB – West Pilbara Basin; MBB – Marble Bar Basin; NS – Nullagine Syncline; MC – Meentheena Centrocline; GRA – Gregory Range Area; SPA – Southwest Pilbara Area. Prior work on the stratigraphy (Thorne & Trendall, 2001), paleomagnetism (Strik, 2004), and geochronology (Blake et al., 2004, and references therein) is summarized in part **(b)**. The colored error bars for geochronology data correspond to outcrop areas outlined in part **(a)**. Yellow lines indicate the two intervals of Fortescue stratigraphy discussed in this paper, between Packages 0 and 1 and Packages 7 and 8.

of the oldest and best-preserved Archean flood basalt successions from a continental rift (Blake, 1993), with an estimated basaltic volume of 250,000 km^3 (Thorne & Trendall, 2001). The Fortescue has the potential to not only yield insights into the rate of continental drift occurring in the Archean, but also into how these processes may have affected evolving life on Earth on the eve of the Great Oxidation Event.

The Fortescue Group has been subject to prior lithological (Thorne & Trendall, 2001), geochronological, and paleomagnetic study that suggest its suitability for a detailed stratigraphic approach (Figure 1b). Blake (2001) divided the Fortescue into 12 unconformity-bounded packages, which were later dated with SHRIMP U-Pb zircon geochronology (Blake et al., 2004). Guided by Blake's stratigraphic framework, Strik et al. (2003) published the first paleomagnetic study of the Fortescue Group, which yielded an apparent polar wander path for the ca. 60 Myr depositional history of the group, and the earliest known reversal in Earth's geomagnetic field. There are two intervals in the Fortescue Group where the Pilbara craton appears to have been moving rapidly (Strik et al., 2003; Strik, 2004). Analytical errors on the order of millions of years for the current ages for the Fortescue inhibit the calculation of Pilbara drift rates in the short time span of these potentially rapid intervals. Additionally, the difficulty in correlating rocks from distant regions of the Fortescue (Figure 1a) precludes the possibility of integrating the current paleomagnetic and geochronological datasets.

Presented here are the results of an integrated stratigraphic, paleomagnetic, and geochronological study aiming to quantify the plate velocity of the Pilbara during these two intervals of potentially rapid motion. With four new high-precision U-Pb CA-ID-TIMS ages, we are able to provide improved velocity constraints that exceed both modern and Mesoarchean drift rates. We revisit the classification of the Fortescue Group as a large igneous province, and comment on its potential for calibrating the Precambrian Geologic Time Scale. Whether or not the Fortescue meets the criteria for classification as a large igneous province, it can provide numerous insights into tectonics, magmatism, and the geodynamo of the Archean Earth system.

GEOLOGIC CONTEXT

The Fortescue Group is an ~6 km thick succession comprising flood basalts, mafic tuffs, felsic volcanics, and clastic sediments currently exposed over 40,000 km^2 of the Pilbara craton. It unconformably overlies the 3.5-2.9 Ga granite-greenstone terrane of northwestern Australia (Thorne & Trendall, 2001). The Fortescue Group is mostly undeformed, and at most was metamorphosed to the prehnite-pumpellyite-epidote phase (Blake et al., 2004). The Fortescue is divided into the lower Nullagine Supersequence, and the Upper Mount Jope Supersequence, each thought to represent a phase of continental rifting (Blake, 1993). Blake (2001) later divided these supersequences into 12 unconformity-bound packages. Even though unconformities are decreasingly obvious higher in the Fortescue stratigraphy (lacking obvious changes in bedding or lithology, or signs of erosion), significant time gaps are thought to have occurred between each package (Blake, 2001).

The onset of Fortescue Group deposition, beginning with the Nullagine Supersequence, occurred in geographically disconnected fault-bounded basins (Blake, 1993). The earliest Fortescue Group unit, the braided fluvial sedimentary succession of the Bellary Formation, is found only in the Marble Bar Basin. It is overlain by the subaerial Mount Roe Basalt (Packages 0–1, as classified by Blake (2001) and Strik (2004)), which marks the base of the Fortescue in the rest of the Pilbara. These basalts are followed by the mostly sedimentary Hardey Formation, which also consists of a felsic porphyry and minor mafic components (Packages 2–4; Blake, 2001). By the time the Mount Jope Supersequence began, the Fortescue Group had coalesced across the craton. The Mount Jope Supersequence begins with the subaerial Kylena Basalt (Packages 5–6), which gives way to the volcaniclastics and carbonates of the Tumbiana Formation (Package 7), followed by emplacement of the Maddina Basalt (Packages 8–10), and ultimately, marine sediments of the Jeerinah Formation (Packages 11–12). While the entire Fortescue Group underwent regional subsidence, increased normal faulting in the southern part of the craton led to coastal depositional environments and subaqueous volcanism, in contrast to continued subaerial conditions in the northern Pilbara (Thorne & Trendall, 2001). Four mafic dyke suites (Black Range, Mount Maggie, Five Mile Creek, and Castle Creek) have been geochemically and paleomagnetically correlated to the Fortescue Group (Strik et al., 2003). While the Fortescue Group is suggested to be one of Earth's oldest continental flood basalts, with an estimated volume of 250,000 km^3 (Thorne & Trendall, 2001) its long duration of emplacement and varied geologic record may complicate that assessment, despite the physical resemblance of its basaltic packages to other Phanerozoic large igneous provinces (Thorne & Trendall, 2001).

Determining a rate of plate motion for the Archean Pilbara craton has been dependent on findings from geochronology and paleomagnetism. When first described, the Fortescue Group was identified as Proterozoic, since it lacked the greenstones characteristic of Archean sequences (Blake, 2001). The first attempt to date the group with a Rb-Sr whole rock isochron yielded an age of 2124±195 Ma (Trendall, 1975). The first conventional zircon age for the Fortescue Group was 2768±13 Ma (upper intercept), for the Package 2 Spinaway Porphyry (Pidgeon, 1984), Arndt et al. (1991) produced the first suite of sensitive high-resolution ion microprobe (SHRIMP) zircon U-Pb ages for the Fortescue Group, which ranged from 2775±10 for a felsic volcanic rock from the base of the Mount Roe Basalt to 2684±6 for an ignimbrite member of the Jeerinah Formation. Blake et al. (2004) produced 11 high precision SHRIMP ages for the Fortescue, and ranging from 2766±2 for the Spinaway Porphyry, to 2715±2 for a reworked felsic tuff in Package 11, yet dates obtained for a number of packages overlapped within analytical uncertainty. There are no age constraints on Package 0 because it has been defined only on the basis of its paleomagnetic direction. Without precise age constraints, the observation of Strik (2004) that there was 70° of movement of the virtual geomagnetic pole (VGP) between Package 0 and 1, and 14.4° of movement across the Package 7–8 boundary could not allow for the calculation of the rate of motion for the Pilbara craton during these most notable changes in paleogeography.

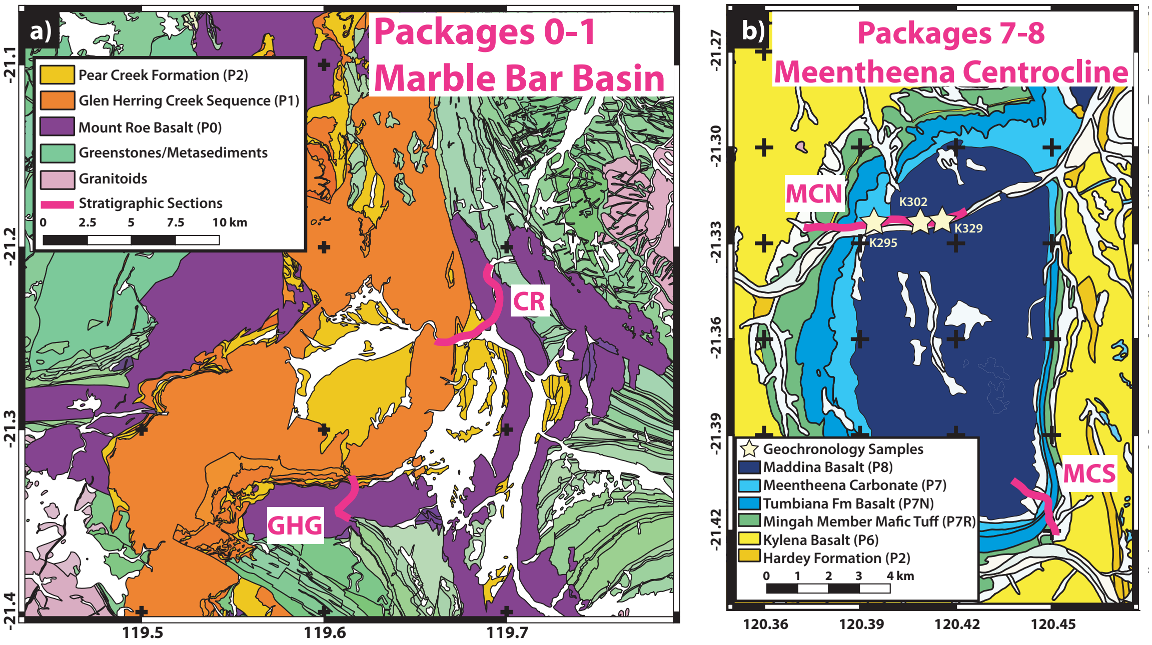

Figure 2. Regional maps with stratigraphic sections. The Glen Herring Gorge (GHG) and Coongan River (CR) Package 0-1 stratigraphic sections were measured in the Marble Bar Basin, as seen on the geologic map in part **(a)**. Sections of Packages 7-8 were measured in the Meentheena Centrocline, both North (MCN) and South (MCS) sections seen in part **(b)**.

METHODS

Two field seasons in summers 2013 and 2014 were undertaken in the Fortescue Group, in which stratigraphic sections were measured and sampled at four different localities. Two sections were measured at dm-scale across the Package 0–1 boundary at Glen Herring Gorge (GHG; 900 m) and Coongan River (CR; 900 m) (Figure 2a). For Packages 7–8, two sections were measured on opposite sides of the Meentheena Centrocline (Figure 2b); the Meentheena Centrocline North (MCN) section was 900 m thick, while the Meentheena Centrocline South (MCS) section had a thickness of 600 m. Unit thicknesses and lithologies, as well as the stratigraphic positions of paleomagnetism sample sites and geochronology samples, were recorded in each section (Figure 3).

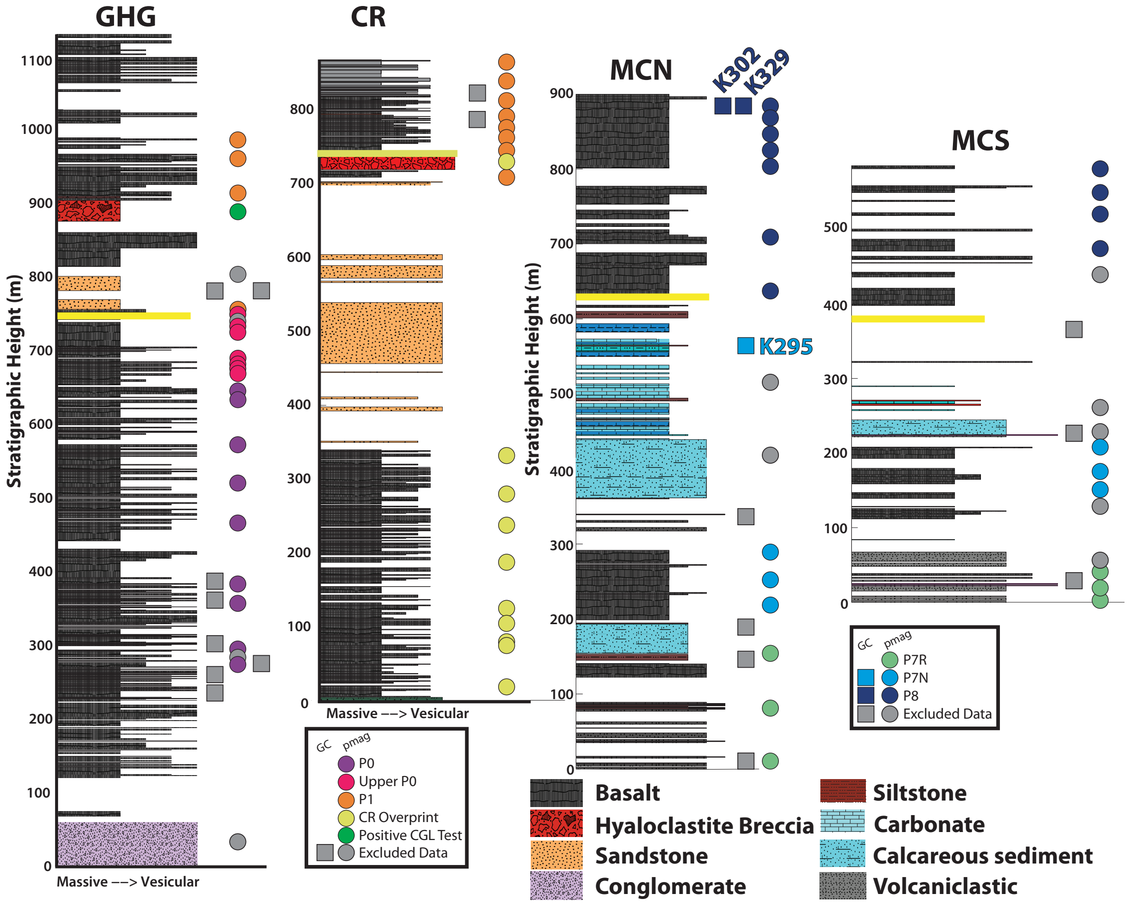

Figure 3. Measured stratigraphic sections. The four sections measured for this study are shown here, with lithological legend and positions of paleomagnetic sample sites (circles) and geochronology samples (squares), color-coded by directional group. Grey circles indicate paleomagnetic sites not included in site means due to present day field overprints or scattered directions; grey squares indicate interbeds sampled that either didn't yield zircons or yielded inherited zircons. Yellow lines indicate proposed package boundaries.

Paleomagnetism

Eight hundred forty-six paleomagnetic cores were drilled from 75 sites, and oriented by magnetic and solar compasses. Most sites were single stratigraphic horizons (lava flows) with 5–10 samples collected, but JK1319, JK1321, JK1328, and JK1417 consist of multiple stratigraphic heights with 1–2 samples per horizon. Three sites, JK1315 (GHG Package 1 hyaloclastite breccia), JK1407 (GHG Package 0 basal conglomerate), and

JK1435 (CR Package 1 hyaloclastite breccia), each consist of 20 clasts sampled for conglomerate tests on the age of paleomagnetic remanence (Watson, 1956). No significant deviation of magnetic declination from the regional average (1.7°) was observed in any of the sites sampled.

Samples were trimmed to ∼10 cm^3 specimens and analyzed at the MIT Paleomagnetism Laboratory using a cryogenic DC-SQuID magnetometer (sensitivity with sample holder $\sim 10^{-9}$ Am^2) with automated sample changer (Kirschvink et al., 2008). NRM measurements were followed by a liquid nitrogen, low-temperature demagnetization step, and underwent Alternating Field (AF) demagnetization at steps of 0, 2.5, 5, 7.5, and 10 mT. Samples then were subject to ~20 successive high-temperature demagnetization steps of decreasing intervals up to 600°C, when measurements' intensity decreased by two orders of magnitude. Typical demagnetization steps were 100°C, 200°C, 250°C, 300°C, 350°C, 400°C, 450°C, 480°C, 500°C, 520°C, 530°C, 540°C, 550°C, 560°C, 568°C, 575°C, 580°C, 585°C, 590°C, 595°C, 600°C. Each sample's magnetic components were resolved with Principal Component Analysis (Kirschvink, 1980), using software created by Jones (2002) — least-squares fits were applied to successive demagnetization steps that represented the characteristic remanence magnetization (ChRM) of each sample. All samples with mean angular deviation (MAD) greater than 10° were omitted from locality means. Mean declination (D), inclination (I), precision parameters (k), and 95% confidence limits (α95) were calculated to find the average ChRM of each sampling site using Fisher (1953) statistics.

Since almost all sandstone and all but ~20 basalt samples lost remanence at or below 580°C, the primary magnetic mineral is inferred to be magnetite. The remaining 20 basalt samples, which lost signal between 600 and 675°C, are interpreted to contain hematite, which likely formed during initial cooling, since the hematite component gives the same direction as the magnetite component for each sample. Carbonate samples lost remanence at or below 340°C, suggesting titanomagnetite or pyrrhotite as the primary magnetic mineral.

Geochronology

Twenty-one interflow units were logged and collected as potential geochronology samples in all Package 0-1 and 7-8 stratigraphic sections, and from the Package 2 Spinaway Porphyry. Four samples yielded zircons of Neoarchean age (~2.7 Ga). Sample photographs can be found in Supplemental Figure 1. Geochronology methods are as described in Kasbohm & Schoene (2018).

Zircon separation and preparation

Zircons were separated from their host rock through standard methods of crushing, gravimetric-, and magnetic-separation techniques using a Bico Braun "Chipmunk" Jawcrusher, disc mill, hand pan, hand magnet, Frantz isodynamic separator, and methylene iodide. Zircons from the least magnetic and most dense mineral separate were transferred in bulk to quartz crucibles and annealed in a muffle furnace at 900°C for 48 hours after Mattinson (2005). After annealing, 20-40 zircon grains from each sample were photographed and picked in reagent-grade ethanol for analysis. Euhedral grains with a range of morphologies were selected, while those with visible cracks, inclusions, and cores were avoided. Individual grains were transferred using stainless steel picking tools to separate 3-mL Savillex Hex beakers containing distilled acetone and taken to the clean lab for analysis.

U-Pb zircon ID-TIMS analysis

Single zircon grains were loaded into 200 uL Savillex "micro"-capsules with 100 µL 29 M HF + 15 µL 3N HNO_3 for a single leaching step in high-pressure Parr bombs at 185°C for 12 h to remove crystal domains affected by Pb-loss (Mattinson, 2005). Grains were rinsed post-leaching in 6 N HCl, MQ H2O, 3N HNO_3, and 29 M HF prior to spiking with EARTHTIME ^{205}Pb-^{233}U-^{235}U tracer and addition of 100uL 29 M HF + 15 µL 3N HNO_3 (Condon et al., 2015; McLean et al., 2015). Zircons were then dissolved to completion in Parr bombs at 210°C for 48 h. Dissolved zircon solutions were subsequently dried down, dissolved in 100 µL 6N HCl, and converted to chlorides in Parr bombs at 185°C for 12 h, after which solutions were dried again and brought up in 50 µL 3N HCl. The U-Pb and trace element aliquots were then separated by anion exchange chromatography using 50 µL columns and AG-1 X8 resin (200-400 mesh, chloride from Eichrom) (Krogh, 1973), and dried down with a microdrop of 0.015 M H_3PO_4. The dried U and Pb aliquot was loaded in a silica gel emitter (Gerstenberger & Haase, 1997) to an outgassed zone-refined Re filament.

Isotopic determinations were performed using an Isotopx Phoenix62 thermal ionization mass spectrometer (TIMS) at Princeton University, with Pb analysis performed in peak-hopping mode on a Daly-photomultiplier ion-counting detector. A correction for mass-dependent Pb fractionation was applied using a Pb fractionation of 0.182±0.041%/amu, as determined by repeat measurements of NBS982 at Princeton. Daly-photomultiplier deadtime was monitored, as determined by repeat measurements of the NBS 982 standard. Corrections for interfering isotopes under masses 202, 204, and 205 were made cycle-by-cycle by measuring masses 201 and 203 and assuming they represent $^{201}BaPO_4$ and ^{203}Tl and using natural isotopic abundances to correct for $^{202}BaPO_4$, $^{204}BaPO_4$, $^{205}BaPO_4$, and ^{205}Tl.

UO_2 measurements were performed in static mode on Faraday cups with a bulk U fractionation correction calculated from the deviation of measured $^{233}U/^{235}U$ from the known tracer $^{233}U/^{235}U$ (0.995062±0.000054 (1σ)), and an oxide composition of $^{18}O/^{16}O$ of 0.00205 was used (Nier, 1950). Data reduction was performed using the programs Tripoli and U-Pb Redux (Bowring et al., 2011; McLean et al., 2011) and the decay constants of Jaffey et al. (1971). All Pbc was attributed to laboratory blank with a mean isotopic composition determined by total procedural blank measurements (see Supplemental Table 1 for values). Two different blank corrections are applied; Pre-Side Filaments (PSF) was used for measurements made prior to January 2018, when the lab began routinely heating side filaments prior to analyses, and Side Filaments (SF) for measurements made after. Uncertainties in reported U-Pb zircon dates are at the 95% confidence level and exclude tracer calibration and decay constant uncertainties. Correction for initial ^{230}Th disequilibrium in the $^{206}Pb/^{238}U$ system was made on a fraction-by-fraction basis by estimating $(Th/U)_{magma}$ using $(Th/U)_{zircon}$ determined by

TIMS and a mean $(Th/U)_{zircon\text{-}magma}$ partition coefficient ratio of 0.19±0.11, which encompasses the range of values for $(Th/U)_{zircon\text{-}magma}$ partition coefficients obtained from glasses from a variety of volcanic settings (Claiborne et al., 2018). Uncertainties for the resulting $(Th/U)_{magma}$ were also calculated on a fraction-by-fraction basis, propagating the uncertainty in the $(Th/U)_{zircon\text{-}magma}$ partition coefficient.

RESULTS

Volcanostratigraphy

1. Packages 0-1: Mount Roe Basalt

The lowermost part of the Fortescue stratigraphy has an unconformable boundary with the underlying granite-greenstone terrain. At GHG, the Fortescue overlies the Duffer Formation, and at CR, it overlies the Apex Basalt; these are members of the greenstone Warrawoona Group, with ages ranging from 3525–3426 Ma (Van Kranendonk et al., 2007). The earliest unit in the Fortescue stratigraphy was recognized by Blake (1984) as the clastic sedimentary Bellary Formation, which outcrops discontinuously only in the Marble Bar Basin; it is the base of the section at GHG (Figure 3). Regionally, the Bellary Formation consists of up to 700 m of silicified, coarse-grained quartzofeldspathic sandstone and conglomerate, with cm–dm scale clasts of banded iron formation and sediments. The mode of deposition for the formation is interpreted as a braided fluvial environment (Blake, 1993). The next stratigraphic unit at GHG, and the base of the section at CR, is comprised of hundreds of meters of subaerial lavas of the Mount Roe Basalt. The 76 lava flows measured at GHG and the 51 lava flows measured at CR displayed similar internal textures. Most lava flows began with pipe vesicles at the base of the flow. This is followed by a massive interval, which typically constitutes the majority of flow thickness, and frequently contains isolated bands of vesicles or pods of vesicles, interpreted as representing paths of volatile escape from a cooling flow (Thorne & Trendall, 2001). Above the massive interior of the flow, the lava flow becomes increasingly vesicular until the most vesicular flow top, in which vesicles are either scattered randomly or aligned in bedding-parallel sheets. In each measured section, three categories of vesicularity were identified (1V=<25%, 2V=25–50%, 3V=>50%), corresponding to the width of stratigraphic intervals in Figure 3. Some lava flows were overlain by thin glassy interbeds, sampled as potential ash beds. Near the boundary between Packages 0 and 1, aphyric lavas were replaced with those containing mm-cm scale plagioclase phenocrysts seen singularly or in a glomeroporphyritic array.

In the Marble Bar Basin, Package 1 of Strik (2004) corresponds to the Glen Herring Creek Sequence of Blake (1984). The basal unit of the sequence is ~100 m of coarse-grained sand to gritstone, with cross beds occasionally present and showing north-to-south flow directions. Above the sandstone, a 10 m flow of a distinctive basalt with much larger plagioclase phenocrysts (few cm-scale) was observed at GHG and CR, followed by 30 m of a hyaloclastite breccia and a few meters of pillow basalts, indicating a brief interval of subaqueous eruption. Subaerial basaltic lava flows return after these basal units; 18 lava flows were measured at GHG, through the end of available basalt outcrop, and 17 lava flows were measured at CR, though basalt flows continued above the end of the measured section.

2. Packages 7-8: Tumbiana Formation & Maddina Basalt

Stratigraphic sections were measured across the Package 7–8 transition at MCN and MCS (Figure 3). Package 7 lithostratigraphically corresponds to the Tumbiana Formation, comprised of the basal Mingah Member volcaniclastic sequence overlain by the Meentheena Member carbonates and stromatolites. MCN is the Pelican Pool type section where Lipple (1975) first described the members of the Tumbiana. The first unit observed in the field was 150 m of a fine- to medium-grained basaltic sandstone, recognized as a mafic tuff (Blake, 2001). Weathered units of this sediment were marked by mm-scale vugs, while more coherent beds exhibited cross beds, teepee structures, and desiccation cracks. Accretionary lapilli of 2–10 mm diameter were prominently interbedded in the mafic tuff, either in layers of cm–dm scale thickness or filling hollows such as desiccation cracks. Lapilli showed an internally concentric structure, and are interpreted as primary pyroclastic fall deposits from subaerial hydroclastic eruptions (Thorne & Trendall, 2001). Grain size sorting of the lapilli varied from well- to poorly-sorted, and lapilli layers were sometimes observed to be reverse-graded.

Above the mafic tuff, at MCN, minor microbialite layers were observed (possibly under cover at MCS), followed by three coherent subaerial basalt flows observed at both sections. As in Package 0, the flows exhibited a massive base and vesicular top, but were substantially thicker than the Mount Roe Basalt flows (~30 m each in Package 7, rather than <10 m). The flows were aphryic and sometimes had pipe vesicles at the base of the flow. The basalts were followed by cover (with a coherent bed of lapilli observed in both sections), and then by the Meentheena Member calcareous sediments (mostly under cover at MCS). This unit began with spheroidally-weathering calcareous sandstone, which became cross-bedded with a north-to-south flow direction at the meter scale up-section. The sandstone was overlain by carbonate with laminated or ripple bedding. Climbing ripples and minor interbedded silt layers were observed in the carbonate. Stromatolites ranged from cm–m scale and were observed with both columnar and domal morphologies. A layer of well-sorted mm-scale lapilli was found near the top of the carbonate succession in both sections, and may serve as a stratigraphic tie-point; it was sampled for geochronology at MCN (K295). After a small amount of cover, the Package 8 Maddina Basalt began to outcrop.

The 200–300 m of Maddina Basalt outcropping at MCN and MCS consists of subaerial flows ranging from massive to vesicular textures, as with the other basalts described above. The massive portion of the flows commonly contain vesicle cylinders. At both MCN and MCS, the first Maddina Basalt flows are coarse-grained with visible sub-mm pyroxene phenocrysts (identified as augite in petrographic studies (Thorne & Trendall, 2001)). An interbedded accretionary lapilli unit overlies the uppermost measured flow at MCN and was sampled for geochronology (K302 and K329, described below); no lapilli tuffs were found interbedded with Package 8 lava flows at MCS.

Paleomagnetism

The stratigraphic positions of each sample site are shown with circles on Figure 3. Colored circles indicate sample sites that are included in mean directions and discussed below; greyed-out circles represent sites not discussed due to scattered ChRM directions or present local field overprints. All Site mean directions and directional groups are provided in Supplemental Table 2, with equal area plots of paleomagnetic data for each

Paleomagnetic Pole	Code	Age	Method	Pole lat	Pole long	A95	1	2	3	4	5	6	7	Total	Test
Package 0	P0	>2772±2		4.7	92.2	9.4	0	1	1	1	1	0	1	5	cgl
Upper Package 0	Upper P0	2772±2 Ma	SHRIMP-b	-8.3	115.6	13.7	1	1	1	1	1	0	1	6	cgl
Package 1	P1	>2762.111±0.68 Ma	ID-TIMS-z	-44.4	169	8.3	1	1	1	1	1	0	0	5	cgl
CR Overprint	CR Overprint			-54.7	142.6	7.7	0	1	1	0	1	0	0	3	
Package 7 Reversed	P7R			-34.1	175	10.7	0	1	1	1	1	1	0	5	fold
Package 7 Normal	P7N	>2718.69±0.99 Ma	ID-TIMS-z	-61.4	135.6	9.1	0	1	1	1	1	1	0	5	fold
Package 8	P8	2718.06±0.90 Ma	ID-TIMS-z	-68.4	175.3	9.5	1	1	1	1	1	0	0	5	fold

Table 1. Summary data for virtual geomagnetic poles. This table summarizes the paleomagnetic poles calculated for this study, compared with data from existing poles, along with ages and quality criteria of Van der Voo (1990).

directional group in Supplemental Figure 2. Table 1 summarizes VGPs calculated for this study, evaluating them against the quality criteria of Van der Voo (1990).

1. Packages 0-1: Mount Roe Basalt

For the most part, samples from Packages 0 and 1 exhibited excellent stability to thermal demagnetization, with single component behavior (Figure 4). Unblocking temperatures were most consistently high, mostly between 550 and 580°C. Samples were generally well-clustered within each locality, and four different directional groups emerged from the two sections sampled.

The lowermost basalts at GHG (0-650 m in stratigraphic height) yielded a mean ChRM direction (northwest and moderately down) that broadly agreed with the Package 0 of Strik (2004). A pole is calculated at 4.7°N, 092.2°E, A95 = 9.4° (9 sites, 57 samples). Samples collected between 650 and 752 m were found to exhibit a different direction, with declination now north and east, and steep downward inclination. These are clustered into an “Upper Package 0” direction, with a pole calculated at 8.3°S, 115.6°E, A95 = 13.7° (7 sites, 65 samples; Figure 5a). Package 1 directions are obtained at GHG

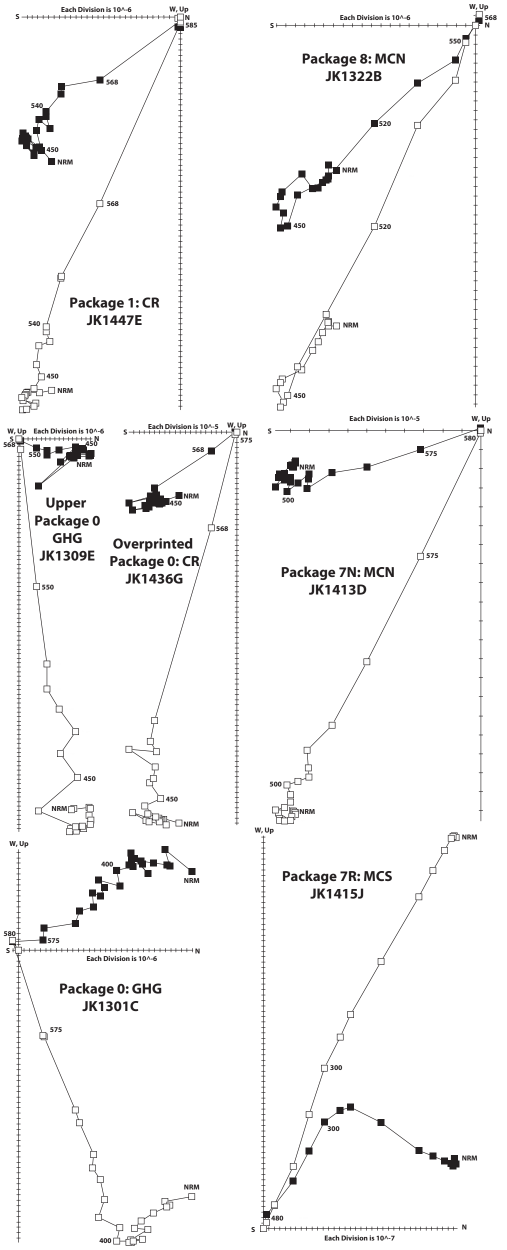

Figure 4. Orthogonal projection diagrams of paleomagnetic samples. These plots show the demagnetization behavior of representative samples from each of the directional groups in this study; numbers indicate temperature steps.

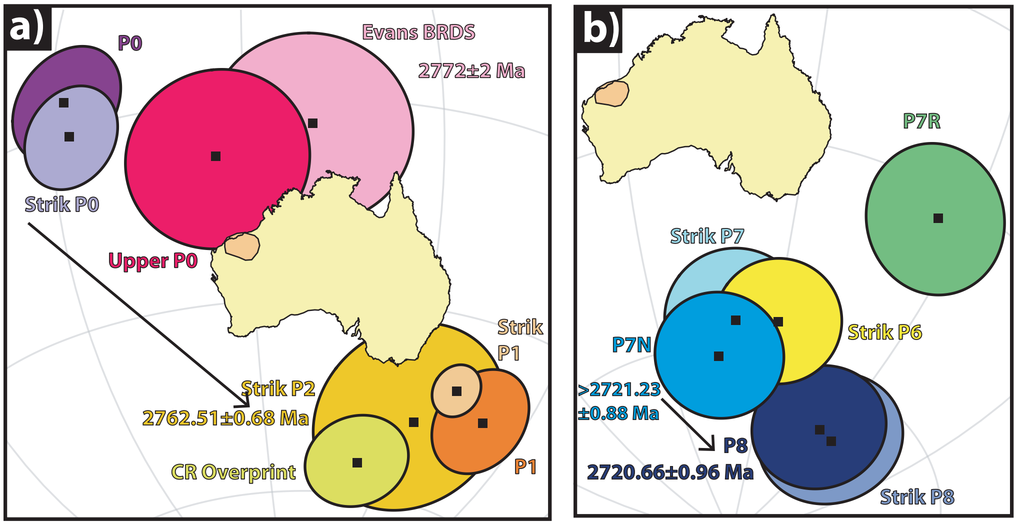

Figure 5. Virtual geomagnetic poles. The virtual geomagnetic poles calculated in this study for the Pilbara craton (highlighted in orange, in its current position) are shown in part **(a)** for Packages 0-1, and part **(b)** for Packages 7-8, compared to prior directions obtained by Strik (2004) and Evans et al. (2017). VGP ages are from this study except for that of the BRDS, which is from Wingate (1999).

beginning at 756 m, prior to the outcrop of sandstone, and continued through the top of the section. A conglomerate test on clasts of a hyaloclastite breccia at 904 m was found to be positive, following Watson (1956), with an R value of 4.8 less than the accepted cutoff of 6.98 for the 19 samples included (Figure 6), indicating that the magnetization at GHG is primary. This test also meets the criteria for positive support of uniformly random directions in the Bayesian conglomerate test of Heslop & Roberts (2018).

While only ~15 km away from GHG, CR yielded a markedly different set of paleomagnetic results in the lower half of the section. Basalt flows that were thought to represent Package 0 yielded a south and moderately dipping down ChRM direction, distinct from Package 0 at GHG; a VGP is calculated at 54.7°S, 142.6°E, A95=7.7° (9 sites, 71 samples). Strik (2004) also found that the lower basaltic unit on the east side of the Marble Bar Basin gave directions more similar to Package 1 than the expected

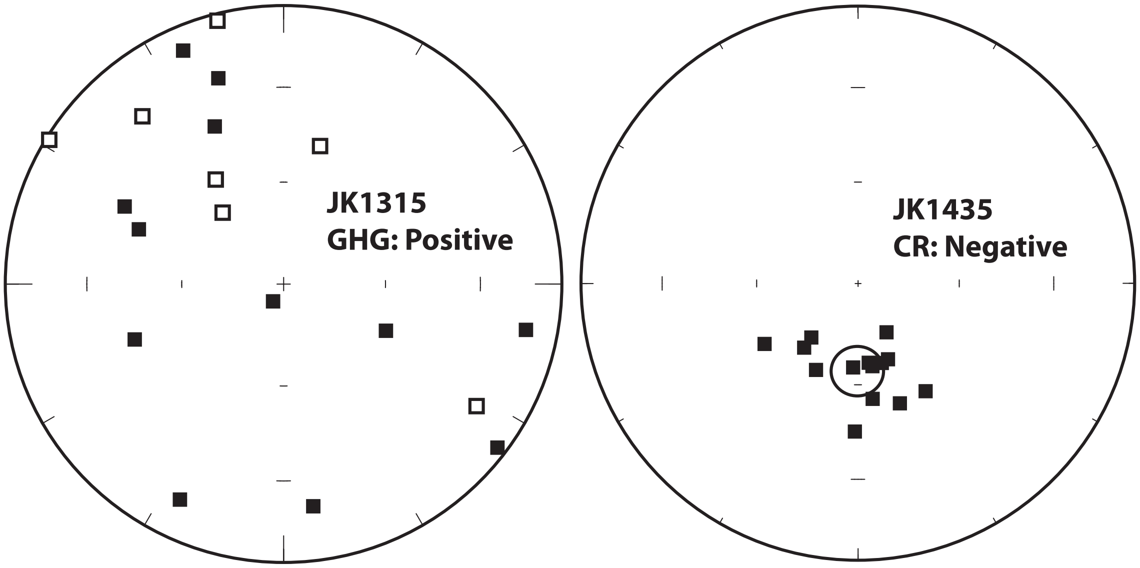

Figure 6. Conglomerate test results. These plots show the result of conglomerate tests performed on the Package 1 hyaloclastite breccia at GHG and CR. Scattered ChRM directions at GHG indicate a positive conglomerate test, and clustered directions at CR indicate a failed test.

Package 0, and grouped these eastern sites with Package 1. However, the lower CR basalts exhibited a different direction from the southeast and steeply down direction of Package 1 lava flows at both GHG and CR, which when combined yield a VGP of 44.4°S, 169°E, A05 = 8.3 (12 sites, 87 samples).

One complicating factor in interpreting the results from CR is that the hyaloclastite breccia in this section, occurring just above the base of Package 1, yielded a negative conglomerate test (Figure 6). It failed the Watson (1956) conglomerate test, with an R value of 13.6 exceeding the allowed 5% significance level of 5.98, and exhibits very strong support for unimodal directions, failing the Bayesian conglomerate test of Heslop & Roberts. In fact, these clasts broadly show the same ChRM direction as the lower CR basalt flows. For this reason, we interpret the lower CR flow direction to represent an overprint of Package 0, which was perhaps imparted during subsequent deposition of Package 2 of the Fortescue Group (Figure 5a). Because the directions obtained for Package 1 at CR cluster well with those obtained from GHG, as well as directions obtained by Strik (2004), we interpret these directions as primary, despite the failed test on the breccia in this section. The paleolatitudes obtained for the Package 0, Upper Package 0, and Package 1 poles are 51.9±9.4°, 76.3±7.7°, and 43±8.3°, respectively.

2. Packages 7-8: Tumbiana Formation & Maddina Basalt

Samples from almost all of the volcaniclastic and basalt paleomagnetic sites at the Package 7–8 transition showed excellent stability to thermal demagnetization, primarily with single-component behavior and unblocking temperatures of 480°C for the volcaniclastics in the lower part of the sections and 568-580°C for the basalts in the upper part of the sections (Figure 4). There was mostly good clustering of characteristic remanent magnetization (ChRM) directions from each locality. Sites with samples exhibiting inconsistent ChRM directions are excluded from the calculated mean directions presented here (JK1320, JK1423, with unblocking temperatures <300°), as are the calcareous sandstones and carbonates of JK1321, JK1328, and JK1424. These sedimentary units have unblocking temperatures of <340° and show a wide scatter of ChRM directions around the present local field. A low temperature overprinting event is inferred.

The Package 7 volcaniclastic sediments at the base of the MCN and MCS sections yield northwest directions dipping moderately upward, in contrast to the overlying Package 7 basalt flows, which dip steeply south and down. This directional change either results from some overprint of the volcaniclastic units, given their relatively lower unblocking temperatures, or from a magnetic field reversal. If a reversal occurred, its stratigraphic height would be 140 m at MCN, or ~30 m at MCS, as samples collected from sites at these positions yielded dual polarity. The Package 8 basalts sampled yielded a moderate south to southeast, moderately downward dipping direction of ChRM. Mean directional groups and calculated VGPs are provided in Supplemental Table 2.

In light of our field stability tests, and directional agreements from normally magnetized Package 7 and 8 with results from Strik (2004), we suggest that our sampling at MCS and MCN reflects primary magnetization from Packages 7 and 8. Some uncertainty remains regarding the reversely magnetized Package 7 volcaniclastics. Strik (2004) observed sites with reversed polarity in Package 7 (from one basalt flow in the Boodalyeri Creek Area and a correlated sill in the West Pilbara Basin), suggesting that the reversed polarity described here is a reliable result. However, there is a 20-40° offset in declination between these units and our 7R sediments. An alternative interpretation, possibly bolstered by the lower unblocking temperatures of the 7R units, is that these represent and overprinted direction. Strik (2004) described a "Medium Temperature" direction that is northwest and moderately inclined upward, but our results show a steeper inclination. The VGP we calculate for Package 7R is distant from Package 7N, as well as the results of Strik (2004) for Package 6-8 and "Medium Temperature" components (Figure 5b). If this result is trustworthy, it could be interpreted as actual plate motion occurring as Pilbara oscillated between latitudes of 48±8.9° during Package 6 (Strik 2004), 39±10.7°

during Package 7R, 48±9.1° during Package 7N and then 31±9.5° during Package 8 emplacement.

Geochronology

The stratigraphic positions of each sample are shown with squares on Figure 3. Colored squares represent samples that yielded zircon ages and are discussed below; greyed-out squares represent samples that either did not yield zircon or yielded only detrital or inherited grains. All geochronology samples collected in the Package 0-1 sections suffered from inheritance, yielding ages ~3.3 Ga; the distribution of zircon dates from GHG are shown in Supplemental Figure 3. Concordia plots with some zircon images from each sample are given in Figure 7. Weighted mean ages were calculated from a number of overlapping individual zircon dates that overlapped with the Concordia line. A small number of grains with younger ages were excluded from weighted means because they may have been affected by Pb-loss; some older grains were excluded from weighted means when they were resolvably offset in age from the weighted mean population.

1. Package 2: Spinaway Porphyry

Sample J339 (21.76549°S, 129.091807°E) of massive quartz-feldspar porphyry was collected on Route 138 (Marble Bar Road) in the Nullagine Syncline, to serve as a minimum age for Package 0-1. Thousands of zircons were separated from this sample, and they are semi-translucent, with some colorless and others orange. Zircons range in morphology from equant and small (<100 μm) to long (>200 μm) with pronounced termination points. Twenty-one were selected for analysis, and 14 were successfully dated. For this sample and others, a number of zircons were lost due to dissolution during chemical abrasion or zircon loss during chemistry; other analyses were unsuccessful due to discordance, high Pb blank relative to radiogenic Pb, or inheritance. Zircons range in age from 2767.1±4.9 Ma to 2761.5±2.1 Ma; all dates and ages reported in this paper are $^{207}Pb/^{206}Pb$ ages. The weighted mean age of the sample is 2762.51±0.68/0.68/6.9 Ma (MSWD = 0.53, n = 8). This age is somewhat offset and more precise than the prior radiometric age of 2766±2 Ma obtained for the Spinaway Porphyry (Blake et al., 2004).

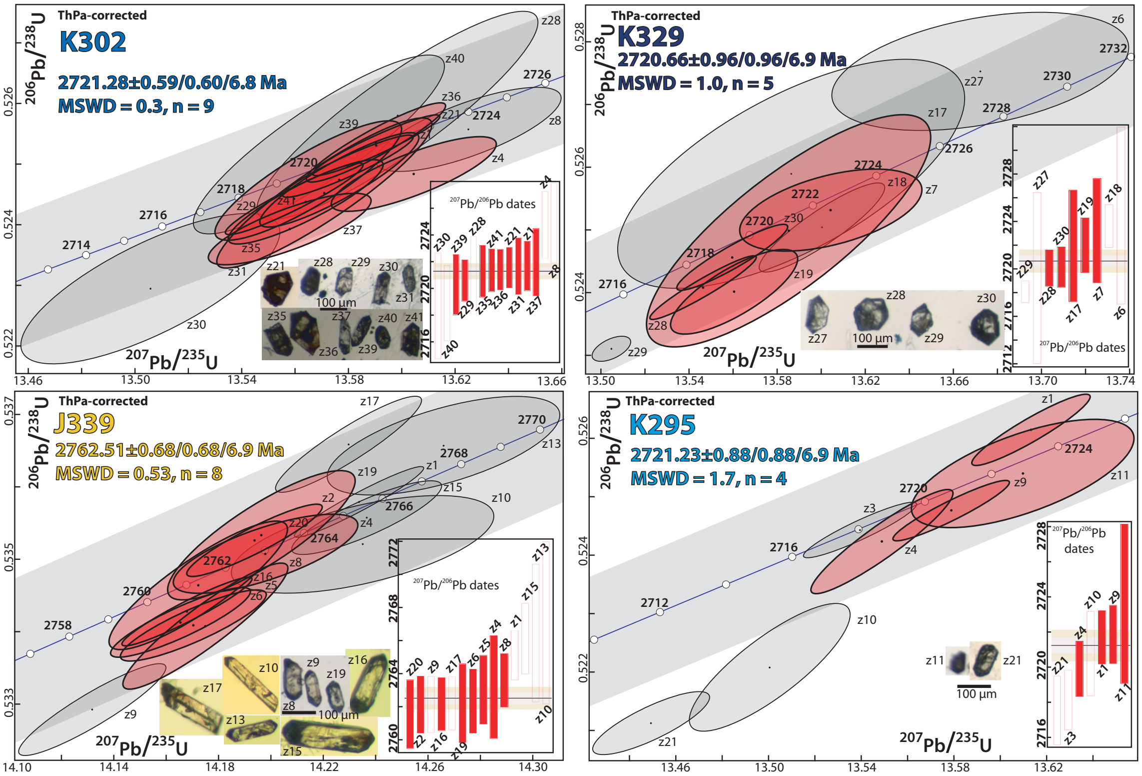

Figure 7. Geochronology data. These Concordia plots show new geochronology results from the Fortescue Group, with weighted mean ages and zircon images. Interception with the Concordia line indicates closed-system behavior.

2. Packages 7-8: Tumbiana Formation & Maddina Basalt

Sample K295 (21.323106°S, 120.394508°E) was collected in the MCN section, and is comprised of an accretionary lapilli tuff interbedded with the upper carbonates of the Meentheena Member, providing an age for uppermost Package 7. Lapilli were ~1 mm scale (Supplemental Figure 1). Approximately 50 zircons were separated from this sample, and they were ~50 µm in size, opaque, equant, and slightly rounded. Twenty-seven were selected for analysis, and 8 were successfully dated. Zircons range in age from 2747.6±2.0 Ma to 2717.5±2.0 Ma. The weighted mean age of the sample is 2721.23±0.88/0.88/6.9 Ma (MSWD = 1.7, n = 4). This age improves precision yet agrees with a SHRIMP age of 2721±4 for a tuff 300 m into the volcaniclastic section of Package 7 in the Nullagine Syncline (Blake et al., 2004).

Samples K302 and K329 were collected from two different outcrops of 1 cm-scale accretionary lapilli tuff, that were along strike from each other at the same stratigraphic height and immediately overlying the uppermost Package 8 lava flow at MCN. For sample K302 (21.323551°S, 120.409556°E), which had a lower density of lapilli, approximately 100 zircons were separated from this sample, and they were euhedral, prismatic, blocky and opaque in appearance. Forty-one zircons were selected for analysis, and 14 were successfully dated. Zircons range in age from 2724.9±3.0 Ma to 2718.7±4.0 Ma. The weighted mean age is as 2721.28±0.59/0.60/6.8 Ma (MSWD = 0.3, n = 9).

For sample K329 (21.323073°S, 120.413734°E), approximately 100 zircons were separated from this sample, and they are glassy, prismatic, and mostly euhedral in appearance, with half equant and half tabular morphologies. Thirty zircons were selected for analysis, and nine were successfully dated. Zircons range in age from 2724.5±7.4 Ma to 2718.06±0.90 Ma. The weighted mean age of the sample is 2720.66±0.96/0.96/6.9 (MSWD = 1.0, n = 5). Our ages for K302 and K329 agrees well with each other, and with the SHRIMP age of 2718±3 Ma obtained in an accretionary lapilli tuff interbedded with Package 8 lava flows in the Nullagine Syncline (Blake et al., 2004).

Because the ages obtained for these 3 samples collected from Packages 7 and 8 overlap within 2σ uncertainty, the ages were incorporated into a Markov Chain Monte Carlo simulation using a Gibbs sampler to refine their ages, based on the stratigraphic height of each sample (Schoene et al., 2019). The results of this model yield ages of 2721.57±0.64 Ma for K295, 2721.18±0.51 Ma for K302, and 2720.52±0.80 Ma for K329. These model ages overlap with our weighted mean ages, but improve precision for each age.

DISCUSSION

Our stratigraphically-constrained paleomagnetic and geochronological analyses of the Fortescue Group yield a number of insights, with implications for Pilbara plate motion during the Archean, Fortescue magmatism, and calibration of the Precambrian Geologic Timescale. These are detailed in the following sections.

1. Neoarchean Pilbara plate motion

There is a significant change in the paleogeography of the Pilbara craton during emplacement of the Package 0-1 Mount Roe Basalt flows. Between the lower and upper

Package 0 directions, there is 2970±1844 km of displacement between the VGPs, and between Upper Package 0 and Package 1, there is 6505±1778 km of displacement between the VGPs (Figure 5a). Since all zircons dated from GHG and CR were inherited, a plate velocity across these two transitions cannot be calculated at this time with our data.

However, the direction we obtain from Upper Package 0 agrees well with a new pole for the Black Range Dolerite Suite (BRDS) of dykes (Evans et al., 2017), which have been previously correlated to the Mount Roe Basalt based on geochronology. A SHRIMP zircon study yielded 2763±13 Ma and 2775±10 Ma ages for the Mount Roe Basalt (Arndt et al., 1991), a TIMS study on air-abraded zircons produced an age of 2767±3 Ma for the Mount Roe Basalt, and a SHRIMP baddeleyite study of the BRDS provided an age of 2772±2 Ma (Wingate, 1999). The age of 2772±2 Ma (Wingate, 1999) is still accepted as the best age estimate of the BRDS following additional ID-TIMS baddeleyite work on the suite (Evans et al., 2017). Given the overlapping position of the VGPs for the BRDS and Upper Package 0, the age of 2772±2 Ma can therefore be applied to this portion of the Mount Roe Basalt; the other Mount Roe Basalt ages cannot be correlated with our results, as it is unclear whether they constrain the paleogeography of Package 0 or Package 1.

We agree with the interpretation of Evans et al. (2017) that the most parsimonious explanation of the plate motion evidenced by VGPs from Package 0, Upper Package 0/BRDS, and Package 1 result from horizontal plate motion of the Pilbara craton, rather than a block rotation, the preferred interpretation of Strik (2004). In this way, as described by Evans et al. (2017), the craton crossed the polar circle during emplacement of these basalt packages. We can attempt to constrain a minimum rate of the second portion of this motion, between Upper Package 0 and Package 1, using our new high-precision Package 2 age of the Spinaway Porphyry of 2762.51±0.68 Ma as a minimum age for Package 1. We calculate a minimum rate of 68.5±24.2 cm/a, which far exceeds the fastest plate motion observed on Earth today, of ~15 cm/a.

Higher in the Fortescue Stratigraphy, during the emplacement of the Tumbiana Formation and Maddina Basalts of Packages 7 and 8, our new results also suggest significant cratonic motion to account for the 4115±1559 km of distance of the VGP from Package 7R from the poles for the underlying Package 6 and the overlying Package 7N, which overlap geographically. As Strik (2004) described, plate motion across the boundary between Packages 7 and 8 may not have been significant, as the VGPs for each unit overlap; we calculate a distance of 1984±1460 km between the VGPs of these packages (Figure 5b), with overlapping paleolatitudes within uncertainty. Our new high-precision ages from these units allow for the calculation of a maximum plate velocity. Geochronology sample J295 was collected from a lapilli tuff in the uppermost carbonates of the Tumbiana Formation, which overlie the basalt that yielded the Package 7N direction, and so its age of 2718.69±0.99 Ma serves as a minimum age for Package 7N. Combined with the Package 8 age of 2718.06±0.90 from K329, a maximum velocity could be hundreds of cm/a, though the high geological uncertainty of this estimate renders it of little utility.

Our calculated minimum plate velocity of 68.5±24.2 cm/a for the Pilbara as it drifted across the pole from the Upper Package 0 to Package 1 position is noteworthy not only because it exceeds modern rates, but also because it is far greater than the plate velocity calculated for the Pilbara craton during the Mesoarchean. A new paleomagnetic pole from the ~3180 Ma Honeyeater Basalt sampled in the Eastern Pilbara allows for a calculated minimum plate velocity of 2.5 cm/a in the 170 Ma prior to 3180 Ma, and ≥0.37±0.47 cm/a between 3180 Ma and Package 0 emplacement (Brenner et al., in press). While a hotter Archean Earth with more rapid mantle convection or true polar wander have been invoked previously as possible explanations for rapid drift rates, these results show that Archean plate velocities were not uniformly fast or decreasing monotonically.

2. Timing of Fortescue Magmatism

With an estimated basaltic volume of 250,000 km^3 (Thorne & Trendall, 2001), the Fortescue Group invites comparison to other continental flood basalt provinces, such as the Columbia River Basalt Group or the Deccan Traps. Indeed, the basaltic volume of the Fortescue is 20% greater than that of the Columbia River Basalt Group (Reidel, 2015). However, Thorne & Trendall (2001) offer three primary objections to the classification of the Fortescue Group as a continental flood basalt. While the northern exposures of the Fortescue suggest predominantly subaerial, ‘continental’ emplacement, the basalts of the southern Fortescue are predominantly subaqueous, as if they erupted in a passive continental margin. Second, the Fortescue ‘basalts’ are geochemically basaltic andesites, while other continental flood basalts are more tholeiitic. Third, while most continental flood basalts are deposited over less than 1 Ma, the depositional history of the Fortescue covers up to 60 Ma (Thorne & Trendall, 2001).

In recent decades, large igneous provinces (LIPs) have been defined more broadly to be more inclusive of a wider array of geologic expressions of voluminous magmatism, such as oceanic LIPs and silicic LIPs. While ‘continental flood basalt’ is generally used to describe a LIP on land, the subaqueous emplacement and more felsic geochemistry of the Fortescue basalts would not preclude the classification of the Fortescue as a large igneous province. However, the 60 Ma duration of Fortescue emplacement would be its most notable disqualifying factor, as LIPs should occur over a short duration (<5 Ma), or with multiple short pulses over a maximum of a few 10s of Ma (Ernst & Youbi, 2017). A recent review of high-precision geochronology of large igneous provinces suggests that all well-dated LIPs were emplaced in <1 Ma (Kasbohm et al., 2020).

Since the Fortescue Group contains three distinct basaltic formations (Mount Roe, Kylena, and Maddina Basalts), perhaps each of these could be considered as individual LIPs. Volume estimates for each of these units are 72,000 km^3, 68,000 km^3, and 110,000 km^3 ((Thorne & Trendall, 2001), though these may be hampered by limited geologic preservation. While the Mount Roe and Kylena Basalts no longer satisfy the >100,000 km^3 volume cutoff for LIP classification, the Maddina Basalt (Packages 8-10 could still qualify as a continental flood basalt with its larger volume. Our geochronology shows a minimum duration of 1.05±1.02 Ma for the emplacement of Package 8 at MCN, suggesting that the rest of the Maddina Basalt could have been emplaced in a few Ma or less.

While the Fortescue Group may or may not meet specific criteria for LIP classification, assessing its emplacement dynamics may yield insights for an early prototype of LIP magmatism. One aspect of more recent LIP emplacement that is not always well-known is the relative timing of intrusive and extrusive magmatism (Kasbohm et al., 2020). By contrast, our paleomagnetic correlation showing the temporal coincidence of the Mount Roe Basalt flows of Upper Package 0 and the intrusive activity of the BRDS conclusively places the widespread BRDS within the temporal and stratigraphic context of the Fortescue Group, and allows for a temporal correlation between dikes and lava flows.

Another crucial aspect of LIP emplacement to consider is the duration of hiatuses. The Fortescue Group, with its prolonged sedimentary or felsic-intrusive dominated intervals, is more complicated than a typical LIP. The Package 1-10 subdivisions of Blake (2001) were initially envisioned to be bounded by significant time breaks in the Fortescue stratigraphy. Our geochronology sampling at the boundary between Packages 7 and 8 yield the first high-precision temporal constraints on one of these hiatuses, since J295 is in the uppermost Package 7, and K302 overlies the Maddina Basalts in Package 8. While Blake (2001) noted the Package 7–8 boundary was likely relatively short (1-5 Ma), and subsequent geochronology produced a duration of ~3 Ma (Blake et al., 2004), we show that the time elapsed between these two samples (whose dates overlap within uncertainty) is 1.05±1.02 Ma, suggesting that the actual amount of time elapsed before Package 8 volcanism started is much less. Therefore, it seems that time breaks between these packages may be less significant than previously thought.

3. Calibrating the Precambrian Geologic Timescale

The integrated magnetostratigraphy and high-precision geochronology of the Fortescue presented here offers a detailed look at two different intervals of basalt eruptions during the emplacement of one of Earth's oldest continental flood basalts. Indeed, the base of the Mount Roe Basalts has been suggested as a Precambrian Global Boundary Stratotype Section and Point (GSSP) for the lower boundary of the Neoarchean Era (and proposed 'Methanian' Period) at ~2780 Ma, because the Fortescue Group, as potentially one of the first continental flood basalts, exemplifies the widespread crustal formation, global magmatism, and microbial life speculated to be characteristic of this time in Earth history (Van Kranendonk et al., 2012). Similarly, Ernst et al. (2020) suggest that LIPs provide natural boundaries for the Geologic Timescale based on their useful frequency of 20-30 Ma and their suggested connections to environmental change. Apart from its lack of a high-precision age constraint, the base of the Mount Roe Basalt (Package 0) seems like a suitable Precambrian GSSP, and future work is required to obtain a date for this interval, with two-fold goals of timescale calibration and velocity calculations.

Another aspect of the Geologic Timescale to which the Fortescue may contribute is the global magnetostratigraphy recorded in the Geomagnetic Polarity Timescale (GPTS). Strik (2003) documented Earth's oldest known magnetic field reversal between Packages 1 and 2, which we now constrain with a minimum age of 2762.11±0.66 Ma on the

Spinaway Porphyry, and the previously existing maximum age of 2772±2 Ma from the BRDS (Evans et al., 2017; Wingate, 1999). While polarity reverts to normal after Package 2, our data and analyses described in Strik (2004) suggest that a second reversed polarity interval occurs at the base of Package 7, in the Tumbiana Formation, at ~2720 Ma. Normal polarity returns at or before 2718.69±0.99, based on our zircon age from the Tumbiana stromatolites overlaying the normally magnetized basalts. Thus, we find that Earth's polarity reversed four times between 2772 and 2718 Ma, reflecting past observations that magnetic field reversals were more infrequent in the Precambrian (Dunlop & Yu, 2004). The durations of each polarity chron defined would potentially be ~10 Ma during the Package 2 reversed interval, ~35 Ma during the normal chron when Packages 3-6 were deposited, and ~1 Ma for the reversed interval in Package 7. The pattern of the long normal chron (during the deposition of Packages 3-6) followed by the brief reversed interval in Package 7 reflects patterns in other Precambrian successions, where long intervals (30-40 Ma) of uniform polarity are juxtaposed with intervals of rapid reversals (Elston et al., 2002; Gallet et al., 2012; Pavlov & Gallet, 2010). This alternation between reversing and non-reversing regimes may reflect the sensitivity of the geodynamo to changing heat flux patterns at the core-mantle boundary, in a time prior to the crystallization of the inner core (Gallet et al., 2012).

CONCLUSIONS

By using a stratigraphic approach to integrate paleomagnetic and high-precision geochronological data from the Fortescue Group, we provide crucial new constraints on plate velocities, large igneous province magmatism, and magnetic field reversals in the

Archean. We show that the Pilbara craton drifted at a minimum rate of 68.5±24.2 cm/a over an interval of 10 Ma in the Neoarchean, a rate far exceeding both background drift rates for the craton, and modern rates of plate motion. Our new age of 2721.23±0.88 Ma for the Tumbiana Formation provides the first high-precision U-Pb zircon age constraint on Archean stromatolites. The new constraints described here on plate tectonic rates, timing of magmatism, and magnetic field reversals show how one of Earth's oldest large igneous provinces may enlighten future investigations of its successors.

ACKNOWLEDGEMENTS

We thank A. Maloof, A. Campion, and E. Bolton for assistance in the field, and R. Fu for support in the MIT Paleomagnetism Lab.21919 This material is based upon work supported by the NSF Graduate Research Fellowship under grant no. DGE-1656466.

REFERENCES

Arndt, N. T., Nelson, D. R., Compston, W., Trendall, A. F., & Thorne, A. M. (1991). The age of the Fortescue Group, Hamersley Basin, Western Australia, from ion microprobe zircon U-Pb results. *Australian Journal of Earth Sciences*, *38*(3), 261–281. https://doi.org/10.1080/08120099108727971

Blake, T. S. (1993). Late Archaean crustal extension, sedimentary basin formation, flood basalt volcanism and continental rifting: the Nullagine and Mount Jope Supersequences, Western Australia. *Precambrian Research*, *60*(1–4), 185–241. https://doi.org/10.1016/0301-9268(93)90050-C

Blake, T. S. (2001). Cyclic continental mafic tuff and flood basalt volcanism in the Late Archaean Nullagine and Mount Jope supersequences in the eastern Pilbara, Western Australia. *Precambrian Research*, *107*(3–4), 139–177. https://doi.org/10.1016/S0301-9268(00)00135-2

Blake, T. S., Buick, R., Brown, S. J. A., & Barley, M. E. (2004). Geochronology of a Late Archaean flood basalt province in the Pilbara Craton, Australia: Constraints on basin evolution, volcanic and sedimentary accumulation, and continental drift rates. *Precambrian Research*, *133*(3–4), 143–173. https://doi.org/10.1016/j.precamres.2004.03.012

Bowring, J. F., McLean, N. M., & Bowring, S. A. (2011). Engineering cyber infrastructure for U-Pb geochronology: Tripoli and U-Pb-Redux. *Geochemistry, Geophysics, Geosystems*, *12*(6). https://doi.org/10.1029/2010GC003479

Claiborne, L. L., Miller, C. F., Gualda, G. A. ., Carley, T. L., Covey, A. K., Wooden, J. L., & Fleming, M. A. (2018). Zircon as Magma Monitor: Robust,Temperature-Dependent Partition Coefficients from Glass and Zircon Surface and Rim Measurements from Natural Systems. In D. E. Moser, F. Corfu, J. R. Darling, S. M. Reddy, & K. Tait (Eds.), *Microstructural Geochronology: Planetary Records Down to Atom Scale* (1st ed., pp. 3–33).

Condon, D. J., Schoene, B., McLean, N. M., Bowring, S. A., & Parrish, R. R. (2015). Metrology and traceability of U-Pb isotope dilution geochronology (EARTHTIME Tracer Calibration Part I). *Geochimica et Cosmochimica Acta*, *164*, 464–480. https://doi.org/10.1016/j.gca.2015.05.026

Davies, G. F. (1992). On the emergence of plate tectonics. *Geology*, *20*(11), 963–966. https://doi.org/10.1130/0091-7613(1992)020<0963:OTEOPT>2.3.CO;2

Dunlop, D. J., & Yu, Y. (2004). Intensity and polarity of the geomagnetic field during precambrian time. *Geophysical Monograph Series*, *145*, 85–100. https://doi.org/10.1029/145GM07

Elston, D. P., Enkin, R. J., Baker, J., & Kisilevsky, D. K. (2002). Tightening the Belt: Paleomagnetic-stratigraphic constraints on deposition, correlation, and deformation of the Middle Proterozoic (ca. 1.4 Ga) Belt-Purcell Supergroup, United States and Canada. *Bulletin of the Geological Society of America*, *114*(5), 619–638. https://doi.org/10.1130/0016-7606(2002)114<0619:TTBPSC>2.0.CO;2

Ernst, R. E., & Youbi, N. (2017). How Large Igneous Provinces affect global climate, sometimes cause mass extinctions, and represent natural markers in the geological record. *Palaeogeography, Palaeoclimatology, Palaeoecology*, *478*, 30–52. https://doi.org/10.1016/j.palaeo.2017.03.014

Evans, D. A. D., Smirnov, A. V., & Gumsley, A. P. (2017). Paleomagnetism and U–Pb geochronology of the Black Range dykes, Pilbara Craton, Western Australia: a Neoarchean crossing of the polar circle. *Australian Journal of Earth Sciences*, *64*(2), 225–237. https://doi.org/10.1080/08120099.2017.1289981

Gallet, Y., Pavlov, V., Halverson, G., & Hulot, G. (2012). Toward constraining the long-term reversing behavior of the geodynamo: A new “Maya” superchron ~1 billion years ago from the magnetostratigraphy of the Kartochka Formation (southwestern Siberia). *Earth and Planetary Science Letters*, *339–340*, 117–126. https://doi.org/10.1016/j.epsl.2012.04.049

Gerstenberger, H., & Haase, G. (1997). A highly effective emitter substance for mass spectrometric Pb isotope ratio determinations. *Chemical Geology*, *136*(3–4), 309–312. https://doi.org/http://dx.doi.org/10.1016/S0009-2541(96)00033-2

Hamilton, W. B. (1998). Archean magmatism and deformation were not products of plate tectonics. *Precambrian Research*, *91*(1–2), 143–179. https://doi.org/10.1016/S0301-9268(98)00042-4

Jaffey, A. H., Flynn, K. F., Glendenin, L. E., Bentley, W. C., & Essling, A. M. (1971). Precision measurement of half-lives and specific activities of ^{235}U and ^{238}U. *Physical Review C*, *4*(5), 1889–1906. https://doi.org/10.1103/PhysRevC.4.1889

Kasbohm, J. J., & Schoene, B. (2018). Rapid eruption of the Columbia River flood basalt and correlation with the mid-Miocene climate optimum. *Science Advances*, *4*(9), 1–

8. https://doi.org/10.1126/sciadv.aat8223

Kasbohm, J. J., Schoene, B., & Burgess, S. D. (2020). Radiometric constraints on the timing, tempo, and effects of large igneous province emplacement. In R. E. Ernst, A. J. Dickson, & A. Bekker (Eds.), *Large Igneous Provinces: A Driver of Global Environmental and Biotic Changes*. American Geophyiscal Union.

Korenaga, J. (2003). Energetics of mantle convection and the fate of fossil heat. *Geophysical Research Letters*, *30*(8), 1–4. https://doi.org/10.1029/2003GL016982

Van Kranendonk, M. J., Altermann, W., Beard, B. L., Hoffman, P. F., Johnson, C. M., Kasting, J. F., et al. (2012). *A Chronostratigraphic Division of the Precambrian: Possibilities and Challenges*. *The Geologic Time Scale 2012* (Vol. 1–2). https://doi.org/10.1016/B978-0-444-59425-9.00016-0

Krogh, T. E. (1973). A low-contamination method for hydrothermal decomposition of zircon and extraction of U and Pb for isotopic age determinations. *Geochimica et Cosmochimica Acta*, *37*(3), 485–494. https://doi.org/10.1016/0016-7037(73)90213-5

Mattinson, J. M. (2005). Zircon U-Pb chemical abrasion ("CA-TIMS") method: Combined annealing and multi-step partial dissolution analysis for improved precision and accuracy of zircon ages. *Chemical Geology*, *220*(1–2), 47–66. https://doi.org/10.1016/j.chemgeo.2005.03.011

McLean, N. M., Bowring, J. F., & Bowring, S. A. (2011). An algorithm for U-Pb isotope dilution data reduction and uncertainty propagation. *Geochemistry, Geophysics, Geosystems*, *12*(6). https://doi.org/10.1029/2010GC003478

McLean, N. M., Condon, D. J., Schoene, B., & Bowring, S. A. (2015). Evaluating uncertainties in the calibration of isotopic reference materials and multi-element isotopic tracers (EARTHTIME Tracer Calibration Part II). *Geochimica et Cosmochimica Acta*, *164*, 481–501. https://doi.org/10.1016/j.gca.2015.02.040

Nier, A. O. (1950). A redetermination of the relative abundances of the isotopes of carbon, nitrogen, oxygen, argon, and potassium. *Physical Review*, *77*(6), 789–793. https://doi.org/10.1103/PhysRev.77.789

Pavlov, V., & Gallet, Y. (2010). Variations in geomagnetic reversal frequency during the Earth's middle age. *Geochemistry, Geophysics, Geosystems*, *11*(1), n/a-n/a. https://doi.org/10.1029/2009gc002583

Reidel, S. P. (2015). The Columbia River Basalt Group: a flood basalt province in the Pacific Northwest, USA. *Geoscience Canada*, *42*, 151–168. https://doi.org/10.1007/s13398-014-0173-7.2

Schoene, B., Eddy, M. P., Samperton, K. M., Keller, C. B., Keller, G., Adatte, T., & Khadri, S. F. R. (2019). U-Pb constraints on pulsed eruption of the Deccan Traps across the end-Cretaceous mass extinction. *Science*, *363*(6429), 862–866. https://doi.org/10.1126/science.aau2422

Strik, G., Blake, T. S., Zegers, T. E., White, S. H., & Langereis, C. G. (2003). Palaeomagnetism of flood basalts in the Pilbara Craton, Western Australia: Late Archaean continental drift and the oldest known reversal of the geomagnetic field. *Journal of Geophysical Research*, *108*(B12), 1–21. https://doi.org/10.1029/2003jb002475

Strik, G. H. M. A. (2004). *Palaeomagnetism of late Archaean flood basalt terrains: implications for early Earth geodynamics and geomagnetism*. Universiteit Utrecht.

Thorne, A., & Trendall, A. (2001). *Geology of the Fortescue Group, Pilbara Craton,*

Western Australia. *Bulletin of Geological Survey of Western Australia* (Vol. 144).
Van der Voo, R. (1990). The reliability of paleomagnetic data. *Tectonophysics*, *184*(1), 1–9. https://doi.org/10.1016/0040-1951(90)90116-P
Watson, G. S. (1956). A test for randomness of directions. *Geophysical Supplements to the Monthly Notices of the Royal Astronomical Society*, *7*(4), 160–161.
Wingate, M. T. D. (1999). Ion microprobe baddeleyite and zircon ages for Late Archaean mafic dykes of the Pilbara Craton, Western Australia. *Australian Journal of Earth Sciences*, *46*(4), 493–500. https://doi.org/10.1046/j.1440-0952.1999.00726.x
De Wit, M. J. (1998). On Archean granites, greenstones, cratons and tectonics: does the evidence demand a verdict? *Precambrian Research*, *91*(1–2), 181–226. https://doi.org/10.1016/S0301-9268(98)00043-6

SUPPLEMENTAL MATERIALS

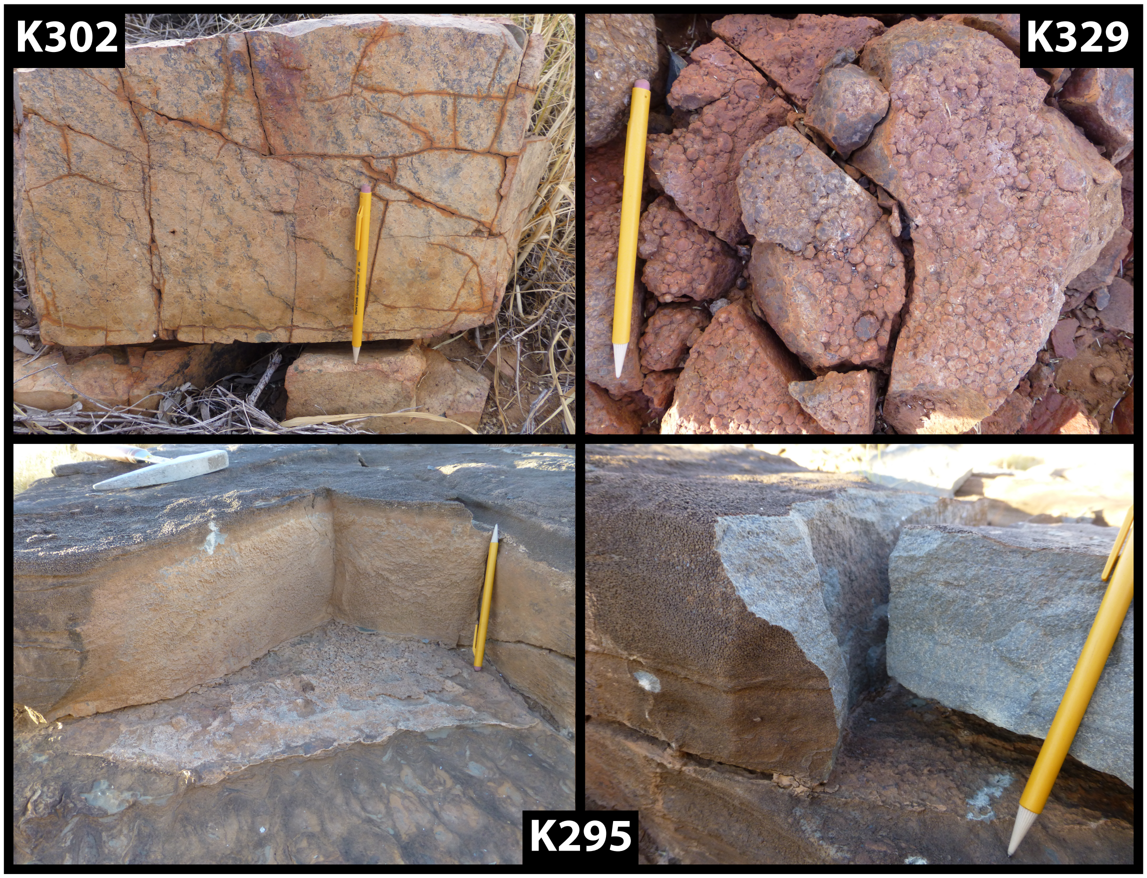

Supplemental Figure 1. Geochronology sample photos. Outcrop photos from geochronology samples K295, K302, and K329 are provided here, with pencil for scale (Photo credit: Jennifer Kasbohm, Princeton University).

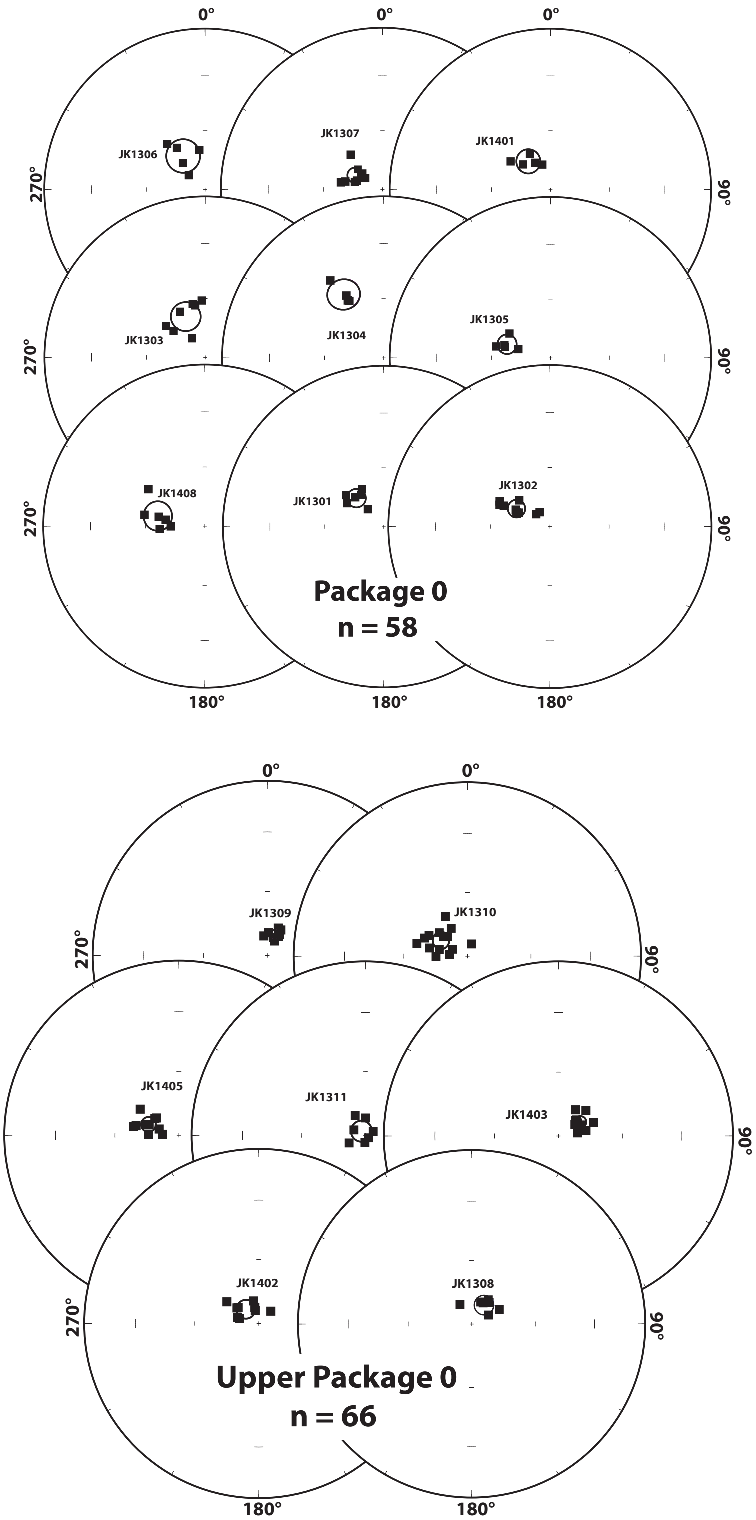

Supplemental Figure 2. Equal area plots of paleomagnetic sites. ChRM directions for each paleomagnetic sample included in all sample site means used to calculate virtual geomagnetic poles are shown in these plots. Plots are arranged in stratigraphic order, from bottom left to right, to top left to right.

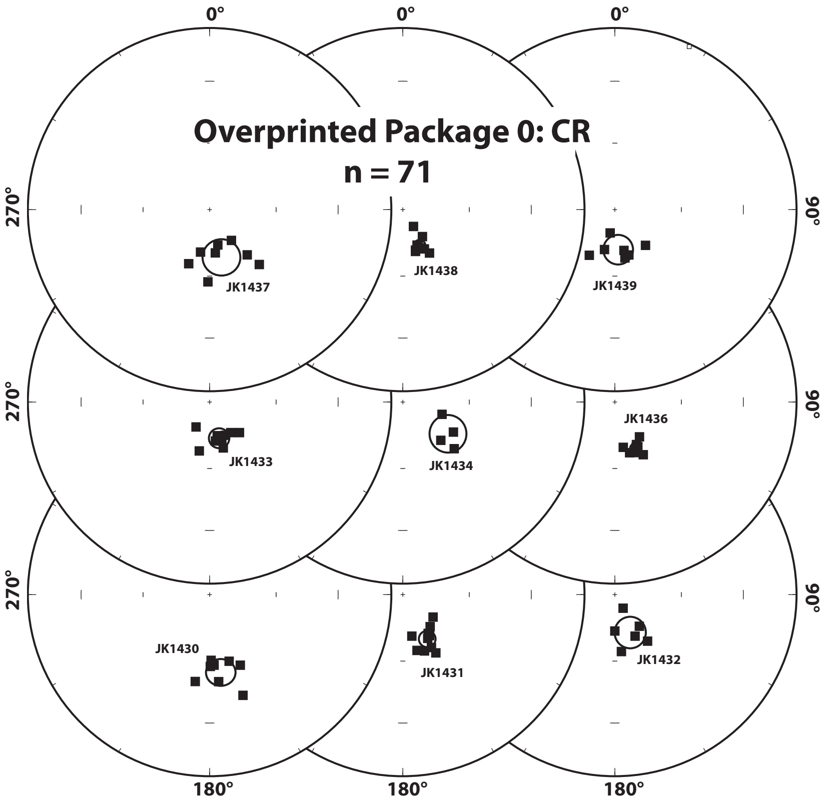

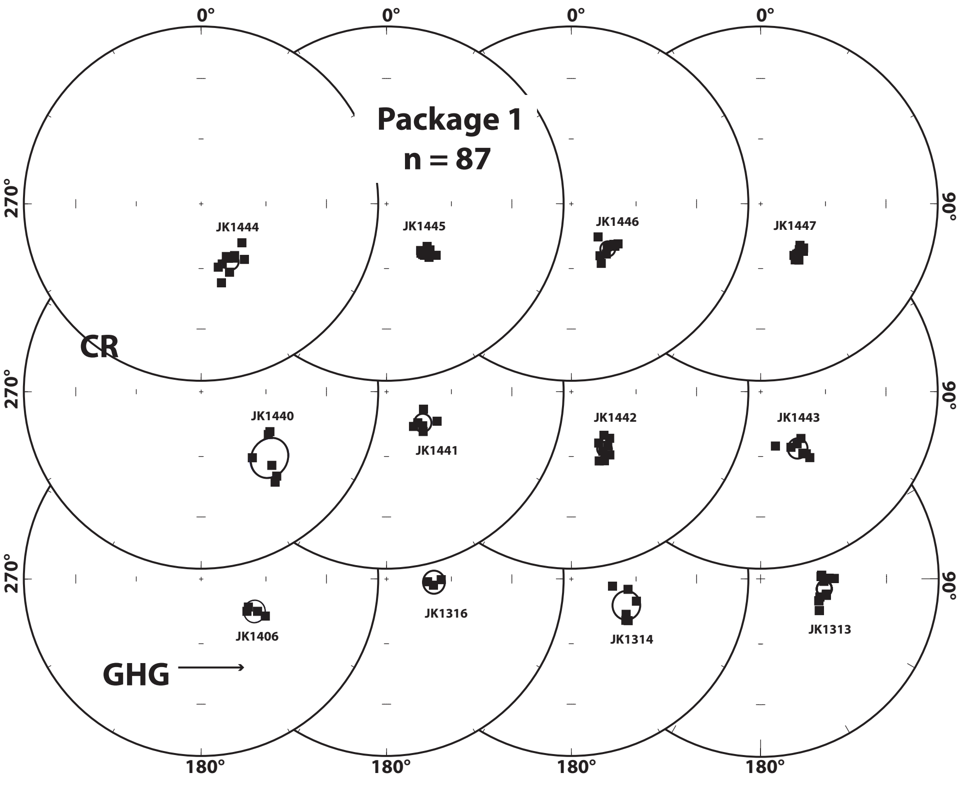

Supplemental Figure 2 (cont)

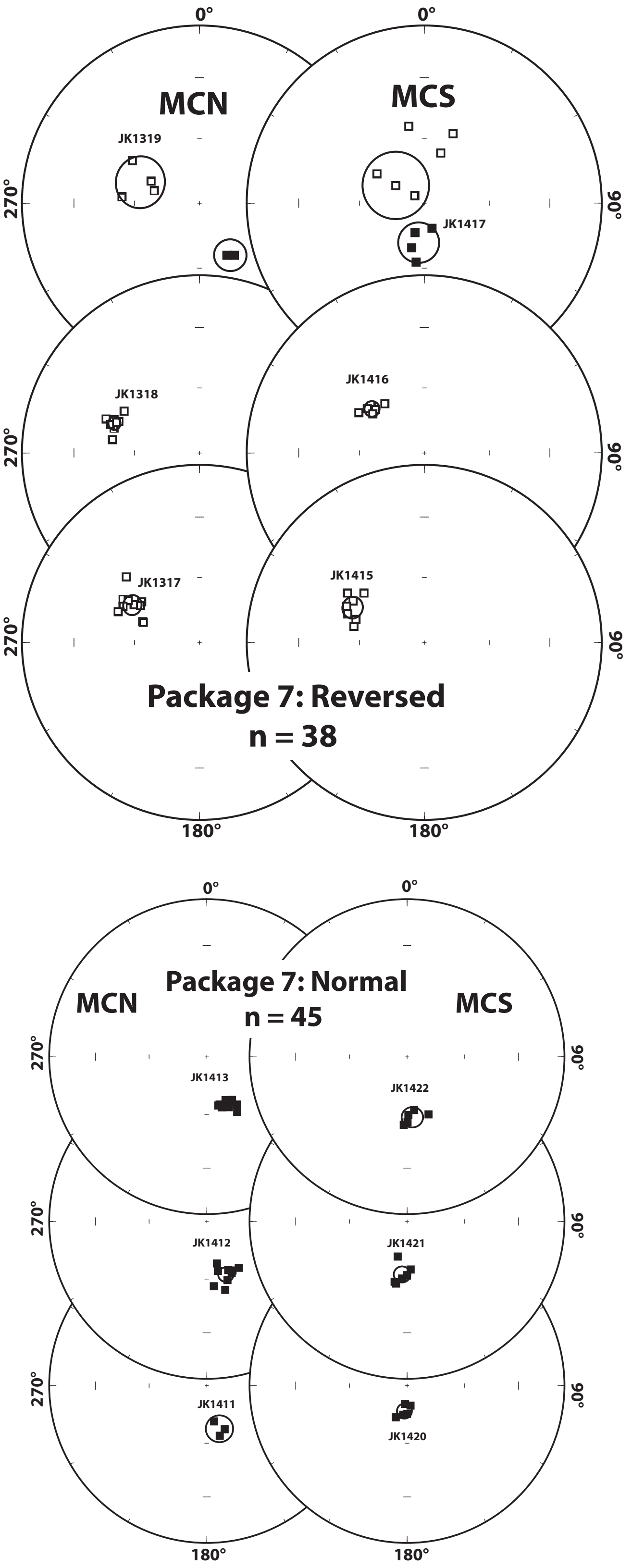

Supplemental Figure 2 (cont)

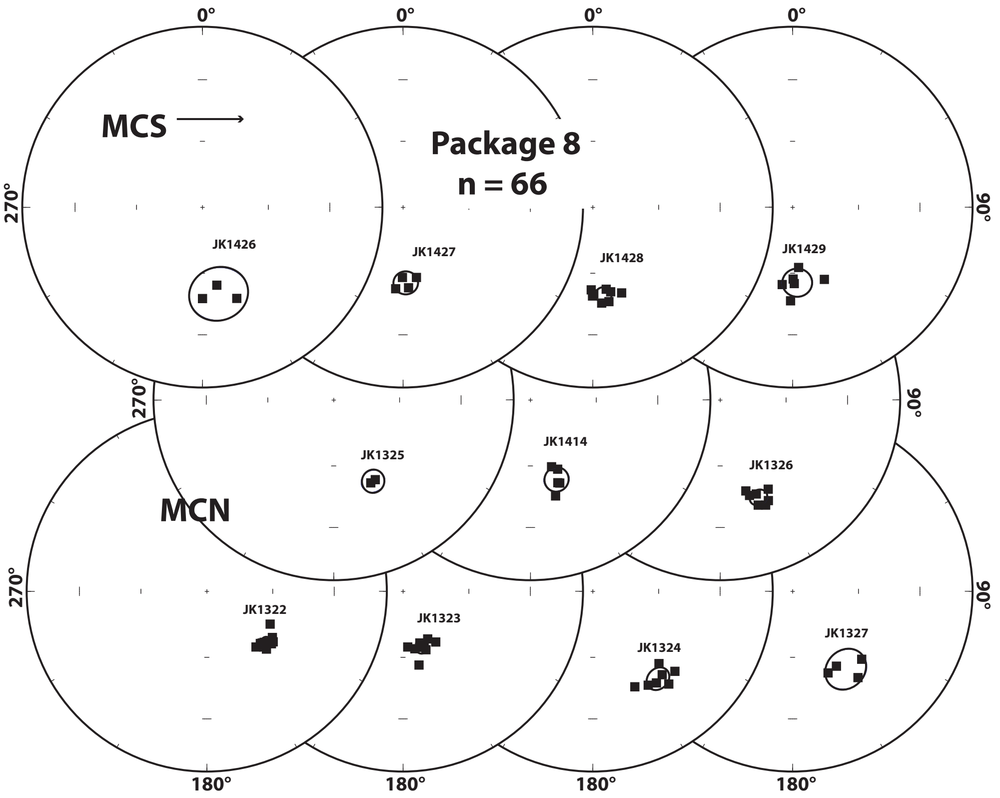

Supplemental Figure 2 (cont)

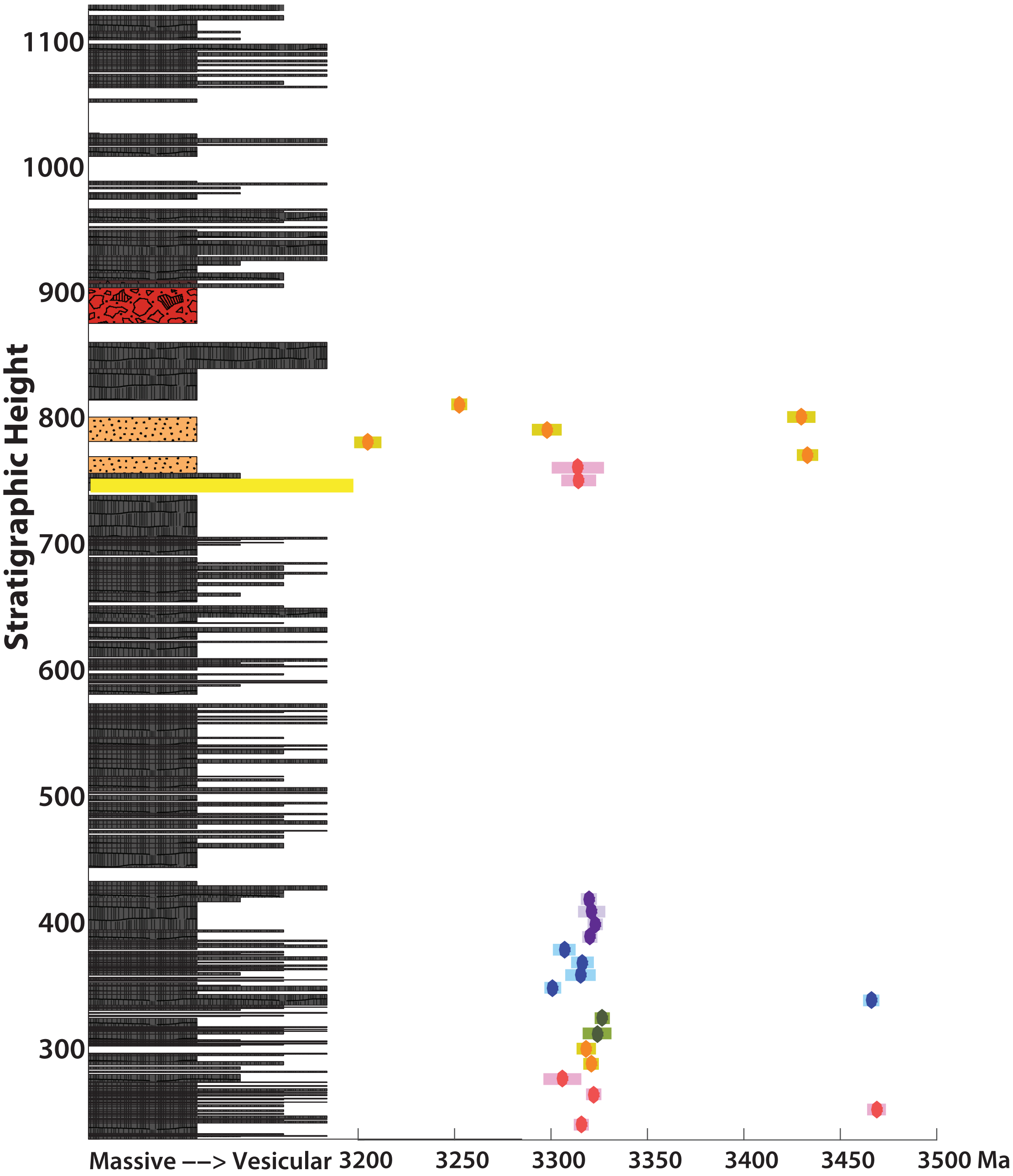

Supplemental Figure 3. Glen Herring Gorge zircon dates. This figure shows the distribution of zircon dates obtained for geochronology samples collected from the Glen Herring Gorge section. These dates are similar to ages reported for the Duffer (3465±3 Ma) and Wyman Formations (3325±4 Ma), which outcrop near the basalt unconformity at GHG, as well as the Corunna Downs Granitoid Complex (3313-3300 Ma), located immediately southeast of the Marble Bar Basin (Australian Stratigraphic Units Database).

Supplemental Table 1. U-Pb geochronology data. Data acquired by CA-ID-TIMS is presented in a separate file, with various corrections as specified in the notes beneath the table.

Supplemental Table 2. Paleomagnetic site mean directions and calculated poles. Directional and statistical data for each paleomagnetic sample site are provided in this table, with virtual geomagnetic pole data calculated for each directional group.

Supplemental Table 1: U-Pb geochronology data

	Dates (Ma)							Composition					Isotopic Ratios									
Sample	206Pb/ 238U	±2σ absolute	207Pb/ 235U	±2σ absolute	207Pb/ 206Pb	±2σ absolute	% disc	Pb* (pg)	Pbc (pg)	Pb*/ Pbc	Th/ U	Th/ U(magma)	206Pb/ 204Pb	208Pb/ 206Pb	206Pb/ 238U	±2σ %	207Pb/ 235U	±2σ %	207Pb/ 206Pb	±2σ %	Corr. coef.	Blank model
zircon	a		b		a,b		c	d	e	f	g	h	i	j	j		j		j			
K329	**21.323073°S, 120.413734°E**																					
z6	2731.0	4.0	2727.3	4.7	2724.5	7.4	-0.2	16.63	1.31	12.74	0.66	3.47	685	0.18	0.5275145	0.179	13.6722127	0.493	0.1880609	0.450	0.404	PSF
z7	2721.7	2.8	2722.6	2.9	2723.2	4.4	0.1	82.83	3.82	21.70	0.58	3.05	1173	0.16	0.5253020	0.124	13.6043639	0.304	0.1879158	0.263	0.495	PSF
z17	2720.3	7.8	2721.2	4.5	2721.9	4.7	0.1	10.07	0.55	18.18	0.51	2.68	1035	0.14	0.5249721	0.353	13.5852023	0.475	0.1877690	0.282	0.804	SF
z18	2720.5	3.0	2722.3	2.0	2723.6	1.8	0.1	41.10	0.36	114.59	0.61	3.21	6298	0.17	0.5250250	0.135	13.6003421	0.210	0.1879593	0.103	0.892	SF
z19	2716.2	2.9	2719.5	2.0	2722.0	2.3	0.2	103.13	1.39	74.29	0.64	3.37	4067	0.18	0.5239994	0.129	13.5604725	0.213	0.1877751	0.135	0.777	SF
z27	2724.1	7.7	2721.3	5.5	2719.2	7.2	-0.2	5.33	0.52	10.21	0.52	2.74	589	0.14	0.5258810	0.347	13.5863766	0.580	0.1874607	0.436	0.659	SF
z28	2716.5	2.1	2718.5	1.7	2720.1	1.5	0.1	208.36	0.59	354.67	0.58	3.05	19553	0.16	0.5240655	0.097	13.5463741	0.178	0.1875563	0.085	0.950	SF
z29	2712.33	0.85	2715.62	0.61	2718.06	0.90	0.2	127.62	1.10	116.45	0.54	2.84	6485	0.15	0.5230906	0.038	13.5047621	0.065	0.1873286	0.043	0.547	SF
z30	2718.5	2.2	2719.5	1.8	2720.2	1.7	0.1	58.42	0.49	118.44	0.63	3.32	6481	0.17	0.5245495	0.100	13.5596269	0.186	0.1875665	0.095	0.924	SF
K302	**21.323551°S, 120.409556°E**																					
z1	2719.2	3.3	2720.6	2.1	2721.7	1.8	0.1	184.51	2.03	91.06	0.59	3.11	4858	0.16	0.5247258	0.148	13.5766179	0.220	0.1877385	0.105	0.892	PSF
z4	2719.7	2.6	2722.6	2.2	2724.7	2.5	0.2	409.29	8.60	47.57	0.54	2.84	2571	0.15	0.5248226	0.117	13.6045048	0.227	0.1880894	0.147	0.800	PSF
z8	2722.8	2.9	2724.0	2.4	2724.9	3.0	0.1	77.88	2.07	37.59	0.53	2.79	2040	0.15	0.5255590	0.132	13.6249888	0.255	0.1881086	0.177	0.744	PSF
z21	2721.7	2.1	2721.6	1.7	2721.6	1.5	0.0	87.38	0.28	316.04	0.42	2.21	18038	0.12	0.5252971	0.095	13.5904512	0.175	0.1877253	0.085	0.943	SF
z28	2723.7	7.3	2722.2	3.7	2721.0	2.9	-0.1	30.77	0.56	54.70	0.59	3.11	3029	0.16	0.5257884	0.327	13.5983896	0.387	0.1876595	0.171	0.894	SF
z29	2717.9	2.5	2719.5	1.8	2720.6	1.5	0.1	126.15	0.36	346.07	0.60	3.16	19010	0.17	0.5244133	0.113	13.5596829	0.190	0.1876160	0.086	0.942	SF
z30	2711.7	5.3	2715.7	3.4	2718.7	4.0	0.3	13.86	0.67	20.64	0.65	3.42	1140	0.18	0.5229312	0.237	13.5057615	0.359	0.1873996	0.238	0.750	SF
z31	2718.3	5.2	2720.2	2.8	2721.7	2.1	0.1	22.61	0.37	61.72	0.62	3.26	3392	0.17	0.5245091	0.236	13.5709971	0.297	0.1877383	0.123	0.911	SF
z35	2717.7	2.9	2719.8	2.0	2721.3	1.9	0.1	26.63	0.39	67.76	0.58	3.05	3751	0.16	0.5243631	0.133	13.5639913	0.214	0.1876936	0.112	0.878	SF
z36	2721.9	2.8	2721.6	1.8	2721.4	1.5	0.0	248.99	0.26	972.27	0.60	3.16	53410	0.16	0.5253434	0.124	13.5903370	0.192	0.1877072	0.085	0.924	SF
z37	2715.8	2.5	2719.3	2.1	2722.0	2.5	0.2	79.10	2.08	38.10	0.59	3.11	2114	0.16	0.5239152	0.112	13.5579967	0.225	0.1877710	0.148	0.794	SF
z39	2719.2	4.2	2719.8	2.4	2720.3	2.2	0.0	23.50	0.24	98.32	0.60	3.16	5415	0.17	0.5247148	0.188	13.5649605	0.258	0.1875812	0.131	0.862	SF
z40	2721.7	6.2	2720.1	3.3	2718.9	2.8	-0.1	14.84	0.41	36.60	0.50	2.63	2068	0.14	0.5253099	0.281	13.5689399	0.347	0.1874236	0.166	0.875	SF
z41	2720.2	2.2	2720.9	1.7	2721.3	1.6	0.0	77.81	0.50	154.49	0.58	3.05	8528	0.16	0.5249513	0.098	13.5798147	0.180	0.1877020	0.090	0.933	SF
K295	**21.323106°S, 120.394508°E**																					
z1	2725.2	2.6	2723.2	1.8	2721.7	1.5	-0.1	275.65	0.72	382.68	0.53	2.79	20589	0.15	0.5261311	0.116	13.6132588	0.188	0.1877423	0.085	0.928	PSF
z3	2717.9	2.0	2718.0	1.7	2718.1	1.7	0.0	98.39	0.71	138.97	0.60	3.16	7386	0.17	0.5244172	0.091	13.5394932	0.180	0.1873353	0.097	0.926	PSF
z4	2717.1	3.8	2718.7	2.1	2719.9	1.6	0.1	223.11	0.53	421.40	0.59	3.11	22398	0.16	0.5242186	0.170	13.5489470	0.226	0.1875371	0.088	0.926	PSF
z5	2738.6	9.3	2743.8	4.2	2747.6	2.0	0.3	64.29	0.60	107.36	0.63	3.32	5664	0.17	0.5292980	0.418	13.9128115	0.449	0.1907255	0.114	0.965	PSF
z9	2719.3	2.2	2720.8	1.8	2721.9	1.6	0.1	135.37	1.02	132.16	0.53	2.79	7122	0.15	0.5247485	0.098	13.5788138	0.185	0.1877607	0.094	0.934	PSF
z10	2708.0	4.6	2715.3	2.4	2720.8	2.4	0.5	42.94	0.91	47.06	0.60	3.16	2515	0.16	0.5220666	0.209	13.5005206	0.257	0.1876371	0.142	0.824	PSF
z11	2722.0	3.9	2722.9	3.3	2723.6	4.5	0.1	31.48	1.40	22.55	0.56	2.95	1224	0.15	0.5253843	0.176	13.6096672	0.353	0.1879596	0.272	0.647	PSF
z21	2704.0	2.3	2711.7	1.8	2717.5	2.0	0.5	70.43	0.75	93.94	0.57	3.00	5203	0.16	0.5211117	0.103	13.4493482	0.188	0.1872684	0.114	0.819	SF
J339	**21.76549°S, 129.091807°E**																					
z1	2765.8	2.0	2765.4	1.6	2765.1	1.5	0.0	1587.30	4.50	352.37	0.80	4.21	17928	0.22	0.5357784	0.091	14.2336593	0.173	0.1927638	0.084	0.957	PSF
z2	2763.6	2.1	2762.7	1.7	2762.1	1.7	0.0	340.21	2.91	116.83	0.83	4.37	5921	0.23	0.5352477	0.093	14.1937418	0.182	0.1924138	0.098	0.918	PSF
z4	2762.8	2.3	2763.0	2.4	2763.2	3.1	0.0	84.33	2.43	34.70	0.66	3.47	1831	0.18	0.5350625	0.102	14.1979635	0.248	0.1925376	0.185	0.723	PSF
z5	2758.6	2.1	2761.2	1.9	2763.0	2.1	0.2	183.56	2.71	67.67	0.77	4.05	3478	0.21	0.5340717	0.092	14.1703840	0.197	0.1925201	0.121	0.867	PSF
z6	2758.8	2.0	2760.8	1.8	2762.3	1.9	0.1	145.65	1.81	80.27	0.81	4.26	4087	0.22	0.5341147	0.090	14.1654748	0.188	0.1924379	0.112	0.883	PSF
z8	2758.6	3.7	2761.5	2.1	2763.6	1.6	0.2	63.32	0.25	253.63	0.79	4.16	13363	0.22	0.5340628	0.163	14.1749861	0.222	0.1925858	0.091	0.919	SF
z9	2753.8	2.7	2758.6	1.9	2762.1	1.7	0.3	73.64	0.71	103.21	0.78	4.11	5469	0.21	0.5329104	0.119	14.1317861	0.199	0.1924141	0.097	0.912	SF
z10	2763.3	2.8	2765.5	3.3	2767.1	4.9	0.1	63.93	2.88	22.19	1.14	6.00	1073	0.31	0.5351921	0.126	14.2350070	0.352	0.1929932	0.296	0.577	PSF
z13	2769.1	2.9	2767.6	3.0	2766.4	4.1	-0.1	34.80	1.42	24.43	0.68	3.58	1287	0.19	0.5365545	0.127	14.2659096	0.311	0.1929211	0.250	0.624	PSF
z15	2764.9	2.1	2765.6	1.9	2766.1	2.1	0.0	555.03	8.75	63.44	0.80	4.21	3239	0.22	0.5355611	0.095	14.2365746	0.201	0.1928815	0.126	0.854	PSF
z16	2759.5	2.0	2761.0	1.7	2762.2	1.6	0.1	123.19	0.63	195.58	0.76	4.00	10031	0.21	0.5342642	0.089	14.1679383	0.175	0.1924175	0.090	0.947	PSF
z17	2769.1	2.8	2765.1	1.9	2762.2	1.6	-0.2	202.62	1.18	171.70	0.74	3.89	8844	0.20	0.5365741	0.124	14.2296542	0.196	0.1924238	0.091	0.914	PSF
z19	2763.9	3.7	2762.9	2.4	2762.2	2.4	-0.1	31.02	0.64	48.34	0.71	3.74	2608	0.19	0.5353180	0.167	14.1963751	0.252	0.1924242	0.140	0.842	SF
z20	2761.0	3.7	2761.3	2.3	2761.5	2.1	0.0	33.43	0.59	56.95	0.80	4.21	3011	0.22	0.5346261	0.166	14.1722560	0.240	0.1923459	0.121	0.873	SF

a Corrected for initial Th/U disequilibrium using radiogenic 208Pb and Th/U[magma] specified.

b Corrected for initial Pa/U disequilibrium using initial fraction activity ratio [231Pa]/[235U] = 1.10000.

c % discordance = 100 - (100 * (206Pb/238U date) / (207Pb/206Pb date))

d Total mass of radiogenic Pb.

e Total mass of common Pb.

f Ratio of radiogenic Pb (including 208Pb) to common Pb.

g Th contents calculated from radiogenic 208Pb and 230Th-corrected 206Pb/238U date of the sample, assuming concordance between U-Pb Th-Pb systems.

h Th/U ratio of magma from which mineral crystallized.

i Measured ratio corrected for fractionation and spike contribution only.

j Measured ratios corrected for fractionation, tracer and blank. Values for ET535 are found in Condon et al. (2015) and McLean et al. (2015). Blank model values are as follows:

SF	206Pb/204Pb	18.628271±0.317714	PSF	18.065374±0.419833
	207Pb/204Pb	15.796256±0.232017		15.259599±0.295693
	208Pb/204Pb	38.535874±0.375848		37.141426±0.841275

Supplemental Table 2: Paleomagnetic site mean directions and calculated poles

		Strat				*			k	a95	VGP	VGP	
Site	Section	Height	Lat	Long	n	**N**	D	I	**K**	**A95**	lat	long	plat
Package 0													
JK1407 C	GHG	56.7	-21.35	119.61	20	X	23.7	-68.4	48.02	4.8			
JK1408	GHG	284.9	-21.34	119.62	6	*	282.1	65.7	71.5	7.3	-8.0	78.3	
JK1409	GHG	289.1	-21.34	119.62	2	X	307.4	71.8	46.7	26.1			
JK1301	GHG	293.7	-21.34	119.62	6	*	316.5	70.0	170.9	4.7	5.9	95.6	
JK1302	GHG	359.9	-21.34	119.62	10	*	298.4	70.9	108.7	4.4	-2.7	89.5	
JK1303	GHG	372.4	-21.34	119.62	7	*	334.4	67.0	57.5	7.4	15.4	102.8	
JK1304	GHG	458.9	-21.34	119.62	4	*	327.7	51.5	101.9	7.9	28.2	88.7	
JK1305	GHG	513.9	-21.34	119.62	5	*	287.3	66.7	195.2	4.9	-5.4	80.9	
JK1306	GHG	570.6	-21.34	119.62	5	*	326.7	69.6	64.9	8.5	10.0	100.2	
JK1307	GHG	630.4	-21.20	119.70	9	*	297.1	74.5	161.6	3.8	-6.4	93.9	
JK1401	GHG	644.7	-21.20	119.70	6	*	321.8	71.8	24.7	6.2	5.6	99.7	
					57	**9**	**311.5**	**68.6**	**66.8**	**6.3**	**4.7**	**92.2**	**51.9**
									30.8	**9.4**			
CR Package 0 Overprint													
JK1430	CR	14.8	-21.34	119.62	8	*	172.2	54.3	68.7	6.3	-74.7	144.7	
JK1431	CR	79.3	-21.34	119.62	10	*	151.4	67.3	155.7	3.7	-53.4	150.7	
JK1432	CR	80.5	-21.34	119.62	6	*	157.8	71.7	74.0	7.2	-51.1	139.1	
JK1433	CR	103.8	-21.34	119.62	9	*	165.8	73.3	117.5	4.5	-50.8	131.2	
JK1434	CR	123.9	-21.34	119.62	4	*	125.3	65.2	92.0	8.3	-39.1	165.3	
JK1437	CR	186.1	-21.20	119.70	8	*	166.5	67.9	40.1	8.3	-58.5	136.0	
JK1438	CR	235.8	-21.20	119.70	10	*	155.2	72.3	325.9	2.5	-49.5	140.0	
JK1439	CR	279.1	-21.20	119.70	7	*	175.2	72.0	70.4	6.7	-54.0	124.2	
JK1436	CR	332.6	-21.33	119.62	9	*	156.4	67.3	463.2	2.3	-55.6	146.8	
JK1435 C	CR	724.7	-21.30	119.70	14	X	180.6	64.1	27.2	7.5			
					71	**9**	**158.6**	**68.6**	**98.3**	**5.2**	**-54.7**	**142.6**	**51.9**
									45.7	**7.7**			
Upper Package 0													
JK1402	GHG	661	-21.20	119.70	9	*	317.9	81.1	123.8	4.4	-8.1	107.9	
JK1308	GHG	667.4	-21.33	119.62	7	*	033.6	79.4	148.9	4.6	-4.8	114.7	
JK1405	GHG	682.9	-21.20	119.70	10	*	289.6	75.0	176.6	3.5	-10.0	92.8	
JK1311	GHG	699.6	-21.33	119.62	7	*	317.4	87.3	129.5	4.9	-17.3	115.8	
JK1403	GHG	725.8	-21.30	119.70	10	*	057.4	77.9	294.8	2.7	-7.8	139.2	
JK1309	GHG	739.3	-21.33	119.62	8	*	019.5	79.7	512.5	2.3	-2.4	126.2	
JK1404	GHG	743.8	-21.20	119.70	10	X	294.3	-02.0	01.2	77.5			
JK1310	GHG	752.8	-21.33	119.63	14	*	300.5	75.6	91.5	4.0	-6.2	96.3	
					65	**7**	**342.2**	**83.0**	**72.1**	**7.2**	**-8.3**	**115.6**	**76.3**
									20.3	**13.7**			
Package 1													
JK1406	GHG	756.8	-21.33	119.62	4	*	121.3	61.1	255.1	5.0	-37.1	172.2	
JK1312	GHG	801.5	-21.33	119.62	9	X	007.6	-66.6	119.7	4.5			
JK1315 C	GHG	904.5	-21.32	119.62	17	X							
JK1316	GHG	907.5	-21.33	119.62	3	*	093.9	68.1	377.2	5.2	-18.9	161.0	
JK1314	GHG	948.9	-21.32	119.62	6	*	115.6	61.7	89.6	6.5	-32.8	171.5	
JK1313	GHG	957.7	-21.32	119.62	10	*	098.9	60.3	170.4	3.5	-20.4	172.0	
JK1440	CR	712.7	-21.30	119.70	6	*	134.1	45.2	48.3	8.9	-47.9	192.9	
JK1441	CR	744.7	-21.30	119.70	6	*	130.5	67.9	219.4	4.1	-41.6	159.5	
JK1442	CR	764.5	-21.30	119.70	8	*	149.7	59.4	237.8	3.4	-58.1	166.5	
JK1443	CR	782.4	-21.30	119.70	7	*	147.0	58.5	151.4	4.6	-56.6	169.8	
JK1444	CR	794.8	-21.30	119.70	10	*	153.4	59.9	151.1	3.7	-60.2	162.8	
JK1445	CR	814.2	-21.30	119.70	10	*	141.0	60.8	841.6	1.6	-51.4	168.5	

Supplemental Table 2: Paleomagnetic site mean directions and calculated poles

JK1446	CR	839.7	-21.30	119.70	8	*	141.3	63.2	223.7	3.5	-50.6	164.1	
JK1447	CR	862.6	-21.30	119.70	9	*	142.2	61.2	787.2	1.7	-52.1	167.3	
					87	**12**	**132.0**	**61.8**	**57.4**	**5.8**	**-44.4**	**169.0**	**43**
									28.3	**8.3**			
Package 7: Mingah Member, Tumbiana Formation volcaniclastics													
JK1317	MCN	1.6	-21.3	120.4	10	*	299.0	-54.1	108.7	4.4	-35.3	182.3	
JK1318	MCN	79.8	-21.3	120.4	8	*	289.3	-48.0	303.8	3.0	-26.5	187.6	
JK1319r	MCN	140	-21.3	120.4	4	*	289.4	-60.7	48.5	11.5	-28.2	173.4	
JK1415	MCS	1.3	-21.4	120.5	7	*	296.0	-52.9	137.3	4.8	-32.8	183.6	
JK1416	MCS	20.6	-21.4	120.5	6	*	309.9	-58.3	299.3	3.5	-43.9	176.4	
JK1417r	MCS	20.7-29.8	-21.4	120.4	3	*	302.4	-74.5	43.2	15.4	-34.1	150.1	
					38	**6**	**297.0**	**-58.3**	**64.9**	**8.4**	**-34.1**	**175.0**	**39.0**
									40.2	**10.7**			
Package 7: Mingah Member, Tumbiana Formation basalts													
JK1319n	MCN	140	-21.3	120.4	2	*	149.2	62.0	588.3	7.3	-56.3	162.6	
JK1411	MCN	229.4	-21.3	120.4	3	*	163.5	66.6	204.4	7.1	-59.3	141.7	
JK1412	MCN	251.9	-21.3	120.4	9	*	160.2	60.5	152.7	3.9	-63.8	155.5	
JK1413	MCN	276.8	-21.3	120.4	10	*	156.3	62.9	392.9	2.3	-59.8	155.2	
JK1320	MCN	361.4	-21.3	120.4	0	X	scattered						
JK1417n	MCS	33-38.5	-21.4	120.4	4	*	188.0	71.7	72.6	9.4	-54.4	112.8	
JK1418	MCS	52	-21.4	120.5	7	X	270.8	14.0	25.1	11.3			
JK1419	MCS	125.6	-21.4	120.4	3	X	200.7	53.8	50.7	14.2			
JK1420	MCS	146.9	-21.4	120.4	5	*	186.2	76.7	301.4	4.0	-46.5	116.6	
JK1421	MCS	169.4	-21.4	120.4	8	*	185.3	62.3	172.0	4.3	-67.4	110.4	
JK1422	MCS	206.6	-21.4	120.4	5	*	174.9	58.3	157.8	5.5	-71.9	133.2	
JK1423	MCS	224.6	-21.4	120.5	0	X	scattered						
					45	**8**	**168.7**	**65.7**	**86.8**	**6.0**	**-61.4**	**135.6**	**48.0**
									38.1	**9.1**			
Package 7: Meentheena Member, Tumbiana Formation carbonates and sediments													
JK1321	MCN	400.4	-21.3	120.4	37	X	304.1	-50.4	08.2	8.8			
JK1328	MCN	439.2	-21.3	120.4	31	X	341.2	-69.4	20.2	5.9			
JK1424	MCS	258.3	-21.4	120.4	7	X	083.3	-40.4	07.8	21.1			
Package 8: Maddina Basalts													
JK1322	MCN	637.5	-21.3	120.4	10	*	130.4	54.4	372.6	2.4	44.7	361.8	
JK1323	MCN	709.3	-21.3	120.4	10	*	161.6	63.1	277.9	2.8	62.2	329.2	
JK1324	MCN	805.7	-21.3	120.4	7	*	143.2	39.3	122.8	5.1	55.9	381.8	
JK1327	MCN	830	-21.3	120.4	7	*	145.5	46.4	76.8	9.1	58.1	371.9	
JK1325	MCN	830	-21.3	120.4	2	*	154.2	48.5	1185.7	5.1	65.4	365.8	
JK1414	MCN	893.2	-21.3	120.4	5	*	161.8	51.6	156.8	5.5	70.5	352.6	
JK1326	MCN	896.6	-21.3	120.4	7	*	158.3	41.5	222.1	3.8	69.8	379.1	
JK1425	MCS	441	-21.4	120.4	4	X	260.6	-77.6	35.2	13.6			
JK1426	MCS	471.6-476.6	-21.4	120.4	3	*	169.4	49.3	64.9	12.6	77.1	345.6	
JK1427	MCS	522.3	-21.4	120.4	4	*	177.8	55.5	214.7	5.4	75.2	307.4	
JK1428	MCS	555.3	-21.4	120.4	8	*	173.1	49.5	219.1	3.5	79.1	333.7	
JK1429	MCS	585.6	-21.4	120.4	6	*	176.5	55.5	85.3	6.7	75.0	311.4	
					66	**11**	**158.7**	**51.3**	**49.7**	**6.5**	**-68.4**	**175.3**	**31**
									31.9	**9.5**			

Chapter 3

Rapid eruption of the Columbia River flood basalt and correlation with the mid-Miocene climate optimum

---

This chapter is taken from

Kasbohm, J.J., Schoene, B. (2018). Rapid eruption of the Columbia River flood basalt and correlation with the mid-Miocene climate Optimum. Science Advances, 4(9), 1-8. https://doi.org/10.1126/sciadv.aat8223

ABSTRACT

Flood basalts, the largest volcanic events in Earth history, are thought to drive global environmental change because they can emit large volumes of CO_2 and SO_2 over short geologic timescales. Eruption of the Columbia River Basalt Group (CRBG) has been linked to elevated atmospheric CO_2 and global warming during the Mid-Miocene Climate Optimum (MMCO) ~16 million years ago. However, a causative relationship between volcanism and warming remains speculative as the timing and tempo of CRBG eruptions is not well known. Here, we use U-Pb geochronology on zircon-bearing volcanic ash beds intercalated within the basalt stratigraphy to build a high-resolution CRBG eruption record. Our dataset shows that more than 95% of the CRBG erupted between 16.7 and

15.9 Ma, twice as fast as previous estimates. By suggesting a recalibration of the geomagnetic polarity timescale, these data support that the onset of flood volcanism is nearly contemporaneous with that of the MMCO.

INTRODUCTION

The Columbia River Basalt Group (CRBG) is the youngest, smallest, and best-preserved continental flood basalt. It erupted ~210,000 km^3 of lava in the Pacific Northwest, USA between ~17 and 5 Ma. Forty-three distinct stratigraphic members with volume estimates have been defined using regional correlations based on detailed mapping, geochemistry, and paleomagnetic data (*1*). While many flood basalts have been implicated in mass extinction events (*2*), the CRBG is not associated with a mass extinction event and its total volume is up to an order of magnitude smaller than other flood basalts. However, single members yielded comparable volumes of lava (thousands of km^3) to single formations of large igneous provinces implicated in mass extinctions (e.g., Deccan Traps (*3*)), and therefore may have had comparable short-term climate impacts (*4*). The ~17-15 Ma Mid-Miocene Climate Optimum (MMCO) is marked by high latitude sea surface temperatures 4-6°C above background temperature (*5*) and is associated with vertebrate migrations and increased species originations (*6*). In paleoclimate records, the MMCO is marked by a benthic $\delta^{18}O$ minimum, a benthic $\delta^{13}C$ maximum, an ice sheet extent minimum (*7*), and a variety of pCO_2 proxies which indicate a possible doubling of atmospheric CO_2 levels to greater than 400 ppm (*8–10*). Given the apparent timing of both events, many studies have suggested that the environmental perturbations of the

MMCO are connected to CRBG eruptions (*1*, *8*, *11*), but high-precision geochronologic data that link the two events are lacking (*7*).

While most flood basalt provinces are thought to relate to mantle plume-driven processes, models for the origin of the CRBG include a mantle plume source (*12*), but also subduction-related processes such as slab tear (*13*) or slab rollback (*14*). Central to this debate is that the CRBG was erupted during a period of active regional volcanism, including subduction volcanism of the Cascade arc, rhyolitic volcanism of the Yellowstone-Snake River Plain hotspot track, the High Lava Plains of Central Oregon, and bimodal volcanism related to Basin and Range extension in Northern Nevada (Fig. 1). The CRBG began erupting from a north-trending linear fissure system in eastern Washington, eastern Oregon, western Idaho, and northern Nevada, in a back-arc setting between the Cascades and Rocky Mountains. Volcanism progressed from south to north, and the regional tectonic and geomorphic setting guided flows hundreds of km from east to west (*1*). An improved understanding of the timing of CRBG eruptions, the volumetric rates at which they were emplaced, and the rate at which they propagated geographically through the province are essential constraints on geodynamic models for the CRBG origin.

In this paper, we aim to test the hypothesis that there is a temporal relationship between CRBG eruptions and the MMCO by establishing an accurate and precise age model for the eruption of the CRBG. Decades of study have produced a high-resolution stratigraphic framework for the CRBG. The 350 tholeiitic basalt to basaltic andesite

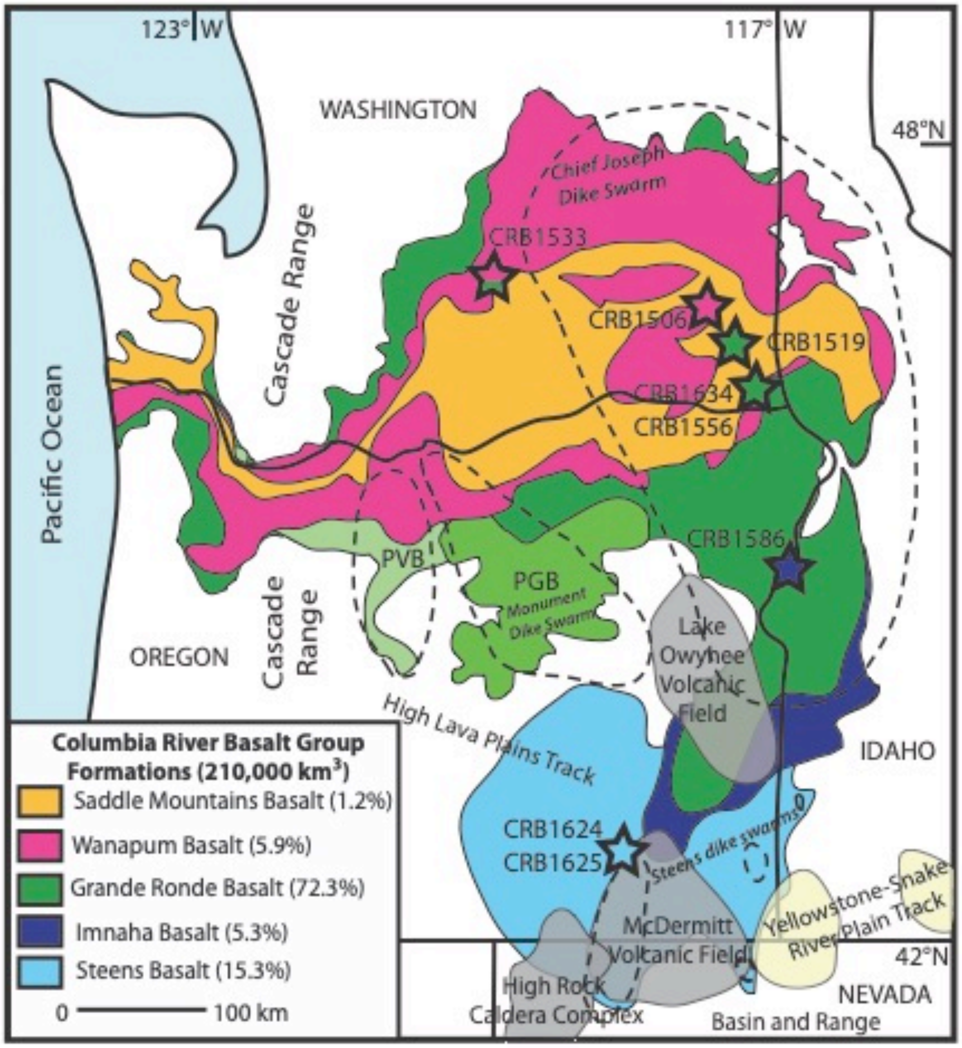

Fig. 1. Map of Columbia River Basalt Group and Regional Volcanism. The map shows the areal extent of each formation of the CRBG, and the legend provides the volume contribution of each formation. Stars represent geochronology sample collection sites; dashed lines enclose areal extent of source dike swarms. The Prineville Basalt (PVB) and Picture Gorge Basalt (PGB) are coeval with the Grande Ronde Basalt, and represent 1.4% of total CRB volume, and are grouped with the Grande Ronde Basalt for all volume estimates presented here (*1*).

flows of the CRBG are divided into five formations: the Steens (31,800 km^3; 15.3% of total volume), Imnaha (11,000 km^3; 5.3%), Grande Ronde (150,100 km^3; 72.3%), Wanapum (12,175 km^3; 5.9%), and Saddle Mountains Basalts (2,424 km^3; 1.2%), which are comprised by a total of 43 stratigraphic members, containing 1-20 lava flows each

(*1*). Magnetic field reversals were ongoing during the eruption of the CRBG. While the magnetic stratigraphy first was developed in the field using a portable fluxgate magnetometer during mapping efforts (*1*), some detailed modern paleomagnetic data have since been published (*15*, *16*). The Steens Basalt erupts during a reversal from reversed to a normal polarity interval (sometimes referred to as R_0 and N_0 (*17*)), which continues through the Imnaha Basalt. The Grande Ronde Basalt is marked by two couplets of magnetic field reversals (locally defined magnetostratigraphic units are known as R1, N1, R2, N2). The N2 normal magnetozone continues through the majority of the Wanapum Basalt, which exhibits a final reversed interval (*1*, *18*, *19*).

The majority of ages published on the CRBG have uncertainties that preclude the development of an unambiguous chronology for the timing and duration of CRBG volcanism. For example, in a review of K-Ar and $^{40}Ar/^{39}Ar$ geochronology for the CRBG, a preferred chronology was developed with eruption of the Steens Basalt at 16.9–16.7 Ma, the Imnaha Basalt at 16.7–16.0 Ma, the Grande Ronde Basalt at 16.0–15.6 Ma, the Wanapum Basalt at 15.6–15.0 Ma, and the Saddle Mountains Basalt in several distinct events between 15–6 Ma (*4*). This eruptive age model is based on geochronologic analyses with large uncertainties (>1 Ma) that make adherence to stratigraphic order difficult to address, and the result is that it is inconsistent with the Geomagnetic Polarity Timescale (GPTS) (*4*, *20*). For instance, this age model suggests a normally magnetized interval lasting ~600 ka through the Imnaha Basalt, which exceeds the duration of any normal chrons occurring around 16 Ma in different calibrations of the GPTS (*20*). Other inconsistencies are discussed in greater detail in the Results section. New high-precision

^{40}Ar/^{39}Ar dates derived from feldspar phenocrysts in silicic tuffs interbedded in the Steens Basalt have revised its eruptive duration to ~16.75-16.54 Ma, and propose that the Steens magnetic field reversal occurred at 16.603±0.028 Ma (*21*) (dates recalculated with Fish Canyon sanidine age of Kuiper *et al.* (*22*); see Supplement). These new data highlight the potential that additional precise geochronology has to resolve the timing and duration of CRBG volcanism and its correlation to the GPTS and MMCO.

RESULTS

In thus study we use U-Pb zircon geochronology by chemical abrasion-isotope dilution-thermal ionization mass spectrometry (CA-ID-TIMS), which can achieve the precision (~0.1%) and accuracy required to address the issues with prior age models outlined above. Because basalts are generally too low in Si and Zr to saturate zircon, we follow the sampling strategy of Schoene *et al.* (*23*) by collecting silicic volcanic ash from between basalt flows and dating them by U-Pb geochronology on single zircon crystals. These ash beds were sourced from contemporaneous regional silicic volcanism, and deposits include ash-bearing paleosols (referred to as "redboles" in the remainder of this paper), interflow volcaniclastic sediments, and pumice-bearing airfall tuff (Fig. 2, Fig. S1). Zircons separated from these samples (Fig. S2) were dated by CA-ID-TIMS at Princeton University.

Data from eight horizons within the CRBG, reported as ^{206}Pb/^{238}U dates from single zircons taken from a population of dated grains with 95% confidence intervals, are shown in Fig. 3. Dates on single crystals within each sample spread beyond analytical

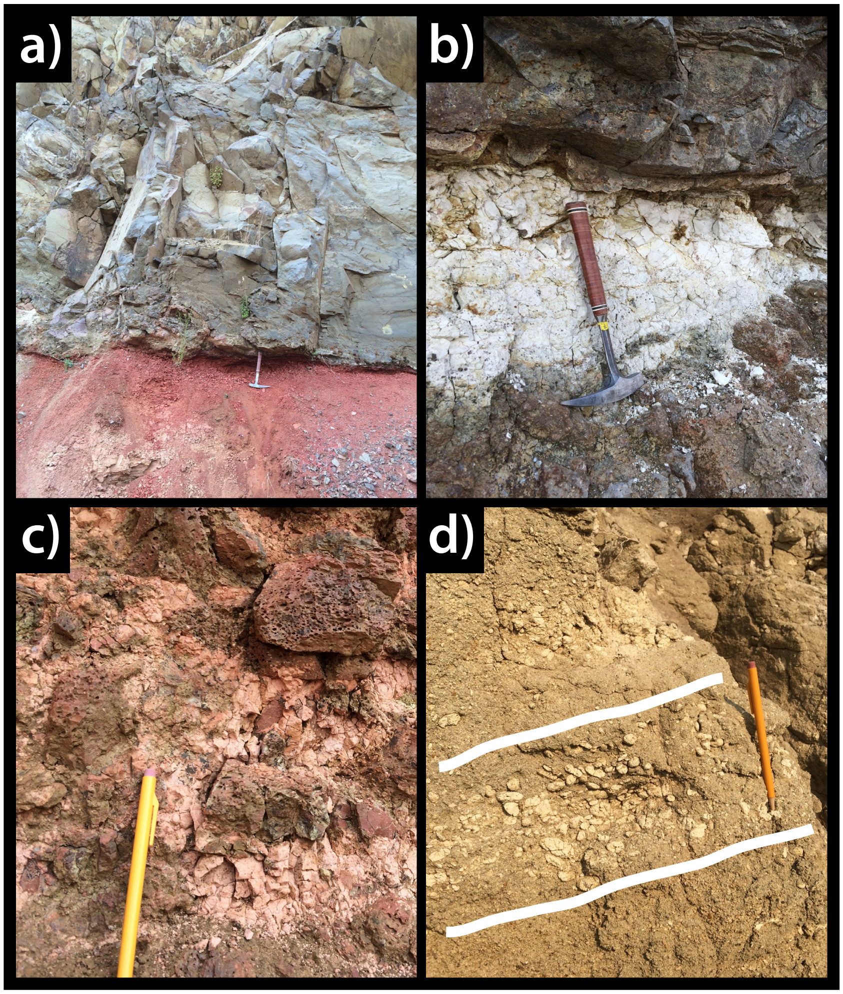

Fig. 2. Columbia River Basalt Group Geochronology Samples. Certain interflow lithologies were targeted for sampling and found to contain magmatic zircons, allowing for high-precision dating techniques to be applied: **(A)** redboles, analogous to those found in the Deccan Traps (similar to CRB1519, CRB1556, CRB1624, CRB1625, and CRB1634); **(B)** ashes deposited from Cascade subduction volcanism or other silicic centers (CRB1506, CRB1586); **(C)** ash-bearing sediments trapped in brecciated basalt flow tops; and **(D)** pumice clasts in the Vantage sedimentary interbed (CRB1533); the horizon with these cm-scale clasts is outlined in white.

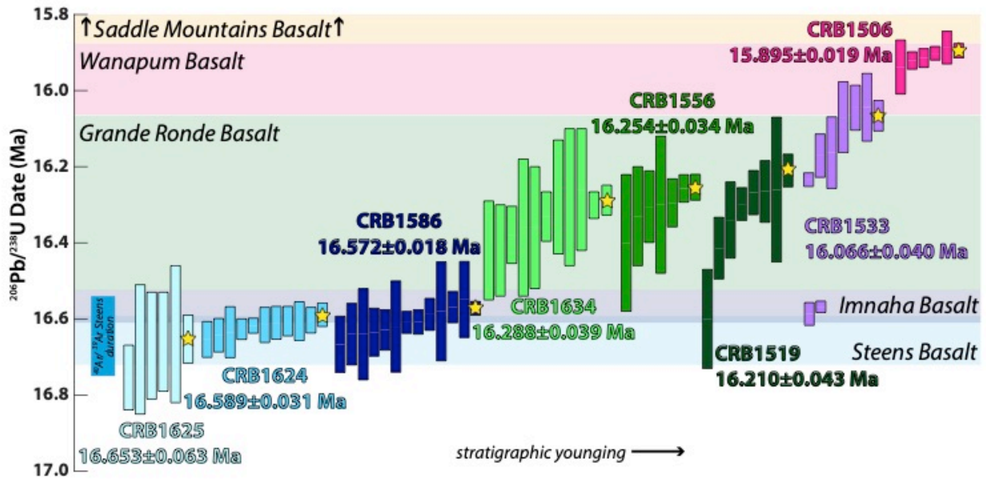

Fig. 3. U-Pb Zircon CA-ID-TIMS Geochronological Data. Rank order plot of geochronological data presented in this study, with sample names and the youngest, most precise zircon age starred and labeled. Error bars represent 2σ uncertainty, and stratigraphic younging is from left to right. We present a timeline, shown with background shading and labels, for the eruption of each formation based on the stratigraphic position of these samples and consistent with our geochronology results. Steens Basalt geochronology is compared to the most recent ^{40}Ar/^{39}Ar geochronology results (*21*), and is found to overlap U-Pb data when recalculated with the Fish Canyon Sanidine age of Kuiper *et al.* (*22*).

uncertainty, a common observation in volcanic ashbeds, because zircon can retain radiogenic Pb at temperatures of >900°C. A spread in crystallization dates beyond analytical uncertainty can reflect growth of zircon in the magmatic system prior to eruption, incorporation of pre-eruptive zircon from the volcanic edifice during eruption, or inheritance from the rock hosting the magmatic system (*24*, *25*). In light of these potential sources for complex zircon populations deposited within the CRBG ashes, we use the youngest single concordant analysis, excluding low precision analyses, as an estimate for the age of the ash (*26*) (Fig. 3). This approach is tested by dating a large number of zircons from each sample to obtain multiple analyses that overlap with the youngest grain, and further requiring that samples from stratigraphically higher positions in the CRBG are in chronological order. A growing database of zircon geochronology from a variety of tectonic settings, using a variety of U-Pb analytical methods, shows that the youngest zircon analysis from continuous age population (excluding outliers that can be explained by residual Pb loss) overlaps with independent eruptive ages (*27*, *28*). We also show in the Supplement that our use of single youngest zircon ages overlaps with weighted mean ages calculated from multiple grains for each sample, though we prefer the youngest zircon age as the more conservative interpretation. Our dates from the Steens Basalt show excellent agreement with ages derived from high-precision ^{40}Ar/^{39}Ar sanidine geochronology (*21*) (Fig. 3).

Our zircon ages improve estimates for the timing and duration of each formation of the CRBG stratigraphy (Fig. 3), and indicate that 95% of its total volume erupted in 758±66 ka (Fig. S3). The upper 72% of the Steens Basalt volume erupted between 16.653±0.063 and 16.589±0.031 Ma. The latest Steens eruptions occurred concurrently with Imnaha Basalt eruptions, which we have dated at 16.572±0.018 Ma. While we currently do not have an estimate for the onset of the overlying Grande Ronde Basalt, four samples from the upper half fall in stratigraphic order and show its termination by 16.066±0.040 Ma. Two samples from the bottom and top of the Wapshilla Ridge Member of the Grande Ronde Basalt, which comprises 20% of the total CRBG volume, gave dates overlapping within uncertainty of 16.288±0.039 and 16.254±0.034 Ma. These ages come from a single stratigraphic section, and the age of the upper bound is indistinguishable at the 95% confidence interval from the age from a redbole that is in the same stratigraphic position but is found 44 km away (16.210±0.043 Ma). Finally, the lower 77% of the Wanapum Basalt finished erupting before 15.895±0.019 Ma (Fig. 3). Our dated samples bracket 95% of the eruptive history of the CRBG, and these data show that the CRBG erupted 2.4 times faster than the previous estimates (*4*). Our ages agree with the relative chronology of the existing stratigraphic framework (*1*), and bolster regional correlation through geochemical and paleomagnetic data.

Combined with detailed volume estimates for each member of the CRBG (*1*), our new zircon ages yield effusion rates throughout the eruptive history of the CRB and provide a timeline for the release of CO_2, SO_2, and other gases into the atmosphere. For the main phase of eruption (Steens, Imnaha, and Grande Ronde Basalts), we calculate an average effusion rate of 0.334 ± 0.042 km^3/yr, which is double the prior estimate of 0.178 km^3/yr for the same interval (*12*). During the eruption of the Wanapum Basalt, the rate slows to 0.055 ± 0.014 km^3/yr, whereas during the Wapshilla Ridge Member, the average rate calculated is 1.18 km^3/yr, with a minimum rate of 0.376 km^3/yr. However, because our ages for the top and bottom of this voluminous member in a single stratigraphic section overlap, effusion rates were likely far greater than the average values. A potential constraint for the maximum rate can be derived from prior estimates for the minimum duration of the 1,300 km^3 Roza Member to be 14 years (*29*), and the ca. 100 years or more needed to develop thin redbole horizons (*30*). Because there are at least 18 (and as many as 28) lava flow units in the Wapshilla Ridge Member (*31*) and 8 more redboles between the samples we dated, we estimate that peak eruption rates could be as high as 20-40 km^3/yr for a duration of thousands of years.

The eruptive pulse for the Wapshilla Ridge Member is an order of magnitude higher than *average* effusion rates calculated for other large igneous provinces associated with mass extinction events: 1-2 km^3/yr for the Deccan Traps (*23*), 3-5 km^3/yr for the Central Atlantic Magmatic Province (*32*), and 1-4 km^3/yr for the Siberian Traps (*33*). However, records from other flood basalts do not have the stratigraphic resolution to calculate effusive rates during high flux pulses compared to long-term average rates. More generalized models for the total climatic impact during flood basalt eruption will be dependent on delineating the timing of eruption pulses, such as the Wapshilla Ridge Member, from background fluxes.

DISCUSSION

Our age model provides quantitative constraints that must be satisfied by any geologic or geodynamic model for CRBG volcanism. In particular, the mechanism must be consistent with: (1) eruption duration of ~750 ka from 16.65-15.90 Ma; (2) an average effusion rate of 0.334±0.042 km^3/yr, with pulses of >>1 km^3/yr; (3) simultaneous eruptions at Steens Mountain and in the Imnaha Basalt vents 300 km away; and (4) an average linear geographic propagation rate of eruption of 0.37±0.08 m/yr to the north, given distances between the vents sourcing Imnaha through Wanapum eruptions. These criteria alone may be currently insufficient to fingerprint a mantle plume or subduction-related origin of the CRBG, both of which allow for eruptions to occur in this time frame (*13*, *34*). The geographic propagation rate of 0.37±0.08 m/yr for CRB volcanism is also compatible with either model: a small plume head has been modeled to spread at 0.2-0.3 m/yr (*35*), while the proposed slab tear is modeled to propagate at 0.45 m/yr (*13*). This northward propagation rate is about three times faster than those calculated for the McDermitt and High Rock dike swarms that propagate to the south of Steens Mountain (0.12 m/yr and 0.14 m/yr, respectively) (*36*), showing that the potential radial propagation from Steens Mountain did not occur at the same velocity radially. Further modeling with our new quantitative constraints is required to better understand the process that allowed for CRBG eruption.

Determining the relative timing of CRBG volcanism and the MMCO requires independent chronologies that are equally precise. However, the early- and middle-Miocene is one of the most problematic periods in the Neogene for establishing precise independent chronologies in marine sediments due to the difficulty in obtaining undisturbed stratigraphic sections that yield reliable magnetostratigraphy, biostratigraphy, astronomical tuning, and radiometric ages (*20*). All timescales proposed for the middle-Miocene depend directly or indirectly on correlation with the GPTS, for which there are currently several proposals, the most recent being the Geologic Time Scale (GTS) 2012 (*20*). GTS 2012 was derived from the seafloor anomaly profiles of the Antarctic and Australian plates and assuming a relatively constant spreading rate tuned to give a 23.03 Ma age for the Oligocene-Miocene boundary (*20*). GTS 2012 rejected an astronomically-tuned record of Mid-Miocene $\delta^{18}O$ and magnetostratigraphy from ODP Site 1090 in the subantarctic south Atlantic, whose record extends from the Oligocene-Miocene boundary to ~15.9 Ma, because the tuned record yields ages for chron boundaries that do not meet the assumption of constant seafloor spreading rates in the Pacific (*20*). The most recent age model for the CRBG (*4*) attempts to reconcile $^{40}Ar/^{39}Ar$ geochronology with GTS

2012. However, the resulting age model is inconsistent with the existing GPTS and is clearly in need of refinement (Fig. 4).

Our new age model for the CRBG permits a more robust correlation of CRBG magnetostratigraphy with existing proposals for the GPTS (Fig. 4). However, this exercise also indicates that some prior proposals for the GPTS, including GTS 2012, are in error. For example, the most recent age model for the CRBG has the Imnaha Basalt, which is entirely normally polarized, erupting through several magnetic reversals and thus is not permissible. Similarly, the existing age model places the Grande Ronde Basalt, which records two reversed and two normal intervals, within a single normal chron. By comparison, in our proposed correlation illustrated in Fig. 4, the Imnaha Basalt erupted entirely during chron C5Cn.3n, while the Grand Ronde Basalt erupted during C5Cn.2r-C5Cn.1n – consistent with observed magnetostratigraphy in the basalts.

Using this baseline correlation with the GPTS, we can refine four proposed reversal ages (Fig. 4). Our ages in the Upper and Lower Steens bracket the "Steens Reversal" (between magnetozones R_0 and N_0, and chrons C5Cr and C5Cn.3n) which can be conservatively constrained to 16.637±0.079/0.089 Ma (95% confidence intervals given for internal uncertainty/decay constant uncertainty). This estimate compares favorably with the estimate of 16.603±0.028/0.36 Ma obtained through recent $^{40}Ar/^{39}Ar$ sanidine geochronology (*21*). Our samples from the base and top of the Wapshilla Ridge Member constrain the timing and provide a minimum duration for C5Cn.1r, to begin no later than 16.288±0.039/0.046, and to end no earlier than 16.210±0.043/0.047 Ma, because the

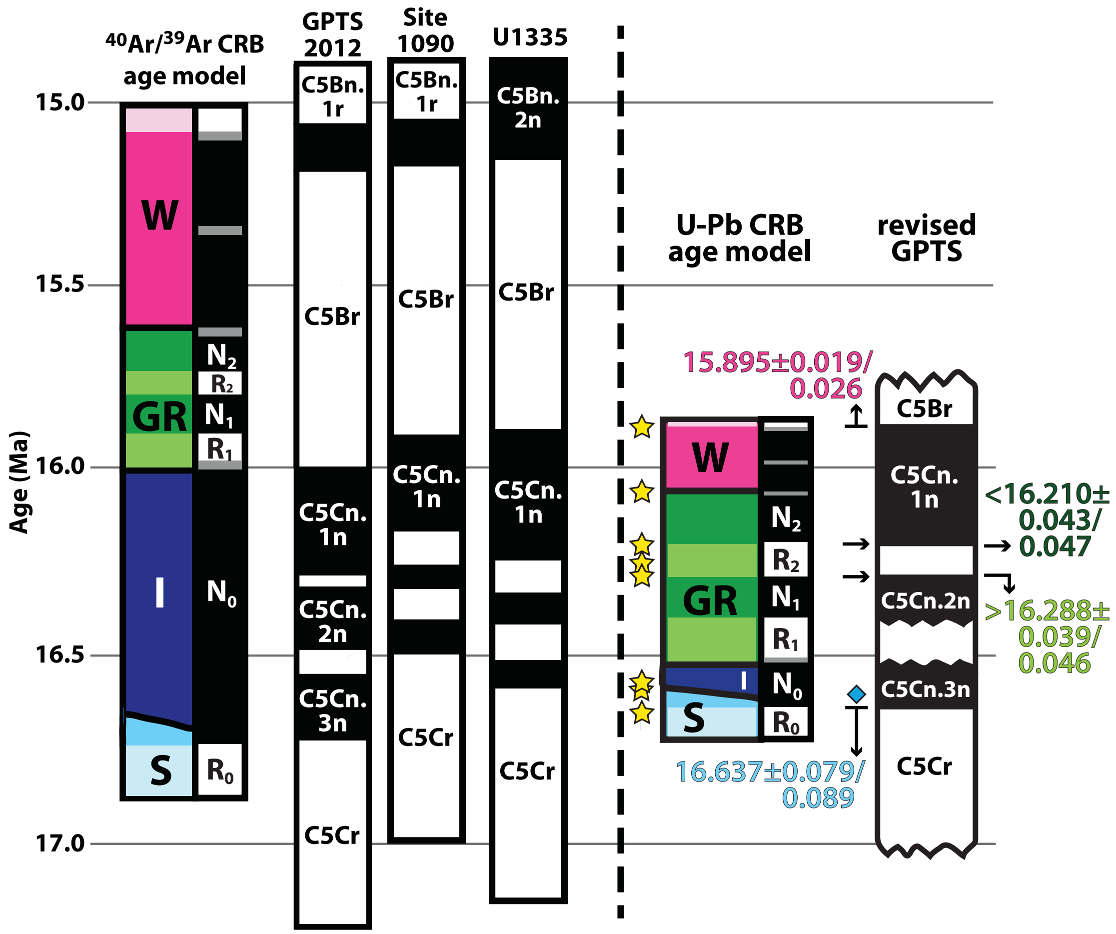

Fig. 4. Revised CRBG Eruptive Timeline, Magnetostratigraphy, and GPTS Correlation. U-Pb geochronology suggests a timeline of the eruption for each formation (from Fig. 3) as well as a revised GPTS consistent with CRBG magnetostratigraphy ((*1*) and references therein). These are compared to the eruptive chronology derived from ^{40}Ar/^{39}Ar geochronology (*4*) and different GPTS calibrations (*20*, *37*, *46*). Given the magnetic polarity of different stratigraphic members, U-Pb geochronology constrains the age of four different chron boundaries (straight lines), identified with arrows and ages with internal and decay constant uncertainties. Estimated chron boundaries are shown with zigzag lines, and are not yet constrained by geochronology. Lighter shades of color in the stratigraphic column represent reversed polarity intervals in CRBG magnetostratigraphy, also shown by adjacent reversal stratigraphy to the right of each CRBG age model. Stars indicate the youngest zircon ages obtained for each sample in the study, and letters label each formation (S – Steens Basalt; I – Imnaha Basalt; GR – Grande Ronde Basalt; W – Wanapum Basalt). The blue diamond represents the age of the Steens reversal obtained in Mahood & Benson (*21*), recalculated with the Fish Canyon Sanidine age of Kuiper *et al.* (*22*), to be 16.603±0.028/0.36 Ma, which is consistent with our results.

Wapshilla Ridge Member comprises the majority of volume of the second reversed magnetostratigraphic unit of the Grande Ronde Basalt (R2) (*31*). The end of C5Cn.1n (N2) is well-constrained by our age of 15.895±0.019/0.026 Ma for the top of the transitionally magnetized Roza Member, which immediately overlies the normally magnetized Frenchman Springs Member, especially given prior estimates that the Roza Member erupted in as little as 14 years (*29*). Our initial data do not identify any significant hiatuses in eruptions – no more than ~200 ka elapse between any two of our samples, during which volcanism is known to be ongoing even though we do not present zircon data from these intervals (Fig. S3). Therefore, high-precision geochronology can be used to bound the ages of magnetically-characterized CRB flows and to further refine the record of middle-Miocene magnetic field reversals. Our proposed GPTS is also consistent with the astronomically-derived age model for the magnetic reversal stratigraphy at Site U1335 in the equatorial Pacific (Fig. 4) (*37*), indicating an independent verification for our proposed age model for the GPTS.

Given the inconsistencies described above for the GPTS, demonstrating a link between the eruption of the CRBG and the MMCO requires a careful assessment of the age models used to develop proxy records across the MMCO. For example, the $\delta^{11}B$ proxy record for pCO_2 at ODP Site 761 indicates that atmospheric CO_2 increases at 16.5 Ma (*8*), which agrees well for our suggested timing of the onset of voluminous Grande Ronde Basalt volcanism. However, the age model for Site 761 (*38*) depends on biostratigraphic (*39*) or isotopic events (*40*) tied to calibrations of the GPTS (*41*) that we have shown to be inaccurate. Recent work describing the $\delta^{13}C$ and $\delta^{18}O$ records from IODP Site U1337 identifies the onset of the MMCO at 16.9 Ma (*42*), which precedes our timing for all CRBG eruptions. This site has an age model derived from an astronomical solution (*43*) without radiometric age control or a magnetostratigraphy, thus adding subjectivity to the chosen isotopic tie points used to calibrate the tuning (*44*) and making correlation with our eruptive record difficult.

One way forward is to use proxy records from sites that contain reliable magnetostratigraphy (*37*, *45*). Benthic δ^{18}O values – a proxy for deep-ocean temperature - from Sites 1090 (*46*) and U1335 (*37*) (Fig. 5) indicate that the decline in δ^{18}O values began during what is interpreted as C5Cr, reaching a nadir (the MMCO) during C5Cn.3n-C5Cn.1r. While it is currently difficult to validate the identification of C5Cr from site 1090 given potential for hiatuses in the record, it is corroborated by the astronomical model of U1335 and is interpreted to be the same chron in which CRB eruptions began with the Lower Steens Basalt. Although the absolute timing of the onset of the MMCO cannot be confirmed by our data, the astronomically tuned record from U1335 compared to our geochronology show that the decrease in δ^{18}O preceded the eruption of Steens Basalt lava flows by 100-200 ka. CRBG volcanism may have played a role in eliciting global warming through cryptic degassing of CO_2 as magma migrated through dike swarms prior to surface eruptions (*7*). Alternatively, the apparent mismatch between the onset of the CRBG and the MMCO may indicate that the two events are unrelated. Regardless, the δ^{18}O minimum appears coeval with the eruption of the Grande Ronde Basalt, suggesting that a link may exist. Further work that refines age models for climate proxy records across the MMCO and investigates rates of eruptions for the CRBG is

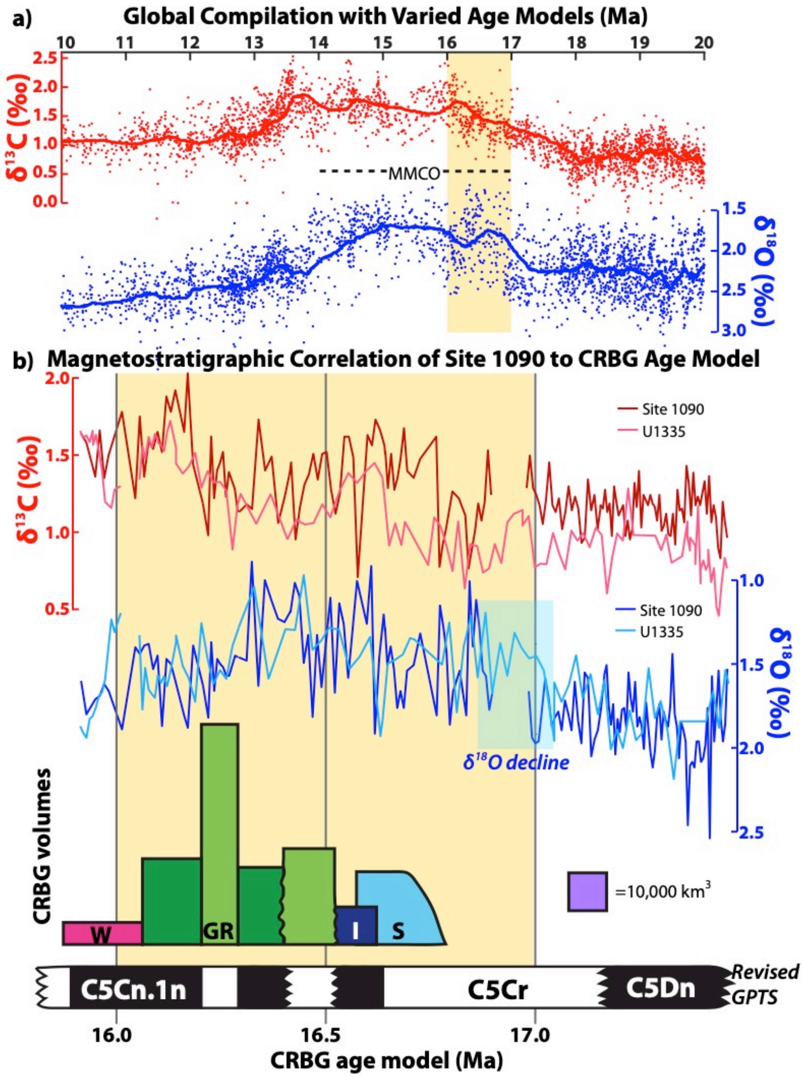

Fig. 5. Correlation of the Columbia River Basalt Group with the Mid-Miocene Climate Optimum. (A) A compilation of proxy records exhibiting the MMCO (*47*), with age constraints as reported in each study. Although ages are susceptible to uncertainties in the Mid-Miocene timescale, the magnitude of the isotopic signals are not. **(B)** In order to compare zircon geochronology results for CRBG eruptions to paleoclimate proxy records of the MMCO, it is necessary to bypass age models tied to outdated calibrations of the GPTS. The robust magnetostratigraphy of Sites 1090 (*45*, *46*) and U1335 (*37*) allows for correlation of these isotopic records to our CRBG eruption chronology and refined GPTS. The area of each colored rectangle corresponds to the volume of each formation (*1*) (S – Steens Basalt; I – Imnaha Basalt; GR – Grande Ronde Basalt; W – Wanapum Basalt), with width constrained by zircon ages (slanted boundary indicates that the onset of Steens Basalt volcanism is not yet constrained); polarity of the basalt flows is taken from Reidel (*1*) and references therein. Yellow shading compares global proxy data at 17-16 Ma (lacking an age model based on absolute geochronology) with volcanic events occurring 17-16 Ma, while the light blue shading highlights the onset of the MMCO in both records with the drop in δ^{18}O.

required before it can be determined if the CRBG caused the MMCO. While our work constrains the age of the top of chron C5Cr, there are not yet absolute age constraints for either the bottom of C5Cr, or for the onset of the MMCO. Because the record for U1335 has an astronomical age model constrained by isotopic correlations with Site U1337 (*37*, *42*), and does not have an absolute age defining the base of chron C5Cr, a tighter correlation of the CRBG and MMCO could be observed, particularly if the chron began later in time than is currently proposed. These uncertainties in the timing of this magnetic field reversal and the beginning of the MMCO must be resolved to better assess if the CRBG played a causative role in the MMCO.

Despite uncertainties present in Mid-Miocene age models, global proxy data (*47*) indicate that the MMCO continued for >1 Ma after the cessation of the majority of CRBG volcanism (Fig. 5). The time lag between the cessation of volcanism and a return to cooler climatic conditions could be understood as a consequence of the long response time of negative feedbacks within the global carbon cycle that regulate atmospheric CO_2 and Earth's temperature on geologic timescales. These feedbacks include interactions between temperature, the chemical weathering of continental silicate minerals, and the burial of CO_2 in marine carbonate sediments (*48*). While the sensitivity of the silicate weathering feedback remains poorly understood, recent estimates for response times vary from ~200-500 ka (*49*) and are consistent with the stabilization of atmospheric CO_2 (i.e. return to baseline conditions) on ~1 Ma timescales.

Our age model of CRBG emplacement shortens the duration of volcanism from 1.9 Ma (*4*) to 750 ka and correlates the onset of CRBG volcanism and the onset of the MMCO to within ~100 ka. A shorter duration of CRBG volcanism implies higher average CO_2 emissions and higher peak CO_2 concentrations during volcanism, to be compared with marine proxy records. However, current proxy records for atmospheric CO_2 during the MMCO are too coarse for a close comparison to the eruptive history of the CRBG, further inhibiting the ability to assess whether or not the CRBG caused the MMCO. Furthermore, establishing a quantitative link between CRBG volcanism and changes in the global carbon cycle and atmospheric CO_2 is hampered by uncertainties in the amount of CO_2 emitted by flood basalts from dissolved mantle carbon in addition to 'cryptic' sources, such as organic or inorganic sediments volatilized through contact with basaltic flows or sills (*7*). Armstrong McKay *et al.* (*7*), using a main phase CRBG eruptive duration of 900 ka, model that 4090-5670 Pg of emitted carbon can yield the observed changes in benthic $\delta^{13}C$ and atmospheric CO_2, although this amount includes a substantial component of cryptic degassing beyond the expected volatile release of subaerial basalt flows. Future studies should focus on further revision of the Mid-Miocene timescale and a high-resolution climate proxy record spanning the 700 ka duration of CRBG volcanism to explore the extent to which the timing of CRBG volcanism agrees with changes in atmospheric CO_2. Such studies will lead to an improved understanding of the MMCO, more general models linking volcanism to climate change, and could be crucial for understanding why some flood basalts apparently result in mass extinctions and others do not.

MATERIALS AND METHODS

Methods are as described in Schoene *et al.* (*23*) and Samperton *et al.* (*50*).

Zircon separation and preparation

Zircons were separated from their host rock through standard methods of crushing, gravimetric-, and magnetic-separation techniques using a Bico Braun "Chipmunk" Jawcrusher, disc mill, hand pan, hand magnet, Frantz isodynamic separator, and methylene iodide. Zircons from the least magnetic and most dense mineral separate were transferred in bulk to quartz crucibles and annealed in a muffle furnace at 900°C for 48 hours after Mattinson (*51*). After annealing, 20-40 zircon grains from each sample were photographed (Fig. S2) and picked in reagent-grade ethanol for analysis. Given the low radiogenic Pb content of the samples, cathodoluminescence images were not obtained. Euhedral grains with a range of morphologies were selected, while those with visible cracks, inclusions, and cores were avoided. Individual grains were transferred using stainless steel picking tools to separate 3-mL Savillex Hex beakers containing distilled acetone and taken to the clean lab for analysis.

U-Pb zircon ID-TIMS analysis

Single zircon grains were loaded into 200 uL Savillex "micro"-capsules with 100 μL 29 M HF + 15 μL 3N HNO_3 for a single leaching step in high-pressure Parr bombs at 185°C for 12 h to remove crystal domains affected by Pb loss (*51*). Grains were rinsed post-leaching in 6 N HCl, MQ H2O, 3N HNO_3, and 29 M HF prior to spiking with

EARTHTIME (^{202}Pb-)^{205}Pb-^{233}U-^{235}U tracer and addition of 100uL 29 M HF + 15 µL 3N HNO_3 (*52*, *53*). Zircons were then dissolved to completion in Parr bombs at 210°C for 48 h. Dissolved zircon solutions were subsequently dried down, dissolved in 100 µL 6N HCl, and converted to chlorides in Parr bombs at 185°C for 12 h, after which solutions were dried again and brought up in 50 µL 3N HCl. The U-Pb and trace element aliquots were then separated by anion exchange chromatography using 50 µL columns and AG-1 X8 resin (200-400 mesh, chloride from Eichrom) (*54*), and dried down with a microdrop of 0.015 M H_3PO_4. The dried U and Pb aliquot was loaded in a silica gel emitter (*55*) to an outgassed zone-refined Re filament.

Isotopic determinations were performed using an IsotopX PhoeniX-62 thermal ionization mass spectrometer (TIMS) at Princeton University, with Pb analysis performed in peak-hopping mode on a Daly-photomultiplier ion-counting detector. A correction for mass-dependent Pb fractionation was applied in one of two ways. For double-Pb spiked analyses (^{202}Pb-^{205}Pb, ET2535), a cycle-by-cycle fractionation correction was calculated from the deviation of measured ^{202}Pb/^{205}Pb from the known tracer ^{202}Pb/^{205}Pb (0.99924±0.00027 (1σ)). For single-Pb spiked analyses (^{205}Pb, ET535), a Pb fractionation of 0.182±0.041%/amu was used, as determined by repeat measurements of NBS982 at Princeton. A Daly-photomultiplier deadtime of 28.8 ns was used, as determined by repeat measurements of NBS standards. Corrections for interfering isotopes under masses 202, 204, and 205 were made cycle-by-cycle by measuring masses 201 and 203 and assuming they represent $^{201}BaPO_4$ and ^{203}Tl and using natural isotopic abundances to correct for $^{202}BaPO_4$, $^{204}BaPO_4$, $^{205}BaPO_4$, and ^{205}Tl.

UO_2 measurements were performed in static mode on Faraday cups with a bulk U fractionation correction calculated from the deviation of measured $^{233}U/^{235}U$ from the known tracer $^{233}U/^{235}U$ (0.995062±0.000054 (1σ)), and an oxide composition of $^{18}O/^{16}O$ of 0.00205 was used (*56*). Data reduction was performed using the programs Tripoli and U-Pb Redux (*57*, *58*) and the decay constants of Jaffey *et al.* (*59*). All Pbc was attributed to laboratory blank with a mean isotopic composition determined by total procedural blank measurements (see Table S1 for values). Two different blank models were generated to assess data collected before (OC) and after (SF) January 2017, when the laboratory began heating side filaments before collecting data on the mass spectrometer, which was found to reduce interferences. Uncertainties in reported U-Pb zircon dates are at the 95% confidence level and exclude tracer calibration and decay constant uncertainties. Correction for initial ^{230}Th disequilibrium in the $^{206}Pb/^{238}U$ system was made on a fraction-by-fraction basis by estimating $(Th/U)_{magma}$ using $(Th/U)_{zircon}$ determined by TIMS and a mean $(Th/U)_{zircon\text{-}magma}$ partition coefficient ratio of 0.19±0.11, which encompasses the range of values for $(Th/U)_{zircon\text{-}magma}$ partition coefficients obtained from glasses from a variety of volcanic settings (*60*). Uncertainties for the resulting $(Th/U)_{magma}$ were also calculated on a fraction-by-fraction basis, propagating the uncertainty in the $(Th/U)_{zircon\text{-}magma}$ partition coefficient. Overall, these corrections for ^{230}Th disequilibrium affect our results by no more than ±10 ka, compared to an alternative approach using a constant $(Th/U)_{magma}$ of 3.5±1.0 (see Supplement).

ACKNOWLEDGMENTS

We thank S. Reidel and B. Martin for assisting with stratigraphic classification of the samples, and J. Murray, S. Bartusek, and K. Duffey for assisting with fieldwork and sample preparation. M. Eddy, J. Higgins, M. Long, and S. Reidel provided thoughtful feedback on an earlier version of this manuscript. We thank S. Burgess and two anonymous reviewers for suggestions that greatly improved the manuscript. **Funding:** This material is based upon work supported by the National Science Foundation Graduate Research Fellowship under Grant No. DGE-1656466, by Princeton Environmental Institute at Princeton University through the Walbridge Fund, and by the Princeton University Department of Geosciences Scott Vertebrate Fund. **Author contributions:** J.K. and B.S. devised the study, conducted fieldwork, interpreted results, and prepared the manuscript; J.K. performed most zircon analyses. **Competing interests:** The authors declare no competing financial interests. **Data and materials availability:** All data needed to evaluate the conclusions in the paper are present in the paper and/or the Supplementary Materials. Additional data related to this paper may be requested from the authors.

SUPPLEMENTAL INFORMATION

Sample Descriptions

Samples dated in this study were collected from roadcuts or natural exposures in Washington, Oregon, and Idaho in summers 2015 and 2016. Detailed sample descriptions are provided here, in stratigraphic order from oldest to youngest. Outcrop photographs are provided in Fig. S1, and zircon photographs are provided in Fig. S2.

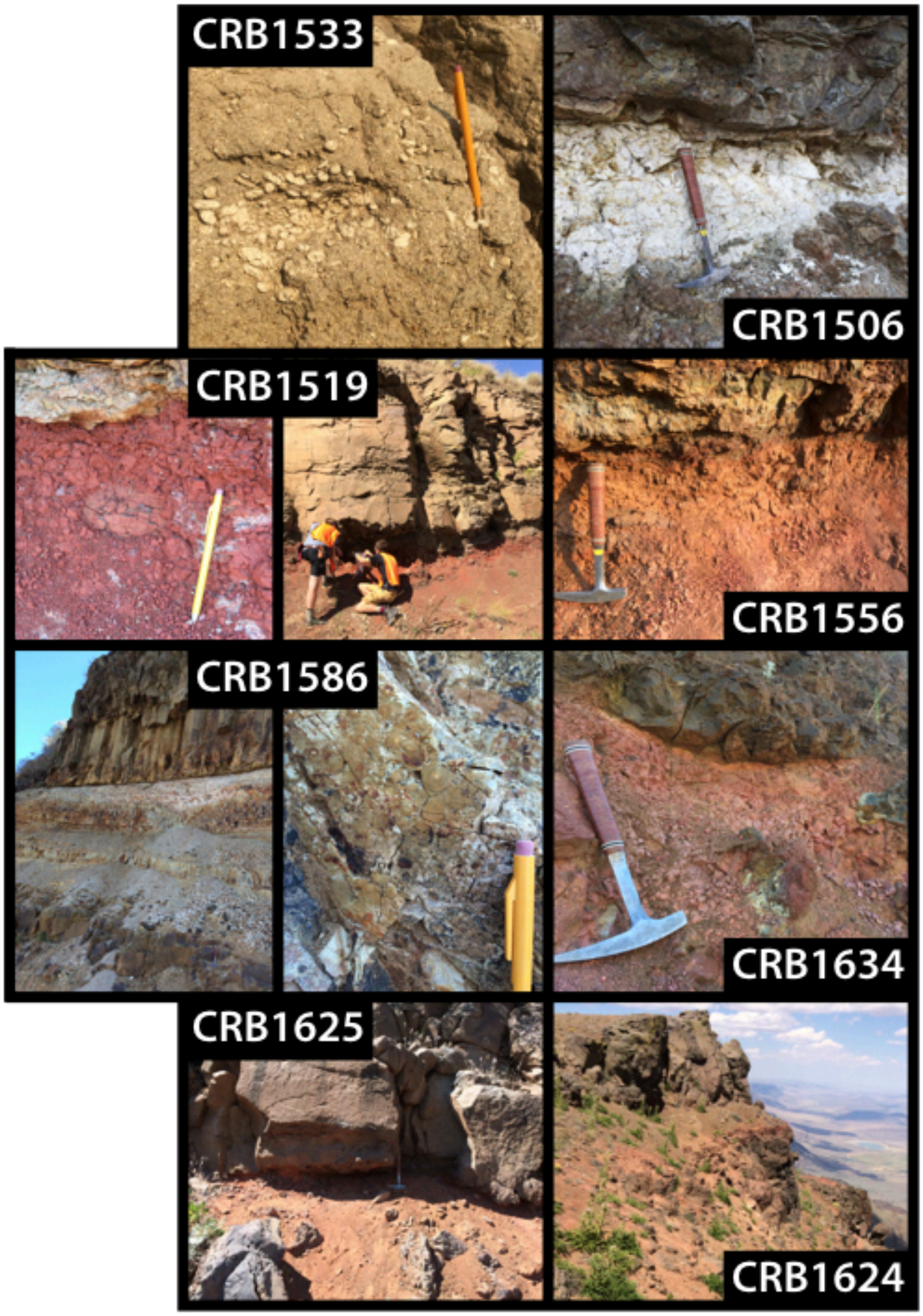

Fig. S1. Geochronology Sample Photos. Outcrop-scale and/or hand-sample scale photos of each geochronology sample are provided here, with stratigraphic younging from bottom to top (Photo credit: Jennifer Kasbohm, Princeton University).

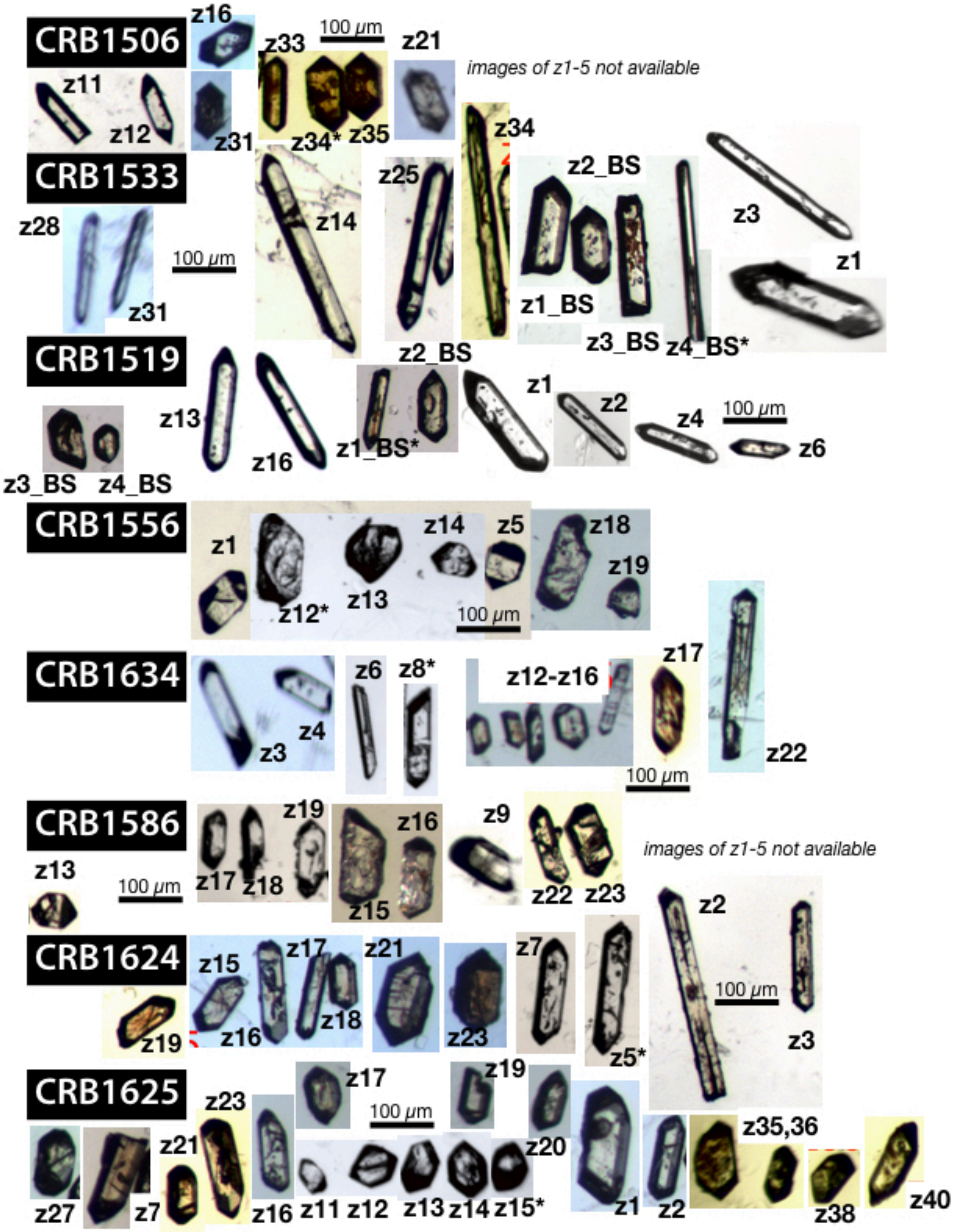

Fig. S2. Zircon Photos. Optical images of zircons under transmitted light are presented here, with stratigraphic younging from bottom to top. Zircons present a range of morphologies, but the majority are euhedral with sharp crystal terminations, indicating an igneous rather than detrital origin. The zircon yielding the youngest, most precise analysis for each sample is starred.

CRB1625 (42.67542°N, 118.68724°W, elevation 2255 m)

This sample was collected from a ~0.5 m thick redbole between two Lower Steens Basalt flows, (based on the stratigraphy of Johnson *et al.* (*60*)) on the western side of Steens Mountain. The fine red sediment overlay a brecciated flow top and contained abundant vitreous microphenocrysts, black round lithic fragments, and subangular fragments of basaltic pumice up to 1 mm in size.

Fewer than 100 zircons were separated from this sample, and many of these grains are rounded and appear detrital. Some grains are euhedral, and ranged from equant to a high aspect ratio. Many grains are tinted orange, while some are clear. Forty grains were selected for analysis, and 19 were successfully dated. For this sample and the other samples described below, grains that were not successfully dated were lost at some stage of zircon chemistry prior to dating, or were dated and either did not fall on the Concordia line or exhibited a ratio of radiogenic Pb to common Pb that was ≤1. Six of these grains were ca. 16.7 Ma, with a dispersion of 120 ka, while the other 13 are inherited. Both the Mid-Miocene and inherited grains exhibited a range of morphologies. The youngest grains were often euhedral, and ranged from equant to an aspect ratio of at least 4:1. While some of the young grains were glassy and transparent, others were opaque. While a few of the analyses exhibited elevated common Pb content (>1 pg), others had low common Pb (<0.3 pg) but also low radiogenic Pb content (<1 pg), yielding generally less precise zircon ages for this sample than for the others in this study.

CRB1624 (42.66626°N, 118.56479°W, elevation 2966 m)
This sample was collected from a ~0.5 m thick redbole interbedded between Upper Steens Basalt flows (*60*) at the East Rim Lookout on Steens Mountain. The sampled horizon was a fine pink sediment infilling a brecciated flow top, and contained abundant vitreous microphenocrysts with few dark round lithic fragments.

Hundreds of zircons were obtained from this sample, with a range of morphologies. Generally, grains were angular to subangular, with fewer round detrital grains. The grains ranged from equant to higher aspect ratios, though few were acicular. Most of the grains are orange, while a few are clear and glassy. Twenty-three grains were selected for analysis, and 11 were successfully dated. The youngest grains appear to be the most euhedral, and range in size from <100 to over 300 μm. All of the grains were found to be ca. 16.6 Ma, with a dispersion of <70 ka. The precision of these analyses is attributed to high radiogenic Pb content (up to 34 pg) of the grains and low common Pb content (often <0.3 pg) in the analyses.

CRB1586 (44.83067°N, 116.90138°W, elevation 641 m)
This sample was collected from a ~0.5 m thick bed of lapilli tuff interbedded between columnar Imnaha Basalt flows on route 71 south of Brownlee Dam in Idaho. Accretionary lapilli are mm-cm scale and exhibit concentric banding around lithic nuclei.

Fewer than 50 zircons were separated from this sample, and are found to be glassy, somewhat blocky, and ranging in morphology from equant to tabular. Most of the grains are around 100 μm in length. Twenty-three grains were selected for analysis, and of these, 14 were successfully dated. One grain was found to be inherited, while the other 13 are dated to ~16.6 Ma, with a dispersion of 120 ka. The youngest and most precise grains are among the largest analyzed, and have a high radiogenic Pb content (1-6 pg).

CRB1634 (46.05072°N, 117.23906°W, elevation 538 m)

This sample was collected from a redbole in the lower flows of the Wapshilla Ridge Member of the Grande Ronde Basalt, on Rattlesnake Grade in southeastern Washington. The redbole infills topography on the underlying brecciated flow top, with a maximum thickness of 0.3 m, but pinches out over a few meters width. The redbole contains a few mm-scale light and dark lithic fragments, with some vitreous phenocrysts.

Hundreds of zircons were obtained from this sample, ranging in size from 50-250 μm. Most are orange in color but a few are clear. Half of the zircons presented an acicular morphology, 20% appeared equant, and the rest have a medium aspect ratio. Twenty-four zircons were selected for analysis, and eleven were successfully dated. All zircons were found to be ca. 16.3 Ma, with a dispersion of 160 ka. The youngest grains appear somewhat wide, clear, and euhedral, and the most precise analyses came from zircons with the greatest amount of radiogenic Pb (1-2 pg).

CRB1556 (46.08543°N, 117.17870°W, elevation 1145 m)

This sample was collected from the same stratigraphic section as CRB1634, from a 0.6 m thick redbole between lava flows of the Meyer Ridge Member, immediately overlying the Wapshilla Ridge Member. The horizon was most coherent in its upper half, and displayed few vitreous phenocrysts and rare lithics.

The sample yielded 19 zircons, and all were picked for analysis; 7 were successfully dated. The zircons were either <100 μm and equant or larger and more tabular. A few were euhedral with pointy edges, while others appeared fragmented at the edges. The youngest, most precise analyses came from the largest grains. Even though these grains were not euhedral, they possessed the greatest amount of radiogenic Pb (1-2 pg). The grains exhibit a dispersion of 150 ka around ca. 16.3 Ma.

CRB1519 (46.44171°N, 117.39066°W, elevation 701 m)

This sample was collected from a redbole found under a lava flow of the Meyer Ridge Member and overlying a lava flow Wapshilla Ridge Member, representing the same stratigraphic interval as CRB1556 but found 44 km away on US-12 east of Pomeroy, WA. The sample is fine-grained, with abundant vitreous microphenocrysts and few angular lithic fragments.

Hundreds of zircons were separated from this sample, and they appear mostly clear and glassy, with a few orange grains. Most present typical aspect ratio, while 10% are acicular and a few grains are equant. Many grains are subangular, with pointy tips slightly worn down. Twenty-one grains were selected for analysis, and 10 were successfully dated. Two of the zircons analyzed were inherited, and appear somewhat opaque; five zircons were ca. 16.2 Ma but an age dispersion of 400 ka, outside the range of analytical uncertainty. The youngest grains each have one euhedral tip, are longer than 100 μm, and the most precise analyses were for zircons with a higher radiogenic Pb content (2-4 pg).

CRB1533 (46.95243°N, 119.99783°W, elevation 227 m)
This sample was collected from 2 kg of 1-10 cm-scale pumice clasts embedded in the volcaniclastic sediments of the Vantage Interbed type locality in Vantage, WA (Stop 7 in Tolan *et al.* (*61*)). Phenocrysts in the pumice contained quartz and sanidine, and the sampled horizon consisted of 1.4 m of the total 5.6 m of the Vantage Interbed exposed at the outcrop. The Vantage Interbed lies over the Basalt of Museum of the Sentinel Bluffs Member of N2 of the Grande Ronde Basalt, and under the Basalt of Ginkgo of the Frenchman Springs Member of the Wanapum Basalt.

Several thousand zircons were obtained from this sample, and all are clear, prismatic, and euhedral. The zircons range in size from 50-300 μm, and about 10% are equant grains, while 10% of the grains are acicular. Forty zircons were selected for analysis, and 11 of these were successfully dated, with 9 grains found younger than 17 Ma. The age dispersion of these samples is greater than 500 ka, well beyond analytical uncertainty, suggesting pre-eruptive crystallization. The youngest grains appear to be the most acicular in morphology, and the most precise analyses are due to high radiogenic Pb content of 5-15 pg.

CRB1506 (46.73914°N, 117.75500°W, elevation 470 m)
This sample was collected from 0.3 m of a fine white crumbly ash, with few round lithic fragments and glassy phenocrysts, interbedded between the overlying Basalt of Lolo and the underlying Basalt of Rosalia of the Priest Rapids Member of the Wanapum Basalt, on WA-127 southeast of Endicott, WA.

Hundreds of zircons were obtained from this sample, most of which are clear and subangular to subrounded. While a few zircons were angular, none were acicular. Thirty-five grains were selected for analysis, and 10 were successfully dated. Four of these were inherited, and the remaining six grains have a uniform age distribution within 2σ uncertainty, of ca. 15.9 Ma. The youngest and most precise dates were obtained from somewhat opaque, orange-tinted zircons that were euhedral, and had high radiogenic Pb content of 11-40 pg.

S2 U-Pb Age Interpretations

Given the physical characteristics of both rock samples and zircons, the geochronology samples for this study are interpreted to be volcanic in origin, and deposited by unrelated regional silicic volcanism during cessations in CRBG volcanism. The presence of phenocrysts, lithic fragments, and fragments of basaltic pumice found at the hand sample scale are consistent with ash deposits, and the euhedral and prismatic appearance of the zircons are consistent with magmatic textures, with little evidence for rounding seen in alluvial or eolian grains.

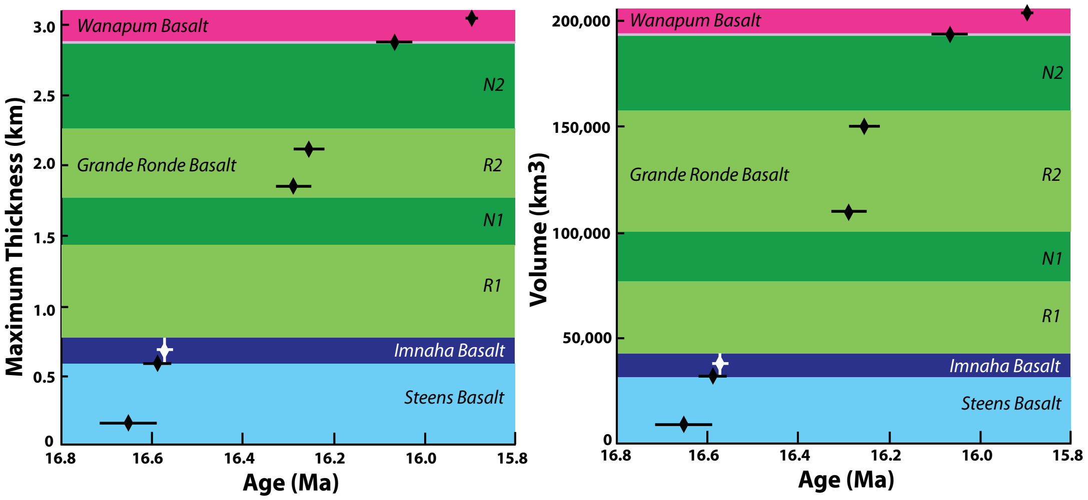

Fig. S3. Thickness and Volume versus Age Plots. Detailed area and volume estimates for each member of the CRBG stratigraphy allows for plots of cumulative maximum thickness and volume versus age. Youngest zircon ages with 2σ uncertainty for the samples dated in this study are plotted here. Cumulative thickness and volume are color-coded by CRBG formation as labeled on the plots.

Full U-Pb isotope results are given in Table S1, maximum thickness and volume versus age plots are given in Fig. S3, and Concordia plots for each sample are given in Fig. S4. All dates are presented with 2σ uncertainty, which represents internal errors only. In Table S2, alternative age interpretations are also given with 2σ uncertainties of ±X/Y/Z. X is used for most of the geochronological uncertainty described in this paper, and indicates internal uncertainties only for comparison with U-Pb dates from labs using ET-(2)535 tracer solution. Y also incorporates tracer calibration uncertainties for comparison with other U-Pb dates determined with different tracer solution. Z includes full systematic uncertainties, including decay constants, to allow for comparison with other radioisotopic dates or astrochronologically-determined timescales that may be tied to other radioisotopic dates that are not derived from the U-Pb system (*62*, *63*).

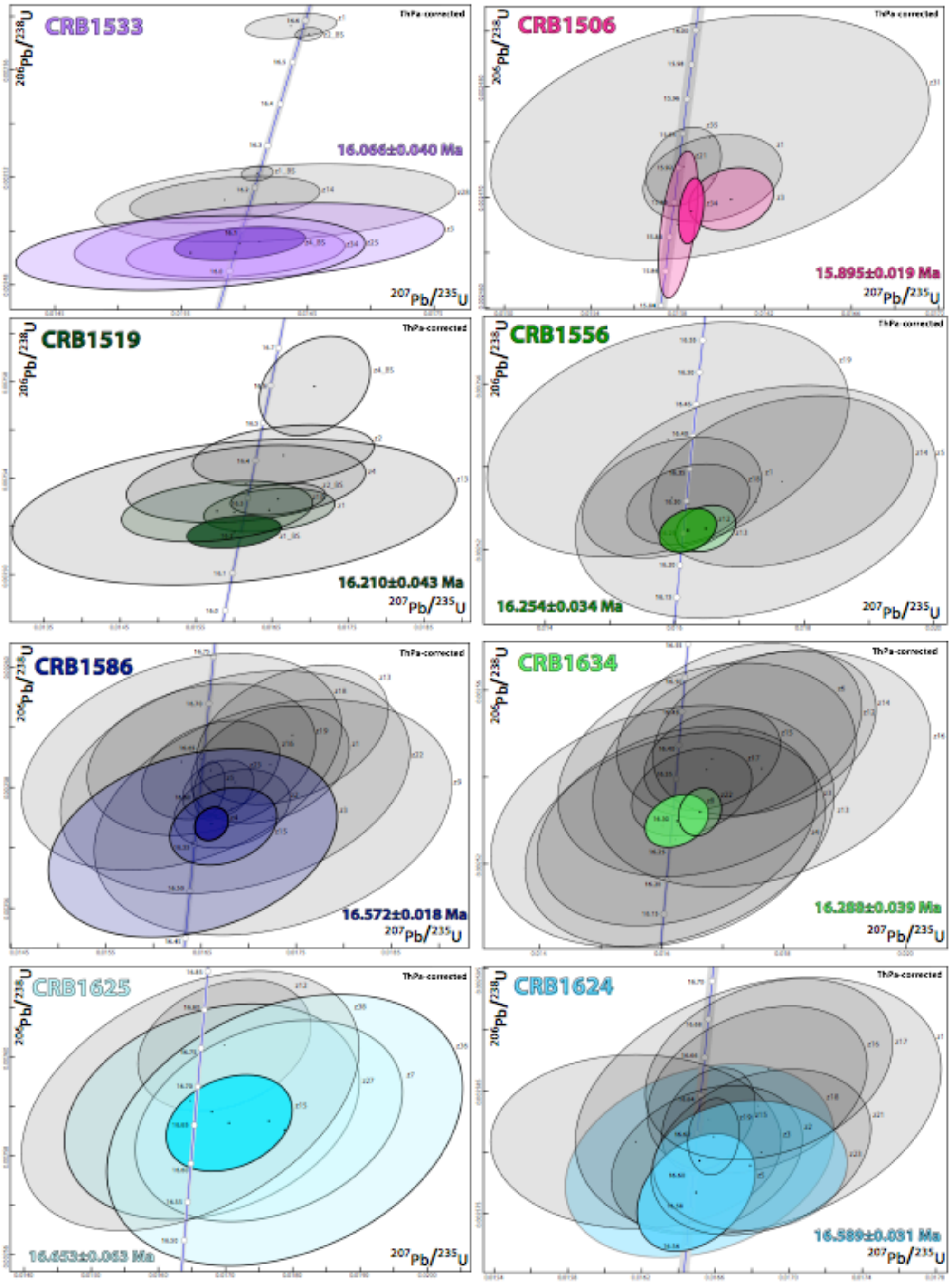

Fig. S4. Concordia Plots for U-Pb ID-TIMS Geochronological Data. U-Pb isotopic data for each analysis is available in Table S1. Each ellipse is labelled and represents a zircon analysis, with the width of the ellipse representing 2σ uncertainty. The red ellipses are those analyses that are included in the "Youngest Few Zircons" weighted means described in Table S2, while the gray ellipses are not included in those weighted means. The shading around the Concordia line represents uncertainties in the U decay constants. Almost all ellipses overlap with Concordia, indicating closed-system behavior.

The ages we present in this study are influenced by how we dealt with the issue of Th/U disequilibrium in zircon, and our decision to present the single youngest, most-precise analysis as the age of each ashbed, rather than weighted means. Both of these decisions are discussed below, and ultimately, neither interpretation substantially affects our major conclusions about the timing and duration of CRBG eruptions.

Th/U disequilibrium correction in zircon

During zircon crystallization, ^{238}U is preferentially incorporated into the crystal lattice over ^{230}Th, an intermediate daughter product, causing the system to depart from secular equilibrium and ages to be underestimated. Often, a minimal correction is made to address this fractionation. Either zircons are assumed to crystallize from a magma with a uniform (Th/U), or a uniform partition coefficient between Th and U from the liquid is assumed, and then the (Th/U) of the magma is calculated on a fraction by fraction basis, using the model (Th/U) of each zircon determined from the ^{208}Pb/^{206}Pb ratios (*64*). Given the likelihood that the zircons in this study were crystallized from a variety of different magmatic systems, we prefer the constant partition coefficient approach for correcting Th/U disequilibrium. A recently published, comprehensive study (*59*) measures partition coefficients in zircon-glass pairs from a range of volcanic settings; volcanic glasses are assumed to display the same partitioning as the magma from which they crystallize. All measurements of Th/U partitioning in the study fell in the range of 0.06-0.3, so we use a conservative estimate of 0.19±0.11 (2σ) to calculate $(\mathrm{Th/U})_{\mathrm{magma}}$ for each zircon, using the ^{208}Pb/^{206}Pb obtained for each zircon during mass spectrometry. To assess the impact of this correction, we also reduce our youngest zircon ages (upon which our interpretations depend) with a constant $(Th/U)_{magma}$ of 3.5±1.0 (2σ), which encompasses the majority of igneous liquids (Table S2). We find that our preferred interpretation with a constant Th/U partition coefficient adjusts our dates by no more than 10 ka, and adds no more than 5 ka of uncertainty to each age.

Interpretation of zircon crystallization age spectra

The zircons dated from each geochronology sample displayed a dispersion in ages ranging from 40-500 ka (apart from inherited grains). We interpret this as geological scatter caused by pre-eruptive zircon crystallization or incorporation of zircons from older material in the same volcanic system (*23*), because the dispersion in most cases goes beyond analytical uncertainty. Therefore, the zircon that crystallized most recently should best time the eruption of the volcanic ash, and for this reason we interpret the youngest, most precise zircon dates as representing the age of the horizons in this study. Although Pb loss in zircons may sometimes cause U-Pb dates to be biased too young, chemical abrasion on young zircons nearly eliminates this effect. We find the pattern in our dataset of younging ages with increasing height in the CRB stratigraphy as further evidence that Pb loss does not affect our conclusions, as its effects would vary with grain size and U-content, and not systematically with age.

Other geochronological studies often use a weighted mean of several zircon dates to constrain the age of a sample. This approach yields dates with lower uncertainty than the single crystal approach as well as greater assurance that the resulting age is not biased by a young outlier, but should only be used for homogeneous age populations where the only source of scatter is analytical uncertainty, which is not the case for all of our samples, and difficult to justify in most U-Pb datasets even if they overlap within analytical uncertainty. Additionally, including zircons beyond the youngest grain in the final age of the sample may bias the resulting age too old as a result of pre-eruptive crystallization. To assess how well the analytical uncertainty can explain the observed dispersion of crystallization ages, the mean square of weighted deviates (MSWD) may be calculated, and should be ~1, with deviance from 1 varying with the number of analyses included in the weighted mean (*65*). However, a dataset may still be subject to subtle geologic dispersion, even with an MSWD near 1 (*64*), resulting in weighted means that are biased too old.

We compare the single crystal ages presented in this study to weighted mean ages calculated for each sample in Table S2 and Fig. S5. First, we calculate the weighted mean for the youngest few zircons, whose dates overlap with the youngest date, where slight offsets may be caused by analytical uncertainty. We also calculate weighted mean ages using the maximum number of grains allowed to produce an acceptable MSWD near 1. We find that the more grains that are included in the weighted mean, the ages are biased older, though are more precise. Ultimately, as seen in Table S2 and Fig. S5, the decision to use the age of single crystals rather than weighted means ages does not substantially offset our ages, and does not have a major bearing on any of the conclusions presented in this paper. The single crystal approach appears to be the most conservative because it results in larger uncertainty for each age, while overlapping with the weighted mean ages.

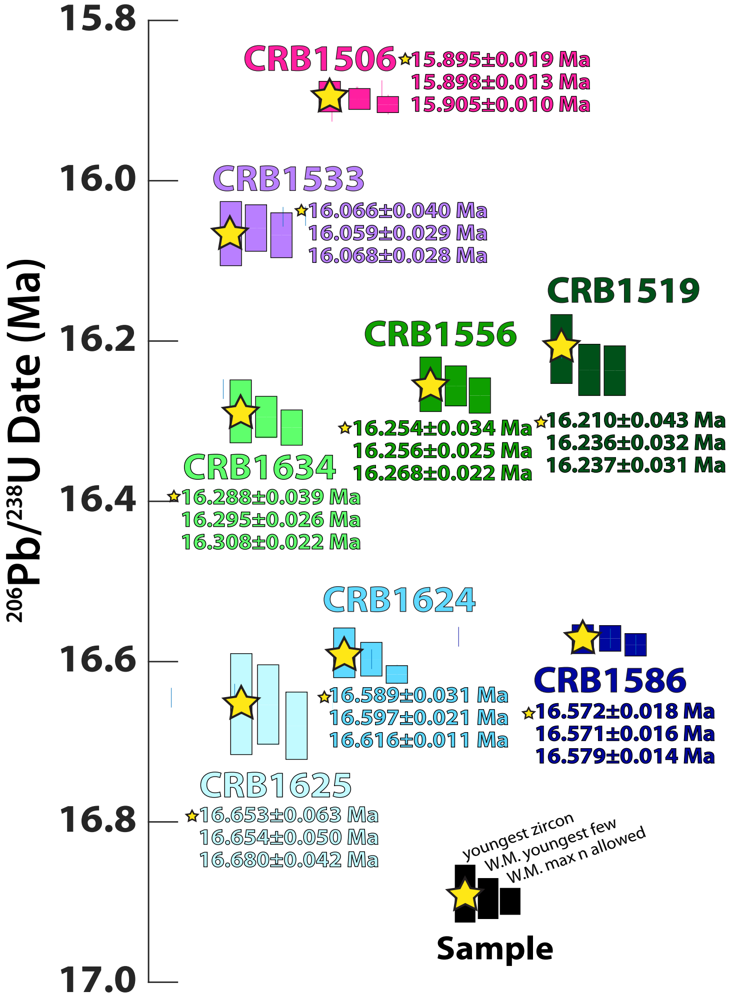

Fig. S5. Alternate Age Interpretations. Our preferred interpretation of single crystals representing the eruptive age of each sample does not substantially offset our results from using weighted mean ages. For each sample, we compare the age of the youngest sample to the a weighted mean age calculated from the youngest few grains, and to a weighted mean age calculated using the maximum number of grains that yield an acceptable MSWD near 1. Even though ages from single crystals exhibit higher 2σ uncertainty, we prefer the youngest zircon interpretation to avoid the effects of pre-eruptive zircon crystallization, as the weighted mean ages all appear biased slightly older. Calculated dates using the different interpretations are given in Table S2.

Comparing with ^{40}Ar/^{39}Ar geochronology

When compared to the most recent ^{40}Ar/^{39}Ar geochronology results (*20*) for the Steens Basalt, we find a similar duration (150 ka compared with 210 ka) but timing 100 ka earlier. However, when the ^{40}Ar/^{39}Ar ages are recalculated through the method of Renne *et al.* (*63*) using the more recent Fish Canyon sanidine age of 28.201 Ma (*21*) instead of 28.02 Ma (*63*), the recalculated range of 16.75-16.54 Ma matches favorably with our results.

Table S1. U-Pb Isotopic Data. Data acquired by CA-ID-TIMS is presented following the references, with various corrections as specified in the notes beneath the table.

	Youngest Zircon									Weighted Means													
		const. partition coefficient				constant Th/U_magma				Youngest Few Zircons							Maximum n allowed for MSWD ≈ 1						
			uncertainty				uncertainty			addtnl			uncertainty			MS	addtnl			uncertainty			MS
sample	zircon	age	X	Y	Z	age	X	Y	Z	zircons	n	age	X	Y	Z	WD	zircons	n	age	X	Y	Z	WD
CRB1625	z15	16.653	0.063	0.071	0.073	16.655	0.062	0.070	0.072	7,27,36	4	16.654	0.050	0.057	0.059	0.018	al	6	16.680	0.042	0.052	0.055	0.82
CRB1624	z5	16.589	0.031	0.032	0.037	16.589	0.029	0.031	0.035	18,23	3	16.597	0.021	0.023	0.029	0.26	all	11	16.616	0.011	0.014	0.023	0.92
CRB1586	z4	16.572	0.018	0.018	0.026	16.582	0.013	0.014	0.023	3,15	3	16.571	0.016	0.017	0.024	0.086	2,9,23	6	16.579	0.014	0.015	0.023	0.94
CRB1634	z8	16.288	0.039	0.043	0.046	16.294	0.038	0.041	0.045	22	2	16.295	0.026	0.030	0.035	0.25	all -15	10	16.308	0.022	0.029	0.034	1.1
CRB1556	z12	16.254	0.034	0.037	0.041	16.264	0.032	0.035	0.039	13	2	16.256	0.025	0.029	0.033	0.014	all	7	16.268	0.022	0.027	0.032	0.88
CRB1519	z1_BS	16.210	0.043	0.044	0.047	16.208	0.043	0.043	0.046	1,16	3	16.236	0.032	0.032	0.037	1.6	13	4	16.237	0.031	0.032	0.036	1.1
CRB1533	z4_BS	16.066	0.040	0.040	0.043	16.065	0.038	0.039	0.042	3,25,34	4	16.059	0.029	0.030	0.035	0.19	28	5	16.068	0.028	0.030	0.034	1.3
CRB1506	z34	15.895	0.019	0.020	0.026	15.904	0.015	0.017	0.024	3,21	3	15.898	0.013	0.014	0.022	0.26	1,35	5	15.905	0.010	0.012	0.021	1.1

preferred interpretation

Table S2. Alternate Age Interpretations. We compare our preferred data interpretation of using the youngest, most precise zircon date for the age of the sample, with a constant Th/U partition coefficient to alternative interpretations. The youngest zircon age with a constant partition coefficient shows no more than 10 ka offset from the youngest zircon age obtained using a constant $(Th/U)_{magma}$. The youngest zircon age can also be compared to weighted mean ages calculated from the youngest few zircons or a weighted mean taken from the maximum number of grains allowing an acceptable MSWD of 1. The effects of these interpretations are described in the text and illustrated in Fig. S5.

REFERENCES

1. S. P. Reidel, The Columbia River Basalt Group: a flood basalt province in the Pacific Northwest, USA. *Geosci. Canada*. **42**, 151–168 (2015).
2. V. E. Courtillot, P. R. Renne, On the ages of flood basalt events. *Comptes Rendus - Geosci.* **335**, 113–140 (2003).
3. S. Self, M. Widdowson, T. Thordarson, A. E. Jay, Volatile fluxes during flood basalt eruptions and potential effects on the global environment: A Deccan perspective. *Earth Planet. Sci. Lett.* **248**, 517–531 (2006).
4. T. L. Barry *et al.*, Eruption chronology of the Columbia River Basalt Group. *Geol. Soc. Am. Spec. Pap.* **497**, 45–66 (2013).
5. A. E. Shevenell, J. P. Kennett, D. W. Lea, Middle Miocene Southern Ocean Cooling and Antarctic Cryosphere Expansion. *Science*. **305**, 1766–1770 (2004).
6. M. Böhme, The Miocene Climatic Optimum: Evidence from ectothermic vertebrates of Central Europe. *Palaeogeogr. Palaeoclimatol. Palaeoecol.* **195**, 389–401 (2003).

7. D. I. Armstrong McKay, T. Tyrrell, P. A. Wilson, G. L. Foster, Estimating the impact of the cryptic degassing of Large Igneous Provinces: A mid-Miocene case-study. *Earth Planet. Sci. Lett.* **403**, 254–262 (2014).
8. G. L. Foster, C. H. Lear, J. W. B. Rae, The evolution of pCO_2, ice volume and climate during the middle Miocene. *Earth Planet. Sci. Lett.* **341–344**, 243–254 (2012).
9. W. M. Kurschner, Z. Kvacek, D. L. Dilcher, The impact of Miocene atmospheric carbon dioxide fluctuations on climate and the evolution of terrestrial ecosystems. *Proc. Natl. Acad. Sci.* **105**, 449–453 (2008).
10. Y. G. Zhang *et al.*, A 40-million-year history of atmospheric CO_2. *Philos. Trans. R. Soc. London.* (2013).
11. D. A. Hodell, F. Woodruff, Variations in the strontium isotopic ratio of seawater during the Miocene: Stratigraphic and geochemical implications. *Paleoceanography*. **9**, 405–426 (1994).
12. V. E. Camp, Origin of Columbia River Basalt: Passive rise of shallow mantle, or active upwelling of a deep-mantle plume? *Geol. Soc. Am. Spec. Pap.* **497**, 181–199 (2013).
13. L. Liu, D. R. Stegman, Origin of Columbia River flood basalt controlled by propagating rupture of the Farallon slab. *Nature*. **482**, 386–389 (2012).
14. M. D. Long *et al.*, Mantle dynamics beneath the Pacific Northwest and the generation of voluminous back-arc volcanism. *Geochemistry, Geophys. Geosystems*. **13**, 1–22 (2012).
15. A. R. Dominguez, R. Van Der Voo, Secular variation of the middle and late Miocene geomagnetic field recorded by the Columbia River Basalt Group in Oregon, Idaho and Washington, USA. *Geophys. J. Int.* **197**, 1299–1320 (2014).
16. N. A. Jarboe, R. S. Coe, J. M. G. Glen, Evidence from lava flows for complex polarity transitions : the new composite Steens Mountain reversal record. *Geophys. J. Int.* **186**, 580–602 (2011).
17. T. L. Tolan *et al.*, An introduction to the stratigraphy, structural geology, and hydrogeology of the Columbia River Flood-Basalt Province: A primer for the GSA Columbia River Basalt Group field trips. *Geol. Soc. Am. F. Guid.* **15**, 599–643 (2009).
18. S. P. Reidel *et al.*, The Grande Ronde Basalt, Columbia River Basalt Group; Stratigraphic descriptions and correlations in Washington, Oregon, and Idaho. *Geol. Soc. Am. Spec. Pap.* **239**, 21–53 (1989).
19. D. A. Swanson, T. L. Wright, P. R. Hooper, R. D. Bentley, Revisions in Stratigraphic Nomenclature of the Columbia River Basalt Group. *Geol. Surv. Bull.* **1457–G**, G1–G59 (1979).
20. F. J. Hilgen, L. J. Lourens, J. A. Van Dam, in *The Geologic Time Scale* (2012).
21. G. A. Mahood, T. R. Benson, Using $^{40}Ar/^{39}Ar$ ages of intercalated silicic tuffs to date flood basalts: Precise ages for Steens Basalt Member of the Columbia River Basalt Group. *Earth Planet. Sci. Lett.* **459**, 340–351 (2017).
22. K. F. Kuiper *et al.*, Synchronizing rock clocks of earth history. *Science.* **320**, 500–504 (2008).
23. B. Schoene *et al.*, U-Pb geochronology of the Deccan Traps and relation to the end-Cretaceous mass extinction. *Science.* **347**, 182–184 (2015).

24. J. I. Simon, P. R. Renne, R. Mundil, Implications of pre-eruptive magmatic histories of zircons for U-Pb geochronology of silicic extrusions. *Earth Planet. Sci. Lett.* **266**, 182–194 (2008).
25. J. S. Miller, J. E. P. Matzel, C. F. Miller, S. D. Burgess, R. B. Miller, Zircon growth and recycling during the assembly of large, composite arc plutons. *J. Volcanol. Geotherm. Res.* **167**, 282–299 (2007).
26. B. Schoene, J. Guex, A. Bartolini, U. Schaltegger, T. J. Blackburn, Correlating the end-Triassic mass extinction and flood basalt volcanism at the 100 ka level. *Geology*. **38**, 387–390 (2010).
27. J. L. Crowley, B. Schoene, S. A. Bowring, U-Pb dating of zircon in the Bishop Tuff at the millennial scale. *Geology*. **35**, 1123–1126 (2007).
28. T. A. Rivera, M. D. Schmitz, B. R. Jicha, J. L. Crowley, Zircon petrochronology and ^{40}Ar/^{39}Ar sanidine dates for the mesa falls tuff: Crystal-scale records of magmatic evolution and the short lifespan of a large yellowstone magma chamber. *J. Petrol.* **57**, 1677–1704 (2016).
29. T. Thordarson, S. Self, The Roza Member, Columbia River Basalt Group: A gigantic pahoehoe lava flow field formed by endogenous processes? *J. Geophys. Res. Solid Earth*. **103**, 27411–27445 (1998).
30. A. Chenet *et al.*, Determination of rapid Deccan eruptions across the Cretaceous-Tertiary boundary using paleomagnetic secular variation: 2. Constraints from analysis of eight new sections and synthesis for a 3500-m-thick composite section. *J. Geophys. Res. Solid Earth*. **114** (2009).
31. S. P. Reidel, T. L. Tolan, The Grande Ronde Basalt, Columbia River Basalt Group. *Geol. Soc. Am. Spec. Pap.* **497**, 117–153 (2013).
32. T. J. Blackburn *et al.*, Zircon U-Pb geochronology links the end-triassic extinction with the central Atlantic magmatic province. *Science.* **340** (2013), pp. 941–945.
33. S. D. Burgess, S. A. Bowring, High-precision geochronology confirms voluminous magmatism before, during, and after Earth's most severe extinction. *Sci. Adv.* **1**, e1500470–e1500470 (2015).
34. M. A. Coble, G. A. Mahood, Initial impingement of the Yellowstone plume located by widespread silicic volcanism contemporaneous with Columbia River flood basalts. *Geology*. **40**, 655–658 (2012).
35. E. d'Acremont, S. Leroy, E. B. Burov, Numerical modelling of a mantle plume: The plume head-lithosphere interaction in the formation of an oceanic large igneous province. *Earth Planet. Sci. Lett.* **206**, 379–396 (2003).
36. T. R. Benson, G. A. Mahood, M. Grove, Geology and ^{40}Ar/^{39}Ar geochronology of the middle Miocene McDermitt volcanic field, Oregon and Nevada: Silicic volcanism associated with propagating flood basalt dikes at initiation of the Yellowstone hotspot. *Bull. Geol. Soc. Am.* **129**, 1027–1051 (2017).
37. K. G. D. Kochhann *et al.*, Eccentricity pacing of eastern equatorial Pacific carbonate dissolution cycles during the Miocene Climatic Optimum. *Paleoceanography*. **31**, 1176–1192 (2016).
38. A. Holbourn, W. Kuhnt, J. A. Simo, Q. Li, Middle Miocene isotope stratigraphy and paleoceanographic evolution of the northwest and southwest Australian margins (Wombat Plateau and Great Australian Bight). *Palaeogeogr. Palaeoclimatol. Palaeoecol.* (2004).

39. W. A. Berggren, D. V. Kent, C. C. Swisher, M. Aubry, in *Geochronology, Time Scales, and Global Stratigraphic Correlation* (1995).
40. F. Woodruff, S. Savin, Mid-Miocene isotope stratigraphy in the deep sea: High-resolution correlations, paleoclimatic cycles, and sediment preservation. *Paleoceanography* (1991).
41. S. C. Cande, D. V. Kent, Revised calibration of the geomagnetic polarity timescale for the Late Cretaceous and Cenozoic. *J. Geophys. Res. Solid Earth* (1995).
42. A. Holbourn, W. Kuhnt, K. G. D. Kochhann, N. Andersen, K. J. Sebastian Meier, Global perturbation of the carbon cycle at the onset of the Miocene Climatic Optimum. *Geology*. **43**, 123–126 (2015).
43. J. Laskar *et al.*, A long-term numerical solution for the insolation quantities of the Earth. *Astron. Astrophys.* **428**, 261–285 (2004).
44. A. Holbourn, W. Kuhnt, M. Schulz, J. A. Flores, N. Andersen, Orbitally-paced climate evolution during the middle Miocene "Monterey" carbon-isotope excursion. *Earth Planet. Sci. Lett.* (2007), doi:10.1016/j.epsl.2007.07.026.
45. J. E. T. Channell *et al.*, Eocene to Miocene magnetostratigraphy, biostratigraphy, and chemostratigraphy at ODP site 1090 (sub-Antarctic South Atlantic). *Bull. Geol. Soc. Am.* **115**, 607–623 (2003).
46. K. Billups, H. Pälike, J. E. T. Channell, J. C. Zachos, N. J. Shackleton, Astronomic calibration of the late Oligocene through early Miocene geomagnetic polarity time scale. *Earth Planet. Sci. Lett.* **224**, 33–44 (2004).
47. J. C. Zachos, G. R. Dickens, R. E. Zeebe, An early Cenozoic perspective on greenhouse warming and carbon-cycle dynamics. *Nature*. **451**, 279–283 (2008).
48. J. C. G. Walker, P. B. Hays, J. F. Kasting, A negative feedback mechanism for the long-term stabilization of Earth's surface temperature. *J. Geophys. Res.* **86**, 9776 (1981).
49. D. A. Stolper, M. L. Bender, G. B. Dreyfus, Y. Yan, J. A. Higgins, A Pleistocene ice core record of atmospheric O2 concentrations. *Science.* **353**, 1427–1430 (2016).
50. K. M. Samperton *et al.*, Magma emplacement, differentiation and cooling in the middle crust: Integrated zircon geochronological-geochemical constraints from the Bergell Intrusion, Central Alps. *Chem. Geol.* **417**, 322–340 (2015).
51. J. M. Mattinson, Zircon U-Pb chemical abrasion ("CA-TIMS") method: Combined annealing and multi-step partial dissolution analysis for improved precision and accuracy of zircon ages. *Chem. Geol.* **220**, 47–66 (2005).
52. D. J. Condon, B. Schoene, N. M. McLean, S. A. Bowring, R. R. Parrish, Metrology and traceability of U-Pb isotope dilution geochronology (EARTHTIME Tracer Calibration Part I). *Geochim. Cosmochim. Acta*. **164**, 464–480 (2015).
53. N. M. McLean, D. J. Condon, B. Schoene, S. A. Bowring, Evaluating uncertainties in the calibration of isotopic reference materials and multi-element isotopic tracers (EARTHTIME Tracer Calibration Part II). *Geochim. Cosmochim. Acta*. **164**, 481–501 (2015).
54. T. E. Krogh, A low-contamination method for hydrothermal decomposition of zircon and extraction of U and Pb for isotopic age determinations. *Geochim. Cosmochim. Acta*. **37**, 485–494 (1973).
55. H. Gerstenberger, G. Haase, A highly effective emitter substance for mass

spectrometric Pb isotope ratio determinations. *Chem. Geol.* **136**, 309–312 (1997).

56. A. O. Nier, A redetermination of the relative abundances of the isotopes of carbon, nitrogen, oxygen, argon, and potassium. *Phys. Rev.* **77**, 789–793 (1950).
57. J. F. Bowring, N. M. McLean, S. A. Bowring, Engineering cyber infrastructure for U-Pb geochronology: Tripoli and U-Pb-Redux. *Geochemistry, Geophys. Geosystems*. **12** (2012), doi:10.1029/2010GC003479.
58. N. M. McLean, J. F. Bowring, S. A. Bowring, An algorithm for U-Pb isotope dilution data reduction and uncertainty propagation. *Geochemistry, Geophys. Geosystems*. **12** (2012), doi:10.1029/2010GC003478.
59. A. H. Jaffey, K. F. Flynn, L. E. Glendenin, W. C. Bentley, A. M. Essling, Precision measurement of half-lives and specific activities of ^{235}U and ^{238}U. *Phys. Rev. C*. **4**, 1889–1906 (1971).
60. L. L. Claiborne *et al.*, in *Microstructural Geochronology: Planetary Records Down to Atom Scale*, D. E. Moser, F. Corfu, J. R. Darling, S. M. Reddy, K. Tait, Eds. (ed. 1, 2018), pp. 3–33.
61. J. A. Johnson, C. J. Hawkesworth, P. R. Hooper, G. Ben Binger, "Major- and Trace-Element Analyses of Steens Basalt, Southeastern Oregon" (1998).
62. J. L. Tolan, T.L.; Martin, B.S.; Reidel, S.P.; Kauffman, J.D.; Garwood, D.L.; Anderson, Stratigraphy and tectonics of the central and eastern portions of the Columbia River Flood-Basalt Province: An overview of our current state of knowledge. *Geol. Soc. Am. F. Guid.* **15**, 645–672 (2009).
63. B. Schoene, J. L. Crowley, D. J. Condon, M. D. Schmitz, S. A. Bowring, Reassessing the uranium decay constants for geochronology using ID-TIMS U-Pb data. *Geochim. Cosmochim. Acta*. **70**, 426–445 (2006).
64. P. R. Renne *et al.*, Intercalibration of standards, absolute ages and uncertainties in ^{40}Ar/^{39}Ar dating. *Chem. Geol.* **145**, 117–152 (1998).
65. B. Schoene, in *Treatise on Geochemistry: Second Edition* (2014).
66. I. Wendt, C. Carl, The statistical distribution of the mean squared weighted deviation. *Chem. Geol. Isot. Geosci. Sect.* **86**, 275–285 (1991).

	Dates (Ma)							Composition					Isotopic Ratios									Corrections	
Sample	206Pb/ 238U	±2σ absolute	207Pb/ 235U	±2σ absolute	207Pb/ 206Pb	±2σ absolute	% disc	Pb* (pg)	Pbc (pg)	Pb*/ Pbc	Th/ U	Th/ U(magma)	206Pb/ 204Pb	208Pb/ 206Pb	206Pb/ 238U	±2σ %	207Pb/ 235U	±2σ %	207Pb/ 206Pb	±2σ %	Corr. coef.	Blank model	Tracer
zircon	a		b		a,b		c	d	e	f	g	h	i	j	j		j		j			k	l
CRB1506																						SF	ET535
z34	15.895	0.019	15.979	0.059	28.6	8.5	63.0	43.15	0.83	51.96	0.39	2.05	3315	0.13	0.0024551	0.095	0.0158661	0.369	0.0468923	0.341	0.399	SF	ET535
z21	15.887	0.043	15.918	0.091	21	12	54.5	18.98	0.48	39.76	0.38	2.00	2545	0.12	0.0024538	0.260	0.0158055	0.574	0.0467363	0.491	0.519	SF	ET535
z3	15.902	0.018	16.16	0.19	55	29	77.1	11.58	0.77	15.06	0.27	1.42	976	0.09	0.0024561	0.088	0.0160505	1.213	0.0474162	1.192	0.273	OC	ET2535
z1	15.914	0.025	16.08	0.32	41	47	71.0	20.48	2.18	9.40	0.31	1.63	610	0.10	0.0024580	0.144	0.0159643	2.001	0.0471266	1.963	0.297	OC	ET2535
z35	15.921	0.023	15.94	0.17	19	26	52.5	33.03	2.20	15.03	0.41	2.11	968	0.13	0.0024591	0.123	0.0158301	1.097	0.0467091	1.065	0.311	SF	ET535
z31	15.938	0.071	16.1	1.0	35	149	67.6	9.43	3.06	3.09	0.43	2.16	206	0.14	0.0024618	0.447	0.0159518	6.345	0.0470161	6.219	0.313	OC	ET535
z12	20.85	0.12	22.1	1.8	159	193	87.7	1.51	0.74	2.04	0.71	3.74	137	0.23	0.0032252	0.588	0.0219882	8.439	0.0494682	8.261	0.335	SF	ET535
z16	39.16	0.14	38.5	1.9	-1	117	-667.9	1.71	0.46	3.75	0.53	2.79	248	0.17	0.0060791	0.346	0.0386766	4.934	0.0461636	4.845	0.287	SF	ET535
z11	99.57	0.16	98.9	2.0	83	48	-17.2	10.21	1.37	7.44	0.34	1.79	497	0.11	0.0155515	0.164	0.1022996	2.074	0.0477304	2.033	0.289	SF	ET535
z33	166.56	0.16	166.44	0.72	165	11	-0.2	20.84	0.61	34.15	0.38	2.00	2188	0.12	0.0261600	0.096	0.1781232	0.470	0.0494056	0.450	0.300	SF	ET535
CRB1533																							
z4_BS	16.066	0.040	16.08	0.52	18	76	50.0	5.16	0.78	6.62	0.71	3.74	393	0.23	0.0024817	0.238	0.0159665	3.243	0.0466827	3.169	0.347	OC	ET2535
z25	16.044	0.089	15.7	1.4	-38	213	166.8	1.08	0.55	1.95	0.59	3.26	136	0.19	0.0024780	0.558	0.0155775	8.878	0.0456128	8.748	0.263	SF	ET535
z34	16.045	0.059	16.05	0.86	17	128	47.7	1.28	0.39	3.25	0.72	3.79	208	0.23	0.0024783	0.364	0.0159351	5.417	0.0466548	5.327	0.278	SF	ET535
z3	16.070	0.093	16.2	1.5	41	214	70.7	2.64	1.16	2.27	0.54	2.84	153	0.17	0.0024823	0.579	0.0161224	9.091	0.0471274	8.919	0.327	OC	ET2535
z28	16.163	0.094	16.4	1.4	46	206	73.2	0.55	0.27	2.00	0.76	4.16	134	0.24	0.0024966	0.579	0.0162529	8.773	0.0472357	8.629	0.279	SF	ET535
z14	16.171	0.057	15.96	0.75	-15	112	1221.3	1.62	0.41	3.94	0.64	3.47	252	0.21	0.0024979	0.346	0.0158488	4.759	0.0460388	4.643	0.366	SF	ET535
z1_BS	16.234	0.018	16.22	0.13	14	19	41.6	10.59	0.41	25.62	0.44	2.32	1575	0.14	0.0025078	0.082	0.0161052	0.792	0.0465987	0.776	0.240	OC	ET2535
z2_BS	16.568	0.015	16.63	0.11	25	15	57.3	14.29	0.47	30.27	0.46	2.42	1844	0.15	0.0025597	0.057	0.0165141	0.648	0.0468125	0.634	0.259	OC	ET2535
z1	16.587	0.030	16.49	0.36	2	52	-8.2	15.30	1.70	8.98	0.40	2.11	569	0.13	0.0025626	0.169	0.0163729	2.221	0.0463590	2.174	0.314	OC	ET2535
z31	17.37	0.13	17.3	2.0	3	279	-5.9	0.40	0.27	1.47	0.66	3.47	105	0.21	0.0026852	0.749	0.0171637	11.727	0.0463798	11.556	0.259	SF	ET535
z3_BS	31.086	0.043	30.90	0.49	16	37	-31.9	4.75	0.38	12.47	0.44	2.32	775	0.14	0.0048202	0.135	0.0309028	1.604	0.0465184	1.544	0.475	OC	ET2535
CRB1519																							
z1_BS	16.210	0.043	16.12	0.62	2	92	6.3	2.35	0.45	5.19	0.48	4.00	331	0.15	0.0025028	0.266	0.0160033	3.882	0.0463965	3.815	0.281	OC	ET2535
z13	16.26	0.19	16.1	2.9	-5	434	-65.8	1.25	1.42	0.88	0.37	3.08	75	0.12	0.0025110	1.209	0.0160067	18.282	0.0462531	17.980	0.281	SF	ET535
z16	16.265	0.081	15.9	1.3	-40	191	165.0	2.28	1.01	2.26	0.49	4.08	159	0.16	0.0025114	0.503	0.0157810	7.978	0.0455941	7.852	0.280	SF	ET535
z1	16.268	0.058	16.58	0.86	62	123	79.0	4.94	1.38	3.58	0.40	3.33	238	0.13	0.0025118	0.357	0.0164678	5.251	0.0475705	5.161	0.283	OC	ET2535
z2_BS	16.298	0.043	16.69	0.63	74	88	81.8	4.29	0.86	4.99	0.40	3.33	325	0.13	0.0025165	0.261	0.0165823	3.775	0.0478131	3.710	0.279	OC	ET2535
z4	16.34	0.10	16.3	1.6	7	231	24.7	1.99	1.00	1.98	0.39	3.25	140	0.13	0.0025227	0.640	0.0161605	9.745	0.0464810	9.578	0.292	OC	ET2535
z2	16.414	0.081	16.8	1.2	67	168	80.1	2.00	0.75	2.67	0.47	3.92	179	0.15	0.0025346	0.496	0.0166531	7.175	0.0476742	7.040	0.303	OC	ET2535
z4_BS	16.60	0.13	17.18	0.73	99	98	85.4	1.51	0.34	4.43	0.31	2.58	296	0.10	0.0025633	0.806	0.0170651	4.289	0.0483067	4.131	0.286	OC	ET2535
z6	17.81	0.13	18.2	2.0	73	259	79.5	1.57	0.91	1.72	0.43	3.58	123	0.14	0.0027518	0.759	0.0181122	11.079	0.0477590	10.876	0.299	OC	ET2535
z3_BS	78.734	0.035	78.86	0.27	83	8	8.4	53.71	1.09	49.21	0.09	0.75	3326	0.03	0.0122734	0.044	0.0807707	0.352	0.0477510	0.342	0.241	OC	ET2535
CRB1556																							
z12	16.254	0.034	16.32	0.44	26	64	59.3	1.54	0.26	5.91	0.35	1.89	397	0.11	0.0025109	0.200	0.0162068	2.733	0.0468346	2.678	0.308	SF	ET535
z13	16.257	0.036	16.60	0.46	66	66	79.7	1.52	0.27	5.68	0.44	2.37	373	0.14	0.0025114	0.212	0.0164844	2.809	0.0476273	2.764	0.244	SF	ET535
z18	16.295	0.063	16.32	0.95	21	139	54.3	1.03	0.37	2.77	0.31	2.75	198	0.10	0.0025159	0.387	0.0162103	5.867	0.0467507	5.765	0.295	SF	ET535
z5	16.30	0.18	17.4	2.8	169	371	91.1	0.87	0.78	1.12	0.37	1.95	87	0.12	0.0025178	1.127	0.0172598	16.172	0.0497400	15.879	0.293	OC	ET535
z1	16.305	0.094	16.1	1.4	-18	206	470.5	0.92	0.49	1.86	0.34	1.95	138	0.11	0.0025185	0.578	0.0159607	8.659	0.0459827	8.493	0.318	SF	ET535
z14	16.33	0.13	17.8	2.0	217	261	92.9	0.59	0.38	1.56	0.40	2.11	114	0.13	0.0025228	0.825	0.0176580	11.489	0.0507871	11.265	0.305	OC	ET535
z19	16.40	0.18	16.0	2.8	-41	419	162.0	0.31	0.33	0.95	0.34	2.83	80	0.11	0.0025317	1.125	0.0158992	17.565	0.0455673	17.228	0.328	SF	ET535
CRB1634																							
z8	16.288	0.039	16.36	0.52	28	76	60.7	0.97	0.19	5.08	0.46	2.47	334	0.15	0.0025161	0.231	0.0162509	3.210	0.0468644	3.152	0.286	SF	ET535
z22	16.301	0.035	16.75	0.35	81	50	82.8	1.98	0.22	9.07	0.55	2.89	568	0.18	0.0025183	0.206	0.0166327	2.112	0.0479247	2.085	0.178	SF	ET535
z3	16.26	0.16	16.3	2.5	28	358	61.4	0.54	0.50	1.08	0.48	2.79	85	0.16	0.0025116	0.985	0.0162257	15.170	0.0468764	14.930	0.274	SF	ET535
z13	16.28	0.18	16.1	2.8	-6	418	-101.2	0.35	0.36	0.97	0.62	3.58	77	0.20	0.0025146	1.106	0.0160183	17.566	0.0462204	17.321	0.251	SF	ET535
z4	16.28	0.15	16.4	2.3	29	333	62.7	0.70	0.60	1.16	0.44	2.58	91	0.14	0.0025147	0.915	0.0162565	14.102	0.0469072	13.868	0.287	SF	ET535
z17	16.331	0.065	16.61	0.99	57	141	77.1	0.62	0.22	2.78	0.49	2.68	190	0.16	0.0025227	0.397	0.0164972	6.003	0.0474503	5.893	0.306	SF	ET535
z6	16.36	0.16	16.9	2.4	87	341	83.9	0.27	0.25	1.11	0.52	3.00	87	0.17	0.0025276	0.972	0.0167415	14.594	0.0480589	14.360	0.272	SF	ET535
z16	16.36	0.18	17.8	2.8	210	358	92.7	0.23	0.23	1.01	0.57	3.32	80	0.18	0.0025278	1.078	0.0176451	15.691	0.0506487	15.427	0.276	SF	ET535
z15	16.379	0.075	16.9	1.1	98	154	85.4	0.56	0.23	2.45	0.48	2.63	170	0.15	0.0025302	0.457	0.0168346	6.631	0.0482770	6.509	0.299	SF	ET535
z14	16.42	0.12	17.8	1.8	209	235	92.7	0.27	0.19	1.46	0.38	2.21	111	0.12	0.0025360	0.746	0.0176894	10.343	0.0506117	10.144	0.300	SF	ET535
z12	16.42	0.13	17.4	2.0	154	268	90.2	0.29	0.21	1.36	0.55	3.16	101	0.18	0.0025366	0.799	0.0172786	11.620	0.0494264	11.431	0.270	SF	ET535
CRB1586																							
z4	16.572	0.018	16.73	0.18	39	25	68.7	5.97	0.33	17.98	0.34	1.79	1139	0.11	0.0025603	0.079	0.0166153	1.074	0.0470877	1.054	0.278	OC	ET2535
z3	16.55	0.10	16.5	1.5	14	219	39.4	2.16	1.02	2.12	0.46	2.42	146	0.15	0.0025571	0.610	0.0164188	9.242	0.0465897	9.082	0.293	OC	ET2535
z15	16.569	0.041	16.85	0.56	57	79	76.7	6.64	1.15	5.79	0.36	1.89	377	0.12	0.0025599	0.242	0.0167397	3.368	0.0474482	3.307	0.282	OC	ET535
z9	16.58	0.13	17.4	1.9	129	252	88.4	3.33	1.94	1.71	0.44	2.32	122	0.14	0.0025614	0.765	0.0172615	10.887	0.0488994	10.688	0.292	OC	ET535
z2	16.588	0.042	16.94	0.61	67	85	79.5	1.92	0.36	5.34	0.48	2.53	339	0.15	0.0025627	0.246	0.0168279	3.617	0.0476455	3.554	0.289	OC	ET2535
z23	16.608	0.032	16.80	0.37	44	53	71.3	3.82	0.52	7.41	0.45	2.42	481	0.15	0.0025659	0.179	0.0166856	2.244	0.0471849	2.197	0.297	SF	ET535
z5	16.609	0.029	16.70	0.17	30	23	62.3	22.23	1.13	19.61	0.40	2.11	1222	0.13	0.0025661	0.161	0.0165917	0.998	0.0469154	0.969	0.257	OC	ET2535
z22	16.62	0.12	17.0	1.8	68	255	79.7	0.55	0.34	1.61	0.78	4.26	111	0.25	0.0025671	0.716	0.0168632	10.893	0.0476647	10.719	0.274	SF	ET535
z16	16.629	0.053	16.72	0.72	30	102	61.7	2.85	0.70	4.05	0.67	3.63	257	0.22	0.0025691	0.311	0.0166065	4.356	0.0469017	4.260	0.339	SF	ET535
z1	16.635	0.063	17.34	0.83	117	111	87.2	2.87	0.73	3.91	0.36	1.89	261	0.12	0.0025701	0.374	0.0172310	4.821	0.0486465	4.721	0.305	OC	ET2535
z18	16.64	0.12	16.4	1.7	-16	244	715.7	0.41	0.24	1.69	0.55	3.05	121	0.18	0.0025704	0.698	0.0163005	10.315	0.0460149	10.102	0.336	SF	ET535
z19	16.640	0.081	16.6	1.2	14	172	39.8	1.38	0.53	2.63	1.07	5.74	159	0.34	0.0025709	0.485	0.0165098	7.272	0.0465961	7.168	0.247	SF	ET535
z13	16.667	0.074	17.6	1.0	144	132	89.4	1.56	0.45	3.47	0.59	3.11	220	0.19	0.0025751	0.446	0.0174625	5.770	0.0492051	5.621	0.368	SF	ET535
z17	125.72	0.19	125.6	2.2	124	43	0.0	7.72	0.95	8.09	0.32	1.68	541	0.10	0.0196800	0.155	0.1317101	1.866	0.0485610	1.827	0.293	SF	ET535
CRB1624																							
z5	16.589	0.031	16.614	0.321	20	45	50.9	2.98	0.23	12.75	0.68	3.58	745	0.22	0.0025630	0.173	0.0165011	1.948	0.0467147	1.890	0.373	OC	ET535
z23	16.603	0.034	16.908	0.527	60	75	77.6	34.73	6.32	5.49	0.61	3.21	347	0.20	0.0025652	0.194	0.0167957	3.139	0.0475082	3.135	0.052	SF	ET535

Table 1: U-Pb Isotopic Data

z18	16.606	0.051	16.633	0.730	21	105	51.5	1.74	0.48	3.65	0.43	2.32	248	0.14	0.0025655	0.301	0.0165205	4.424	0.0467243	4.349	0.280	SF	ET535
z2	16.606	0.039	16.672	0.519	26	74	58.3	2.89	0.53	5.47	0.62	3.32	345	0.20	0.0025656	0.225	0.0165595	3.136	0.0468326	3.075	0.300	SF	ET535
z21	16.610	0.043	16.967	0.596	68	83	79.6	26.93	4.92	5.47	0.51	2.63	344	0.16	0.0025663	0.255	0.0168545	3.539	0.0476536	3.471	0.300	OC	ET535
z3	16.616	0.046	16.287	0.789	-32	119	189.9	2.90	0.61	4.74	0.83	4.42	287	0.27	0.0025671	0.268	0.0161742	4.881	0.0457167	4.886	0.006	SF	ET535
z19	16.618	0.020	16.709	0.140	30	20	61.7	5.72	0.27	21.12	0.53	2.79	1309	0.17	0.0025675	0.098	0.0165964	0.843	0.0469021	0.833	0.155	SF	ET535
z15	16.627	0.027	16.681	0.253	24	36	56.3	2.91	0.24	12.16	0.61	3.26	745	0.20	0.0025689	0.149	0.0165685	1.529	0.0467982	1.482	0.355	SF	ET535
z7	16.635	0.067	16.951	0.993	62	138	78.1	2.07	0.71	2.91	0.64	3.47	191	0.21	0.0025700	0.402	0.0168385	5.905	0.0475405	5.800	0.293	SF	ET535
z16	16.643	0.044	16.946	0.597	60	83	77.5	1.24	0.25	4.98	0.81	4.37	301	0.26	0.0025713	0.256	0.0168336	3.553	0.0475026	3.483	0.307	SF	ET535
z17	16.654	0.047	17.008	0.671	67	93	79.5	1.05	0.23	4.47	0.85	4.58	270	0.27	0.0025730	0.278	0.0168964	3.977	0.0476482	3.907	0.284	SF	ET535
CRB1625																							
z15	16.653	0.063	17.17	0.94	90	128	84.0	0.71	0.24	2.97	0.55	3.00	199	0.18	0.0025728	0.374	0.0170557	5.499	0.0481022	5.407	0.278	SF	ET535
z36	16.64	0.18	18.0	2.6	202	337	92.3	1.91	1.54	1.24	0.49	2.32	92	0.16	0.0025719	1.073	0.0178838	14.806	0.0504555	14.506	0.313	OC	ET535
z7	16.66	0.13	17.8	2.0	170	258	90.9	3.48	2.07	1.69	0.58	3.05	116	0.19	0.0025733	0.792	0.0176465	11.262	0.0497570	11.057	0.292	OC	ET535
z27	16.67	0.14	16.9	2.2	52	307	74.5	1.09	0.85	1.29	0.56	2.95	97	0.18	0.0025752	0.846	0.0167991	13.068	0.0473335	12.859	0.278	SF	ET535
z38	16.68	0.17	16.6	2.5	4	358	2.7	0.30	0.25	1.22	0.53	2.79	93	0.17	0.0025774	1.021	0.0164797	15.253	0.0463940	14.864	0.410	SF	ET535
z12	16.754	0.085	17.1	1.3	66	177	78.9	0.58	0.26	2.19	0.59	3.21	151	0.19	0.0025885	0.510	0.0169849	7.580	0.0476109	7.449	0.289	SF	ET535
z1	17.297	0.026	17.25	0.26	11	36	27.1	8.01	0.71	11.32	0.64	3.37	690	0.21	0.0026731	0.136	0.0171381	1.541	0.0465208	1.502	0.325	SF	ET535
z11	17.84	0.11	19.5	1.8	231	208	92.7	0.54	0.32	1.68	0.52	2.74	121	0.17	0.0027580	0.647	0.0194136	9.158	0.0510748	9.000	0.277	SF	ET535
z17	18.578	0.040	18.92	0.51	62	63	75.1	1.49	0.24	6.16	0.63	3.32	385	0.20	0.0028724	0.210	0.0188112	2.701	0.0475195	2.642	0.318	SF	ET535
z2	18.643	0.055	18.50	0.76	0	97	-59.8	5.02	1.06	4.76	1.08	5.68	272	0.35	0.0028824	0.292	0.0183883	4.124	0.0462889	4.041	0.317	SF	ET535
z40	19.818	0.093	19.8	1.4	16	171	26.4	1.98	0.84	2.34	0.60	3.16	159	0.19	0.0030652	0.471	0.0196786	7.206	0.0465827	7.097	0.261	SF	ET535
z16	19.895	0.054	20.24	0.76	61	89	72.7	2.10	0.45	4.65	0.67	3.53	292	0.21	0.0030772	0.265	0.0201384	3.783	0.0474849	3.712	0.297	SF	ET535
z19	20.095	0.041	20.14	0.50	26	59	46.0	2.76	0.32	8.53	1.63	8.58	422	0.52	0.0031084	0.194	0.0200414	2.491	0.0467822	2.441	0.292	SF	ET535
z35	21.026	0.057	20.70	0.75	-17	87	417.2	3.88	0.59	6.52	1.35	7.11	346	0.43	0.0032533	0.268	0.0205982	3.645	0.0459403	3.592	0.231	SF	ET535
z20	23.393	0.047	23.75	0.61	61	61	66.7	1.60	0.25	6.34	0.57	3.00	402	0.18	0.0036217	0.195	0.0236754	2.611	0.0474321	2.564	0.274	SF	ET535
z13	23.482	0.080	23.7	1.2	42	117	54.9	1.26	0.37	3.38	0.57	3.00	223	0.18	0.0036356	0.338	0.0235863	4.977	0.0470738	4.892	0.283	SF	ET535
z21	23.923	0.039	23.96	0.45	27	45	34.8	6.55	0.67	9.75	0.90	4.74	561	0.29	0.0037042	0.156	0.0238775	1.901	0.0467726	1.857	0.319	SF	ET535
z23	47.954	0.074	47.59	0.82	29	41	-41.4	5.84	0.55	10.57	0.60	3.16	653	0.19	0.0074529	0.153	0.0479881	1.755	0.0467198	1.714	0.311	SF	ET535
z14	49.511	0.049	49.54	0.32	51	15	10.4	6.10	0.24	25.09	0.37	1.95	1618	0.12	0.0076963	0.098	0.0499996	0.664	0.0471386	0.631	0.393	SF	ET535

a Corrected for initial Th/U disequilibrium using radiogenic 208Pb and Th/U[magma] specified.
b Corrected for initial Pa/U disequilibrium using initial fraction activity ratio [231Pa]/[235U] = 1.10000.
c % discordance = 100 - (100 * (206Pb/238U date) / (207Pb/206Pb date))
d Total mass of radiogenic Pb.
e Total mass of common Pb.
f Ratio of radiogenic Pb (including 208Pb) to common Pb.
g Th contents calculated from radiogenic 208Pb and 230Th-corrected 206Pb/238U date of the sample, assuming concordance between U-Pb Th-Pb systems.
h Th/U ratio of magma from which mineral crystallized.
i Measured ratio corrected for fractionation and spike contribution only.
j Measured ratios corrected for fractionation, tracer and blank.
k Two different blank models were used to reduce data - Outliers Culled model (OC), and Side Filaments (SF). Values are:

OC	206Pb/204Pb	18.168317±0.384235	SF	206Pb/204Pb	18.628271±0.317714
	207Pb/204Pb	15.348332±0.273090		207Pb/204Pb	15.796256±0.232017
	208Pb/204Pb	37.350513±0.773909		208Pb/204Pb	38.535874±0.375848

l Values for ET535 and ET2535 are found in ref. 31 and ref. 32.

Chapter 4

Eruption history of the Columbia River Basalt Group constrained by U-Pb geochronology

This chapter is in review at Geology, with authors J. Kasbohm, B. Schoene, and J. Murray

ABSTRACT

Large igneous provinces have been connected to a number of Earth's most severe environmental crises. A surge in detailed high-precision geochronological studies has revised estimates of the timing and tempo of their emplacement, which are necessary to assess causality in global perturbations. We present new U-Pb geochronology from zircon-bearing volcanic ashes in the Columbia River Basalt Group (CRBG), the youngest and best-studied continental flood basalt, which is temporally connected to the global warming and elevated CO_2 of the Miocene Climate Optimum. By combining new ages with our recently published dataset, we find that main phase CRBG volcanism occurred at a relatively constant rate of 0.3-0.5 km^3/a, with a small likelihood of hiatuses beyond ~80 ka, and that the Grande Ronde Basalt (GRB), the largest CRB formation encompassing 72% of its total volume, was emplaced in 505+51/-61 ka beginning at

~16.57 Ma. Our model also yields ages for magnetic field reversals ongoing during CRBG emplacement, which can be used to improve calibration of Miocene paleoclimate records. While proxies suggesting elevated CO_2 levels from 16.5-15.8 Ma may be connected to GRB emplacement, any model invoking the CRBG as a continued source of CO_2 throughout the MCO (until ~14 Ma) requires cryptic outgassing long after eruptions ceased.

INTRODUCTION

Large igneous provinces (LIPs), Earth's most voluminous volcanic events, have punctuated Earth history, leaving evidence for mass extinctions and climatic perturbations in their wake (Ernst & Youbi, 2017). Whether LIPs are associated with mantle plumes (e.g., Deccan Traps, Ontong Java Plateau), continental breakup (Central Atlantic Magmatic Province, Karoo-Ferrar), or combinations of the two (North Atlantic Igneous Province), their surface expression represents an end-member of intrusive and extrusive magmatism. In the past decade, new geochronology has yielded crucial constraints on the timing, duration, and volumetric rates of eruption for a number of LIPs (Blackburn et al., 2013; Burgess et al., 2017; Schoene et al., 2019). However, only a minority of LIPs possess the wide geographic exposure, well-defined stratigraphy, and datable material amenable to detailed geochronological studies (Kasbohm et al., in press). Here we report new temporal constraints on the Columbia River Basalt Group (CRBG), the youngest, best-preserved, and best-studied LIP, which is a well-suited testbed to quantify the tempo of LIP emplacement.

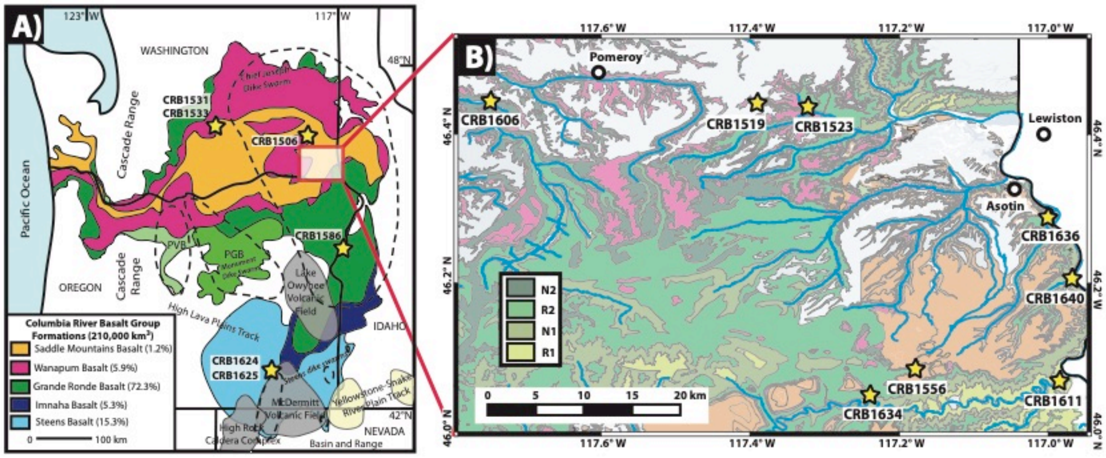

Figure 1. A) Overview map of the CRBG, with areal extents and volume estimates for each formation, and localities of other regional volcanic activity labeled. Dashed lines bracket source dike swarms, and the locations of geochronology samples are starred. In total, the Saddle Mountains Basalt, Picture Gorge Basalt (PGB) and Prineville Basalt (PVB) together comprise 2.6% of the total CRBG volume, and are not discussed further here, or included in any cumulative volume estimates. **B)** Geologic map of CRBG exposure in southeastern Washington.

The CRBG has been the subject of decades of effort to document its geochemistry, paleomagnetism, and mineralogy, leading to a well-defined volcanostratigraphy comprising five main formations and dozens of individual stratigraphic members, each with area and volume estimates obtained through mapping and coring campaigns (Reidel, 2015). The 210,000 km^3 of the CRBG were emplaced in the northwestern USA during the Miocene during active regional volcanism east of the Cascades subduction zone and High Lava Plains track, north of the Basin & Range and silicic caldera complexes, and west of the Yellowstone-Snake River Plain hotspot track (Fig. 1A).

The origin of the CRBG is debated. While some workers hypothesize a mantle plume source, suggesting that the CRBG represents initial impingement of the Yellowstone plume head on the crust (Camp, 2013), others favor subduction-related mechanisms, such as a slab tear (Liu & Stegman, 2012) or slab rollback (Long et al., 2012), and still others favor an interaction of plume and slab (Coble & Mahood, 2012). The CRBG is also noteworthy for its temporal correlation with the Miocene Climate Optimum (MCO), an episode of global warming 17-15 Ma evidenced by paleoclimate proxies indicating a 4-6°C high-latitude sea surface temperature rise (Shevenell et al., 2004) and elevated atmospheric CO_2 levels at or above 400 ppm (Armstrong McKay et al., 2014).

Prior geochronology for the CRBG lacked the accuracy and precision required to fully integrate eruptions into geodynamic models, or assess in detail its connection to the MCO. Barry et al. (2013) reviewed K-Ar and $^{40}Ar/^{39}Ar$ geochronology obtained from CRBG basalts, and suggested that emplacement of the Steens, Imnaha, Grande Ronde, and Wanapum Basalts occurred from 16.9-15.0 Ma. This age model, constructed from individual ages with low (~1 Ma) precision and in some cases poor accuracy, yielded numerous inconsistencies between the magnetic polarity of the basalts and the Geomagnetic Polarity Timescale (GPTS; Hilgen et al., 2012). More recent high-precision $^{40}Ar/^{39}Ar$ and U-Pb zircon geochronology have provided a clearer timeline for CRBG eruptions by dating sanidine or zircon extracted from volcanic ashes or weathering horizons between lava flows (Kasbohm & Schoene, 2018; Mahood & Benson, 2017). A new U-Pb age model for the CRBG suggests that emplacement of 95% of the CRBG volume occurred in ~750 ka beginning at 16.65 Ma, with possible brief intervals of more rapid emplacement (Kasbohm & Schoene, 2018). However, our previous contribution constrained the timing of only one member of the Grande Ronde Basalt (GRB), the largest CRBG formation comprising 72% of its total volume (Reidel, 2015). Here we provide new age constraints on six geochronology samples from the beginning, middle, and end of the GRB. These new data constrain the eruptive tempo of the CRBG and also place tighter age estimates on magnetic reversals observed in the basalt pile, which are critical for building a robust GPTS and therefore age models for climate proxy records.

RESULTS

We use U-Pb zircon geochronology by chemical abrasion – isotope dilution – thermal ionization mass spectrometry (CA-ID-TIMS) to provide accurate and precise age constraints on CRBG interbeds. These interbeds, manifest as ash layers, weathered flow top horizons containing ash material, or the volcaniclastic infill of brecciated basalt flow tops were sampled in central and southeast Washington (Fig. 1B). Individual zircons were separated from each sample and dated through CA-ID-TIMS at Princeton University (see Data Repository for materials and methods).

Individual zircon ^{206}Pb/^{238}U dates from six GRB horizons are presented in Figure 2 with 95% confidence intervals, alongside our prior dataset (Kasbohm & Schoene, 2018). Dates within each sample spread beyond analytical uncertainty as a result of pre-eruptive crystallization derived from prolonged crystallization in the magma, or inheritance of older grains from the host rock or volcanic edifice (Cooper, 2015; Stelten et al., 2015). In Figure 2, we star the youngest and most precise zircon age as one estimate for the age of the interbed. As an additional approach to calculating an eruption age from disperse

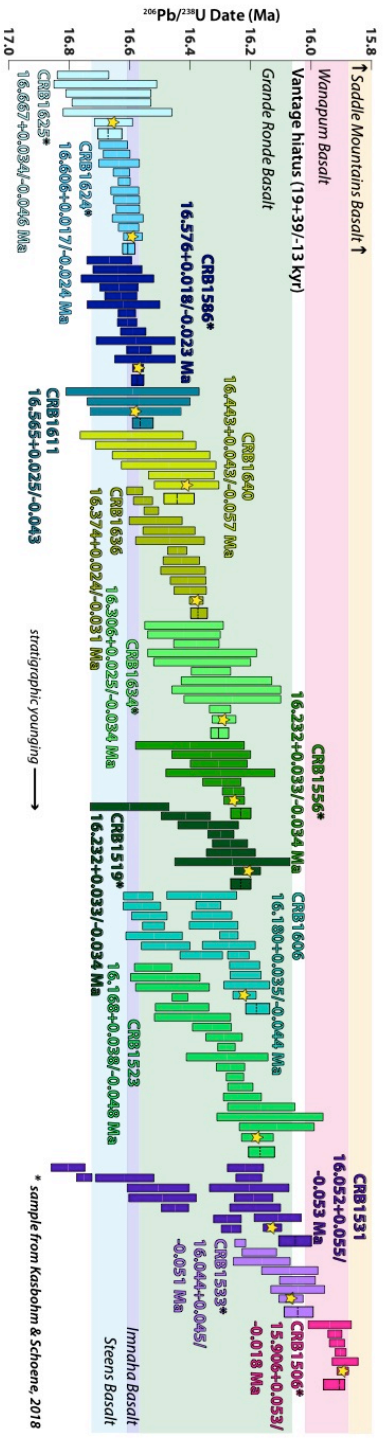

Figure 2. Rank order plot of geochronological data presented in this study, with samples arranged in stratigraphic order (younging left to right), and height of error bars showing 2σ uncertainty. The youngest, most precise single zircon age is starred, and the result of the MCMC age model is highlighted (the rightmost bar for each sample) and labeled as our preferred interpretation. Background shading indicates the timing of eruption for each CRBG formation. Samples with an asterisk are from Kasbohm & Schoene (2018).

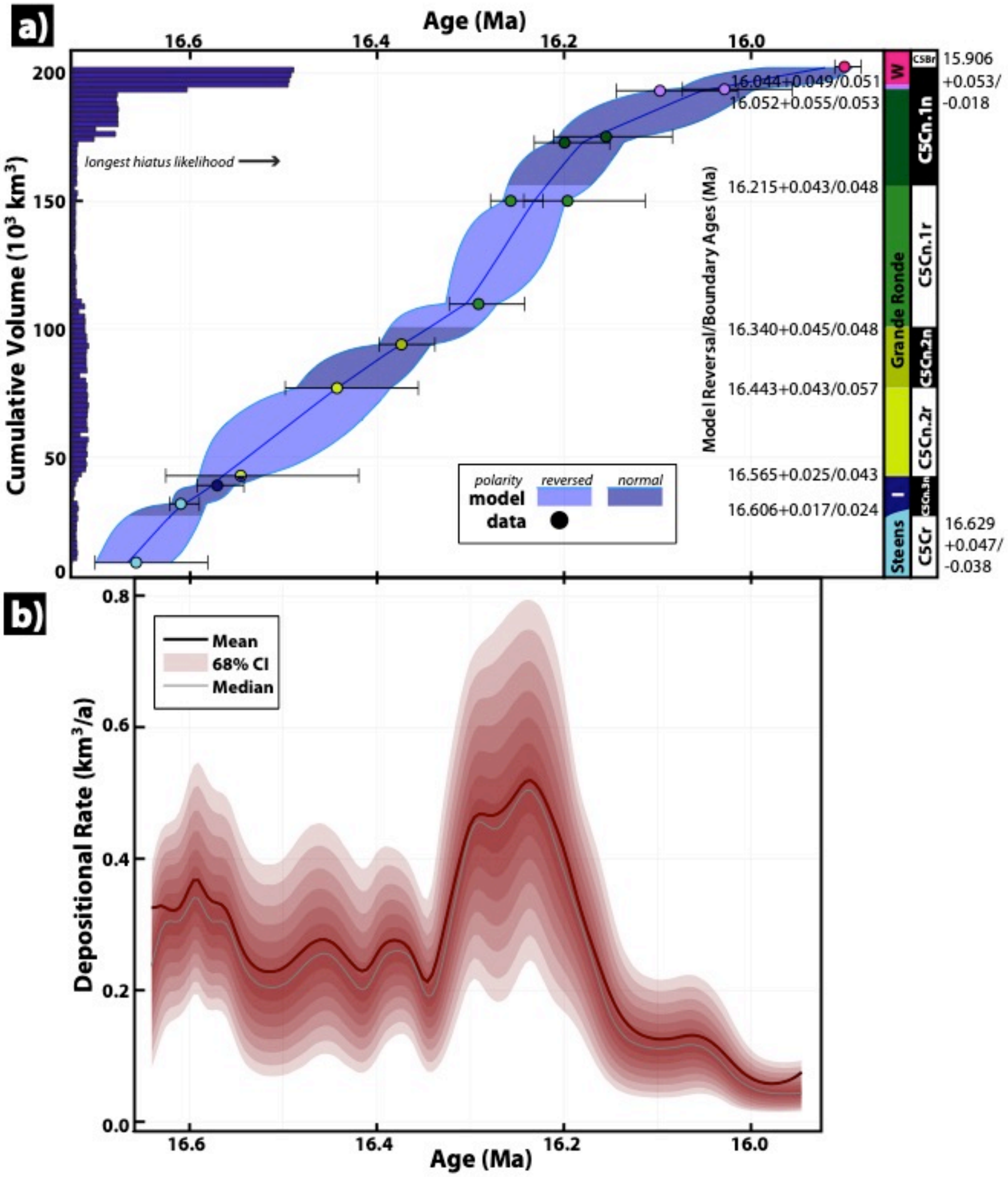

Figure 3. a) Age model for cumulative volume erupted through the CRBG, based on eruptive ages (black lines) from known stratigraphic positions. Blue shading indicates 95% credible interval of the model, and is dark for intervals of normal polarity and light for reversed polarity. Indigo bars on the right indicate the likelihood of the longest CRBG hiatus (most likely 50-80 ka) occurring at each stratigraphic position. The age model also yields magnetic field reversal and formation boundary ages (labeled). **b)** Results from **(a)** for emplacement rates of the CRBG, averaged over 50 ka windows, shown with contours up to 68% credible intervals.

datasets, each sample was subjected to a Bayesian Monte Carlo Markov Chain (MCMC) model, which makes a probabilistic estimate of eruption age based on all of the dates and uncertainties of individual zircons from a sample (Keller et al., 2018); in all cases, the derived eruption ages overlap with the youngest zircon ages (Table DR2). Finally, eruption ages were input into an additional MCMC simulation (Schoene et al., 2019), which imposes stratigraphic order as a constraint to further refine eruption ages, and calculate volumetric eruption rates (Fig. 3), yielding our preferred model age for each CRBG sample (Fig. 2).

Our data yield a high-resolution age model for the vast majority of the CRBG that agrees well with our previous age estimates. The new data provide a more thorough interrogation of the GRB specifically. Interbeds immediately below the first and above the last GRB members constrain the duration of the GRB to 505+51/-61 ka. The age model yields estimates for the timing of the magnetic field reversals bracketing the four magnetostratigraphic units of the GRB, corresponding to chrons C5Cn.2r-C5Cn.1n, as well as the preceding chron C5Cn.3n (Fig. 3). The ages for the bottom and near the top of the Vantage sedimentary interbed, the most prominent though not necessarily the longest-lived interbed in the CRBG (Barry et al., 2010), yield a duration of 19+39/-13 ka. At its sampled type locality, the Vantage interbed exhibits a thin layer of white mud (CRB1531), interpreted as ancestral Columbia River deposits, overlain by 4 m of an ash-rich volcaniclastic lahar sourced from the Cascades (CRB1533) (Tolan et al., 2009). In the field, we observed that the overlying Basalt of Ginkgo (Wanapum Basalt) exhibits load structures, indicating that the volcaniclastic unit was not yet lithified at the time of the Ginkgo eruption.

The modeled eruption rates calculated through the main phase of the CRBG (Steens, Imnaha, and GRB) suggest an average emplacement rate of ~0.3 km^3/a (Fig. 3). An exception to this average rate is evident during the emplacement of the Wapshilla Ridge Member, which appears to have been emplaced at ~0.5 km^3/a during chron C5Cn.1r (R2). As we have previously reported, fluxes slow by an order of magnitude during the emplacement of the Wanapum Basalt, with an average rate of 0.05 km^3/a (Kasbohm & Schoene, 2018). Monte Carlo simulations suggest that the longest possible hiatus of CRBG volcanism was most likely 50-80 ka (Fig. DR4), which would have been most likely to occur in the uppermost portion of the GRB (Fig. 3).

DISCUSSION

Our model for emplacement rates throughout the duration of the CRBG may be compared to other well-dated LIPs. U-Pb ID-TIMS geochronology shows that the CAMP, Deccan Traps, and Siberian Traps were also all emplaced in less than a million years, and the data are pointing towards models demarcated by periods of high eruptive flux 10^4-10^5 years long interspersed with intervals of reduced effusion (see summary in Kasbohm et al., in press). For example, the Deccan Traps emplacement is shown to occur in four pulses of ≤20 km^3/a (Schoene et al., 2019); the Siberian Traps have been modeled to be emplaced as a few pulses lasting 10-100 ka (Pavlov et al., 2019). In the CAMP, some U-Pb dates from dikes and sills fall during apparent eruption hiatuses (Blackburn et al., 2013; Davies et al., 2017), perhaps indicating that in all LIPS, lulls in eruptions need not be lulls in magmatism. In the case of the CRBG, where the stratigraphy is arguably better known than any other LIP, our data show that the longest eruption hiatus during CRBG emplacement was unlikely to be longer than 80 ka. The gradual rather than pulsed emplacement of the CRBG, as well as its smaller total volume, may partly explain why the CRBG is not associated with the more catastrophic environmental and ecological effects of other LIPs. More detailed geochronology is needed to assess whether apparent eruption hiatuses in some LIPs are simply a transition to intrusion-dominated magmatism or regional phenomena and an artifact of incomplete sampling.

Our age model can be used to calculate the frequency and rate of individual eruptions through the GRB. Field observations have provided the number of lava flows in each stratigraphic member (Reidel & Tolan, 2013), and thermal models (Petcovic & Dufek, 2005) combined with thermochronologic data (Karlstrom et al., 2019) have been used to show that feeder dike segments were active for at most 1-10 years with fluxes of 1-3 km^3/a. With the simplistic assumption that each of the 112 GRB lava flows was sourced from 1 dike erupting over 10 years, we find a flow frequency of 1 flow per 2-6 ka for most of the GRB, apart from the interval between samples CRB1635 and CRB1634 (late N1-early R2), when it slows by an order of magnitude to 1 flow per ~11 ka. An interval of 1-10 ka between lava flows is consistent with the timescale on which sedimentary interbeds in the CRBG have been estimated to develop, based on the study of nutrient fluxes and palynoflora captured in these units, which are proxies for duration of exposure calibrated by modern interbeds in Hawaii (Jolley et al., 2008).

Our highly-resolved CRBG age model can yield further insight into the connection of the CRBG with the MCO. As we have previously discussed, one obstacle to comparing the timing of these events has been the disputed calibration of the Miocene Geomagnetic Polarity Timescale (GPTS), for which there are several proposals. Our new GRB ages show greater concordance with the astronomically tuned age model for IODP sites U1335 and U1336 (Kochhann et al., 2016) than with the Neogene GPTS in the Geologic Timescale 2012 (Hilgen et al., 2012), which is based on the spline fit of seafloor geomagnetic anomalies from 17-14 Ma, rather than astronomical tuning (Table DR3). Because some astronomically tuned Miocene climate records do not exhibit the same concordance with our age model (Billups et al., 2004; Pälike et al., 2006), it is important to utilize both tuning and geochronology to assess the timing of magnetic field reversals and gain a full understanding of sedimentation in tuned sections (Machlus et al., 2015; Sahy et al., 2017). Given good agreement between our radiometric ages and the age model of Kochhann et al. (2016), it could be used to recalibrate the Mid-Miocene GPTS, thereby anchoring other paleoclimate proxy records.

Recent work modeling atmospheric CO_2 concentrations during the MCO based on the $\delta^{11}B$ isotopic proxy show a brief increase at ~16.7 Ma, followed by sustained elevated levels from ~16.5-15.8 Ma (Sosdian et al., 2018). If the age models for these records are accurate, this pattern permits a connection between an increase in pCO_2 and the onset of CRBG magmatism. Elevated seawater temperatures, as recorded by $\delta^{18}O$ in foraminifera, continued for another ~1.5 million years after the cessation of main phase volcanism, (until ~14.5 Ma; Zachos et al., 2008). Our geochronology conclusively shows that all but ~1% of CRBG eruptions had ceased by ~15.9 Ma, and therefore, the CRBG cannot be invoked as a source of CO_2 through the entire duration of the MCO. In recent work using carbon cycle modeling to discern the connection between the MCO, CRBG, and the concurrent Monterey Carbon Isotope Excursion, Sosdian et al. (2020) suggest that elevated surface ocean dissolved inorganic carbon (DIC) throughout the MCO was caused by continuous eruption of the CRBG over millions of years, citing an outdated age model of CRBG emplacement rates, from Hooper et al., (2002). Since our new CRBG age model constrains the timing of volcanism to ~16.7-15.9 Ma, with eruptive fluxes double that of Hooper et al. (2002), we suggest that another mechanism of sustaining elevated DIC and seawater temperatures through this interval must be invoked after 15.9 Ma. One, perhaps unlikely, scenario is that elevated crustal geotherms sustained decarbonation reactions of carbon-rich sediments long after CRBG magmatism ceased. Another possible mechanism is a potentially slower silicate weathering feedback allowing for sustained warm conditions following the cessation of main phase CRBG volcanism. Both explanations require better data on the magnitude of each effect, especially since they play a role in explaining carbon cycle observations during other examples of LIP emplacement and environmental change, such as mass extinction events.

CONCLUSION

Our new ages for the GRB and revised age model for the CRBG offer a uniquely detailed view of the dynamics of LIP emplacement. The GRB, representing 72% of total CRBG volume, was emplaced over 505+51/-61 ka, with the longest hiatus unlikely to be longer than 80 ka. The mostly constant and lower volumetric emplacement rates of 0.3-0.5 km^3/a calculated through the main phase of CRBG volcanism likely contributed to its differing environmental effects from other LIPs; rather than association with a cataclysmic mass extinction, the CRBG instead was likely partly responsible for establishing the conditions of the MCO. Further studies that temporally constrain climatic fluctuations through the duration of the MCO and that input our new temporal constraints on CRBG volcanism into carbon cycle models for the MCO will allow for enhanced testing of this connection.

ACKNOWLEDGMENTS

We thank S. Reidel and B. Martin for their assistance defining the stratigraphic position of each geochronology sample. S. Bartusek, K. Duffey, & L. O'Connor provided able assistance in the lab and field. This material is based upon work supported by the NSF Graduate Research Fellowship under grant no. DGE-1656466, by Princeton Environmental Institute at Princeton University through the Walbridge Fund, and by the Princeton University Department of Geosciences Scott Vertebrate Fund.

REFERENCES

Armstrong McKay, D. I., Tyrrell, T., Wilson, P. A., & Foster, G. L. (2014). Estimating the impact of the cryptic degassing of Large Igneous Provinces: A mid-Miocene case-study. *Earth and Planetary Science Letters*, *403*, 254–262. https://doi.org/10.1016/j.epsl.2014.06.040

Barry, T. L., Self, S., Kelley, S. P., Reidel, S. P., Hooper, P. R., & Widdowson, M. (2010). New 40Ar/39Ar dating of the Grande Ronde lavas, Columbia River Basalts, USA: Implications for duration of flood basalt eruption episodes. *Lithos*, *118*(3–4), 213–222. https://doi.org/10.1016/j.lithos.2010.03.014

Barry, T. L., Kelley, S. P., Camp, V. E., Self, S., Jarboe, N. A., & Duncan, R. A. (2013). Eruption chronology of the Columbia River Basalt Group. *Geological Society of*

America Special Paper, *497*, 45–66. https://doi.org/10.1130/2013.2497(02).

Billups, K., Pälike, H., Channell, J. E. T., Zachos, J. C., & Shackleton, N. J. (2004). Astronomic calibration of the late Oligocene through early Miocene geomagnetic polarity time scale. *Earth and Planetary Science Letters*, *224*(1–2), 33–44. https://doi.org/10.1016/j.epsl.2004.05.004

Blackburn, T. J., Olsen, P. E., Bowring, S. A., McLean, N. M., Kent, D. V., Puffer, J. H., et al. (2013). Zircon U-Pb geochronology links the end-Triassic extinction with the Central Atlantic magmatic Province. *Science*. https://doi.org/10.1126/science.1234204

Burgess, S. D., Muirhead, J. D., & Bowring, S. A. (2017). Initial pulse of Siberian Traps sills as the trigger of the end-Permian mass extinction. *Nature Communications*, *8*(1), 164. https://doi.org/10.1038/s41467-017-00083-9

Camp, V. E. (2013). Origin of Columbia River Basalt: Passive rise of shallow mantle, or active upwelling of a deep-mantle plume? *Geological Society of America Special Paper*, *497*, 181–199. https://doi.org/10.1130/2013.2497(07).

Coble, M. A., & Mahood, G. A. (2012). Initial impingement of the Yellowstone plume located by widespread silicic volcanism contemporaneous with Columbia River flood basalts. *Geology*, *40*(7), 655–658. https://doi.org/10.1130/G32692.1

Cooper, K. M. (2015). Timescales of crustal magma reservoir processes: Insights from U-series crystal ages. *Geological Society Special Publication*, *422*(1), 141–174. https://doi.org/10.1144/SP422.7

Davies, J. H. F. L., Marzoli, A., Bertrand, H., Youbi, N., Ernesto, M., & Schaltegger, U. (2017). End-Triassic mass extinction started by intrusive CAMP activity. *Nature Communications*, *8*, 15596. https://doi.org/10.1038/ncomms15596

Ernst, R. E., & Youbi, N. (2017). How Large Igneous Provinces affect global climate, sometimes cause mass extinctions, and represent natural markers in the geological record. *Palaeogeography, Palaeoclimatology, Palaeoecology*, *478*, 30–52. https://doi.org/10.1016/j.palaeo.2017.03.014

Hilgen, F. J., Lourens, L. J., Van Dam, J. A., Beu, A. G., Boyes, A. F., Cooper, R. A., et al. (2012). *Chapter 29 - The Neogene Period*. *The Geologic Time Scale 2012 2-Volume Set*. https://doi.org/10.1016/B978-0-444-59425-9.00029-9

Hooper, P. R., Binger, G. B., & Lees, K. R. (2002). Ages of the Steens and Columbia River flood basalts and their relationship to extension-related calc-alkalic volcanism in eastern Oregon. *Bulletin of the Geological Society of America*, *114*(1), 43–50. https://doi.org/10.1130/0016-7606(2002)114<0043:AOTSAC>2.0.CO;2

Jolley, D. W., Widdowson, M., & Self, S. (2008). Volcanogenic nutrient fluxes and plant ecosystems in large igneous provinces: An example from the Columbia River Basalt Group. *Journal of the Geological Society*, *165*(5), 955–966. https://doi.org/10.1144/0016-76492006-199

Karlstrom, L., Murray, K. E., & Reiners, P. W. (2019). Bayesian markov-chain monte carlo inversion of low-temperature thermochronology around two 8 − 10 m wide columbia river flood basalt dikes. *Frontiers in Earth Science*, *7*(May). https://doi.org/10.3389/feart.2019.00090

Kasbohm, J. J., & Schoene, B. (2018). Rapid eruption of the Columbia River flood basalt and correlation with the mid-Miocene climate optimum. *Science Advances*, *4*(9), 1–8. https://doi.org/10.1126/sciadv.aat8223

Kasbohm, J. J., Schoene, B., & Burgess, S. D. (in press). Radiometric constraints on the timing, tempo, and effects of large igneous province emplacement. In R. E. Ernst, A. J. Dickson, & A. Bekker (Eds.), *Large Igneous Provinces: A Driver of Global Environmental and Biotic Changes*. American Geophyiscal Union.

Keller, C. B., Schoene, B., & Samperton, K. M. (2018). A stochastic sampling approach to zircon eruption age interpretation. *Geochemical Perspectives Letters*, 31–35. https://doi.org/10.7185/geochemlet.1826

Kochhann, K. G. D., Holbourn, A., Kuhnt, W., Channell, J. E. T., Lyle, M., Shackford, J. K., et al. (2016). Eccentricity pacing of eastern equatorial Pacific carbonate dissolution cycles during the Miocene Climatic Optimum. *Paleoceanography*, *31*(9), 1176–1192. https://doi.org/10.1002/2016PA002988

Liu, L., & Stegman, D. R. (2012). Origin of Columbia River flood basalt controlled by propagating rupture of the Farallon slab. *Nature*, *482*(7385), 386–389. https://doi.org/10.1038/nature10749

Long, M. D., Till, C. B., Druken, K. A., Carlson, R. W., Wagner, L. S., Fouch, M. J., et al. (2012). Mantle dynamics beneath the Pacific Northwest and the generation of voluminous back-arc volcanism. *Geochemistry, Geophysics, Geosystems*, *13*(1), 1–22. https://doi.org/10.1029/2012GC004189

Machlus, M. L., Ramezani, J., Bowring, S. A., Hemming, S. R., Tsukui, K., & Clyde, W. C. (2015). A strategy for cross-calibrating U-Pb chronology and astrochronology of sedimentary sequences: An example from the Green River Formation, Wyoming, USA. *Earth and Planetary Science Letters*, *413*, 70–78. https://doi.org/10.1016/j.epsl.2014.12.009

Mahood, G. A., & Benson, T. R. (2017). Using ^{40}Ar/^{39}Ar ages of intercalated silicic tuffs to date flood basalts: Precise ages for Steens Basalt Member of the Columbia River Basalt Group. *Earth and Planetary Science Letters*, *459*, 340–351. https://doi.org/10.1016/j.epsl.2016.11.038

Pälike, H., Frazier, J., & Zachos, J. C. (2006). Extended orbitally forced palaeoclimatic records from the equatorial Atlantic Ceara Rise. *Quaternary Science Reviews*, *25*(23–24), 3138–3149. https://doi.org/10.1016/j.quascirev.2006.02.011

Pavlov, V. E., Fluteau, F. F., Latyshev, A. V, Fetisova, A. M., Elkins-Tanton, L. T., Black, B. A., et al. (2019). Geomagnetic Secular Variations at the Permian-Triassic Boundary and Pulsed Magmatism During Eruption of the Siberian Traps. *Geochemistry, Geophysics, Geosystems*, *20*(2). https://doi.org/10.1029/2018GC007950

Petcovic, H. L., & Dufek, J. D. (2005). Modeling magma flow and cooling in dikes: Implications for emplacement of Columbia River flood basalts. *Journal of Geophysical Research: Solid Earth*, *110*(10), 1–15. https://doi.org/10.1029/2004JB003432

Reidel, S. P. (2015). The Columbia River Basalt Group: a flood basalt province in the Pacific Northwest, USA. *Geoscience Canada*, *42*, 151–168. https://doi.org/10.1007/s13398-014-0173-7.2

Reidel, S. P., & Tolan, T. L. (2013). The Grande Ronde Basalt, Columbia River Basalt Group. *Geological Society of America Special Papers*, *497*(05), 117–153. https://doi.org/10.1130/2013.2497(05).For

Sahy, D., Condon, D. J., Hilgen, F. J., & Kuiper, K. F. (2017). Reducing Disparity in

Radio-Isotopic and Astrochronology-Based Time Scales of the Late Eocene and Oligocene. *Paleoceanography*, *32*(10), 1018–1035. https://doi.org/10.1002/2017PA003197

Schoene, B., Eddy, M. P., Samperton, K. M., Keller, C. B., Keller, G., Adatte, T., & Khadri, S. F. R. (2019). U-Pb constraints on pulsed eruption of the Deccan Traps across the end-Cretaceous mass extinction. *Science*, *363*(6429), 862–866. https://doi.org/10.1126/science.aau2422

Shevenell, A. E., Kennett, J. P., & Lea, D. W. (2004). Middle Miocene Southern Ocean Cooling and Antarctic Cryosphere Expansion. *Science*, *305*, 1766–1770. https://doi.org/10.1126/science.1100061

Sosdian, S. M., Greenop, R., Hain, M. P., Foster, G. L., Pearson, P. N., & Lear, C. H. (2018). Constraining the evolution of Neogene ocean carbonate chemistry using the boron isotope pH proxy. *Earth and Planetary Science Letters*, *498*, 362–376. https://doi.org/10.1016/j.epsl.2018.06.017

Stelten, M. E., Cooper, K. M., Vazquez, J. A., Calvert, A. T., & Glessner, J. J. G. (2015). Mechanisms and timescales of generating eruptible rhyolitic magmas at Yellowstone Caldera from Zircon and sanidine geochronology and geochemistry. *Journal of Petrology*, *56*(8), 1607–1642. https://doi.org/10.1093/petrology/egv047

Tolan, T. L., Martin, B. S., Reidel, S. P., Anderson, J. L., Lindsey, K. A., & Burt, W. (2009). An introduction to the stratigraphy, structural geology, and hydrogeology of the Columbia River Flood-Basalt Province: A primer for the GSA Columbia River Basalt Group field trips. In *Volcanoes to Vineyards: Geologic Field Trips through the Dynamic Landscape of the Pacific Northwest*. https://doi.org/10.1130/2009.fld015(28)

Zachos, J. C., Dickens, G. R., & Zeebe, R. E. (2008). An early Cenozoic perspective on greenhouse warming and carbon-cycle dynamics. *Nature*, *451*, 279–283. https://doi.org/10.1038/nature06588

SUPPLEMENTAL INFORMATION

SAMPLE DESCRIPTIONS

Samples dated in this study were collected from roadcuts or natural exposures in Washington, Oregon, and Idaho in summers 2015 and 2016. Detailed sample descriptions are provided here, in stratigraphic order from oldest to youngest; starred sample descriptions are reproduced from Kasbohm & Schoene (2018). Outcrop photographs are provided in Fig. DR1, and zircon photographs are provided in Fig. DR2.

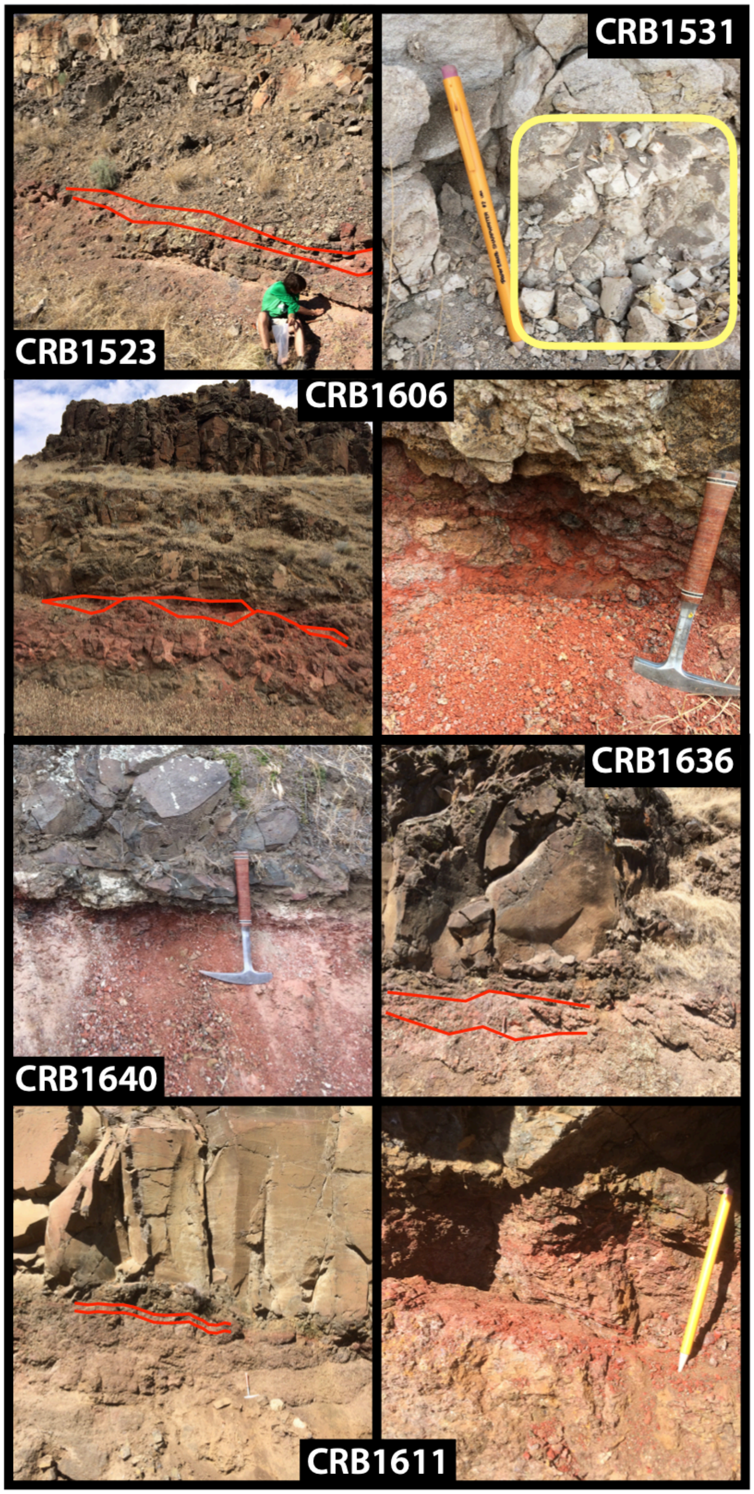

Fig. DR1. Geochronology Sample Photos. Outcrop-scale and/or hand-sample scale photos of each geochronology sample are provided here, with stratigraphic younging from bottom to top (Photo credit: Jennifer Kasbohm, Princeton University).

Fig. DR2. Zircon Photos. Optical images of zircons under transmitted light are presented here, with stratigraphic younging from bottom to top. Zircons present a range of morphologies, but the majority are euhedral with sharp crystal terminations, indicating an igneous rather than detrital origin. The zircon yielding the youngest, most precise analysis for each sample is starred.

CRB1625* (42.67542°N, 118.68724°W, elevation 2255 m)

This sample was collected from a ~0.5 m thick redbole between two Lower Steens Basalt flows, (based on the stratigraphy of (Johnson et al., 1998)) on the western side of Steens Mountain. The fine red sediment overlay a brecciated flow top and contained abundant vitreous microphenocrysts, black round lithic fragments, and subangular fragments of basaltic pumice up to 1 mm in size.

Fewer than 100 zircons were separated from this sample, and many of these grains are rounded and appear detrital. Some grains are euhedral, and ranged from equant to a high aspect ratio. Many grains are tinted orange, while some are clear. Forty grains were selected for analysis, and 19 were successfully dated. For this sample and the other samples described below, grains that were not successfully dated were lost at some stage of zircon chemistry prior to dating, or were dated and either did not fall on the Concordia line or exhibited a ratio of radiogenic Pb to common Pb that was ≤1. Six of these grains were ca. 16.7 Ma, with a dispersion of 120 ka, while the other 13 are inherited. Both the Mid-Miocene and inherited grains exhibited a range of morphologies. The youngest grains were often euhedral, and ranged from equant to an aspect ratio of at least 4:1. While some of the young grains were glassy and transparent, others were opaque. While a few of the analyses exhibited elevated common Pb content (>1 pg), others had low common Pb (<0.3 pg) but also low radiogenic Pb content (<1 pg), yielding generally less precise zircon ages for this sample than for the others in this study.

CRB1624* (42.66626°N, 118.56479°W, elevation 2966 m)

This sample was collected from a ~0.5 m thick redbole interbedded between Upper Steens Basalt flows (*60*) at the East Rim Lookout on Steens Mountain. The sampled horizon was a fine pink sediment infilling a brecciated flow top, and contained abundant vitreous microphenocrysts with few dark round lithic fragments.

Hundreds of zircons were obtained from this sample, with a range of morphologies. Generally, grains were angular to subangular, with fewer round detrital grains. The grains ranged from equant to higher aspect ratios, though few were acicular. Most of the grains are orange, while a few are clear and glassy. Twenty-three grains were selected for analysis, and 11 were successfully dated. The youngest grains appear to be the most euhedral, and range in size from <100 to over 300 μm. All of the grains were found to be ca. 16.6 Ma, with a dispersion of <70 ka. The precision of these analyses is attributed to high radiogenic Pb content (up to 34 pg) of the grains and low common Pb content (often <0.3 pg) in the analyses.

CRB1586* (44.83067°N, 116.90138°W, elevation 641 m)

This sample was collected from a ~0.5 m thick bed of lapilli tuff interbedded between columnar Imnaha Basalt flows on route 71 south of Brownlee Dam in Idaho. Accretionary lapilli are mm-cm scale and exhibit concentric banding around lithic nuclei.

Fewer than 50 zircons were separated from this sample, and are found to be glassy, somewhat blocky, and ranging in morphology from equant to tabular. Most of the grains are around 100 μm in length. Twenty-three grains were selected for analysis, and of these, 14 were successfully dated. One grain was found to be inherited, while the other 13 are dated to ~16.6 Ma, with a dispersion of 120 ka. The youngest and most precise grains are among the largest analyzed, and have a high radiogenic Pb content (1-6 pg).

CRB1611 (46.06924°N, 116.98544°W, elevation 266 m)

This sample was collected from a ~0.2 m layer of brecciated basalt flow top with red sedimentary infill overlying the Rock Creek Member of the Imnaha Basalt and underlying the Buckhorn Springs Member of the Grande Ronde Basalt (R1) along the Grande Ronde River near Rogersburg, WA (Stop 13 in (Reidel et al., 2016)). The sample consists of the fine-grained waxy red sediment, which was found outcropping in thin coherent layers as well as around some basalt clasts.

Fourteen grains were separated from this sample, and most of them appeared equant, glassy, and a mix of euhedral to somewhat rounded. All zircons were picked for analysis, and 6 were successfully dated. For this sample and the other samples described below, grains that were not successfully dated were lost at some stage of zircon chemistry prior to dating, or were dated and either did not fall on the Concordia line or exhibited a ratio of radiogenic Pb to common Pb that was ≤1. Three of these grains were ca. 16.58 Ma, with a dispersion of 20 ka, while the other 3 were inherited. The successful analyses suffered from low radiogenic Pb content (<1 pg), potentially due to the small (≤ 100 μm) size of the zircons, yielding generally less precise zircon ages for this sample than for the others in this study.

CRB1640 (46.21153°N, 116.96839°W, elevation 271 m)

This sample was collected from a ~0.5 m thick redbole overlying a Member of Center Creek lava flow and underlying an undifferentiated R1 Grande Ronde Basalt lava flow in the Schoolhouse Draw section of (Camp, 1976) near Asotin, WA. The sampled horizon was a fine red sediment with a few dark lithic fragments.

A few hundred zircons were obtained from this sample, with a range of morphologies, from small and equant to acicular grains a few hundred microns in length. Many grains were somewhat rounded, and some exhibited inherited cores. Most of the grains are orange, while a few were clear and glassy. Twenty-seven grains were selected for analysis, and 14 were successfully dated. Eight of the grains were inherited, while the other six grains were found to be ca. 16.5 Ma, with a dispersion of 180 ka. The youngest grains are prismatic, euhedral, and exhibit higher aspect ratios. Like CRB1611, the successful analyses suffered from low radiogenic Pb content (<1 pg), yielding generally less precise zircon ages for this sample than for the others in this study.

CRB1636 (46.28875°N, 116.98751°W, elevation 218 m)

This sample was collected from a ~1 m layer of brecciated basalt flow top with red sedimentary infill between lava flows of the Hoskin Gulch Member of the Grande Ronde Basalt (N1) along the Snake River south of Asotin, WA. The sample consists of the fine-grained red, pink, and orange sediment, with mm- to cm-scale dark lithic fragments and few vitreous microphenocrysts.

Approximately 60 zircons were separated from this sample, most of which with somewhat rounded crystal terminations and orange in color. Most of the grains are around 100 μm in length, with a range of aspect ratios. Thirty-eight grains were selected for analysis, and of these, 21 were successfully dated. Nine grains were inherited, while the other 12 are dated to ~16.4 Ma, with a dispersion of 150 ka. The youngest and most precise grains are among the largest or most euhedral analyzed, and have a high radiogenic Pb content (~2 pg).

CRB1634* (46.05072°N, 117.23906°W, elevation 538 m)

This sample was collected from a redbole in the lower flows of the Wapshilla Ridge Member of the Grande Ronde Basalt, on Rattlesnake Grade in southeastern Washington. The redbole infills topography on the underlying brecciated flow top, with a maximum thickness of 0.3 m, but pinches out over a few meters width. The redbole contains a few mm-scale light and dark lithic fragments, with some vitreous phenocrysts.

Hundreds of zircons were obtained from this sample, ranging in size from 50-250 μm. Most are orange in color but a few are clear. Half of the zircons presented an acicular morphology, 20% appeared equant, and the rest have a medium aspect ratio. Twenty-four zircons were selected for analysis, and eleven were successfully dated. All zircons were found to be ca. 16.3 Ma, with a dispersion of 160 ka. The youngest grains appear somewhat wide, clear, and euhedral, and the most precise analyses came from zircons with the greatest amount of radiogenic Pb (1-2 pg).

CRB1556* (46.08543°N, 117.17870°W, elevation 1145 m)

This sample was collected from the same stratigraphic section as CRB1634, from a 0.6 m thick redbole between lava flows of the Meyer Ridge Member, immediately overlying the Wapshilla Ridge Member. The horizon was most coherent in its upper half, and displayed few vitreous phenocrysts and rare lithics.

The sample yielded 19 zircons, and all were picked for analysis; 7 were successfully dated. The zircons were either <100 μm and equant or larger and more tabular. A few were euhedral with pointy edges, while others appeared fragmented at the edges. The youngest, most precise analyses came from the largest grains. Even though these grains were not euhedral, they possessed the greatest amount of radiogenic Pb (1-2 pg). The grains exhibit a dispersion of 150 ka around ca. 16.3 Ma.

CRB1519* (46.44171°N, 117.39066°W, elevation 701 m)

This sample was collected from a redbole found under a lava flow of the Meyer Ridge Member and overlying a lava flow Wapshilla Ridge Member, representing the same stratigraphic interval as CRB1556 but found 44 km away on US-12 east of Pomeroy, WA. The sample is fine-grained, with abundant vitreous microphenocrysts and few angular lithic fragments.

Hundreds of zircons were separated from this sample, and they appear mostly clear and glassy, with a few orange grains. Most present typical aspect ratio, while 10% are acicular and a few grains are equant. Many grains are subangular, with pointy tips slightly worn down. Twenty-one grains were selected for analysis, and 10 were successfully dated. Two of the zircons analyzed were inherited, and appear somewhat opaque; five zircons were ca. 16.2 Ma but an age dispersion of 400 ka, outside the range of analytical uncertainty. The youngest grains each have one euhedral tip, are longer than 100 µm, and the most precise analyses were for zircons with a higher radiogenic Pb content (2-4 pg).

CRB1606 (46.44399°N, 117.74769°W, elevation 496 m)

This sample was collected from a discontinuous ~0.7 m layer of red sedimentary infill of brecciated basalt flow top above the Member of Ortley and below the Fields Spring Member the Grande Ronde Basalt (N2), on Marengo Grade (Majorie Road) near Pomeroy, Washington. The sample is very-fine grained red to pink sediment with a few very fine light grains (possible phenocrysts) and very small, round, dark lithic fragments.

Approximately 1000 euhedral zircons were obtained from this sample, ranging in size from <100-250 µm. Most grains were clear with a medium aspect ratio, while 10-20% of the grains were glassy, acicular, and prismatic. Forty-four zircons were selected for analysis, and eighteen were successfully dated. Zircons were found to be ca. 16.2-16.5 Ma, with a dispersion of 350 ka. The youngest grains appear especially elongate and acicular, and the most precise analyses came from zircons with 1-2 pg of radiogenic Pb.

CRB1523 (46.43582°N, 117.32221°W, elevation 410 m)

This sample was collected from a 10 cm, heterogeneous redbole found in the Fields Spring Member of the Grande Ronde Basalt (N2) on US-12 east of Pomeroy, WA, in the same stratigraphic transect as CRB1519.

Approximately 100 zircons were separated from this sample, and they are a mix of clear and glassy, and somewhat orange grains. Most are equant or present typical aspect ratio, while 10% are acicular. Many grains are slightly rounded. Fifty-three grains were selected for analysis, and 20 were successfully dated. Two of the zircons analyzed were inherited; the rest range in age from ~16.1-16.5 Ma. The youngest grains are mostly acicular and a few hundred microns long, and the most precise analyses were for zircons with a higher radiogenic Pb content (1-4 pg).

CRB1531 (46.95243°N, 119.99783°W, elevation 227 m)

This sample was collected from the lowermost unit of the Vantage Interbed type locality in Vantage, WA (Stop 7 in (Tolan et al., 2009)), which is 15 cm of a white mud, with possible spherules and tiny vitreous phenocrysts. The Vantage Interbed lies over the Basalt of Museum of the Sentinel Bluffs Member of N2 of the Grande Ronde Basalt, and under the Basalt of Ginkgo of the Frenchman Springs Member of the Wanapum Basalt.

Fewer than 100 zircons were obtained from this sample, and all are clear and prismatic, with a mix of rounded and euhedral grains. The zircons range in size from 100-200 μm, and are a mix of equant and normal aspect ratio grains, while 10% of the grains are acicular. Thirty-three zircons were selected for analysis, and 18 of these were successfully dated, with 15 grains found younger than 16.8 Ma. The age dispersion of these samples is greater than 700 ka, well beyond analytical uncertainty, suggesting pre-eruptive crystallization. The youngest grains are prismatic with a medium aspect ratio, and the most precise analyses are due to radiogenic Pb content >1 pg.

CRB1533* (46.95243°N, 119.99783°W, elevation 227 m)

This sample was collected from 2 kg of 1-10 cm-scale pumice clasts embedded in the volcaniclastic sediments of the Vantage Interbed type locality in Vantage, WA (Stop 7 in Tolan *et al.* (*61*)). Phenocrysts in the pumice contained quartz and sanidine, and the sampled horizon consisted of 1.4 m of the total 5.6 m of the Vantage Interbed exposed at the outcrop. The Vantage Interbed lies over the Basalt of Museum of the Sentinel Bluffs Member of N2 of the Grande Ronde Basalt, and under the Basalt of Ginkgo of the Frenchman Springs Member of the Wanapum Basalt.

Several thousand zircons were obtained from this sample, and all are clear, prismatic, and euhedral. The zircons range in size from 50-300 μm, and about 10% are equant grains, while 10% of the grains are acicular. Forty zircons were selected for analysis, and 11 of these were successfully dated, with 9 grains found younger than 17 Ma. The age dispersion of these samples is greater than 500 ka, well beyond analytical uncertainty, suggesting pre-eruptive crystallization. The youngest grains appear to be the most acicular in morphology, and the most precise analyses are due to high radiogenic Pb content of 5-15 pg.

CRB1506* (46.73914°N, 117.75500°W, elevation 470 m)

This sample was collected from 0.3 m of a fine white crumbly ash, with few round lithic fragments and glassy phenocrysts, interbedded between the overlying Basalt of Lolo of the Priest Rapids Member of the Wanapum Basalt and the underlying Roza Member of the Wanapum Basalt, on WA-127 southeast of Endicott, WA.

Hundreds of zircons were obtained from this sample, most of which are clear and subangular to subrounded. While a few zircons were angular, none were acicular. Thirty-five grains were selected for analysis, and 10 were successfully dated. Four of these were inherited, and the remaining six grains have a uniform age distribution within 2σ uncertainty, of ca. 15.9 Ma. The youngest and most precise dates were obtained from somewhat opaque, orange-tinted zircons that were euhedral, and had high radiogenic Pb content of 11-40 pg.

METHODS

Methods are as described in Kasbohm & Schoene (2018), Schoene *et al.* (2015) and Samperton *et al.* (2015).

Zircon Separation and Preparation

Zircons were separated from their host rock through standard methods of crushing, gravimetric-, and magnetic-separation techniques using a Bico Braun “Chipmunk” Jawcrusher, disc mill, hand pan, hand magnet, Frantz isodynamic separator, and methylene iodide. Zircons from the least magnetic and most dense mineral separate were transferred in bulk to quartz crucibles and annealed in a muffle furnace at 900°C for 48 hours after Mattinson (Mattinson, 2005). After annealing, 20-40 zircon grains from each sample were photographed (Fig. DR2) and picked in reagent-grade ethanol for analysis. Given the low radiogenic Pb content of the samples, cathodoluminescence images were not obtained. Euhedral grains with a range of morphologies were selected, while those with visible cracks, inclusions, and cores were avoided. Individual grains were transferred using stainless steel picking tools to separate 3-mL Savillex Hex beakers containing distilled acetone and taken to the clean lab for analysis.

U-Pb Zircon ID-TIMS Analysis

Single zircon grains were loaded into 200 uL Savillex "micro"-capsules with 100 μL 29 M HF + 15 μL 3N HNO_3 for a single leaching step in high-pressure Parr bombs at 185°C for 12 h to remove crystal domains affected by Pb loss (Mattinson, 2005). Grains were rinsed post-leaching in 6 N HCl, MQ H2O, 3N HNO_3, and 29 M HF prior to spiking with EARTHTIME ^{205}Pb-^{233}U-^{235}U tracer and addition of 100uL 29 M HF + 15 μL 3N HNO_3 (Condon et al., 2015; McLean et al., 2015). Zircons were then dissolved to completion in Parr bombs at 210°C for 48 h. Dissolved zircon solutions were subsequently dried down, dissolved in 100 μL 6N HCl, and converted to chlorides in Parr bombs at 185°C for 12 h, after which solutions were dried again and brought up in 50 μL 3N HCl. The U-Pb and trace element aliquots were then separated by anion exchange chromatography using 50 μL columns and AG-1 X8 resin (200-400 mesh, chloride from Eichrom) (Krogh, 1973), and dried down with a microdrop of 0.015 M H_3PO_4. The dried U and Pb aliquot was loaded in a silica gel emitter (Gerstenberger & Haase, 1997) to an outgassed zone-refined Re filament.

Isotopic determinations were performed using an IsotopX PhoeniX-62 thermal ionization mass spectrometer (TIMS) at Princeton University, with Pb analysis performed in peak-hopping mode on a Daly-photomultiplier ion-counting detector. A correction for mass-dependent Pb fractionation was applied using a Pb fractionation of 0.182±0.041%/amu, as determined by repeat measurements of NBS982 at Princeton. A Daly-photomultiplier deadtime of 28.8 ns was used, as determined by repeat measurements of NBS standards. Corrections for interfering isotopes under masses 202, 204, and 205 were made cycle-by-cycle by measuring masses 201 and 203 and assuming they represent $^{201}BaPO_4$ and ^{203}Tl and using natural isotopic abundances to correct for $^{202}BaPO_4$, $^{204}BaPO_4$, $^{205}BaPO_4$, and ^{205}Tl.

UO_2 measurements were performed in static mode on Faraday cups with a bulk U fractionation correction calculated from the deviation of measured $^{233}U/^{235}U$ from the known tracer $^{233}U/^{235}U$ (0.995062±0.000054 (1σ)), and an oxide composition of $^{18}O/^{16}O$ of 0.00205 was used (Nier, 1950). Data reduction was performed using the programs Tripoli and U-Pb Redux (Bowring et al., 2011; McLean et al., 2011) and the decay constants of Jaffey *et al.* (1971). All Pbc was attributed to laboratory blank with a mean isotopic composition determined by total procedural blank measurements (see Table DR1 for values). Uncertainties in reported U-Pb zircon dates are at the 95% confidence level and exclude tracer calibration and decay constant uncertainties. Correction for initial

^{230}Th disequilibrium in the ^{206}Pb/^{238}U system was made on a fraction-by-fraction basis by estimating $(\mathrm{Th/U})_{\mathrm{magma}}$ using $(\mathrm{Th/U})_{\mathrm{zircon}}$ determined by TIMS and a mean $(\mathrm{Th/U})_{\mathrm{zircon\text{-}magma}}$ partition coefficient ratio of 0.19±0.11, which encompasses the range of values for $(\mathrm{Th/U})_{\mathrm{zircon\text{-}magma}}$ partition coefficients obtained from glasses from a variety of volcanic settings (Claiborne et al., 2018). Uncertainties for the resulting $(\mathrm{Th/U})_{\mathrm{magma}}$ were also calculated on a fraction-by-fraction basis, propagating the uncertainty in the $(\mathrm{Th/U})_{\mathrm{zircon\text{-}magma}}$ partition coefficient. We found in our prior work (Kasbohm & Schoene, 2018) that these corrections for ^{230}Th disequilibrium affect our results by no more than ±10 ka, compared to an alternative approach using a constant $(\mathrm{Th/U})_{\mathrm{magma}}$ of 3.5±1.0. Given the likelihood that the zircons in this study were crystallized from a variety of different magmatic systems, we prefer the constant partition coefficient approach for correcting Th/U disequilibrium.

U-PB AGE INTERPRETATIONS

Given the physical characteristics of both rock samples and zircons, the geochronology samples for this study are interpreted to be volcanic in origin, and deposited by unrelated regional silicic volcanism during cessations in CRBG volcanism. The presence of phenocrysts, lithic fragments, and fragments of basaltic pumice found at the hand sample scale are consistent with ash deposits, and the euhedral and prismatic appearance of the zircons are consistent with magmatic textures, with little evidence for rounding seen in alluvial or eolian grains.

Full U-Pb isotope results are given in Table DR1, and Concordia plots for each sample are given in Fig. DR3. All dates are presented with 2σ uncertainty, which represents internal errors only. In Table DR2, alternative age interpretations are also given with 2σ uncertainties of ±X/Y/Z. X is used for most of the geochronological uncertainty

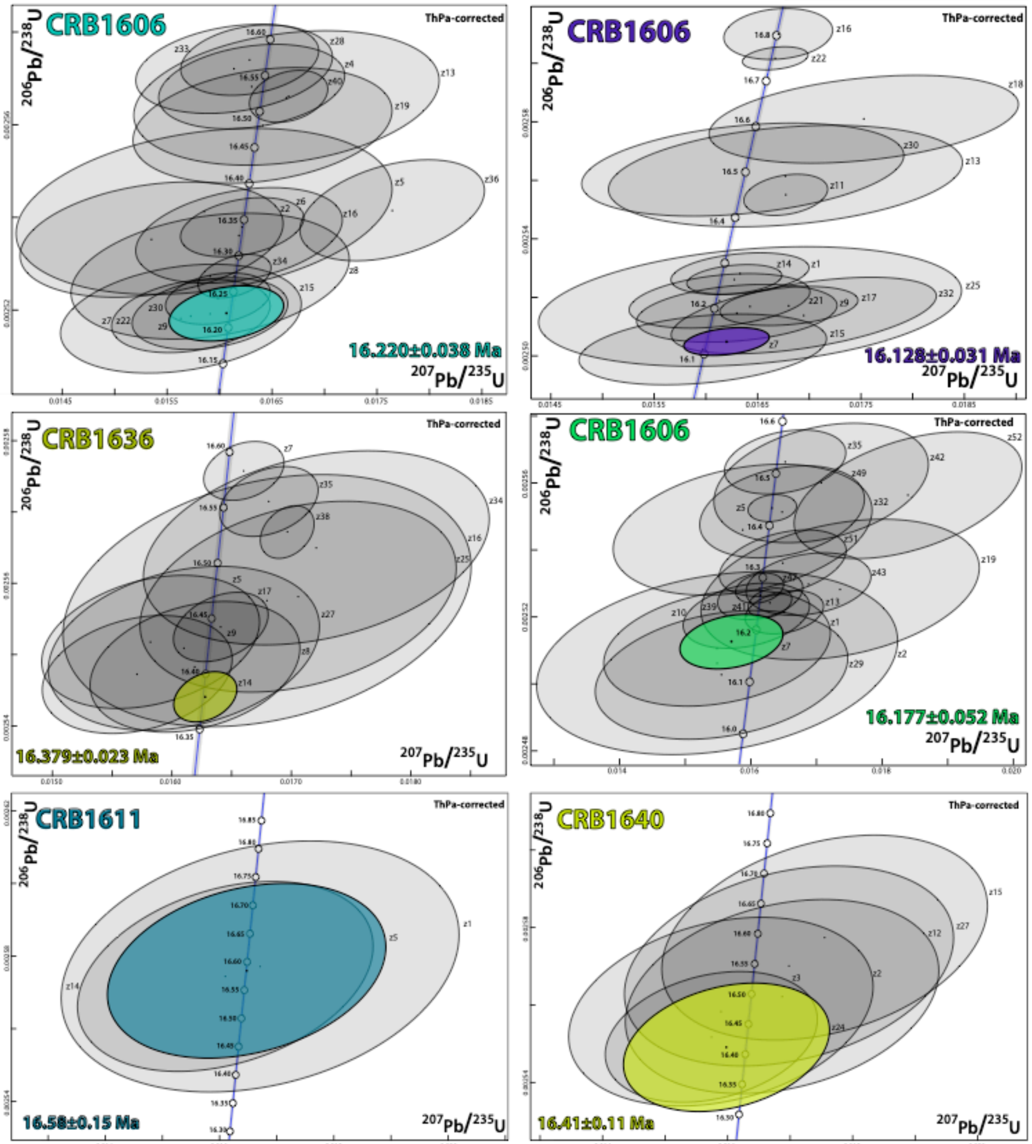

Fig. DR3. Concordia Plots for U-Pb ID-TIMS Geochronological Data. U-Pb isotopic data for each analysis is available in Table DR1. Each ellipse is labelled and represents a zircon analysis, with the width of the ellipse representing 2σ uncertainty. The youngest, most precise zircon age obtained for each sample is highlighted. The shading around the Concordia line represents uncertainties in the U decay constants. Almost all ellipses overlap with Concordia, indicating closed-system behavior.

described in this paper, and indicates internal uncertainties only for comparison with U-Pb dates from labs using ET-(2)535 tracer solution. Y also incorporates tracer calibration uncertainties for comparison with other U-Pb dates determined with different tracer solution. Z includes full systematic uncertainties, including decay constants, to allow for comparison with other radioisotopic dates or astrochronologically-determined timescales that may be tied to other radioisotopic dates that are not derived from the U-Pb system (Renne et al., 1998; Schoene et al., 2006).

Interpretation of Zircon Crystallization Age Spectra

The zircons dated from each geochronology sample displayed a dispersion in ages ranging from 40-700 ka (apart from inherited grains). We interpret this as geological scatter caused by pre-eruptive zircon crystallization or incorporation of zircons from older material in the same volcanic system (Cooper, 2015; Stelten et al., 2015), because the dispersion in most cases goes beyond analytical uncertainty. In Table DR2, we present a variety of different age interpretations to address these complex age spectra. While we suggest that our simulated stratigraphic model ages, based on Bayesian eruption ages with a triangular prior, best address the geologic uncertainty inherent in these interpretations, Table DR2 shows that alternative interpretations yield overlapping results. Therefore, our main conclusions about the dynamics of CRBG emplacement do not depend on the mode of zircon age interpretation.

In Kasbohm & Schoene (2018), we presented the youngest, most precise zircon dates as best representing the ages of the horizons in the study, since that zircon likely crystallized closest in time to the eruption of the volcanic ash. However, even following chemical abrasion, subtle Pb-loss may be difficult to detect. Meanwhile, other geochronological studies use weighted means of several zircon dates to constraint the age of the sample. Although a weighted mean date has lower uncertainty than a single crystal age, it should only be used for homogeneous age populations where all scatter is caused by analytical uncertainty, which is not the best interpretation for our samples, given the complexity of pre-eruptive crystallization. As a mean route between these approaches, in some cases geochronologists calculate the weighted mean age of the youngest few grains. However, as described in Keller et al. (2018), a statistical model for Bayesian eruption ages incorporating timescales of zircon saturation provides a more objective approach for interpreting zircon age spectra, yielding more accurate if somewhat less-precise results. The only subjective element of these model ages is whether a uniform, bootstrapped, or triangular prior of zircon crystallization is chosen (Keller et al., 2018). We prefer the Bayesian eruptive ages, and suggest that a triangular prior, with linear increase of zircon mass as time passes, provides the most geologically relevant interpretation. To further refine our ages, we use a second Markov Chain Monte Carlo simulation taking into account the stratigraphic position and cumulative volume erupted by each sample in succession, and we use the outputs of this model in all figures and discussion in the paper.

							Youngest Zircon					Weighted Means														Bayesian Eruptive Ages												MCMC age model with Triangular Prior		
												Youngest Few Zircons							Maximum n allowed for MSWD ≈ 1							Uniform Prior			Bootstrapped Prior			Melts Volcanic Prior			Triangular Prior					
					Cumulative				uncertainty			addtnl			uncertainty			MS	addtnl			uncertainty			MS															
sample	Latitude (°N)	Longitude (°W)	Elevation (m)	Formation: Member, flow over interbed / under interbed	Volume (km^3)	Lithology	zircon	age	X	Y	Z	zircons	n	age	X	Y	Z	WD	zircons	n	age	X	Y	Z	WD	age	+	-	age	+	-	age	+	-	age	+	-	age	+	-
CRB1625	42.67542	118.68724	2255	Lower Steens	8904	redbole	z15	16.653	0.063	0.071	0.073	7,27,36	4	16.654	0.050	0.057	0.059	0.018	all	6	16.680	0.042	0.052	0.055	0.82	16.651	0.049	0.097	16.658	0.043	0.077	16.645	0.054	0.121	16.658	0.044	0.077	16.667	0.034	0.046
CRB1624	42.66626	118.56479	2966	Upper Steens	31800	breccia infill	z5	16.589	0.031	0.032	0.037	18,23	3	16.597	0.021	0.023	0.029	0.26	all	11	16.616	0.011	0.014	0.023	0.92	16.608	0.013	0.024	16.610	0.012	0.020	16.606	0.015	0.030	16.610	0.012	0.020	16.606	0.017	0.024
CRB1586	44.83067	116.90138	641	Imnaha	39000*	lapilli tuff	z4	16.572	0.018	0.018	0.026	3,15	3	16.571	0.016	0.017	0.024	0.086	2,9,23	6	16.579	0.014	0.015	0.023	0.94	16.566	0.026	0.038	16.571	0.022	0.029	16.558	0.031	0.051	16.571	0.022	0.029	16.576	0.018	0.023
CRB1611	46.06924	116.98544	266	Grande Ronde: Buckhorn Springs (R1) / Imnaha: Rock Creek	42800	breccia infill	z5	16.58	0.15	0.16	0.16	all	3	16.58	0.10	0.11	0.11	0.0086	all	3	16.58	0.10	0.11	0.11	0.0086	16.536	0.088	0.170	16.546	0.081	0.127	16.528	0.094	0.199	16.546	0.080	0.126	16.565	0.025	0.043
CRB1640	46.21153	116.96839	271	Grande Ronde: Center Creek (R1)	73254	redbole	z24	16.41	0.11	0.11	0.11	3	2	16.420	0.076	0.084	0.086	0.051	all	6	16.468	0.056	0.067	0.069	0.97	16.435	0.061	0.110	16.442	0.056	0.090	16.427	0.068	0.141	16.443	0.055	0.087	16.443	0.043	0.057
CRB1636	46.28875	116.98751	218	Grande Ronde: Hoskin Gulch (N1)	94004	breccia infill	z14	16.379	0.023	0.026	0.031	8,9	3	16.385	0.020	0.023	0.029	0.540	5,27	5	16.391	0.018	0.022	0.028	0.94	16.366	0.028	0.053	16.373	0.024	0.036	16.351	0.039	0.095	16.374	0.024	0.036	16.374	0.024	0.031
CRB1634	46.05072	117.23906	538	Grande Ronde: Wapshilla (R2)	109779	redbole	z8	16.288	0.039	0.043	0.046	22	2	16.295	0.026	0.030	0.035	0.25	all -15	10	16.308	0.022	0.029	0.034	1.1	16.286	0.036	0.065	16.291	0.032	0.049	16.279	0.042	0.089	16.292	0.031	0.049	16.306	0.025	0.034
CRB1556	46.08543	117.17870	1145	Grande Ronde: Meyer Ridge (R2) / Grande Ronde: Wapshilla (R2)	150029	redbole	z12	16.254	0.034	0.037	0.041	13	2	16.256	0.025	0.029	0.033	0.014	all	7	16.268	0.022	0.027	0.032	0.88	16.254	0.024	0.043	16.257	0.022	0.034	16.251	0.026	0.056	16.257	0.022	0.034	16.232	0.033	0.034
CRB1519	46.44171	117.39066	701	Grande Ronde: Meyer Ridge (R2) / Grande Ronde: Wapshilla (R2)	150029	redbole	z1_BS	16.210	0.043	0.044	0.047	1,16	3	16.236	0.032	0.032	0.037	1.6	13	4	16.237	0.031	0.032	0.036	1.1	16.181	0.057	0.131	16.197	0.046	0.077	16.142	0.090	0.268	16.196	0.047	0.083	16.232	0.033	0.034
CRB1606	46.44399	117.74769	496	Grande Ronde: Fields Spring (N2) / Grande Ronde: Ortley (N2)	172759	breccia infill	z9	16.220	0.038	0.040	0.044	7,15,22	4	16.218	0.025	0.028	0.033	0.013	8,30	6	16.228	0.020	0.023	0.028	0.43	16.187	0.039	0.070	16.196	0.033	0.050	16.159	0.060	0.135	16.200	0.032	0.048	16.180	0.035	0.044
CRB1523	46.43582	117.32221	410	Grande Ronde: Fields Spring (N2)	175049	redbole	z7	16.177	0.052	0.054	0.057	1,2,29	4	16.165	0.043	0.046	0.049	0.34	10	5	16.185	0.035	0.039	0.042	0.92	16.126	0.068	0.092	16.156	0.053	0.068	16.083	0.089	0.152	16.155	0.056	0.071	16.168	0.038	0.048
CRB1531	46.95243	119.99783	227	Lower Vantage (Wanapum: Frenchman Springs, Ginkgo / Grande Ronde: Sentinel Bluffs, Museum (N2))	192999	white mud	z7	16.128	0.031	0.033	0.037	15	2	16.125	0.028	0.032	0.036	0.17	32	3	16.131	0.027	0.030	0.035	0.99	16.078	0.060	0.133	16.089	0.051	0.089	16.014	0.115	0.314	16.097	0.047	0.083	16.052	0.055	0.053
CRB1533	46.95243	119.99783	227	Upper Vantage (Wanapum: Frenchman Springs, Ginkgo / Grande Ronde: Sentinel Bluffs, Museum (N2))	193567	pumice clasts	z4_BS	16.066	0.040	0.040	0.043	3,25,34	4	16.059	0.029	0.030	0.035	0.19	28	5	16.068	0.028	0.030	0.034	1.3	16.011	0.056	0.112	16.025	0.046	0.072	15.983	0.079	0.192	16.029	0.045	0.073	16.044	0.045	0.051
CRB1506	46.73914	117.75500	470	Wanapum: Priest Rapids, Lolo / Wanapum: Roza	202942	white ash	z34	15.895	0.019	0.020	0.026	3,21	3	15.898	0.013	0.014	0.022	0.26	1,35	5	15.905	0.010	0.012	0.021	1.1	15.898	0.012	0.024	15.900	0.010	0.018	15.897	0.013	0.031	15.900	0.010	0.018	15.906	0.053	0.018
					*estimated																																	**preferred interpretation**		

Table DR2. Alternate Age Interpretations. We present zircon ages using a variety of different age interpretations: youngest, most precise grain; weighted mean of youngest few grains; weighted mean yielding a mean square of weighted deviates (MSWD) near 1, indicating that age dispersion reflects analytical uncertainty; and Bayesian eruptive ages, using a uniform, bootstrapped, and triangular prior and displaying 95% credible intervals (Keller et al., 2018). We highlight the Bayesian eruptive age with triangular prior as our preferred input, and the results from a Markov Chain Monte Carlo simulation based on the stratigraphic position and cumulative volume erupted for each sample provide our preferred age model for the CRBG used in this paper.

Using these six different interpretations, we calculate ages for all of our samples and present them in Figure DR2. Ultimately, all of the interpretations produce overlapping ages, showing that our preferred interpretation does not bias the conclusions of our work.

GEOMAGNETIC POLARITY TIMESCALE CALIBRATION

Our CRBG age model yields ages for magnetic field reversals that occurred during the emplacement of the basalts, as well as chron durations during this period, reported with 95% credible intervals. In Table DR3, we compare our reversal ages to astronomically tuned age models from Sites U1335 and U1336 (Kochhann et al., 2016), Site 1090 (Billups et al., 2004), Site 154 (Pälike et al., 2006), and spline fits from the Astronomically Tuned Neogene Timescale (ATNTS) from the Geologic Time Scale 2012 (Hilgen et al., 2012). We find the greatest agreement between our model and the tuning results of Kochhann et al. (2016).

	CRBG Reversal Age Model					Other GPTS Calibrations					Reversal Age Differences				
Polarity Chron Onset	Cumulative Volume (km^3)	Reversal Age (Ma)	Maximum Reversal Age (Ma)	Minimum Reversal Age (Ma)	Chron Duration (ka)	U1335 Tuned Age (Ma)	U1336 Tuned Age (Ma)	1090 Tuned Age (Ma)	154 Tuned Age (Ma)	ATNTS 2012 Spline Age (Ma)	Δ CRBG Age - U1335 Age (Ma)	Δ CRBG Age - U1336 Age (Ma)	Δ CRBG Age - 1090 Age (Ma)	Δ CRBG Age - 154 Age (Ma)	Δ CRBG Age - ATNTS 2012 Age (Ma)
C5Br	202942	15.906	15.959	15.888	-	15.896	15.994	15.898	15.899	15.974	agrees	-0.035	agrees	agrees	-0.015
C5Cn.1n	157600	16.215	16.259	16.168	296+45-63	16.242	16.261	16.161	16.162	16.268	agrees	-0.002	0.007	0.006	-0.009
C5Cn.1r	101600	16.340	16.385	16.292	126+55/-54	16.34	16.351	16.255	16.256	16.303	agrees	agrees	0.037	0.036	agrees
C5Cn.2n	77000	16.443	16.486	16.386	100+56/-58	16.415	16.434	16.318	16.319	16.472	agrees	agrees	0.068	0.067	agrees
C5Cn.2r	42800	16.565	16.590	16.522	122+51/-45	16.514	16.532	16.405	16.406	16.543	0.008	agrees	0.117	0.116	agrees
C5Cn.3n	23850	16.629	16.677	16.592	65+52/-38	16.582	16.637	16.498	16.499	16.721	0.01	agrees	0.094	0.093	-0.044

Table DR3. Geomagnetic Polarity Timescale Calibration. Using our stratigraphic CRBG age model, we provide here ages for polarity chron onsets and chron durations during CRBG emplacement, reported with 95% credible intervals. We compare our reversal ages to astronomically tuned age models from Sites U1335 and U1336 (Channell et al., 2013; Kochhann et al., 2016; Ohneiser et al., 2013), Site 1090 (Billups et al., 2004), Site 154 (Pälike et al., 2006), and the spline fit based on magnetic seafloor anomalies from the Astronomically Tuned Neogene Timescale (ATNTS) in Geologic Time Scale 2012 (Hilgen et al., 2012). We find the greatest agreement between our model and the tuning results of Kochhann et al. (2016).

HIATUS DURATION CALCULATION

We query our Monte Carlo age model to find the length of the longest hiatus in each model run, and plot the results in the histogram in Figure DR4. This plot shows that the longest hiatus during CRBG emplacement was most likely 50-80 ka, and we show the likelihood of that longest hiatus occurring at each stratigraphic position in Figure 3.

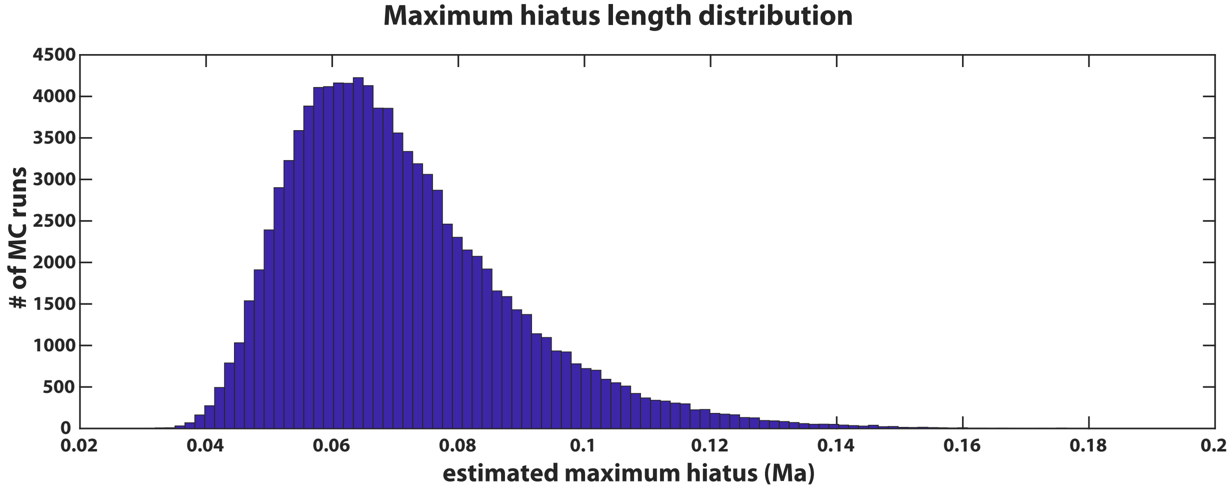

Figure DR4. Maximum hiatus length. This histogram plots the frequency of durations for the longest hiatus calculated for each Monte Carlo simulation. The longest CRBG hiatus was most likely 50-80 ka.

Table DR1. U-Pb Isotopic Data. Data acquired by CA-ID-TIMS is presented following the references, with various corrections as specified in the notes beneath the table.

REFERENCES CITED

Billups, K., Pälike, H., Channell, J. E. T., Zachos, J. C., & Shackleton, N. J. (2004). Astronomic calibration of the late Oligocene through early Miocene geomagnetic polarity time scale. *Earth and Planetary Science Letters*, *224*(1–2), 33–44. https://doi.org/10.1016/j.epsl.2004.05.004

Bowring, J. F., McLean, N. M., & Bowring, S. A. (2011). Engineering cyber infrastructure for U-Pb geochronology: Tripoli and U-Pb-Redux. *Geochemistry, Geophysics, Geosystems*, *12*(6). https://doi.org/10.1029/2010GC003479

Camp, V. E. (1976). *Petrochemical stratigraphy and structure of the Columbia River basalt, Lewiston Basin Area, Idaho-Washington*. Washington State University.

Channell, J. E. T., Ohneiser, C., Yamamoto, Y., & Kesler, M. S. (2013). Oligocene-Miocene magnetic stratigraphy carried by biogenic magnetite at sites U1334 and

U1335 (equatorial Pacific Ocean). *Geochemistry, Geophysics, Geosystems*, *14*, 265–282. https://doi.org/10.1029/2012GC004429

Claiborne, L. L., Miller, C. F., Gualda, G. A. ., Carley, T. L., Covey, A. K., Wooden, J. L., & Fleming, M. A. (2018). Zircon as Magma Monitor: Robust,Temperature-Dependent Partition Coefficients from Glass and Zircon Surface and Rim Measurements from Natural Systems. In D. E. Moser, F. Corfu, J. R. Darling, S. M. Reddy, & K. Tait (Eds.), *Microstructural Geochronology: Planetary Records Down to Atom Scale* (1st ed., pp. 3–33).

Condon, D. J., Schoene, B., McLean, N. M., Bowring, S. A., & Parrish, R. R. (2015). Metrology and traceability of U-Pb isotope dilution geochronology (EARTHTIME Tracer Calibration Part I). *Geochimica et Cosmochimica Acta*, *164*, 464–480. https://doi.org/10.1016/j.gca.2015.05.026

Cooper, K. M. (2015). Timescales of crustal magma reservoir processes: Insights from U-series crystal ages. *Geological Society Special Publication*, *422*(1), 141–174. https://doi.org/10.1144/SP422.7

Gerstenberger, H., & Haase, G. (1997). A highly effective emitter substance for mass spectrometric Pb isotope ratio determinations. *Chemical Geology*, *136*(3–4), 309–312. https://doi.org/http://dx.doi.org/10.1016/S0009-2541(96)00033-2

Hilgen, F. J., Lourens, L. J., Van Dam, J. A., Beu, A. G., Boyes, A. F., Cooper, R. A., et al. (2012). *Chapter 29 - The Neogene Period*. *The Geologic Time Scale 2012 2-Volume Set*. https://doi.org/10.1016/B978-0-444-59425-9.00029-9

Jaffey, A. H., Flynn, K. F., Glendenin, L. E., Bentley, W. C., & Essling, A. M. (1971). Precision measurement of half-lives and specific activities of ^{235}U and ^{238}U. *Physical Review C*, *4*(5), 1889–1906. https://doi.org/10.1103/PhysRevC.4.1889

Johnson, J. A., Hawkesworth, C. J., Hooper, P. R., & Binger, G. Ben. (1998). *Major- and Trace-Element Analyses of Steens Basalt, Southeastern Oregon*.

Kasbohm, J. J., & Schoene, B. (2018). Rapid eruption of the Columbia River flood basalt and correlation with the mid-Miocene climate optimum. *Science Advances*, *4*(9), 1–8. https://doi.org/10.1126/sciadv.aat8223

Keller, C. B., Schoene, B., & Samperton, K. M. (2018). A stochastic sampling approach to zircon eruption age interpretation. *Geochemical Perspectives Letters*, 31–35. https://doi.org/10.7185/geochemlet.1826

Kochhann, K. G. D., Holbourn, A., Kuhnt, W., Channell, J. E. T., Lyle, M., Shackford, J. K., et al. (2016). Eccentricity pacing of eastern equatorial Pacific carbonate dissolution cycles during the Miocene Climatic Optimum. *Paleoceanography*, *31*(9), 1176–1192. https://doi.org/10.1002/2016PA002988

Krogh, T. E. (1973). A low-contamination method for hydrothermal decomposition of zircon and extraction of U and Pb for isotopic age determinations. *Geochimica et Cosmochimica Acta*, *37*(3), 485–494. https://doi.org/10.1016/0016-7037(73)90213-5

Mattinson, J. M. (2005). Zircon U-Pb chemical abrasion (“CA-TIMS”) method: Combined annealing and multi-step partial dissolution analysis for improved precision and accuracy of zircon ages. *Chemical Geology*, *220*(1–2), 47–66. https://doi.org/10.1016/j.chemgeo.2005.03.011

McLean, N. M., Bowring, J. F., & Bowring, S. A. (2011). An algorithm for U-Pb isotope dilution data reduction and uncertainty propagation. *Geochemistry, Geophysics, Geosystems*, *12*(6). https://doi.org/10.1029/2010GC003478

McLean, N. M., Condon, D. J., Schoene, B., & Bowring, S. A. (2015). Evaluating uncertainties in the calibration of isotopic reference materials and multi-element isotopic tracers (EARTHTIME Tracer Calibration Part II). *Geochimica et Cosmochimica Acta*, *164*, 481–501. https://doi.org/10.1016/j.gca.2015.02.040

Nier, A. O. (1950). A redetermination of the relative abundances of the isotopes of carbon, nitrogen, oxygen, argon, and potassium. *Physical Review*, *77*(6), 789–793. https://doi.org/10.1103/PhysRev.77.789

Ohneiser, C., Acton, G., Channell, J. E. T., Wilson, G. S., Yamamoto, Y., & Yamazaki, T. (2013). A middle Miocene relative paleointensity record from the Equatorial Pacific. *Earth and Planetary Science Letters*, *374*, 227–238. https://doi.org/10.1016/j.epsl.2013.04.038

Pälike, H., Frazier, J., & Zachos, J. C. (2006). Extended orbitally forced palaeoclimatic records from the equatorial Atlantic Ceara Rise. *Quaternary Science Reviews*, *25*(23–24), 3138–3149. https://doi.org/10.1016/j.quascirev.2006.02.011

Reidel, S. P., Camp, V. E., Martin, B. S., Tolan, T. L., & Wolff, J. A. (2016). The Columbia River Basalt Group of western Idaho and eastern Washington-Dikes, vents, flows, and tectonics along the eastern margin of the flood basalt province. In R. S. Lewis & K. L. Schmidt (Eds.), *Exploring the Geology of the Inland Northwest: Geological Society of America Field Guide 41* (pp. 127–150). https://doi.org/10.1130/2016.0041(04)

Renne, P. R., Swisher, C. C., Deino, A. L., Karner, D. B., Owens, T. L., & DePaolo, D. J. (1998). Intercalibration of standards, absolute ages and uncertainties in 40Ar/39Ar dating. *Chemical Geology*, *145*(1–2), 117–152. https://doi.org/10.1016/S0009-2541(97)00159-9

Samperton, K. M., Schoene, B., Cottle, J. M., Keller, C. B., Crowley, J. L., & Schmitz, M. D. (2015). Magma emplacement, differentiation and cooling in the middle crust: Integrated zircon geochronological-geochemical constraints from the Bergell Intrusion, Central Alps. *Chemical Geology*, *417*, 322–340. https://doi.org/10.1016/j.chemgeo.2015.10.024

Schoene, B., Crowley, J. L., Condon, D. J., Schmitz, M. D., & Bowring, S. A. (2006). Reassessing the uranium decay constants for geochronology using ID-TIMS U-Pb data. *Geochimica et Cosmochimica Acta*, *70*(2), 426–445. https://doi.org/10.1016/j.gca.2005.09.007

Schoene, B., Samperton, K. M., Eddy, M. P., Keller, G., Adatte, T., Bowring, S. A., et al. (2015). U-Pb geochronology of the Deccan Traps and relation to the end-Cretaceous mass extinction. *Science*, *347*(6218), 182–184. https://doi.org/10.1126/science.aaa0118

Stelten, M. E., Cooper, K. M., Vazquez, J. A., Calvert, A. T., & Glessner, J. J. G. (2015). Mechanisms and timescales of generating eruptible rhyolitic magmas at Yellowstone Caldera from Zircon and sanidine geochronology and geochemistry. *Journal of Petrology*, *56*(8), 1607–1642. https://doi.org/10.1093/petrology/egv047

Tolan, T. L., Martin, B. S., Reidel, S. P., Kauffman, J. D., Garwood, D. L., & Anderson, J. L. (2009). Stratigraphy and tectonics of the central and eastern portions of the

Columbia River Flood-Basalt Province: An overview of our current state of knowledge. *The Geological Society of America Field Guide*, *15*, 645–672. https://doi.org/10.1130/2009.fld015(29)

Table DR1: U-Pb Isotopic Data

	Dates (Ma)							Composition					Isotopic Ratios								
Sample	206Pb/ 238U	±2σ absolute	207Pb/ 235U	±2σ absolute	207Pb/ 206Pb	±2σ absolute	% disc	Pb* (pg)	Pbc (pg)	Pb*/ Pbc	Th/ U	Th/ U(magma)	206Pb/ 204Pb	208Pb/ 206Pb	206Pb/ 238U	±2σ %	207Pb/ 235U	±2σ %	207Pb/ 206Pb	±2σ %	Corr. coef.
zircon	a		b		a,b		c	d	e	f	g	h	i	j	j		j		j		
CRB1531																					
z7	16.128	0.031	16.32	0.41	44	60	72.4	1.70	0.28	6.05	0.24	1.26	418	0.08	0.0024912	0.190	0.0162039	2.553	0.0471954	2.499	0.317
z15	16.110	0.078	16.1	1.2	13	177	39.6	0.887	0.40	2.23	0.42	2.21	159	0.14	0.0024885	0.487	0.0159743	7.493	0.0465771	7.357	0.309
z32	16.185	0.084	17.1	1.3	143	172	89.7	1.07	0.25	4.24	0.44	2.32	283	0.14	0.0025001	0.523	0.0169512	7.565	0.0491961	7.310	0.514
z9	16.190	0.064	16.4	1.0	50	140	74.6	1.45	0.53	2.75	0.50	2.63	188	0.16	0.0025009	0.396	0.0163039	5.948	0.0473036	5.850	0.277
z25	16.20	0.13	16.5	2.0	66	292	79.5	1.74	1.37	1.28	0.43	1.58	99	0.14	0.0025046	0.819	0.0164320	12.450	0.0476042	12.255	0.269
z17	16.206	0.043	16.92	0.67	120	92	87.9	0.922	0.22	4.25	0.45	2.37	283	0.14	0.0025033	0.267	0.0168077	3.976	0.0487173	3.906	0.294
z21	16.217	0.060	16.25	0.87	21	128	53.7	0.967	0.31	3.09	0.43	2.26	212	0.14	0.0025051	0.373	0.0161364	5.420	0.0467383	5.307	0.334
z14	16.264	0.033	16.39	0.46	35	67	67.0	2.18	0.35	6.29	0.80	4.21	377	0.26	0.0025124	0.202	0.0162799	2.825	0.0470170	2.775	0.278
z1	16.277	0.046	16.45	0.67	41	96	70.6	1.76	0.44	4.02	0.48	2.53	267	0.15	0.0025144	0.284	0.0163342	4.087	0.0471370	4.012	0.295
z11	16.450	0.045	16.89	0.40	80	56	82.5	2.93	0.40	7.33	0.49	2.58	470	0.16	0.0025414	0.277	0.0167771	2.416	0.0479012	2.354	0.278
z13	16.49	0.11	16.9	1.7	74	239	81.2	1.89	1.22	1.55	0.46	2.42	115	0.15	0.0025478	0.683	0.0167747	10.210	0.0477739	10.048	0.267
z30	16.51	0.10	16.5	1.6	12	225	35.5	0.723	0.41	1.78	0.44	2.32	130	0.14	0.0025499	0.626	0.0163611	9.524	0.0465561	9.349	0.311
z18	16.62	0.10	17.6	1.5	160	196	90.4	0.379	0.20	1.92	0.47	2.47	137	0.15	0.0025672	0.587	0.0175315	8.534	0.0495511	8.352	0.341
z22	16.750	0.025	16.79	0.32	22	45	53.1	4.09	0.46	8.86	0.55	2.89	556	0.18	0.0025880	0.152	0.0166753	1.904	0.0467524	1.866	0.287
z16	16.803	0.056	16.82	0.53	19	75	47.9	1.86	0.23	8.08	0.44	2.32	525	0.14	0.0025963	0.335	0.0167046	3.151	0.0466849	3.117	0.152
CRB1523																					
z7	16.177	0.052	15.82	0.79	-38	120	167.2	1.78	0.53	3.38	0.50	2.63	227	0.16	0.0024989	0.327	0.0157086	5.000	0.0456118	4.920	0.275
z29	16.11	0.12	15.7	1.9	-52	297	142.6	1.08	0.84	1.29	0.31	1.68	103	0.10	0.0024890	0.776	0.0155578	12.371	0.0453550	12.188	0.265
z2	16.14	0.18	15.6	2.8	-66	428	131.1	0.848	0.91	0.93	0.42	2.21	77	0.14	0.0024925	1.099	0.0154905	17.758	0.0450945	17.515	0.250
z1	16.16	0.11	15.6	1.7	-70	269	128.7	1.21	0.82	1.46	0.36	1.89	112	0.11	0.0024969	0.696	0.0154899	11.150	0.0450126	10.988	0.263
z10	16.227	0.063	16.0	1.0	-11	143	-385.2	1.52	0.58	2.64	0.32	1.68	189	0.10	0.0025067	0.390	0.0159363	6.043	0.0461298	5.937	0.302
z13	16.234	0.042	16.63	0.60	74	85	81.6	1.69	0.39	4.37	0.40	2.11	295	0.13	0.0025077	0.258	0.0165143	3.623	0.0477838	3.559	0.281
z41	16.252	0.028	16.41	0.33	40	48	69.6	2.89	0.37	7.89	0.36	1.89	523	0.12	0.0025105	0.175	0.0162960	2.050	0.0470994	2.005	0.299
z39	16.266	0.047	16.26	0.65	16	95	44.8	1.01	0.25	4.00	0.32	1.68	278	0.10	0.0025128	0.291	0.0161487	4.023	0.0466317	3.941	0.312
z19	16.28	0.13	17.5	2.1	186	279	91.9	0.497	0.40	1.25	0.36	1.89	98	0.12	0.0025145	0.839	0.0173651	12.213	0.0501095	11.978	0.311
z47	16.280	0.029	16.25	0.37	12	54	37.2	1.76	0.22	7.82	0.41	2.16	512	0.13	0.0025149	0.178	0.0161386	2.267	0.0465629	2.228	0.254
z43	16.288	0.060	17.0	1.0	118	131	87.7	0.931	0.33	2.83	0.31	1.63	202	0.10	0.0025162	0.372	0.0168834	5.638	0.0486873	5.556	0.252
z51	16.328	0.064	16.60	0.97	57	136	76.9	0.887	0.31	2.88	0.31	1.63	205	0.10	0.0025224	0.396	0.0164914	5.858	0.0474401	5.718	0.384
z32	16.39	0.13	16.0	2.0	-44	297	154.5	0.663	0.51	1.31	0.27	1.42	105	0.09	0.0025324	0.777	0.0158795	12.424	0.0454992	12.212	0.302
z49	16.426	0.088	16.6	1.3	41	179	70.0	3.18	1.53	2.08	0.32	1.68	153	0.10	0.0025376	0.545	0.0164811	7.617	0.0471247	7.480	0.285
z5	16.433	0.026	16.44	0.37	18	54	48.3	4.01	0.49	8.17	0.37	1.95	539	0.12	0.0025388	0.158	0.0163315	2.263	0.0466759	2.244	0.155
z52	16.46	0.12	18.5	1.7	294	208	94.7	0.462	0.26	1.80	0.35	1.84	134	0.11	0.0025427	0.749	0.0183993	9.431	0.0525054	9.117	0.452
z42	16.48	0.11	17.2	1.6	117	221	87.4	0.802	0.49	1.64	0.27	1.42	126	0.09	0.0025463	0.706	0.0170762	9.568	0.0486599	9.370	0.315
z35	16.522	0.062	16.64	0.92	34	132	65.2	1.39	0.47	2.94	0.42	2.21	204	0.13	0.0025526	0.376	0.0165273	5.596	0.0469805	5.499	0.290
CRB1606																					
z9	16.220	0.038	16.18	0.55	11	80	34.1	2.18	0.46	4.72	0.40	2.16	317	0.13	0.0025055	0.238	0.0160697	3.398	0.0465377	3.338	0.284
z15	16.213	0.076	15.7	1.1	-54	176	139.8	1.06	0.47	2.26	0.41	2.16	161	0.13	0.0025045	0.471	0.0156361	7.340	0.0453011	7.226	0.272
z7	16.216	0.051	15.84	0.76	-40	115	161.1	2.18	0.62	3.54	0.49	2.58	237	0.16	0.0025050	0.317	0.0157311	4.803	0.0455661	4.724	0.281
z22	16.220	0.050	16.03	0.74	-13	111	-1707.4	1.98	0.57	3.49	0.40	2.11	239	0.13	0.0025056	0.310	0.0159131	4.662	0.0460833	4.587	0.274
z30	16.240	0.036	16.10	0.50	-5	74	-75.0	6.33	1.19	5.31	0.50	2.63	345	0.16	0.0025087	0.221	0.0159885	3.127	0.0462431	3.074	0.274
z8	16.272	0.087	16.0	1.3	-20	199	346.3	1.46	0.71	2.05	0.61	3.21	141	0.19	0.0025136	0.541	0.0159148	8.334	0.0459409	8.204	0.271
z34	16.272	0.030	16.26	0.35	14	50	42.9	1.61	0.18	8.70	0.46	2.52	559	0.15	0.0025135	0.187	0.0161469	2.155	0.0466124	2.088	0.394
z2	16.322	0.080	15.5	1.3	-115	198	116.1	2.14	1.01	2.12	0.41	2.16	153	0.13	0.0025215	0.495	0.0153568	8.164	0.0441915	8.039	0.281
z16	16.328	0.066	16.30	0.98	13	143	38.1	2.31	0.73	3.16	0.95	5.00	192	0.31	0.0025224	0.409	0.0161900	6.082	0.0465719	5.962	0.323
z6	16.340	0.041	16.33	0.59	15	85	44.1	1.56	0.34	4.63	0.37	1.95	314	0.12	0.0025242	0.253	0.0162203	3.625	0.0466264	3.551	0.325
z5	16.36	0.12	16.0	1.8	-43	271	156.4	0.987	0.67	1.47	0.43	2.26	111	0.14	0.0025276	0.712	0.0158569	11.301	0.0455200	11.130	0.270
z36	16.363	0.070	17.76	0.88	211	112	92.7	1.23	0.30	4.15	0.53	2.79	271	0.17	0.0025278	0.434	0.0176500	4.983	0.0506627	4.829	0.394
z19	16.481	0.080	16.5	1.2	23	178	55.4	1.67	0.80	2.08	0.33	1.79	153	0.11	0.0025461	0.492	0.0164139	7.520	0.0467768	7.408	0.259
z13	16.519	0.093	16.8	1.5	51	206	74.4	1.15	0.65	1.78	0.34	1.79	133	0.11	0.0025521	0.571	0.0166423	8.745	0.0473162	8.613	0.263
z40	16.521	0.036	16.77	0.37	53	52	75.3	2.29	0.32	7.23	0.36	1.89	480	0.12	0.0025525	0.220	0.0166622	2.242	0.0473660	2.189	0.285
z4	16.535	0.059	16.42	0.89	0	129	-20.1	2.24	0.76	2.95	0.39	2.05	205	0.13	0.0025545	0.358	0.0163106	5.436	0.0463289	5.352	0.265
z28	16.559	0.062	16.26	0.94	-28	139	212.0	2.66	0.99	2.68	0.25	1.32	195	0.08	0.0025583	0.378	0.0161436	5.806	0.0457865	5.716	0.269
z33	16.571	0.049	16.40	0.66	-8	96	-198.2	1.07	0.26	4.10	0.29	1.53	285	0.09	0.0025603	0.298	0.0162920	4.036	0.0461720	3.966	0.269
CRB1636																					
z14	16.379	0.023	16.40	0.26	19	38	50.0	2.03	0.20	10.01	0.32	1.68	665	0.10	0.0025304	0.138	0.0162844	1.624	0.0466955	1.586	0.312
z9	16.399	0.053	15.83	0.79	-70	122	128.9	2.16	0.61	3.54	0.66	3.47	228	0.21	0.0025335	0.327	0.0157147	5.058	0.0450073	4.981	0.267
z8	16.406	0.059	16.31	0.88	2	128	-2.7	1.46	0.50	2.93	0.33	1.74	208	0.11	0.0025346	0.363	0.0161980	5.421	0.0463713	5.328	0.287
z27	16.423	0.074	16.2	1.1	-14	168	3643.8	1.92	0.85	2.26	0.34	1.79	164	0.11	0.0025372	0.455	0.0161049	7.046	0.0460574	6.938	0.269
z5	16.429	0.060	15.94	0.91	-57	138	137.6	1.48	0.51	2.91	0.37	1.95	204	0.12	0.0025380	0.369	0.0158267	5.760	0.0452467	5.659	0.303
z17	16.442	0.031	16.53	0.40	29	56	61.4	2.57	0.39	6.65	0.29	1.53	452	0.09	0.0025402	0.191	0.0164142	2.415	0.0468864	2.353	0.359
z16	16.47	0.11	16.9	1.7	81	237	82.6	0.720	0.46	1.55	0.34	1.79	118	0.11	0.0025439	0.698	0.0168014	10.166	0.0479224	9.997	0.274
z25	16.470	0.086	17.2	1.3	117	180	87.4	0.462	0.23	2.01	0.34	1.79	147	0.11	0.0025444	0.528	0.0170612	7.756	0.0486534	7.612	0.304
z34	16.514	0.088	17.3	1.4	131	194	88.6	0.512	0.26	1.95	0.37	1.95	143	0.12	0.0025513	0.536	0.0172135	8.409	0.0489558	8.262	0.303

z38	16.528	0.024	17.08	0.22	96	31	84.9	2.59	0.22	11.97	0.26	1.37	805	0.08	0.0025535	0.143	0.0169700	1.326	0.0482220	1.287	0.320
z35	16.556	0.032	16.93	0.41	70	57	80.3	1.33	0.20	6.63	0.40	2.11	438	0.13	0.0025577	0.191	0.0168160	2.455	0.0477047	2.398	0.333
z7	16.583	0.027	16.72	0.34	36	48	66.9	2.20	0.28	8.00	0.40	2.11	524	0.13	0.0025621	0.160	0.0166071	2.025	0.0470322	1.984	0.285
CRB1640																					
z24	16.41	0.11	16.1	1.6	-30	246	199.0	0.714	0.43	1.65	0.55	2.89	119	0.18	0.0025353	0.655	0.0159867	10.310	0.0457526	10.152	0.271
z3	16.43	0.11	15.9	1.7	-70	259	129.1	0.549	0.33	1.64	0.59	3.11	117	0.19	0.0025381	0.667	0.0157440	10.775	0.0450099	10.613	0.272
z2	16.47	0.16	16.0	2.4	-53	368	142.0	0.851	0.76	1.11	0.53	2.79	87	0.17	0.0025446	0.959	0.0158967	15.318	0.0453296	15.089	0.268
z12	16.50	0.16	17.0	2.5	87	347	83.7	0.865	0.78	1.10	0.59	3.11	85	0.19	0.0025485	0.985	0.0168759	14.852	0.0480489	14.619	0.268
z27	16.55	0.17	17.1	2.6	95	361	84.9	0.291	0.27	1.07	0.52	2.74	84	0.17	0.0025563	1.013	0.0169859	15.498	0.0482130	15.241	0.285
z15	16.59	0.17	17.7	2.6	166	340	90.8	0.668	0.61	1.10	0.50	2.63	86	0.16	0.0025637	1.035	0.0175560	14.836	0.0496888	14.549	0.309
CRB1611																					
z5	16.58	0.15	16.6	2.4	17	350	46.68	0.771	0.69	1.12	0.48	2.47	88	0.153	0.002562	0.94	0.0165	15	0.0467	15	0.276
z14	16.57	0.17	16.2	2.6	-36	383	172.75	0.513	0.46	1.11	0.49	2.58	87	0.157	0.002561	1.0	0.0161	16	0.0456	16	0.322
z1	16.59	0.22	16.8	3.5	51	490	74.20	0.480	0.62	0.77	0.48	2.53	66	0.153	0.002563	1.4	0.0167	21	0.0473	21	0.255

a Corrected for initial Th/U disequilibrium using radiogenic 208Pb and Th/U[magma] specified.
b Corrected for initial Pa/U disequilibrium using initial fraction activity ratio [231Pa]/[235U] = 1.10000.
c % discordance = 100 - (100 * (206Pb/238U date) / (207Pb/206Pb date))
d Total mass of radiogenic Pb.
e Total mass of common Pb.
f Ratio of radiogenic Pb (including 208Pb) to common Pb.
g Th contents calculated from radiogenic 208Pb and 230Th-corrected 206Pb/238U date of the sample, assuming concordance between U-Pb Th-Pb systems.
h Th/U ratio of magma from which mineral crystallized.
i Measured ratio corrected for fractionation and spike contribution only.
j Measured ratios corrected for fractionation, tracer and blank. Values for ET535 are found in Condon et al. (2015) and McLean et al. (2015). Blank model values are as follows:

206Pb/204Pb	18.628271±0.317714
207Pb/204Pb	15.796256±0.232017
208Pb/204Pb	38.535874±0.375848

Chapter 5

High-precision U-Pb zircon geochronology of the Miocene Bisciaro Formation, Contessa Section, Italy: A case study for requisite radiometric calibration of bio- and magnetostratigraphy

---

This will be submitted to a journal with authors J. Kasbohm, B. Schoene, and A. Montanari

---

ABSTRACT

The Contessa section near Gubbio, Italy has yielded numerous insights into Cenozoic Earth history. The deposition of bentonite layers containing zircon in the uppermost, Miocene portion of the section allows for the acquisition of absolute, high-precision ages through U-Pb zircon geochronology. Here, we present four ages from the Contessa – Il Testimone section, which revise prior ^{40}Ar/^{39}Ar geochronology and provide new age constraints on the Bisciaro Formation. We find that the section was deposited between ~22.3 and 20.1 Ma, with a hiatus lasting ~1 Ma in the lower Bisciaro. Our results suggest that biostratigraphic data may be skewed by absence of foraminifera following their

regional first occurrence and preceding their last occurrence, as a result of poor preservation. Additionally, prior magnetostratigraphy overestimated the number of magnetic field reversals due to unreliable data. Given these inconsistencies and the presence of hiatuses in the section, we reject the recent suggestion that the Contessa section could serve as the Burdigalian Global Stratigraphic Section and Point. We suggest that wherever possible, absolute geochronology should be used to calibrate sedimentary sections, as a way to verify the accuracy of age models based on biostratigraphy, magnetostratigraphy, and astronomical tuning.

INTRODUCTION

The Contessa section (Gubbio, Italy), is noteworthy for its nearly continuous sedimentary record of Cenozoic Earth history. Spanning the Jurassic to the Miocene, this section contains the 'Selli' and 'Bonarelli' black shales from which the Createaceous Oceanic Anoxic Events were inferred, hyperthermal events in the early Paleogene and middle Eocene, and sedimentary evidence for intervals of tectonic activity in the Mediterranean (Montanari et al., 1997). Numerous bio-, chemo-, and magnetostratigraphic studies have been performed on this section (Coccioni et al., 2010; Jovane et al., 2007), and many portions of the section have been calibrated in age by astronomical tuning (Galeotti et al., 2010; Jovane et al., 2010).

The Early Miocene Bisciaro Formation, near the top of the Contessa section, is noteworthy for its quantity of volcaniclastic layers that are interbedded with marly and glauconitic limestone. This unit is interpreted as representing the transition from pelagic carbonate deposition to siliciclastic turbidite deposition in the Apennine foredeep, concurrent with a pulse of calc-alkaline intermediate volcanism elsewhere in the Mediterranean (Guerrera et al., 2015; Montanari et al., 1997). Because the volcaniclastic layers contained biotite and plagioclase suitable for dating through $^{40}Ar/^{39}Ar$ geochronology, the Bisciaro was the included in an integrated study of the Early Miocene Contessa-Il Testimone (CT) portion of section that combined $^{40}Ar/^{39}Ar$ geochronology, biostratigraphy, chemostratigraphy, and magnetostratigraphy (Montanari et al., 1997). While astronomical tuning has not yet been successfully performed in the CT section, due to at least three documented hiatuses, the presence of bentonitic layers and advances in radiometric dating encourage an absolute calibration of magnetostratigraphic and biostratigraphic data produced from the 21 m exposed of this section.

Prior $^{40}Ar/^{39}Ar$ geochronology from the CT section yielded ages of 21.88±0.32 Ma and 19.67±0.30 Ma through incremental heating of plagioclase separates. Paleomagnetic and biostratigraphic study suggested that nearly 5 Ma was represented in the CT and overlying CV section, from 22-17 Ma (Montanari et al., 1997). Here, we use high-precision U-Pb CA-ID-TIMS geochronology to produce four new bentonite ages from the CT section. We show that this section represents only 2 Ma of deposition, including an ~1 Ma hiatus. We suggest that the paleomagnetic and biostratigraphic data obtained for this carbonate section may be unreliable, as a result of magnetic mineralogy and poor foraminiferal preservation. Even with our new high-precision geochronology, we reject the recent suggestion of Fabbrini et al. (2019) that the Aquitanian-Burdigalian GSSP (Global Stratotype Section and Point) be placed in the Contessa section, because of these numerous inconsistencies when integrated stratigraphy is attempted. Our work shows the importance of absolute radiometric calibration of sedimentary records, to ground truth bio- and magnetostratigraphy and to more accurately determine the timing and tempo of changes in Earth's climatic and tectonic history.

METHODS

Geochronology samples were collected from the CT section in September 2018 (Figure 1). The geochronology methods below are as described in Kasbohm & Schoene (2018), Schoene *et al.* (2015) and Samperton *et al.* (2015).

Zircon separation and preparation

Zircons were separated from their host rock through standard methods of crushing, gravimetric-, and magnetic-separation techniques using a blender, shatterbox, hand pan, hand magnet, Frantz isodynamic separator, and methylene iodide. Zircons from the least magnetic and most dense mineral separate were transferred in bulk to quartz crucibles and annealed in a muffle furnace at 900°C for 48 hours after Mattinson (Mattinson, 2005). After annealing, 20-40 zircon grains from each sample were photographed (Figure 2) and picked in reagent-grade ethanol for analysis. Given the low radiogenic Pb content of the samples, cathodoluminescence images were not obtained. Euhedral grains with a range of morphologies were selected, while those with visible cracks, inclusions, and cores were avoided. Individual grains were transferred using stainless steel picking tools to separate 3-mL Savillex Hex beakers containing distilled acetone and taken to the clean lab for analysis.

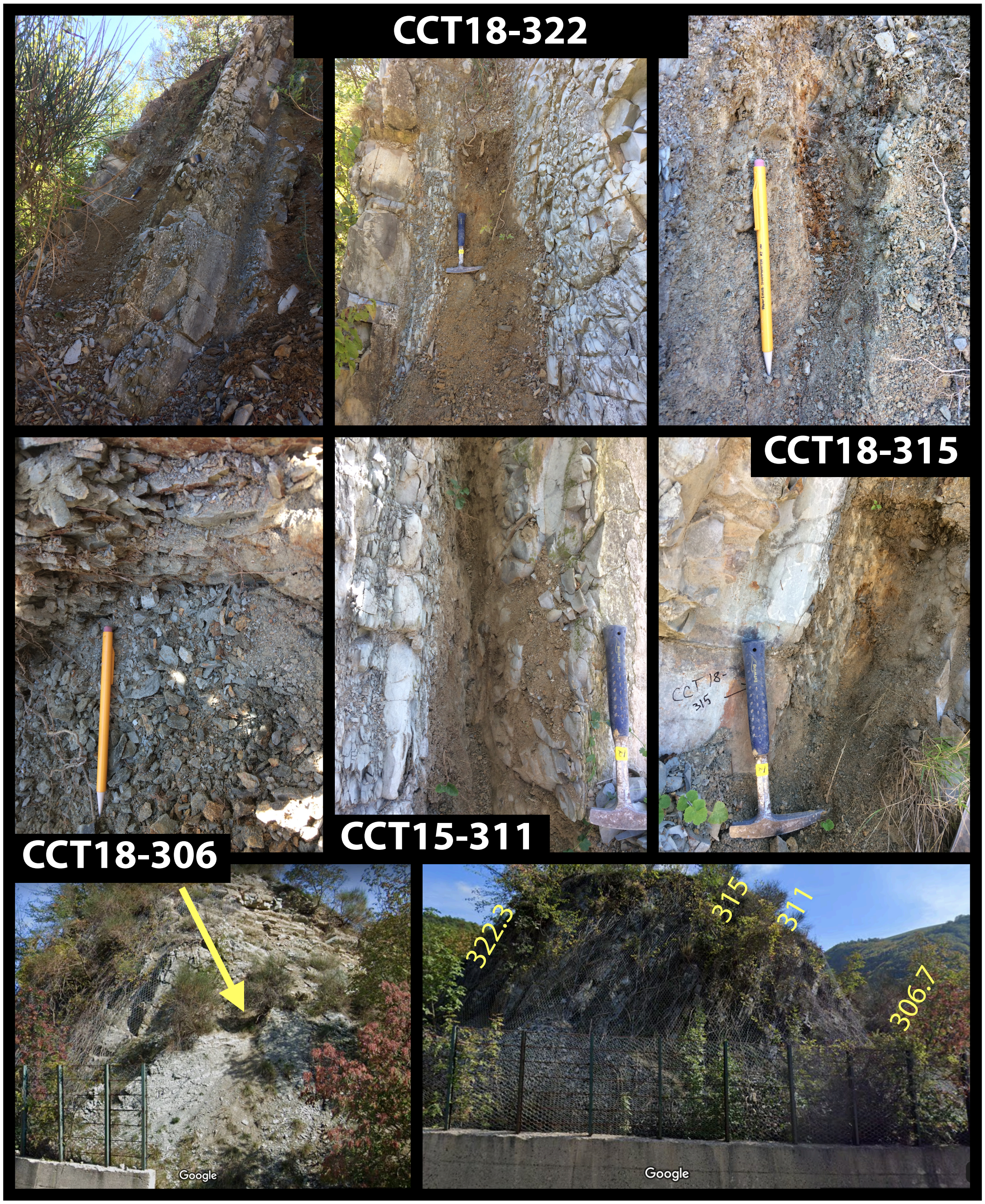

Figure 1: Contessa section outcrop photos. Photos of geochronology samples are provided and labeled in the top two rows, with hammer or pencil for scale (Photo credit: Jennifer Kasbohm). The bottom row shows the position of each sample at outcrop scale (Photo credit: Google Street View).

U-Pb zircon ID-TIMS analysis

Single zircon grains were loaded into 200 uL Savillex "micro"-capsules with 100 μL 29 M HF + 15 μL 3N HNO_3 for a single leaching step in high-pressure Parr bombs at 185°C for 12 h to remove crystal domains affected by Pb loss (Mattinson, 2005). Grains were rinsed post-leaching in 6 N HCl, MQ H2O, 3N HNO_3, and 29 M HF prior to spiking with EARTHTIME ^{205}Pb-^{233}U-^{235}U tracer and addition of 100uL 29 M HF + 15 μL 3N HNO_3 (Condon et al., 2015; McLean et al., 2015). Zircons were then dissolved to completion in Parr bombs at 210°C for 48 h. Dissolved zircon solutions were subsequently dried down, dissolved in 100 μL 6N HCl, and converted to chlorides in Parr bombs at 185°C for 12 h, after which solutions were dried again and brought up in 50 μL 3N HCl. The U-Pb and trace element aliquots were then separated by anion exchange chromatography using 50 μL columns and AG-1 X8 resin (200-400 mesh, chloride from Eichrom) (Krogh, 1973), and dried down with a microdrop of 0.015 M H_3PO_4. The dried U and Pb aliquot was loaded in a silica gel emitter (Gerstenberger & Haase, 1997) to an outgassed zone-refined Re filament.

Isotopic determinations were performed using an IsotopX PhoeniX-62 thermal ionization mass spectrometer (TIMS) at Princeton University, with Pb analysis performed in peak-hopping mode on a Daly-photomultiplier ion-counting detector. A correction for mass-dependent Pb fractionation was applied using a Pb fractionation of 0.182±0.041%/amu, as determined by repeat measurements of NBS982 at Princeton. A Daly-photomultiplier deadtime of 28.8 ns was used, as determined by repeat measurements of NBS standards. Corrections for interfering isotopes under masses 202, 204, and 205 were made cycle-by-cycle by measuring masses 201 and 203 and assuming they represent $^{201}BaPO_4$ and ^{203}Tl and using natural isotopic abundances to correct for $^{202}BaPO_4$, $^{204}BaPO_4$, $^{205}BaPO_4$, and ^{205}Tl.

UO_2 measurements were performed in static mode on Faraday cups with a bulk U fractionation correction calculated from the deviation of measured $^{233}U/^{235}U$ from the known tracer $^{233}U/^{235}U$ (0.995062±0.000054 (1σ)), and an oxide composition of $^{18}O/^{16}O$ of 0.00205 was used (Nier, 1950). Data reduction was performed using the programs Tripoli and U-Pb Redux (Bowring et al., 2011; McLean et al., 2011) and the decay constants of Jaffey *et al.* (1971). All Pbc was attributed to laboratory blank with a mean isotopic composition determined by total procedural blank measurements (see Table DR1 for values). Uncertainties in reported U-Pb zircon dates are at the 95% confidence level and exclude tracer calibration and decay constant uncertainties. Correction for initial ^{230}Th disequilibrium in the $^{206}Pb/^{238}U$ system was made on a fraction-by-fraction basis by estimating $(Th/U)_{magma}$ using $(Th/U)_{zircon}$ determined by TIMS and a mean $(Th/U)_{zircon\text{-}magma}$ partition coefficient ratio of 0.19±0.11, which encompasses the range of values for $(Th/U)_{zircon\text{-}magma}$ partition coefficients obtained from glasses from a variety of volcanic settings (Claiborne et al., 2018). Uncertainties for the resulting $(Th/U)_{magma}$ were also calculated on a fraction-by-fraction basis, propagating the uncertainty in the $(Th/U)_{zircon\text{-}magma}$ partition coefficient. U-Pb data from each analysis is provided in Table 1.

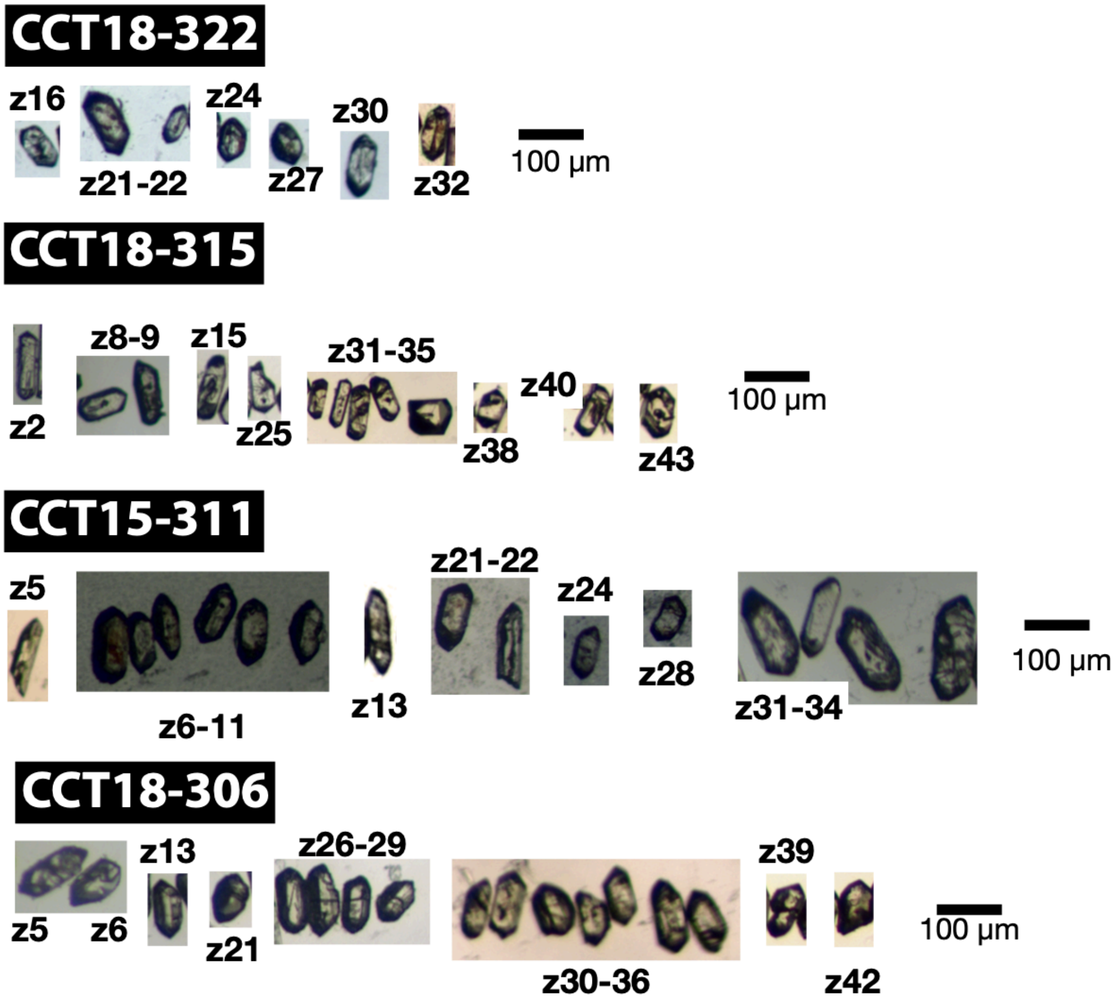

Figure 2: Zircon photos. The zircons yielding dates from each geochronology sample are shown here, exhibiting magmatic morphologies (Photo credit: Jennifer Kasbohm).

RESULTS

Sample descriptions

Outcrop photos of each sample are shown in Figure 1, and zircon images are displayed in Figure 2. Sample CCT18-306 was collected from section height 306.7 m, from the "Livello Raffaello." With a thickness up to 40 cm, the Rafaello is a regional marker bed in the Umbria-Marche basin because it is the first volcaniclastic horizon in the Miocene, found just above the contact with the underlying Scaglia Cinerea (Guerrera et al., 2015).

At the CT section, the sample consists of 18 cm of bentonite, and it is thicker and more lithified than the other samples collected in this study; some excavation of a thin layer of recent cover was required to collect the sample. Zircons separated were ~100 µm in length, euhedral, blocky, and prismatic, with pronounced terminations.

Sample CCT15-311 was collected from a stratigraphic height of 311.3 m, from a horizon also referred to as "CT-WAL" (Montanari et al., 1997). This bentonitic horizon is 15 cm thick, and is noted for the presence of biotite. This sample, as well as the following two bentonites, is recessed from the outcrop relative to the more resistant limestones on other side. Zircons extracted from this sample were euhedral and prismatic, and ranged in morphology from small (~100 µm) and equant to nearly 200 µm and blocky, with a few thin grains.

Sample CCT18-315 was collected at height 315 m, and is ~10 cm thick. The bentonite was somewhat orange in color. Zircons dated from this sample were euhedral and prismatic, with pronounced terminations.

Sample CCT18-322 was collected at height 322.2 m, and is 40 cm thick. The bentonite was not well lithified, and exhibited discontinuous streaks of orange. It is the last volcaniclastic horizon in the CT section, just 50 cm below the end of the outcrop. Zircons separated from this sample were euhedral, blocky, and 50-100 µm in length.

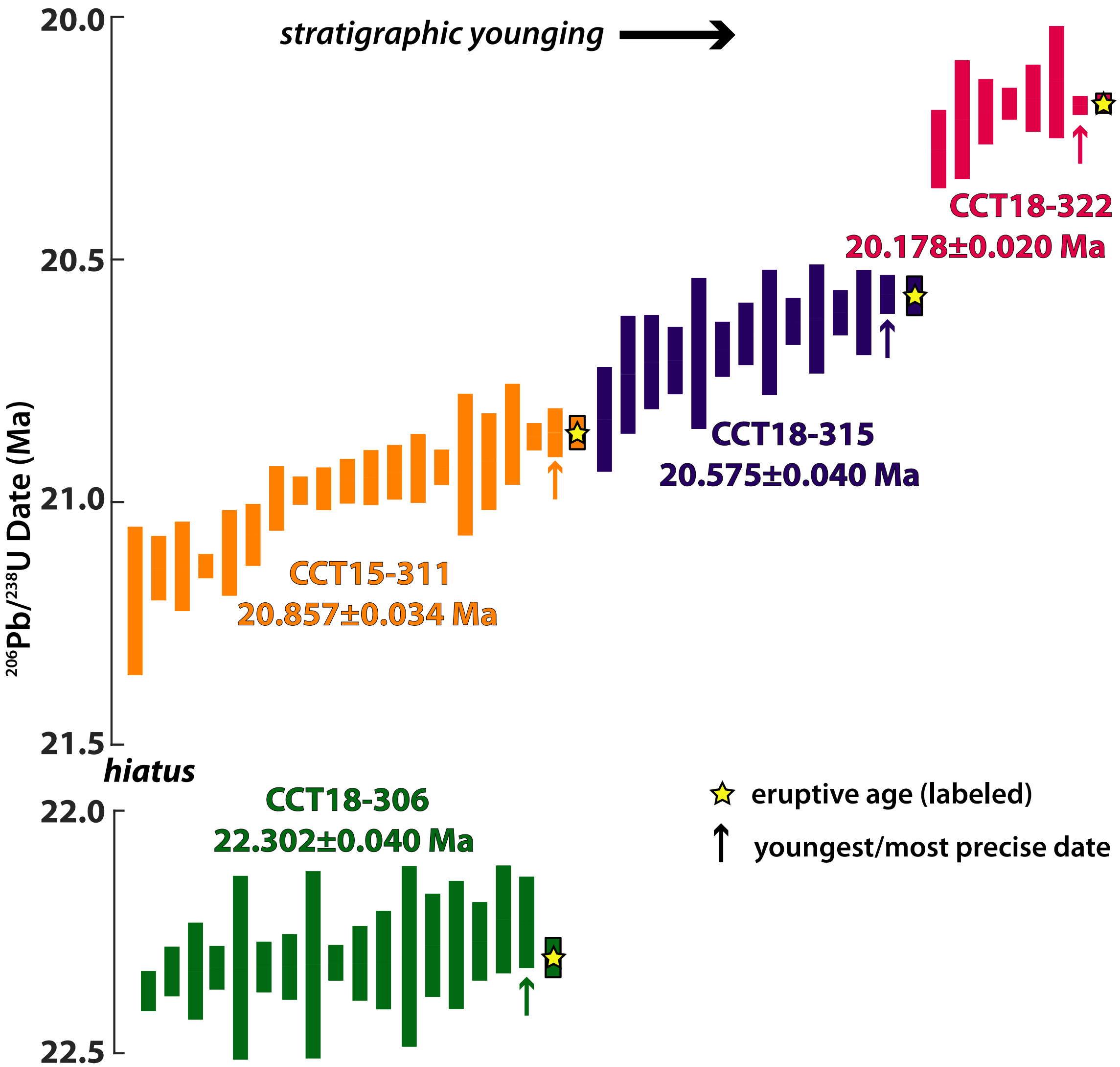

Figure 3: Weighted mean plots. 206Pb/238U dates from each geochronology sample are plotted here, with stratigraphic younging of the younger three samples from left to right. Arrows indicate the youngest and most precise single analysis, and stars and labels show eruptive ages calculated from each sample, which we highlight as our preferred interpretation.

Sample ages

Individual zircon ^{206}Pb/^{238}U dates from these four samples are shown in Figure 3, with 95% confidence intervals, and Concordia plots for each sample are found in Figure 4; each analysis overlaps with the Concordia line, indicating closed-system behavior. Within each sample, dates spread beyond analytical uncertainty, most likely as a result of

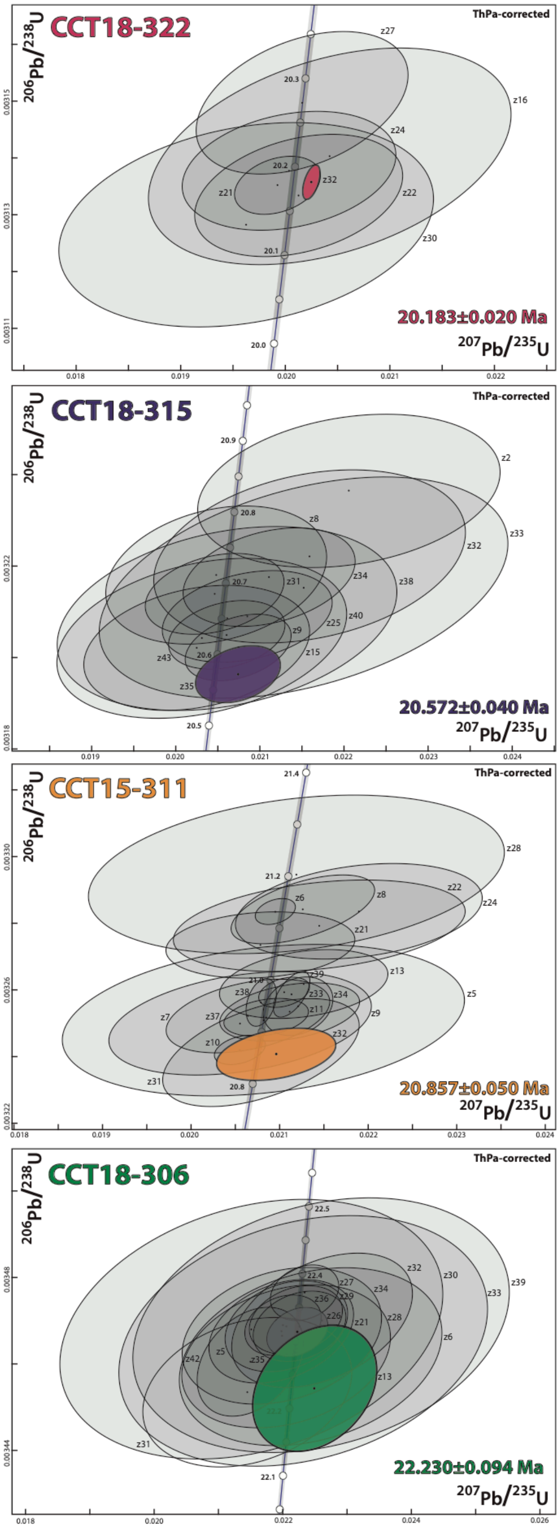

Figure 4: Concordia plots. Concordia plots from each sample are shown here, with the youngest and most precise analysis highlighted and labeled. Intersection with the Concordia line shows that the zircons crystallized in a closed system.

prolonged crystallization in the source magma, or inheritance of older grains from the volcanic edifice or host rock (Cooper, 2015; Stelten et al., 2015). For this reason, in Figure 3 we use arrows to point out the youngest and most precise age as one estimate for the age of each bentonite, and highlight these analyses in Figure 4. As an alternative approach to calculate eruptive ages from disperse datasets, zircon dates and uncertainties from each sample were incorporated into a Bayesian Monte Carlo Markov Chain (MCMC) model, which makes a probabilistic estimate of eruption age based on the dated population of grains from each sample (Keller et al., 2018). Since this approach eliminates all subjectivity and takes into account each zircon dated, we star and label these eruptive ages in Figure 3, and use these ages as our preferred interpretation for the age of each bentonite. However, we compare this interpretation to alternative approaches in Table 1, using youngest zircon or weighted mean ages, and we find that each interpretation produces overlapping ages. Thus, our chosen eruptive age interpretation does not affect the conclusions of this paper. Full U-Pb data is found in Table S1.

	Youngest Zircon					Weighted Means														Bayesian Eruptive Age with Bootstrapped Prior	
						Youngest Few Zircons							Maximum n allowed for MSWD ≈ 1								
			uncertainty			addtnl			uncertainty			MS	addtnl			uncertainty			MS		
sample	zircon	age	X	Y	Z	zircons	n	age	X	Y	Z	WD	zircons	n	age	X	Y	Z	WD	age	uncertainty
CCT18-306	z13	22.230	0.094	0.095	0.098	31,42	3	22.246	0.054	0.055	0.060	0.73	all	17	22.320	0.016	0.021	0.032	1.0	22.302	0.040
CCT15-311	z32	20.857	0.050	0.052	0.057	31,10	3	20.863	0.024	0.027	0.035	0.043	5,9	5	20.868	0.023	0.027	0.035	0.44	20.857	0.034
CCT18-315	z35	20.572	0.040	0.043	0.048	9,15	3	20.590	0.029	0.035	0.041	0.86	25,38,40,43	7	20.609	0.022	0.028	0.036	1.1	20.575	0.040
CCT18-322	z32	20.183	0.020	0.022	0.030	21,22,30	4	20.180	0.016	0.019	0.029	0.28	all	7	20.185	0.015	0.019	0.028	1.0	20.178	0.020
																				preferred interpretation	

Table 1: Alternate Age Interpretations. We compare our preferred eruptive age interpretation with other common ways to address complex zircon populations. All interpretations are internally consistent with little difference in age, showing that our selected interpretation will not affect the conclusions in this paper

We find that the Rafaello bed, sampled in CCT18-306, is aged 22.302±0.040 Ma, compared to 21.88±0.32 Ma obtained through the ^{40}Ar/^{39}Ar geochronology by Montanari et al. (1997) using a Fish Canyon sanidine standard age of 27.84 Ma (Cebula et al., 1986). This age can be recalculated to 22.16±0.3 Ma with an updated Fish Canyon sanidine age of 28.201 Ma (Kuiper et al., 2008). Next, CCT15-311 is found to be 20.857±0.34 Ma, compared to the age of 19.67±0.30 Ma formerly obtained for this horizon (Montanari et al., 1997), recalculated to 19.93±0.3 Ma (Kuiper et al., 2008). Our age for CCT15-315 is 20.575±0.040 Ma, and our age for CCT15-322, at the top of the CT section, is 20.178±0.20 Ma.

DISCUSSION

1. Zircon geochronology provides a new age model for the Miocene Contessa section

Based on the appearance of both rock samples and zircons, we agree with the interpretation of Guerrera et al. (2015) that deposition of Bisciaro Formation volcaniclastics in the CT section represents primary ash fall. To complement their analysis of the mineralogy of the bentonites, which showed 50-75% volcaniclastic supply with a low ratio of reworked to primary grains, we present evidence based on zircon geochronology. The zircons obtained from all four dated bentonite horizons are euhedral and prismatic, consistent with magmatic textures, with little evidence for rounding seen in alluvial or eolian grains (Figure 2). Additionally, the grains dated from each sample comprise fairly uniform age populations, with numerous individual analyses overlapping with our estimated eruptive ages. Our ages reflect stratigraphic order, younging in a clearly resolvable manner from bottom to the top of the section (Figure 3).

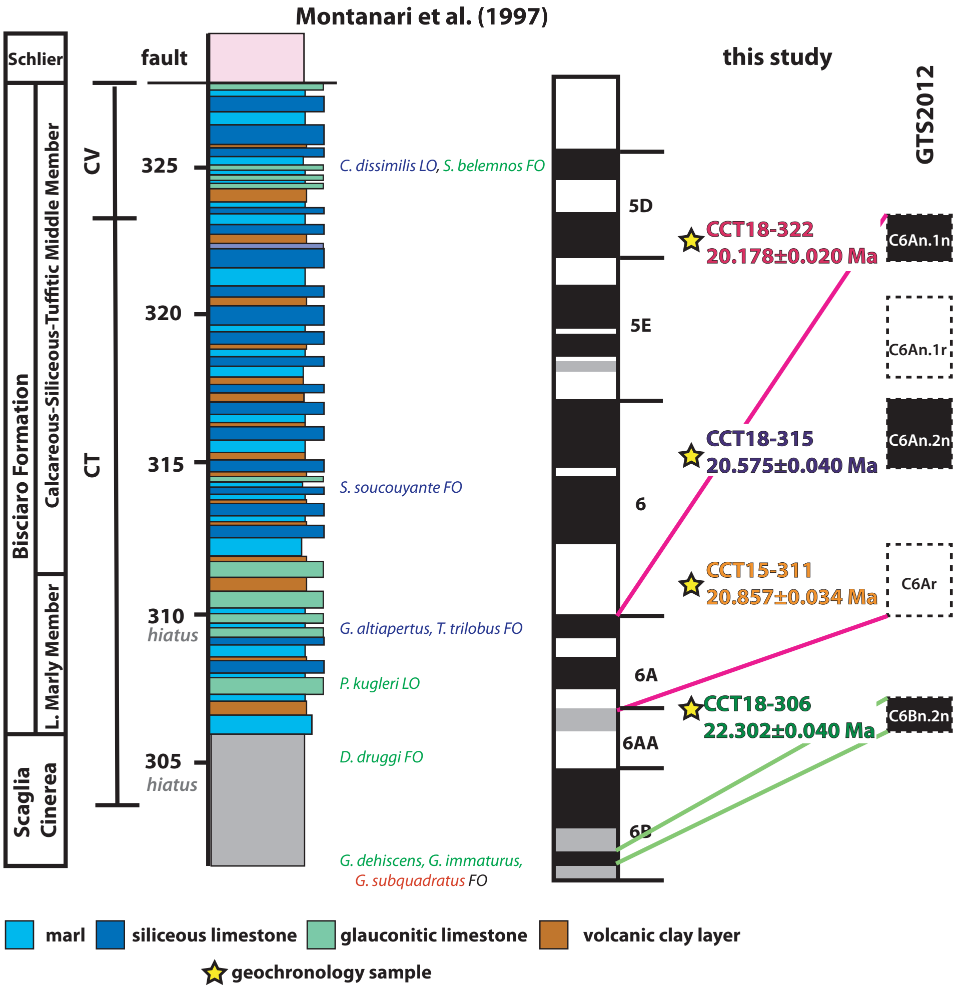

Figure 5: Summary of Contessa section stratigraphic data. The stratigraphic section, paleomagnetic, and biostratigraphic data of Montanari et al. (1997) is reproduced here, alongside our geochronology results. Our ages may be correlated to the Geomagnetic Polarity Timescale presented in Hilgen et al. (2012). We show that polarity chrons inferred match the polarity of samples obtained at each height, though this may be accidental. Biostratigraphic data are color coded in the following manner: green when consistent with our geochronology, blue when consistent with foraminiferal absence, and red when inconsistent with geochronology and absence.

Given the internal consistency of our U-Pb ages, we suggest that they be used to construct a new age model for the CT section. Our ages suggest that biostratigraphy and magnetostratigraphy previously obtained in the CT section (Montanari et al., 1997) overestimate the amount of time represented in the section. Rather than being deposited between 22 and 17 Ma, deposition occurred between ~22.3 and 20.2 Ma. With ~1.4 Ma elapsed between CCT18-306 and CCT15-315, our geochronology supports the biostratigraphic evidence for a substantial hiatus of ~1 Ma between these samples (Montanari et al., 1997).

We find that nearly all of the inconsistencies between our zircon ages and the prior bio-magnetostratigraphic calibration of the section can be resolved by foraminiferal absences and unreliable paleomagnetic data (Figure 5). While foraminiferal abundance and preservation in the Bisciaro Formation ranges from moderately good to very poor, at the CT section, foraminiferal preservation was poor due to recrystallization and deformation (Montanari et al., 1997). This may have led to the absence of foraminifera in the section subsequent to their regional first occurrence, or predating their expected last occurrence. For the most part, each biostratigraphic datum between our first and last geochronology samples either fits this pattern of absence, or falls where expected. We focus here primarily on the biostratigraphic data that falls between our geochronology samples, since we can provide older and younger bounding ages. We do note one exception to our absence hypothesis, in which the first occurrence of *G. subquadratus* occurs at 301.5 m, prior to our sample CCT18-306, dated to 22.3 Ma. However, this first occurrence is expected to be 21.09 Ma in the Mediterranean (Lirer et al., 2019). It is likely that sedimentary reworking may have allowed this species to be found before its anticipated first occurrence.

A number of foraminiferal boundaries are reported between CCT18-306 and CCT15-315, between 22.3 and 20.8 Ma. At 307.4 m, the last occurrence of *P. kugleri* is documented, which is expected to occur at 21.09 Ma in the Mediterranean, at the top of chron C6AA, based on sedimentation rate estimates from the Aquitanian GSSP section at Carrosio-Lemme, Italy (Lirer et al., 2019). This datum is consistent with our eruptive ages. Next, at 309.6 m, the first occurrences of *T. trilobus* and *G. altiaperturus* are documented. Both of these data postdate their expected onset in the Mediterranean; *T. trilobus* is expected to first occur at 22.7 Ma, and *G. altiaperturus* at 21.4 Ma (Lirer et al., 2019). While a hiatus was inferred based on the juxtaposition of these first occurrences (Montanari et al., 1997), the delayed onset of these first occurrences indicates that these foraminifera may be absent due to poor preservation at lower heights in the section, or due to sedimentary reoworking. Additionally, the dinoflagellate cyst *S. soucouyantae* first occurrence occurs at 314 m, likely around 20.6 Ma. In GTS 2012, the same first occurrence is estimated to occur at 22 Ma, which fits the same pattern of absence.

The paleomagnetic data obtained from the CT section documented numerous magnetic field reversals, leading to the suggestion that magnetic polarity chrons C6B through C5D were present in the section (Montanari et al., 1997). By contrast, our U-Pb ages fall during chrons C6Bn.2n through C6An.1n, when compared to Geologic Timescale (GTS) 2012 (Hilgen et al., 2012). For the most part, the magnetic polarity obtained at the stratigraphic position of each geochronology sample matches the polarity inferred from GTS 2012 (Figure 5). However, this may be the result of chance, as the paleomagnetic data overestimates the number of magnetic field reversals present in the section. This inaccuracy may be the result of numerous factors. The magnetic mineralogy of the sample was found to be multi-domain magnetite, which is recognized as an unreliable paleomagnetic recorder (Butler, 1992). Thermal demagnetization above 350°C led to erratic behavior, which is far lower than the 550-580°C unblocking temperatures that lead to reliable data. Rather than vector fitting of demagnetization directions through principle component analysis (Kirschvink, 1980), orthogonal projection diagrams were only visually inspected. Beyond these weaknesses with the data obtained, Montanari et al. (1997) also suggest that anomalous directions may arise through delayed remanence acquisition during lithification, bioturbation, and slow sedimentation rates of 2 m/Ma, based on $^{40}Ar/^{39}Ar$ geochronology.

The large number of magnetic field reversals obtained from the prior paleomagnetic data, $^{40}Ar/^{39}Ar$ geochronology, and the last occurrence of *C. dissimilis* at 325 m (in the CV portion of the section, which is across the highway but inferred as conformable with the top of CT), led to the inference that the top of the CT-CV section extended to ~17 Ma. However, our age for the top of the CT section, within 30 cm of the end of the outcrop, is 20.178±0.020 Ma. While we were unable to obtain geochronology samples from the CV section due to inaccessibility, we suggest that it may face the same obstacles of calibration as were present in the CT section. It is possible that the *C. dissimilis* last occurrence may occur prematurely relative to the Mediterranean record of this event at 17.03 Ma, based on astronomical tuning (Lirer et al., 2019), especially since it occurs concurrently with the first occurrence of calcareous nannonfossil *S. belemnos*, which is suggested to have been extant from 19-18 Ma (Raffi et al., 2006). The number of magnetic field reversals observed in the uppermost portion of the section may also be either overestimated or miscorrelated. Alternatively, sedimentation rates slow significantly, or there is a depositional hiatus between the CT and CV sections.

Our work shows the importance of obtaining reliable age constraints on sedimentary records, from which major events in Earth's climate history are inferred. Unfortunately, carbonate rocks frequently lack the single-domain magnetite that produces reliable paleomagnetic records, and may be easily altered through diagenesis, tectonics, dissolution, or other processes that lead to poor foraminiferal preservation. The presence of hiatuses in the CT section complicates both assessments of biostratigraphic first and last occurrences as well as the assignment of reversal signatures to polarity chrons, and makes the section a poor target for astronomical tuning. High-precision geochronology not only reveals these stratigraphic issues, but also provides a new age model for the section, which can be used to re-calibrate the results of prior and future studies of the Bisciaro Formation at the Contessa section.

2. The Contessa section is not a suitable candidate for the Burdigalian GSSP

A recent integrated stratigraphic study of another nearby outcrop of the Miocene Contessa section, which we will refer to as the Cementerie Barbetti Quarry (CBQ) section, was put forward as a candidate for the Aquitanian-Burdigalian GSSP (Global Stratotype Section and Point) (Fabbrini et al., 2019). This study reported the first occurrence of calcareous nannofossil *Helicosphera ampliaperta*, which is one datum suggested for the Aquitanian-Burdigalian boundary, is accessible along the road to the quarry, and in the opinion of the authors, produced concordant planktonic foraminifera, calcareous nannofossil, and paleomagnetic data from a well-preserved outcrop.

However, given its 1 km distance from the CT section, we suggest that the new CBQ section may be subject to some of the same concerns regarding imperfect paleomagnetic data and foraminiferal absence, leading to delayed first occurrences and premature last occurrences. Although principle component analysis was performed on the paleomagnetic data, and samples taken from the same horizon gave similar directions whether subject to thermal or alternating field demagnetization, the data is still not the best quality. Directional data with maximum angular deviation (MAD) >11° was presented as “Group B” quality data, even though samples that show this level of uncertainty are typically excluded from paleomagnetic studies; they are included here because they are bracketed by directions with lower MADs. Additionally the k values of the mean directions are less than 10, indicating that the data included do not cluster well. The mean directions for each polarity group fail a reversal test, and one sampling horizon yielded both normal and reversed directions (Fabbrini et al., 2019). Despite these uncertainties, the polarity timescale suggested for the section also argues for a hiatus between chrons C6Br and C6AAn, which agrees with our radiometric constraints on the hiatus between CCT18-306 and CCT15-311.

While the foraminiferal preservation in the section is described as generally moderate, there are also intervals of poor preservation, particularly near the volcaniclastic horizons (Fabbrini et al., 2019). We can assess some of the foraminiferal boundaries that are proximal to the volcaniclastic layer identified as the Rafaello level in the CBQ section, which we correlate to CCT-306; above, it is too challenging to correlate the five volcaniclastic horizons in the CBQ section with the other 3 horizons dated at CT. While *G. subquadratus* was found out of stratigraphic order at CT at 301.5 m, below the Raffaello level and prior to its expected first occurrence at 21.4 Ma (Lirer et al., 2019), it falls just above the Raffaello level at CBQ, which would work with our age for Raffaello of 22.302±0.040 Ma (Fabbrini et al., 2019). At CBQ, the first occurrence of *G. altiaperturus*, also expected at 21.4 Ma, is found 6 m below Raffaello, which makes this datum out of order. The first occurrence of *T. trilobus* at CBQ falls 9 m below Raffaello, which is more concurrent with its expected onset of 22.8 Ma (Lirer et al., 2019).

However, the last occurrence of *P. kugleri* is marked at 65 cm below the Raffaello level (Fabbrini et al., 2019), which is in disagreement with the CT section, where it is found 70 cm above Rafaello (Montanari et al., 1997). This inconsistency could be explained by two options. First, the last occurrence at CBQ may precede the Mediterranean last occurrence at 21.09 Ma (Lirer et al., 2019), fitting the pattern of absence observed at CT. At CBQ, *P. kugleri* is described as rare, especially near the base and top of its occurrence, smaller in size, and hardly detectable, which lends support for this option. Alternatively, the Raffaello layer may represent a diachronous horizon, despite its designation as a regional marker bed.

Without a detailed interrogation of its accuracy, however, the biostratigraphic data from CBQ is used to infer that the hiatus described above occurs prior to Raffaello deposition, whereas our data suggests it occurs afterwards. The last occurrence of *P. kugleri* is also used to suggest that the Raffaello layer is 21.09-21.08 Ma (Fabbrini et al., 2019), which is inconsistent with our eruptive age for this horizon. If the layers are the same age (which could be tested with zircon geochronology at CBQ), we suggest that the biostratigraphic age calibration of CBQ is incorrect, at least in this lower interval of the section. Above the Raffaello, there is better agreement between biostratigraphic and paleomagnetic data (Fabbrini et al., 2019).

The comparison of CBQ and CT shows the importance of obtaining high-precision geochronology as a check on biostratigraphic and magnetostratigraphic age calibration, especially for sections treated as possible GSSPs. Due to the biostratigraphic inconsistencies with our radiometric age model, paleomagnetic data that is not of the highest statistical quality, the presence of three major hiatuses in the section, and the difficulty of correlation with sections in its immediate vicinity, we suggest that the CBQ section not be adopted as a GSSP. Furthermore, selecting this section on the basis of its first occurrence of *Helicosphera ampliaperta* should also be questioned, considering that this nannofossil is not common in marine records from ocean basins (Fabbrini et al., 2019), and thus cannot be broadly applied to find the Aquitanian-Burdigalian boundary in the ocean drill core record.

One recent study, from the very stratigraphic section we studied, proves this point. In a study of the Miocene Mediterranean Sr and Nd isotopic record, Cornacchia et al. (2018) collected samples from the CT section that were calibrated in age based on ^{40}Ar/^{39}Ar geochronology from Montanari et al. (1997). One sample, two meters above the Raffaello layer, with an estimated age of 21.1 Ma and elevated $^{87}Sr/^{86}Sr$ levels is suggested to be coeval with the Mi-1a event, reflecting increased continental runoff as a result of greater weathering during a transient glaciation (Cornacchia et al., 2018). The age model from CBQ based on bio- and magnetostratigraphy suggests that this event would postdate their estimated age of 21.09 Ma for the Raffaello, leading Fabbrini et al. (2019) to reject the correlation with the Mi-1a event. By contrast, an age of 21.1 Ma is concurrent with our radiometric age model, bounded by two high-precision eruptive ages, and furthermore, our age model could be used to refine the age estimates of the other CT samples presented in Cornacchia et al. (2018).

3. Geochronology may help constrain the provenance of the Bisciaro volcaniclastics

Petrography of the volcaniclastic layers of the Bisciaro Formation have led to a debate on the source of these layers. Western Sardinia has been the leading candidate as the source of explosive volcanism that produced the Bisciaro ashfall. Montanari et al. (1994) performed a grain size analysis of the felsic fraction of the Raffaello layer, and found that grain size decreased from southwest to northeast through the Umbria-Marche basin, consistent with ash carried by eolian transport from Sardinia. Assorgia et al. (1995) analyzed biotites present in the volcaniclastic units of the Bisciaro and Schlier Formations, and found that their geochemistry matched that of the calc-alkaline volcanic sequence at Bosa, on the west coast of Sardinia. While $^{40}Ar/^{39}Ar$ geochronology has been used to estimate the main phase of early Miocene volcanism on Sardinia to occur between 20.5 and 18 Ma (Gattacceca et al., 2007), this hypothesis could be further tested by performing zircon geochronology on volcanic units in Sardinia, to see if any particular eruptions match our eruptive ages from the CT section. If these argon data are correct and complete, an alternative source of felsic volcanism may be required to explain the presence of the Raffaello level, which we have dated to 22.3 Ma.

By contrast, Guerrera et al. (2015) argue that while Sardinian volcanism may be responsible for fine-grained volcaniclastic pelites in the Bisciaro, it would be too distant to produce the turbiditic volcaniclastic horizons. Instead, they infer a more proximal source of volcanism, from the subduction of the Mesomediterranean microplate under Adria. However, there are no volcanic edifices preserved from this event, potentially as a result of rapid erosion, subsidence, or burial by underthursting (Guerrera et al., 2015). Future high-precision geochronological studies in the Mediterranean could assist with identifying the provenance of the Bisciaro volcaniclastics, and correlating them with other early Miocene volcaniclastic deposits around the Mediterranean (listed in Guerrera et al., 2015).

CONCLUSION

Our new U-Pb zircon eruptive ages at the CT section show the importance of the absolute calibration of the sedimentary sections that document Earth’s climate history, when biostratigraphic and paleomagnetic data may be unreliable, and the section is not amenable to astronomical tuning. In stratigraphic sections with zircon-bearing volcanic ashbeds, absolute ages can and should be used to calibrate the bio- and magnetostratigraphic data by which the Geologic Timescale is constructed.

ACKNOWLEDGMENTS

D. Santiago-Ramos assisted in the field campaign, C. Chiodo helped with field logistics, and L. O'Connor assisted with zircon separation. Funding for this project was provided by Princeton University Department of Geosciences through the Geosciences Student Research Fund and by the Scott Vertebrate Fund.

Supplemental Table 1: U-Pb Data. Following the references, data acquired by CA-ID-TIMS is presented with various corrections as specified in the notes beneath the table.

REFERENCES

Assorgia, A., Chan, L. S., Deino, A. L., Garbarino, C., Montanari, A., Rizzo, R., & Tocco, S. (1995). Volcanigenic and paleomagnetic studies on the Cenozoic calc-alkalic eruptive sequence of Monte Furru (Bosa, mid-western Sardinia). *Giornale Di Geologia*.

Bowring, J. F., McLean, N. M., & Bowring, S. A. (2011). Engineering cyber infrastructure for U-Pb geochronology: Tripoli and U-Pb-Redux. *Geochemistry, Geophysics, Geosystems*, *12*(6). https://doi.org/10.1029/2010GC003479

Butler, R. F. (1992). Paleomagnetism: magnetic domains to geologic terranes. *Paleomagnetism: Magnetic Domains to Geologic Terranes*, (September). https://doi.org/10.5860/choice.29-5708

Cebula, G. T., Kunk, M. J., Mehnert, H. H., Naeser, C. W., Obradovich, J. D., & Sutter, J. F. (1986). The Fish Canyon Tuff, a potential standard for the ^{40}Ar/^{39}Ar and fission-track methods. *Terra Cognita*, *6*, 139–140.

Claiborne, L. L., Miller, C. F., Gualda, G. A. ., Carley, T. L., Covey, A. K., Wooden, J. L., & Fleming, M. A. (2018). Zircon as Magma Monitor: Robust,Temperature-Dependent Partition Coefficients from Glass and Zircon Surface and Rim Measurements from Natural Systems. In D. E. Moser, F. Corfu, J. R. Darling, S. M. Reddy, & K. Tait (Eds.), *Microstructural Geochronology: Planetary Records Down to Atom Scale* (1st ed., pp. 3–33).

Coccioni, R., Frontalini, F., Bancalà, G., Fornaciari, E., Jovane, L., & Sprovieri, M. (2010). The Dan-C2 hyperthermal event at Gubbio (Italy): Global implications, environmental effects, and cause(s). *Earth and Planetary Science Letters*, *297*, 298–305. https://doi.org/10.1016/j.epsl.2010.06.031

Condon, D. J., Schoene, B., McLean, N. M., Bowring, S. A., & Parrish, R. R. (2015). Metrology and traceability of U-Pb isotope dilution geochronology (EARTHTIME Tracer Calibration Part I). *Geochimica et Cosmochimica Acta*, *164*, 464–480. https://doi.org/10.1016/j.gca.2015.05.026

Cooper, K. M. (2015). Timescales of crustal magma reservoir processes: Insights from U-series crystal ages. *Geological Society Special Publication*, *422*(1), 141–174. https://doi.org/10.1144/SP422.7

Cornacchia, I., Agostini, S., & Brandano, M. (2018). Miocene Oceanographic Evolution Based on the Sr and Nd Isotope Record of the Central Mediterranean. *Paleoceanography and Paleoclimatology*, *33*(1), 31–47. https://doi.org/10.1002/2017PA003198

Fabbrini, A., Baldassini, N., Caricchi, C., Foresi, L. M., Sagnotti, L., Dinarés-Turell, J., et al. (2019). In search of the Burdigalian GSSP: New evidence from the Contessa Section (Italy). *Italian Journal of Geosciences*, *138*(2), 274–295. https://doi.org/10.3301/IJG.2019.07

Galeotti, S., Krishnan, S., Pagani, M., Lanci, L., Gaudio, A., Zachos, J. C., et al. (2010). Orbital chronology of Early Eocene hyperthermals from the Contessa Road section, central Italy. *Earth and Planetary Science Letters*, *290*, 192–200. https://doi.org/10.1016/j.epsl.2009.12.021

Gattacceca, J., Deino, A., Rizzo, R., Jones, D. S., Henry, B., Beaudoin, B., & Vadeboin, F. (2007). Miocene rotation of Sardinia: New paleomagnetic and geochronological constraints and geodynamic implications. *Earth and Planetary Science Letters*, *258*(3–4), 359–377. https://doi.org/10.1016/j.epsl.2007.02.003

Gerstenberger, H., & Haase, G. (1997). A highly effective emitter substance for mass spectrometric Pb isotope ratio determinations. *Chemical Geology*, *136*(3–4), 309–312. https://doi.org/http://dx.doi.org/10.1016/S0009-2541(96)00033-2

Guerrera, F., Martín-Martín, M., Raffaelli, G., & Tramontana, M. (2015). The Early Miocene "Bisciaro volcaniclastic event" (northern Apennines, Italy): a key study for the geodynamic evolution of the central-western Mediterranean. *International Journal of Earth Sciences*, *104*(4), 1083–1106. https://doi.org/10.1007/s00531-014-1131-5

Hilgen, F. J., Lourens, L. J., Van Dam, J. A., Beu, A. G., Boyes, A. F., Cooper, R. A., et al. (2012). *Chapter 29 - The Neogene Period*. *The Geologic Time Scale 2012 2-Volume Set*. https://doi.org/10.1016/B978-0-444-59425-9.00029-9

Jaffey, A. H., Flynn, K. F., Glendenin, L. E., Bentley, W. C., & Essling, A. M. (1971). Precision measurement of half-lives and specific activities of ^{235}U and ^{238}U. *Physical Review C*, *4*(5), 1889–1906. https://doi.org/10.1103/PhysRevC.4.1889

Jovane, L., Florindo, F., Coccioni, R., Dinarès-Turell, J., Marsili, A., Monechi, S., et al. (2007). The middle Eocene climatic optimum event in the Contessa Highway section, Umbrian Apennines, Italy. *Bulletin of the Geological Society of America*, *119*(3–4), 413–427. https://doi.org/10.1130/B25917.1

Jovane, L., Sprovieri, M., Coccioni, R., Florindo, F., Marsili, A., & Laskar, J. (2010). Astronomical calibration of the middle Eocene Contessa Highway section (Gubbio, Italy). *Earth and Planetary Science Letters*, *298*, 77–88. https://doi.org/10.1016/j.epsl.2010.07.027

Kasbohm, J. J., & Schoene, B. (2018). Rapid eruption of the Columbia River flood basalt and correlation with the mid-Miocene climate optimum. *Science Advances*, *4*(9), 1–8. https://doi.org/10.1126/sciadv.aat8223

Keller, C. B., Schoene, B., & Samperton, K. M. (2018). A stochastic sampling approach to zircon eruption age interpretation. *Geochemical Perspectives Letters*, 31–35. https://doi.org/10.7185/geochemlet.1826

Kirschvink, J. L. (1980). The least-squares line and plane and the analysis of palaeomagnetic data. *Geophysical Journal of the Royal Astronomical Society*, *62*(3), 699–718. https://doi.org/10.1111/j.1365-246X.1980.tb02601.x

Krogh, T. E. (1973). A low-contamination method for hydrothermal decomposition of zircon and extraction of U and Pb for isotopic age determinations. *Geochimica et Cosmochimica Acta*, *37*(3), 485–494. https://doi.org/10.1016/0016-7037(73)90213-5

Kuiper, K. F., Deino, A. L., Hilgen, F. J., Krijgsman, W., Renne, P. R., & Wijbrans, J. R. (2008). Synchronizing rock clocks of earth history. *Science*, *320*(5875), 500–504. https://doi.org/10.1126/science.1154339

Lirer, F., Foresi, L. M., Iaccarino, S. M., Salvatorini, G., Turco, E., Cosentino, C., et al. (2019). Mediterranean Neogene planktonic foraminifer biozonation and biochronology. *Earth-Science Reviews*, *196*(October 2018), 102869. https://doi.org/10.1016/j.earscirev.2019.05.013

Mattinson, J. M. (2005). Zircon U-Pb chemical abrasion (“CA-TIMS”) method: Combined annealing and multi-step partial dissolution analysis for improved precision and accuracy of zircon ages. *Chemical Geology*, *220*(1–2), 47–66. https://doi.org/10.1016/j.chemgeo.2005.03.011

McLean, N. M., Bowring, J. F., & Bowring, S. A. (2011). An algorithm for U-Pb isotope dilution data reduction and uncertainty propagation. *Geochemistry, Geophysics, Geosystems*, *12*(6). https://doi.org/10.1029/2010GC003478

McLean, N. M., Condon, D. J., Schoene, B., & Bowring, S. A. (2015). Evaluating uncertainties in the calibration of isotopic reference materials and multi-element isotopic tracers (EARTHTIME Tracer Calibration Part II). *Geochimica et Cosmochimica Acta*, *164*, 481–501. https://doi.org/10.1016/j.gca.2015.02.040

Montanari, A., Carey, S., Coccioni, R., & Deino, A. (1994). Early Miocene tephra in the Apennine pelagic sequence: An inferred Sardinian provenance and implications for western Mediterranean tectonics. *Tectonics*, *13*(5), 1120–1134. https://doi.org/10.1029/94TC00295

Montanari, A., Bice, D. M., Capo, R., Coccioni, R., Deino, A. L., DePaolo, D. J., et al. (1997). Integrated stratigraphy of the Chattian to mid-Burdigalian pelagic sequence of the Contessa Valley (Gubbio, Italy). In A. Montanari, G. S. Odin, & R. Coccioni (Eds.), *Miocene Stratigraphy: An Integrated Approach* (pp. 249–277). Elsevier.

Nier, A. O. (1950). A redetermination of the relative abundances of the isotopes of carbon, nitrogen, oxygen, argon, and potassium. *Physical Review*, *77*(6), 789–793. https://doi.org/10.1103/PhysRev.77.789

Raffi, I., Backman, J., Fornaciari, E., Pälike, H., Rio, D., Lourens, L., & Hilgen, F. (2006). A review of calcareous nannofossil astrobiochronology encompassing the past 25 million years. *Quaternary Science Reviews*, *25*(23–24), 3113–3137. https://doi.org/10.1016/j.quascirev.2006.07.007

Samperton, K. M., Schoene, B., Cottle, J. M., Keller, C. B., Crowley, J. L., & Schmitz, M. D. (2015). Magma emplacement, differentiation and cooling in the middle crust: Integrated zircon geochronological-geochemical constraints from the Bergell Intrusion, Central Alps. *Chemical Geology*, *417*, 322–340. https://doi.org/10.1016/j.chemgeo.2015.10.024

Schoene, B., Samperton, K. M., Eddy, M. P., Keller, G., Adatte, T., Bowring, S. A., et al. (2015). U-Pb geochronology of the Deccan Traps and relation to the end-Cretaceous mass extinction. *Science*, *347*(6218), 182–184. https://doi.org/10.1126/science.aaa0118

Stelten, M. E., Cooper, K. M., Vazquez, J. A., Calvert, A. T., & Glessner, J. J. G. (2015). Mechanisms and timescales of generating eruptible rhyolitic magmas at Yellowstone Caldera from Zircon and sanidine geochronology and geochemistry. *Journal of Petrology*, *56*(8), 1607–1642. https://doi.org/10.1093/petrology/egv047

Supplemental Table 1: U-Pb Data

	Dates (Ma)							Composition					Isotopic Ratios								
Sample	206Pb/ 238U	±2σ absolute	207Pb/ 235U	±2σ absolute	207Pb/ 206Pb	±2σ absolute	% disc	Pb* (pg)	Pbc (pg)	Pb*/ Pbc	Th/ U	Th/ U(magma)	206Pb/ 204Pb	208Pb/ 206Pb	206Pb/ 238U	±2σ %	207Pb/ 235U	±2σ %	207Pb/ 206Pb	±2σ %	Corr. coef.
zircon	a		b		a,b		c	d	e	f	g	h	i	j	j		j		j		
CCT18-306																					
z13	22.230	0.094	22.6	1.0	61	100	63.9	5.58	1.22	4.57	1.03	1.02	265	0.33	0.0034545	0.319	0.0225032	4.301	0.0472662	4.193	0.372
z31	22.22	0.11	21.5	1.6	-53	182	151.4	2.09	0.85	2.45	0.82	4.32	158	0.26	0.0034397	0.503	0.0214532	7.572	0.0452544	7.456	0.261
z42	22.269	0.081	21.59	0.82	-53	91	151.9	3.25	0.47	6.98	0.95	5.05	402	0.31	0.0034468	0.365	0.0214999	3.844	0.0452601	3.736	0.337
z6	22.28	0.13	22.5	2.0	49	214	62.5	1.05	0.57	1.86	0.62	3.26	129	0.20	0.0034480	0.597	0.0224381	9.100	0.0472190	8.959	0.268
z28	22.28	0.11	22.1	1.6	8	174	-22.1	2.97	1.15	2.58	1.05	5.53	157	0.34	0.0034481	0.480	0.0220570	7.356	0.0464155	7.242	0.269
z33	22.30	0.19	22.4	2.8	34	303	50.0	3.89	2.68	1.45	1.03	5.42	97	0.33	0.0034516	0.840	0.0223228	12.841	0.0469265	12.653	0.255
z34	22.31	0.10	22.1	1.5	-2	168	-189.1	3.17	1.17	2.72	1.10	5.79	163	0.35	0.0034528	0.458	0.0219911	7.049	0.0462134	6.944	0.258
z26	22.314	0.037	22.32	0.47	23	50	32.9	3.74	0.43	8.74	0.97	5.11	496	0.31	0.0034537	0.165	0.0222310	2.137	0.0467057	2.096	0.285
z21	22.315	0.077	22.1	1.1	-4	121	-274.9	2.37	0.62	3.82	1.06	5.58	223	0.34	0.0034538	0.347	0.0219816	5.116	0.0461797	5.014	0.325
z30	22.32	0.19	21.6	3.0	-56	332	148.2	1.70	1.25	1.36	0.91	4.79	94	0.29	0.0034543	0.870	0.0215165	13.838	0.0451961	13.628	0.271
z5	22.322	0.068	22.15	0.95	4	102	-61.0	4.19	0.96	4.37	0.95	5.00	258	0.31	0.0034550	0.304	0.0220613	4.320	0.0463313	4.244	0.280
z35	22.322	0.052	22.36	0.72	26	76	38.1	4.57	0.81	5.67	0.93	4.89	331	0.30	0.0034550	0.235	0.0222656	3.238	0.0467601	3.182	0.270
z39	22.32	0.19	22.7	2.9	62	304	68.9	1.52	1.10	1.38	0.91	4.79	95	0.29	0.0034553	0.853	0.0226009	12.951	0.0474612	12.757	0.259
z36	22.324	0.045	22.10	0.59	-2	64	-182.7	4.07	0.57	7.18	1.03	5.42	405	0.33	0.0034553	0.202	0.0220084	2.699	0.0462169	2.654	0.259
z32	22.33	0.10	22.7	1.4	62	144	69.2	3.09	0.96	3.23	0.92	4.84	197	0.30	0.0034564	0.450	0.0226160	6.215	0.0474774	6.050	0.397
z29	22.331	0.051	22.30	0.72	19	77	22.7	1.68	0.29	5.74	0.82	4.32	344	0.26	0.0034565	0.229	0.0222086	3.261	0.0466211	3.205	0.275
z27	22.372	0.041	22.43	0.53	29	56	42.8	3.89	0.48	8.02	0.95	5.05	458	0.31	0.0034628	0.185	0.0223437	2.383	0.0468194	2.346	0.239
CCT15-311																					
z32	20.857	0.050	21.06	0.67	45	75	62.5	2.39	0.42	5.74	0.64	3.37	358	0.21	0.0032270	0.244	0.0209656	3.212	0.0471413	3.135	0.351
z31	20.86	0.10	20.9	1.1	25	122	41.1	5.93	1.40	4.22	0.53	2.79	276	0.17	0.0032275	0.503	0.0207934	5.335	0.0467471	5.098	0.509
z10	20.865	0.028	20.66	0.29	-4	33	-192.7	2.82	0.21	13.53	0.60	3.16	830	0.19	0.0032283	0.136	0.0205560	1.402	0.0462022	1.358	0.362
z9	20.92	0.10	20.7	1.5	-9	171	-1354.4	2.16	0.86	2.53	0.67	3.53	167	0.22	0.0032363	0.479	0.0205585	7.208	0.0460936	7.061	0.336
z5	20.92	0.15	20.9	2.3	21	258	33.3	0.76	0.49	1.56	0.65	3.42	111	0.21	0.0032372	0.703	0.0208212	10.905	0.0466690	10.741	0.264
z11	20.928	0.036	20.95	0.47	24	54	39.1	2.18	0.28	7.85	0.70	3.68	477	0.22	0.0032381	0.175	0.0208526	2.288	0.0467269	2.242	0.299
z7	20.931	0.071	20.75	0.92	-1	105	-105.6	1.14	0.28	4.09	0.58	3.05	265	0.19	0.0032385	0.342	0.0206469	4.474	0.0462605	4.351	0.392
z37	20.939	0.056	21.21	0.78	53	87	67.0	1.43	0.26	5.44	1.25	6.58	297	0.40	0.0032397	0.270	0.0211179	3.737	0.0472980	3.652	0.348
z34	20.950	0.056	21.31	0.39	62	43	71.3	6.32	0.55	11.46	0.59	3.11	707	0.19	0.0032414	0.271	0.0212124	1.854	0.0474846	1.806	0.245
z38	20.957	0.046	20.90	0.17	14	19	14.8	72.82	2.87	25.40	1.22	6.42	1328	0.39	0.0032426	0.221	0.0207969	0.823	0.0465378	0.774	0.345
z39	20.973	0.044	21.24	0.20	51	21	66.2	29.06	0.73	40.04	0.86	4.53	2264	0.28	0.0032450	0.210	0.0211401	0.974	0.0472705	0.863	0.604
z33	20.977	0.029	21.15	0.29	41	32	59.7	5.09	0.40	12.86	0.56	2.95	798	0.18	0.0032456	0.139	0.0210551	1.362	0.0470721	1.321	0.342
z13	20.992	0.066	21.37	0.95	64	105	72.1	2.19	0.54	4.01	0.87	4.58	243	0.28	0.0032481	0.318	0.0212761	4.469	0.0475291	4.387	0.291
z21	21.068	0.064	20.9	1.1	0	123	-96.1	1.87	0.57	3.30	0.56	2.95	219	0.18	0.0032597	0.305	0.0207874	5.133	0.0462713	5.092	0.164
z22	21.105	0.088	21.5	1.6	71	180	74.3	0.95	0.34	2.80	0.62	3.26	186	0.20	0.0032656	0.421	0.0214527	7.679	0.0476668	7.556	0.318
z6	21.132	0.025	21.05	0.23	12	25	7.3	6.22	0.35	17.73	0.82	4.32	1022	0.26	0.0032698	0.119	0.0209562	1.081	0.0465031	1.045	0.353
z24	21.133	0.092	22.0	1.4	117	148	83.5	1.45	0.54	2.68	0.62	3.26	178	0.20	0.0032699	0.439	0.0218992	6.364	0.0485951	6.256	0.279
z8	21.136	0.066	21.36	0.81	47	87	63.4	1.61	0.24	6.68	1.25	6.63	360	0.40	0.0032704	0.316	0.0212672	3.811	0.0471842	3.643	0.560
z28	21.20	0.15	21.3	2.3	31	261	49.3	1.18	0.76	1.56	0.65	3.42	111	0.21	0.0032809	0.726	0.0211940	11.080	0.0468717	10.900	0.279
CCT18-315																					
z35	20.572	0.040	20.84	0.50	52	57	67.5	2.29	0.28	8.21	0.91	4.79	474	0.29	0.0031826	0.195	0.0207443	2.429	0.0472941	2.374	0.321
z15	20.609	0.088	20.4	1.3	-10	158	-1454.6	1.15	0.43	2.65	0.70	3.68	174	0.22	0.0031884	0.429	0.0202535	6.628	0.0460914	6.525	0.270
z9	20.610	0.047	20.85	0.63	48	71	65.1	1.28	0.20	6.46	0.80	4.21	386	0.26	0.0031885	0.228	0.0207465	3.036	0.0472115	2.961	0.363
z40	20.62	0.11	20.4	1.7	-4	201	-196.5	2.23	1.03	2.15	0.80	4.21	141	0.26	0.0031905	0.549	0.0203139	8.480	0.0461988	8.329	0.306
z43	20.627	0.048	20.71	0.69	30	79	50.1	3.09	0.56	5.48	0.89	4.74	324	0.29	0.0031912	0.235	0.0206107	3.356	0.0468632	3.297	0.283
z38	20.65	0.13	20.7	2.0	28	231	47.0	1.44	0.76	1.91	0.88	4.63	125	0.28	0.0031948	0.630	0.0206137	9.796	0.0468168	9.633	0.289
z25	20.653	0.064	21.0	1.0	55	114	68.9	2.10	0.55	3.81	0.83	4.37	234	0.27	0.0031953	0.314	0.0208543	4.843	0.0473568	4.757	0.304
z31	20.685	0.057	20.57	0.82	7	95	-17.0	1.74	0.37	4.74	1.00	5.26	276	0.32	0.0032002	0.276	0.0204666	4.030	0.0464045	3.954	0.306
z33	20.69	0.16	21.6	2.4	126	259	84.9	0.48	0.30	1.61	0.55	2.89	116	0.18	0.0032016	0.758	0.0215243	11.286	0.0487819	11.005	0.400
z34	20.709	0.069	21.2	1.0	79	113	76.9	1.03	0.26	3.92	0.86	4.58	238	0.28	0.0032039	0.337	0.0211146	4.843	0.0478195	4.744	0.324
z8	20.71	0.10	20.6	1.3	6	152	-23.3	0.58	0.20	2.87	0.69	3.63	187	0.22	0.0032043	0.472	0.0204854	6.410	0.0463875	6.301	0.264
z32	20.74	0.12	21.7	1.8	129	199	85.2	0.53	0.27	1.96	0.74	3.89	132	0.24	0.0032084	0.591	0.0215957	8.578	0.0488393	8.434	0.277
z2	20.83	0.11	22.2	1.8	168	188	88.4	1.94	0.87	2.24	0.78	4.11	147	0.25	0.0032227	0.520	0.0220630	8.148	0.0496746	8.037	0.244
CCT18-322																					
z32	20.183	0.020	20.355	0.082	41	9	61.2	13.34	0.30	44.08	1.08	5.74	2314	0.35	0.0031220	0.097	0.0202538	0.407	0.0470723	0.362	0.541
z30	20.13	0.12	19.7	1.8	-29	218	214.6	2.39	1.20	1.99	0.81	4.26	132	0.26	0.0031145	0.578	0.0196306	9.125	0.0457338	8.995	0.255
z22	20.168	0.069	20.23	0.99	28	116	48.9	1.26	0.32	3.88	0.94	5.00	232	0.30	0.0031197	0.345	0.0201327	4.940	0.0468261	4.839	0.323
z21	20.179	0.033	20.03	0.41	2	49	-48.6	3.55	0.40	8.80	0.77	4.05	523	0.25	0.0031215	0.163	0.0199292	2.057	0.0463256	2.012	0.313
z24	20.195	0.067	20.1	1.0	14	121	19.5	1.40	0.40	3.53	0.85	4.47	217	0.27	0.0031240	0.335	0.0200407	5.098	0.0465470	5.020	0.264
z16	20.21	0.12	20.5	1.7	58	197	70.8	0.96	0.46	2.11	0.75	3.95	140	0.24	0.0031266	0.611	0.0204296	8.486	0.0474119	8.268	0.388
z27	20.272	0.081	20.3	1.0	20	117	34.2	1.66	0.45	3.67	0.81	4.26	227	0.26	0.0031360	0.401	0.0201655	5.024	0.0466579	4.882	0.391

a Corrected for initial Th/U disequilibrium using radiogenic 208Pb and Th/U[magma] specified.

b Corrected for initial Pa/U disequilibrium using initial fraction activity ratio [231Pa]/[235U] = 1.10000.

c % discordance = 100 - (100 * (206Pb/238U date) / (207Pb/206Pb date))

d Total mass of radiogenic Pb.
e Total mass of common Pb.
f Ratio of radiogenic Pb (including 208Pb) to common Pb.
g Th contents calculated from radiogenic 208Pb and 230Th-corrected 206Pb/238U date of the sample, assuming concordance between U-Pb Th-Pb systems.
h Th/U ratio of magma from which mineral crystallized.
i Measured ratio corrected for fractionation and spike contribution only.
j Measured ratios corrected for fractionation, tracer and blank. Values for ET535 are found in Condon et al. (2015) and McLean et al. (2015). Blank model values are as follows:

206Pb/204Pb	18.628271±0.317714
207Pb/204Pb	15.796256±0.232017
208Pb/204Pb	38.535874±0.375848

Chapter 6

Radiometric constraints on the timing, tempo, and effects of large igneous province emplacement

This chapter is taken from

Kasbohm, J.J., Schoene, B., Burgess, S. (in press). Radiometric constraints on the timing, tempo, and effects of large igneous province emplacement. In: Ernst, R.E., Dickson, A.J., Bekker, A. (eds.), Large Igneous Provinces: A Driver of Global Environmental and Biotic Changes*. AGU Geophysical Monograph 255.*

ABSTRACT

There is an apparent temporal correlation between large igneous province (LIP) emplacement and global environmental crises, including mass extinctions. Advances in the precision and accuracy of geochronology in the past decade have significantly improved estimates of the timing and duration of LIP emplacement, mass extinction events, and global climate perturbations, and in general have supported a temporal link between them. In this chapter, we review available geochronology of LIPs and of global extinction or climate events. We begin with an overview of the methodological advances permitting improved precision and accuracy in LIP geochronology. We then review the

characteristics and geochronology of 12 LIP/event couplets from the past 700 Ma of Earth history, comparing the relative timing of magmatism and global change, and assessing the chronologic support for LIPs playing a causal role in Earth's climatic and biotic crises. We find that 1) improved geochronology in the last decade has shown that nearly all well-dated LIPs erupted in < 1 Ma, irrespective of tectonic setting; 2) for well-dated LIPs with correspondingly well-dated mass extinctions, the LIPs began several hundred ka prior to a relatively short duration extinction event, and 3) for LIPs with a convincing temporal connection to mass extinctions, there seems to be no single characteristic that makes a LIP deadly. Despite much progress, higher precision geochronology of both eruptive and intrusive LIP events and better chronologies from extinction and climate proxy records will be required to further understand how these catastrophic volcanic events have changed the course of our planet's surface evolution.

INTRODUCTION (SEE ALSO CHAPTER 1)

In this chapter, after describing the methodological advances that have led to improved accuracy and precision in geochronology, we will review the geochronology of 12 LIP – global environmental change couplets (Figure 1). We chose to focus on LIPs that coincided in time with a dramatic global environmental event, and further narrowed that focus to pairs wherein the LIP and/or the environmental event had been the subject of recent high-precision geochronological study. To complement our narrative review below, we also present a table detailing the samples included in our analysis (Tables 1 & 2). This new compilation is able to highlight some similarities and some differences

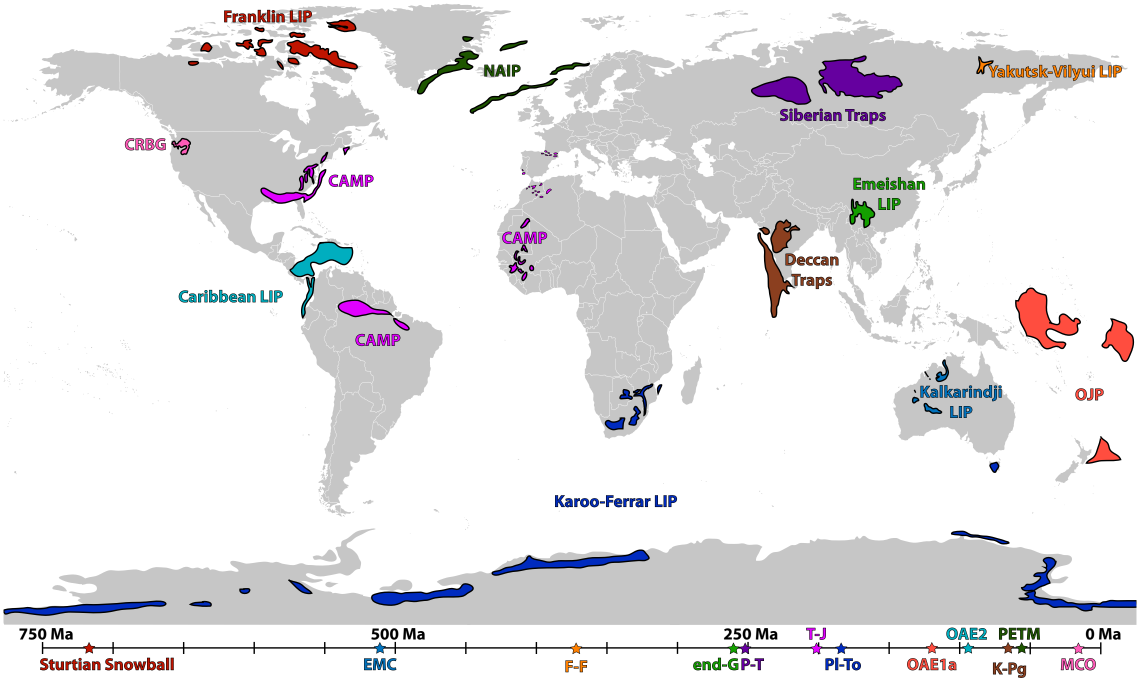

Figure 1: **Map of Large Igneous Provinces.** This map shows the current location of the large igneous provinces described in this chapter, after Bryan & Ferrari (2013). Below, a timeline shows the ages of the global events with which the LIPs are associated. LIP/event couplets are color-coded, and the ages of the LIPs overlap with the ages of the events shown on the timeline. Abbreviations (alphabetized): CAMP – Central Atlantic Magmatic Province; CRBG – Columbia River Basalt Group; EMC – Early-Middle Cambrian extinction; F-F – Frasnian-Famennian extinction; end-G – end-Guadalupian extinction; K-Pg – end-Cretaceous extinction; MCO – Miocene Climate Optimum; NAIP – North Atlantic Igneous Province; OAE – oceanic anoxic event; OJP – Ontong Java Plateau; PETM – Paleocene-Eocene Thermal Maximum; Pl-To – Pliensbachian-Toarcian boundary event; P-T – end-Permian extinction; T-J – end-Triassic extinction.

between LIPs that permit discussion of both the geodynamics of LIPs and their timing relative to environmental catastrophes.

Data reporting

In the sections below and in Table 1, all U-Pb zircon dates reported are ^{238}U/^{206}Pb dates, and all ^{40}Ar/^{39}Ar are reported with the fluence monitor standard age used. All age uncertainties are reported in this paper at 2σ or 95% confidence. When possible, the ages in the text and table are reported at multiple levels of uncertainty, conventionally defined as: [X], the internal or random uncertainty, suitable for intra-lab comparison and inter-lab comparison when the same tracer is used; [Y], the uncertainty in tracer calibration or the age of the reference material used, for comparisons between labs using different ages or tracer solutions; and [Z], the uncertainty including decay constant uncertainty, permitting comparison between different geochronological methods (Schoene, 2014). High-precision U-Pb dates are calibrated with an EARTHTIME tracer, unless otherwise indicated in the text or in Table 1. To facilitate comparison of high-precision geochronology to that obtained for environmental crises, we have plotted the relative timing of both events with corresponding uncertainties in Figure 2.

Many of the datasets are plotted as probability density functions (Figures 3-7 & 9-10) to display the range of dates obtained from a LIP by various approaches; for plotting purposes, the maximum probability of each dataset included in these figures has been scaled to a probability of 1. It is important to note that none of these plots are meant to represent rates or pulses of magmatism – they simply are a way to display what dates have been produced from rocks sampled for comparison purposes. Determining eruptive or intrusive rates requires integration of geologic and stratigraphic data with geochronology (e.g. Siberian Traps, CAMP, Deccan, NAIP).

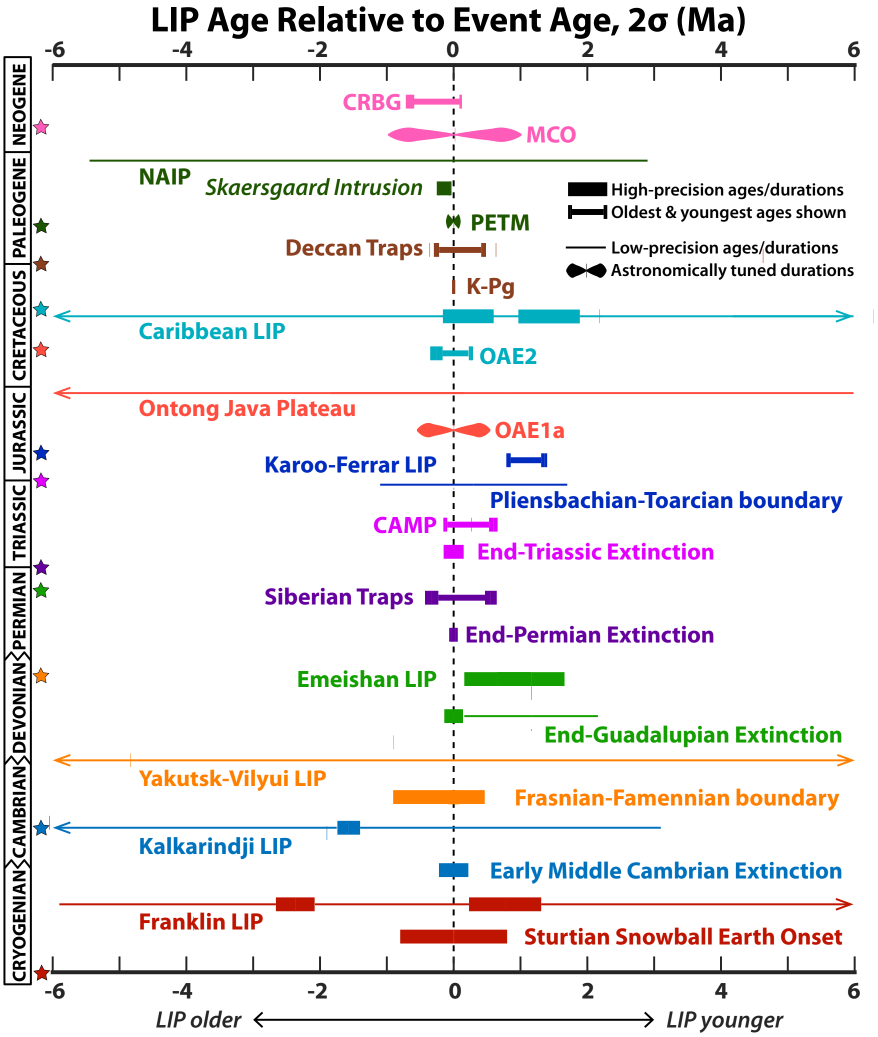

Figure 2: **Relative Timing of LIP Eruptions and Environmental Events.** This figure plots the timing and duration of each LIP, relative to that of the environmental event with which it is associated, plotted adjacently. For each couplet, 0 (black dashed line) is set at the most precise age constraint for the environmental change, or at the midpoint of the event's duration. Ages are plotted with 2σ analytical uncertainties [X], except for the End-Guadalupian constraint, shown with [Y] to reflect comparison with different tracers, and Yakutsk-Vilyui LIP/Frasnian-Famennian, which are shown with [Z] to compare $^{40}Ar/^{39}Ar$ and U-Pb results (arrows extending for the Yakutsk-Vilyui LIP indicate that the [Z] uncertainties extend beyond the bounds of the graph). The 0 line is removed for the Deccan Traps/K-Pg ages, since the high-precision extinction ages appear thinner than the line; U-Pb and $^{40}Ar/^{39}Ar$ calibrations are plotted separately to avoid inclusion of systematic uncertainties. Wide lines represent high-precision ages or durations, and thin lines represent low-precision ages. For populations shaped like an "I", the oldest and youngest ages in a dataset are plotted with uncertainties, and there are a number of intervening high-precision ages between those bounds. The durations of OAE1a, the PETM, and the MCO have astronomical rather than radiometric age constraints, and so are demarcated with curved bars. Abbreviations are the same as those given for Figure 1.

Geochronology of 12 pairs of LIPs and environmental crises

Franklin LIP & Sturtian Snowball Earth

The Neoproterozoic Franklin LIP consists of lava flows, dikes, and sills emplaced over 2.25 million km^2 stretching across northern Canada from Alaska to Greenland. As one of the largest dike swarms on Earth, it includes diabase dikes up to 20 m wide in mainland Canada, Baffin Island, and Greenland, with sills on Victoria Island, Northwest Territories, and Greenland (Denyszyn et al., 2009). The Natkusiak volcanics of Victoria Island represent the thickest extrusive member of the Franklin LIP, with a maximum thickness of ~1100 m (Cox et al., 2015).

Baddeleyite U-Pb ID-TIMS ages from Franklin dikes in Ellesmere Island, Devon Island, and Greenland indicate that the swarm was emplaced from 721±2 Ma to 712±2 Ma (Denyszyn et al., 2009). More recent work has yielded a baddeleyite date for a diabase sill from the Minto Inlier on Victoria Island of 716.33±0.54 Ma (Macdonald et al., 2010), and a U-Pb CA-ID-TIMS detrital zircon date of 719.47±0.29 Ma for a volcaniclastic unit in the Kikiktat volcanics in Arctic Alaska, which are interpreted to be connected to the Franklin LIP on the basis of this age overlap, proximity in paleogeography, and petrogenetic similarities (Cox et al., 2015). These dates from the Franklin LIP have been noted for their general synchronicity with the onset of the Sturtian Snowball Earth event, a period of global glaciation preceded by a large negative excursion in $\delta^{13}C$ (Macdonald et al., 2010). The cooling that potentially caused the runaway ice albedo feedback, allowing for these conditions, is hypothesized to be connected to the emplacement of the

Franklin LIP (Macdonald et al., 2010). In this model, the equatorial paleolatitude for the Franklin LIP would have maximized CO_2 drawdown through the silicate weathering feedback (Goddéris et al., 2003; Macdonald et al., 2010). Further, the emplacement of the Natkusiak sills into sulfur-rich evaporites of the Shaler Supergroup could have allowed for cooling through injection of sulfate aerosols into the stratosphere (Macdonald & Wordsworth, 2017).

Maclennan et al. (2018) present CA-ID-TIMS zircon ages for the onset of Sturtian glaciation from tuffs underlying the Negash Diamictite of the Tambien Group in Ethiopia at 719.68±0.46 and 719.68±0.56, as well as a tuff 2 m above the preceding nadir in $\delta^{13}C$ at 735.25±0.25 Ma. Assuming a constant sediment accumulation rate in the basin, they suggest that the base of the diamictite was deposited at 717.1+0.7/-0.9 Ma. This estimate agrees well with findings from the Coal Creek Inlier in Yukon, Canada, where CA-ID-TIMS zircon dates bracket the onset of glaciation to between 717.43±0.14 Ma and 716.9±0.4 Ma (Macdonald et al., 2010, 2017). The previously mentioned sample from the Kikiktat Volcanics also underlies the Sturtian Hula Hula diamictite, providing another maximum age constraint for glaciation at 719.47±0.29 Ma (Cox et al., 2015), while a volcaniclastic interval within the Ghubrah diamictite in the Huqf Supergroup of Oman provides a minimum age constraint of 711.5±0.3 Ma. Collectively, these results indicate a globally synchronous onset for the Sturtian glaciation at the several million year level (Maclennan et al., 2018).

High-precision geochronology indicates concurrent onset of the Sturtian glaciation and Franklin sill emplacement on Victoria Island (Figure 2) (Macdonald et al., 2010), though baddeleyite dates suggest Franklin intrusions likely began a few million years earlier elsewhere in the province (Denyszyn et al., 2009). These age constraints leave open the possibility that weathering of the Franklin LIP could have contributed to the cooling climate prior to the Sturtian Snowball Earth, even if it may not have been the primary driver of the event.

Difficulties in sampling accessibility and preservation of the Franklin LIP result in a paucity of high-precision dates for the Franklin LIP relative to other, more accessible LIPs. While there is decent horizontal coverage across the regional breadth of the LIP, the lack of continuous preserved extrusive sections prohibit a comprehensive vertical sampling strategy, which would be the ideal way in which to assess eruption rates and durations in the province. To date, most ages have been generated from dikes and sills, which lack stratigraphic context and relative order, and it is thus unclear when the bulk of magmatism occurred (Macdonald et al., 2010). Additionally, the total volume emplaced by the Franklin LIP is unknown, which inhibits attempts to model climatic impact. While its equatorial paleolatitude provides a useful condition for maximizing CO_2 drawdown through silicate weathering, this effect may not have been as significant if the volume of the LIP was small.

Kalkarindji LIP & Early-Middle Cambrian Extinction

The Kalkarindji LIP was emplaced in Australia, and is the oldest known Phanerozoic LIP (Glass & Phillips, 2006). Encompassing the Antrim Plateau Volcanics and Table Hill Volcanics, among other units found to have similar geochemistry, the Kalkarindji is characterized by tholeiitic basalt to basaltic andesite dikes, sills, and lava flows emplaced over 2.1 million km^2 across northern and central Australia (Evins et al., 2009), with a minimum estimated volume of 500,000 km^3 (Glass & Phillips, 2006). Individual lava flows range from 20-200 m, and the thickest stratigraphic sections of the province expose a cumulative thickness of 1500 m (Jourdan et al., 2014). However, limited exposure prevents the development of robust stratigraphic division of the province.

U-Pb CA-ID-TIMS and ^{40}Ar/^{39}Ar dates from distant regions of the Kalkarindji yield ages overlapping at 511 Ma (Jourdan et al., 2014). Zircons extracted from the Milliwindi dolerite dike in the northern portion of the province were dated through CA-ID-TIMS, and yielded a weighted mean age of 510.67±0.62 Ma ([Z]; MSWD = 2.0, n = 5). Baddeleyites extracted from mafic enclaves, the product of Kalkarindji sills intruding basement rock in the Munro well, were dated with TIMS and yielded a concordant upper intercept crystallization age of 511±5 Ma (MSWD = 1.6). Plagioclase from dolerite sills in the Table Hill Volcanics, in the southern extent of the province, was dated via ^{40}Ar/^{39}Ar to 510±4 Ma (MSWD = 0.74); pyroxene extracted from the same sills has been dated with ^{40}Ar/^{39}Ar to 506.28±3.40 Ma ([X]; MSWD = 0.64) (Ware & Jourdan, 2018). Most of these ages agree within uncertainty, obscuring the relative order of emplacement of these units and tentatively suggesting relatively brief emplacement of the province (Jourdan et al., 2014).

The Early-Middle Cambrian (EMC; Series 2-3, Stage 4-5) extinction is the first significant extinction following the Cambrian explosion, with more than 45% of genera going extinct (Jourdan et al., 2014). Reef-building archeocyaths and a variety of reef-dwelling organisms, including many trilobites suffered most prominently (Zhuravlev & Wood, 1996). The period is marked by oceanic anoxia, a positive excursion in $\delta^{34}S$ (Hough et al., 2006), a negative excursion in $\delta^{13}C$ (Gozalo et al., 2013), and sea-level fall recognized as the Hawke Bay regression, hypothesized to be caused by uplift resulting from a mantle plume (Williams & Gostin, 2000).

The age of the EMC extinction has been bracketed by ID-TIMS U-Pb zircon geochronology on air-abraded zircons from three different ash beds in the Somerset Street Member of the Hanford Brook Formation of New Brunswick, Canada, in the Cambrian Series 2, Stage 4, and dated with ID-TIMS following air abrasion (Landing et al., 1998). The youngest grains from each of these samples were all ~511 Ma, thus the authors prefer a date of 511±1 Ma for the stratigraphic unit, which can be interpreted as a maximum age for the stratigraphic unit, though this date should be treated with caution as it was acquired before chemical abrasion was introduced to ID-TIMS (Mattinson, 2005), and without the use of the EARTHTIME spike (Condon et al., 2015). More recently, Harvey et al. (2011) performed CA-ID-TIMS zircon geochronology on an ashbed at the base of the Upper Comley Sandstone Formation in Shropshire, England, in the Cambrian

Series 3, Stage 5. The ash was dated to 509.10±0.22/0.56/0.77 Ma, yielding a minimum age for the EMC extinction.

The temporal connection between the eruption of the Kalkarindji LIP and the EMC extinction was noted by Glass & Phillips (2006), and strengthened by the most recent high-precision geochronology of both the LIP and extinction (Harvey et al., 2011; Jourdan et al., 2014). The precise minimum age of the EMC from Harvey et al. (2011) overlaps with the baddeleyite and $^{40}Ar/^{39}Ar$ dates of Jourdan et al., (2014), though it postdates the zircon age obtained by Landing et al. (1998) by 1 Ma. This proximity in time, combined with analysis of volcanic breccias noting the explosive nature of some of the Kalkarindji volcanism, and sulfur concentration measurements from <50-1900 μg/g, leads to the suggestion that the Kalkarindji LIP played a causative role in the EMC extinction (Jourdan et al., 2014).

While there is strong evidence suggesting a temporal correlation between these two events, the resolution of the geochronology cannot discern the relative order of the extinction versus volcanism. There is a paucity of high-precision geochronology samples, which are from disparate regions (i.e., not from a single vertical section). Because all current dates overlap, the duration of Kalkarindji eruptions cannot yet be constrained other than by estimation of maximum and minimum durations based upon the uncertainty on these dates. The limited surface exposure of the LIP also inhibits calculation of volume estimates for the province.

Yakutsk-Vilyui LIP & Frasnian-Famennian (Late Devonian) Mass Extinction

The Yakutsk-Vilyui LIP was emplaced on the northeastern Siberian platform in a triple junction rift system associated with the Late Devonian breakup of the eastern margin of Siberia. Dikes, lava flows, sills, and layered basalt breccia, with some intercalated ashes and tuffs, are found in outcrops on the Lena, Markha, and Viluy rivers (Ricci et al., 2013). The Viluy rift, the NE/SW-striking branch of the triple junction, is 800 km long and 450 km wide, and is bounded by parallel dike swarms on either side that are 700 km in length (Ricci et al., 2013). There is a wide range in estimates for the volume of the Yakutsk-Vilyui LIP. Polyansky et al. (2017) tally the total length of middle Paleozoic mafic dikes in the region, multiplied by thicknesses of 50-250 m, in addition to the volume of basalts and sills calculated from borehole and surface exposure, to estimate a minimum volume for the province of 100,000-215,000 km^3. Meanwhile, others estimate that over 300,000 km^3 erupted from the Viluy rift; if similar volumes were erupted from the other branches of the triple junction, the total volume emplaced by the Yakutsk-Vilyui LIP may have been up to 1 million km^3 (Ricci et al., 2013). The uncertainty in volume estimates may arise from the fact that exposure of the Yakutsk-Vilyui LIP is currently limited due to erosion, the overlying Siberian Traps LIP to the west, and thick Mesozoic sedimentary cover to the east (Ricci et al., 2013).

While there is a lack of high-precision geochronology for the Yakutsk-Vilyui LIP relative to other LIPs, ^{40}Ar/^{39}Ar work by Courtillot et al. (2010) provide ^{40}Ar/^{39}Ar plateau ages of 372.46±1.4 Ma and 362.36±1.8 Ma (2σ analytical uncertainties, recalculated with FCs = 28.201 Ma (Kuiper et al., 2008)). Incorporating these results with other new dates from plagioclase phenocrysts separated from sills and lava flows, Ricci et al. (2013) also identify two separate $^{40}Ar/^{39}Ar$ age groups, at 366.6±3.4 and 379.0±3.4 Ma (2σ total error, recalculated with FCs = 28.201 Ma (Kuiper et al., 2008)), although individual ages in each of these groups overlap with individual ages from the other group at the 2σ level.

The Frasnian-Famennian mass extinction, as one of the “Big Five” mass extinctions of the Phanerozoic, resulted in the disappearance of >75% of marine species, particularly affecting reef systems, stromatoporoids, and benthic and planktonic marine invertebrates. The extinction took place in five pulses over a few Ma in the late Frasnian through early Famennian (McGhee, 2013). After the extinction began, there were two episodes of marine anoxia, known as the Kellwasser events, in the Upper Famennian, and a positive carbon isotope excursion (Joachimski et al., 2002; Joachimski & Buggisch, 1993). Hypotheses for the causal mechanism of the extinction include fluctuating sea level, bolide impact, the development of terrestrial plants (Algeo & Scheckler, 1998), and massive volcanism of the Yakutsk-Vilyui LIP (Racki, 1998; Ricci et al., 2013).

A bentonite horizon in uppermost Frasnian sediments in Steinbruch Schmidt, Germany, located 2.5 m below the Frasnian-Famennian boundary and between the Upper and Lower Kellwasser events, was dated with U-Pb ID-TIMS zircon geochronology to 377.2±1.7 Ma; interpolating between this date and other ID-TIMS ages in the late Famennian led to an estimate of 376.1±1.7 Ma for the Frasnian-Famennian boundary (Kaufmann et al., 2004). However, this date was found to be inconsistent with a Re-Os study that dated the Frasnian-Famennian boundary to 372.4±3.8 Ma (Turgeon et al.,

2007) and with a Monte Carlo analysis used in the most recent Geologic Time Scale, which placed the boundary at 372.2±1.6 Ma (Becker et al., 2012). Following this disagreement, Percival et al. (2018) restudied the Steinbruch Schmidt bentonite with modern chemical abrasion U-Pb ID-TIMS zircon geochronology, and obtained a date of 372.360±0.053/0.11/0.41 Ma. This date overlaps with the Re-Os date and with statistically calibrated ages. The prior ID-TIMS date may be incorrect because it predates the introduction of the chemical abrasion technique (Mattinson, 2005), thereby leading to ambiguity in how to interpret a complicated age spectrum that may have resulted from unresolved Pb-loss. Several of the younger single crystal dates in that study, interpreted there as having been affected by Pb-loss, also overlap with the most recent CA-ID-TIMS date (Kaufmann et al., 2004).

Astronomical tuning of the Kellwasser horizons in a number of stratigraphic sections suggests a time interval of 400-450 ka between the Kellwasser horizons (De Vleeschouwer et al., 2017). With this estimate and assuming a constant sediment accumulation rate, Percival et al. (2018) place the Frasnian-Famennian boundary at 371.86±0.08 Ma, which postdates the $^{40}Ar/^{39}Ar$ age for the Siljan impact crater in Sweden of 377±2 Ma (Reimold et al., 2005).

Given the sparse dates and low precision for Yakutsk-Vilyui LIP geochronology, it is possible that volcanic eruptions were concurrent with the Frasnian-Famennian boundary, and the pulses of extinction before and after the boundary. Alternatively, future high-precision dating of the LIP may find that these events are unrelated. An enrichment of sedimentary Hg has been observed at or near the Frasnian-Famennian boundary in three different sedimentary records, indicating that, if Hg enrichment is a robust proxy-stratigraphic marker of active LIP volcanism, there may have been ongoing Yakutsk-Vilyui LIP activity during the Upper Kellwasser horizon (Racki et al., 2018).

Emeishan LIP & End-Guadalupian (Late Permian) Mass Extinction

The Emeishan LIP represents one of the primary eruptions of continental flood basalts on Pangea during the Late Permian. Approximately 300,000 km^3 erupted over 250,000 km^2 of the Yangtze craton (southwest China and northern Vietnam) in eastern Pangea, at roughly equatorial latitude (Shellnutt, 2014). However, the current exposure of the Emeishan LIP likely does not reflect its original extent, as the region has undergone extensive post-emplacement deformation due to the collision of the North China block and South China block during the Mesozoic, and the Indo-Eurasian collision during the Cenozoic (Shellnutt et al., 2012). The Emeishan LIP consists of flood basalts, layered mafic-ultramafic intrusions, and silicic plutonic rocks. Ultramafic (picritic) rocks are found in the lower half of the flood basalts, while silicic volcanic rocks (andesite, trachyte, rhyolite, ignimbrite) and basaltic andesites are found in the upper half. The thickness of the LIP ranges from 1-5 km in the west of the province to 0.2-2.6 km in the east, with an average thickness of 700 m (Shellnutt, 2014).

Geologic, paleontological, and paleomagnetic evidence suggest the Emeishan LIP erupted rapidly. In basalt sequences, few flows have weathered flow tops beneath overlying flows or sediments (Shellnutt, 2014). The majority of Emeishan units have been identified as normal polarity thought to represent a single chron, with a few upper units indicating a reversed polarity, leading to the assessment that the LIP erupted in ≤1-2 Ma (Ali et al., 2002; Zheng et al., 2010), corresponding to the Capit-N normal chron of the Geomagnetic Polarity Timescale (Henderson et al., 2012). The Emeishan LIP has also been the subject of numerous geochronological studies of volcanic and plutonic rocks, yielding more than 50 published ^{40}Ar/^{39}Ar, U-Pb SHRIMP, U-Pb LA-ICP-MS, and U-Pb ID-TIMS ages, which range from the Capitanian (266±5 Ma) through the early Triassic (246±4 Ma) (Shellnutt et al., 2012) (Figure 3). This seemingly long duration, in conflict with the brief duration suggested by paleomagnetic studies, likely arises from inaccurate geochronologic studies, low precision of analyses, and uncertainty regarding the relationship between volcanic and plutonic rocks. ^{40}Ar/^{39}Ar ages range from 256.2±0.8 to 251.5±0.9 Ma, suggesting that the Emeishan LIP emplacement extended past the Permian-Triassic boundary, concurrent with onset of Siberian Traps emplacement. Shellnut (2014) interpret these younger ages as erroneous, compromised by open system behavior resulting from post-emplacement thermal resetting by regional tectonic events.

Recent high-precision U-Pb zircon CA-ID-TIMS dates have refined understanding of the timing and duration of Emeishan LIP emplacement. Shellnutt et al. (2012) reported three ages from diabase dikes, ranging between 259.4±0.8 Ma (MSWD = 0.2, n = 7) and 257.6±0.5 Ma (MSWD = 0.5, n = 6), and from four granites between 259.6±0.5 Ma (MSWD = 0.5, n = 5) and 258.4±0.6 Ma (MSWD = 1.8, n = 5), indicating emplacement over ~2 Ma, consistent with age constraints from paleomagnetic data (Ali et al., 2002; Zheng et al., 2010). Shellnutt et al. (2012) also refuted the hypothesis that high-Ti rocks represented the waning phase of volcanism, as the high-Ti diabase dikes seem to have erupted throughout the duration of the Emeishan LIP. Additionally, Zhong et al. (2014) dated a felsic ignimbrite in the uppermost portion of the Emeishan LIP lavas with U-Pb CA-ID-TIMS, reporting 259.1±0.5 Ma (MSWD = 0.7, n = 6) as the termination age for the Emeishan LIP. All of these dates were calibrated with a non-EARTHTIME tracer solution, but only reported analytical uncertainty [X]. Combined, these new data suggest that eruption of the Emeishan LIP may have lasted less than 1 Ma, and that volcanism ended more than 7 Ma before the Permian-Triassic boundary (Ramezani & Bowring, 2017).

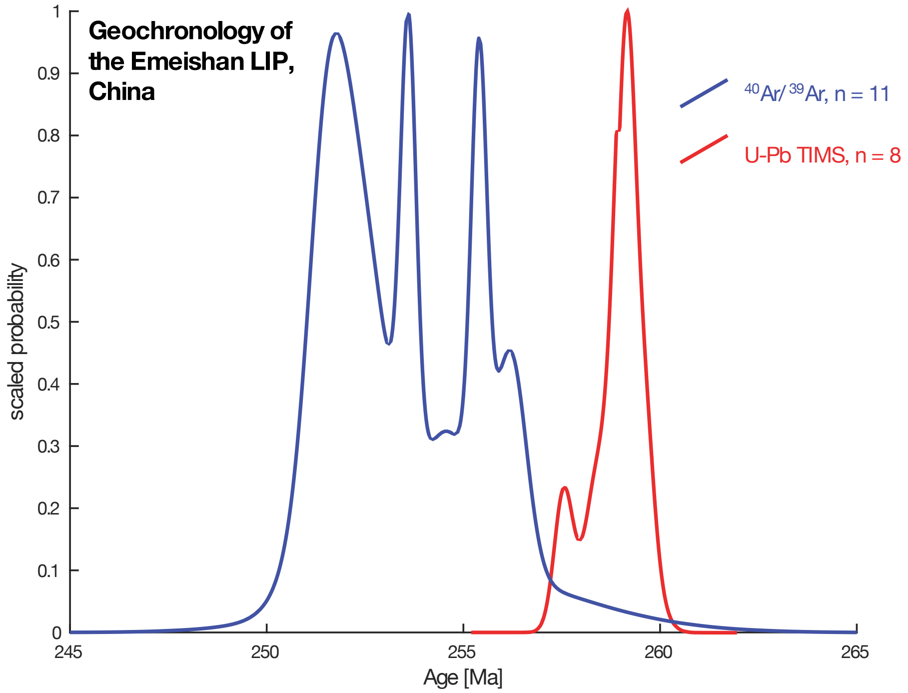

Figure 3: **Emeishan LIP geochronology.** Probability density function for ^{40}Ar/^{39}Ar and U-PbID-TIMS geochronology obtained for the Emeishan LIP, as compiled by Shellnutt, (2014).

The end-Guadalupian mass extinction affected both marine fauna and terrestrial flora and fauna, particularly affecting foraminifera, brachiopods, ammonoids, large bivalves, corals, and plants, though it was far less deadly than the Permian-Triassic mass extinction, which occurred only ~9 Ma later. It is also marked by fluctuations in seawater carbon isotopes and temperatures, and a major sea level regression (Chen et al., 2011; Ramezani & Bowring, 2017). The age of this event has been constrained through CA-ID-TIMS geochronology in both marine and terrestrial sections. Mundil et al. (2004) dated ash beds in the marine Shangsi section in central China above the Guadalupian-Lopingian boundary to 259.1±1.0 Ma (MSWD = 0.3, n=6) and 260.8±0.8 Ma (MSWD = 0.8, n = 5), providing a minimum age for the extinction, though obtained without the EARTHTIME tracer. On land, an ash bed in the lower Beaufort Group of the Karoo Basin in South Africa yielded a weighted mean age of 260.259±0.081/0.14 Ma ([X/Y]; MSWD = 1.5, n = 4, EARTHTIME spike) for the top of the *Tapinocephalus* assemblage zone (Day et al., 2015). Between the *Tapinocephalus* assemblage zone and the following *Pristerognathus* assemblage zone, there is a 74-80% loss of generic richness of all tetrapod fauna, particularly affecting the dinocephalian therapsids (Day et al., 2015).

Prior to publication of high-precision geochronology, the Emeishan LIP was implicated as a potential cause of, or contributor to, the end-Guadalupian mass extinction, as volcanic rocks were interbedded with Permian carbonates that exhibited the extinction (Wignall et al., 2009). The fact that the Emeishan LIP erupted through carbonate-rich sediments lends credence to this proposal, as the emplacement would have allowed for the degassing of thousands of gigatons of CH_4 and 40,000 Gt of CO_2 (Shellnutt et al., 2012). Ganino & Arndt (2009) calculate that observed dolomite-to-marble host-rock thermal metamorphism would have produced 11-26 times more CO_2 than the degassing of magmatic CO_2 from the intrusion. $\delta^{18}O$ evidence for warming immediately before the Guadalupian-Lopingian boundary may reflect such an influx of CO_2 (Chen et al., 2011). The shorter duration of Emeishan emplacement proposed by Shellnutt et al. (2012) and Zhong et al. (2014) suggest a more intense pulse of degassing of the carbonate-rich country rock that could have caused greater disruption to the biosphere.

The differing levels of precision on ages for Emeishan LIP emplacement and that for the ashes bracketing the end-Guadalupian extinction complicate interpretation of the temporal connection between these events (Figure 2). The most precise constraint on their coincidence is the maximum age of the end-Guadalupian extinction (Day et al., 2015), which suggests that extinction predates the Emeishan LIP (Shellnutt et al., 2012), though the LIP dates are an order of magnitude less precise. This allows for the both the absence or presence of a causal connection between Emeishan LIP magmatism and extinction. Uncertainties for Emeishan dates were not reported at the level to permit comparison of different tracers used [Y]; taking that systematic uncertainty into account would increase the uncertainty on each of the LIP dates, potentially allowing for greater overlap with the extinction constraint of Day et al. (2015). Some geochemical studies of end-Guadalupian sections from various sections globally indicate little climatic disturbance at the time (Sheldon et al., 2014) or a diagenetic, rather than environmentally-controlled carbon isotope excursion (Jost et al., 2014), which complicate the simple hypothesis of the Emeishan LIP causing the end-Guadalupian extinction.

Alternatively, if the extinction occurred closer in time to the minimum, less precise age constraint of Mundil et al. (2004), it may suggest coincidence with Emeishan LIP eruptions. Because the Emeishan dates and that of Mundil et al. (2004) were obtained in the same laboratory with the same tracer solution, these results can be compared considering analytical uncertainty [X] alone. While the Emeishan intrusions described above seem to have been emplaced in ~2 Ma duration around 259 Ma, the difficulty in directly correlating these intrusions with extrusive units does not preclude lavas having been erupted over a different duration. Obtaining ages from lava flows has not yet been possible due to the lack of zircons in basalt flows and thermal resetting affecting $^{40}Ar/^{39}Ar$ geochronology (Shellnutt et al., 2012). Further, the uncertainty in eruptive duration, as well as having only a minimum estimate for the volume of the LIP, prohibits a robust calculation of effusion rate. Finally, obtaining high-precision dates from other sections capturing the end-Guadalupian extinction would aid in better assessing whether extinction was globally synchronous and contemporaneous with emplacement of the Emeishan LIP.

Siberian Traps LIP & End-Permian Extinction

The late Permian to early Triassic Siberian Traps LIP is the largest volume (~3 million km^3) Phanerozoic continental magmatic province (Burgess & Bowring, 2015). Following implication of the Siberian Traps as a potential trigger of the end-Permian mass extinction, efforts to date the timing of LIP emplacement focused primarily on the mineralized intrusions of the Noril'sk region, using the $^{40}Ar/^{39}Ar$ or U-Pb geochronometers (Baksi & Farrar, 1991; Campbell et al., 1992; Dalrymple et al., 1995a; Kamo et al., 1996; Renne, 1995; Renne & Basu, 1991; Venkatesan et al., 1997). This work roughly constrained the timing of Siberian Traps emplacement from ~245 – 253 Ma (see review in Baksi, (2014)). Subsequent $^{40}Ar/^{39}Ar$ on whole rock, plagioclase and biotite separates by Reichow et al. (2002, 2009) increased the overall footprint of Siberian Traps magmatism, and decreased the duration of magmatism to < 2 Ma, with the volumetric bulk of emplacement centered around ~250 Ma. Kamo et al. (2003) corroborated this approximate age via U-Pb geochronology on baddeleyite and zircon, suggesting magmatism occurred over an even shorter interval of ~ 1 Ma, and began immediately prior to 251.7 ± 0.4 Ma (Figure 4). A relatively short duration of "main phase" LIP magmatism is consistent with observations from other LIPs (see other sections of this paper), however some $^{40}Ar/^{39}Ar$ and U-Pb (SIMS and TIMS) geochronology suggests multiple pulses of Siberian Traps emplacement, and contemporaneous granitic magmatism potentially related to the LIP occurring until ~ 20 Ma after emplacement of the main volume (Ivanov et al., 2009, 2013 and references therein; Malitch et al., 2012; Paton et al., 2010; Reichow et al., 2016).

Advances in U-Pb ID-TIMS geochronology permitted reinvestigation of the timing and duration of Siberian Traps emplacement, with a focus on resolving the tempo of main-phase magmatism, the relative timing of pyroclastic, intrusive, and effusive extrusive components of LIP emplacement, and the relative timing of LIP emplacement and the end-Permian mass extinction. Application of the U-Pb CA-ID-TIMS protocol to sills, lavas, and pyroclastic rocks from throughout the LIP by Burgess & Bowring, (2015) and Burgess et al. (2017) suggests emplacement of the volumetric majority of the Siberian

Traps in three distinct stages, all of which occurred within ~1 Ma. In this framework, the Siberian Traps magmatic activity began just prior to 252.24 ± 0.10 Ma, and was characterized by initial pyroclastic eruptions followed by lava effusion. During this emplacement stage, ~2/3 of the total volume of the LIP was emplaced (>1 million km^3). Stage 2 began at 251.907 ± 0.067 Ma and was characterized by cessation of extrusion and the onset of widespread sill-complex formation. Intrusive magmatism continued throughout Stage 2 with no apparent hiatus (see also Svensen et al., 2009), with the close of Stage 2 at 251.483 ± 0.088 Ma. Extrusion of lavas resumed after a ~420 ka hiatus, marking the beginning of Stage 3, wherein both extrusive and intrusive magmatism continued until at least 251.354 ± 0.088 Ma, an age defined by the youngest sill dated in the province (Burgess et al., 2017; Burgess & Bowring, 2015). Estimates of this relatively rapid eruption tempo are supported by magnetic secular variation data, which suggest the early large-volume Siberian Traps lavas were emplaced in a few pulses, each lasting between 10 kyr and 100 kyr (Pavlov et al., 2019).

Temporal coincidence and thus a causal relationship between Siberian Traps LIP emplacement and the end-Permian mass extinction has long been postulated (e.g., Rampino & Stothers, 1988), and efforts to understand the timing and duration of extinction and recovery, and to weigh probable trigger and kill mechanisms have progressed concomitantly with advances in radiometric dating. Early work established a broad timeline for extinction, with the Permian-Triassic boundary at ~251 Ma (Bowring et al., 1998; Renne et al., 1995). Subsequent efforts utilizing both ^{40}Ar/^{39}Ar and U-Pb datasets result in varied placement of the extinction timing, ranging from ~249 – 253 Ma

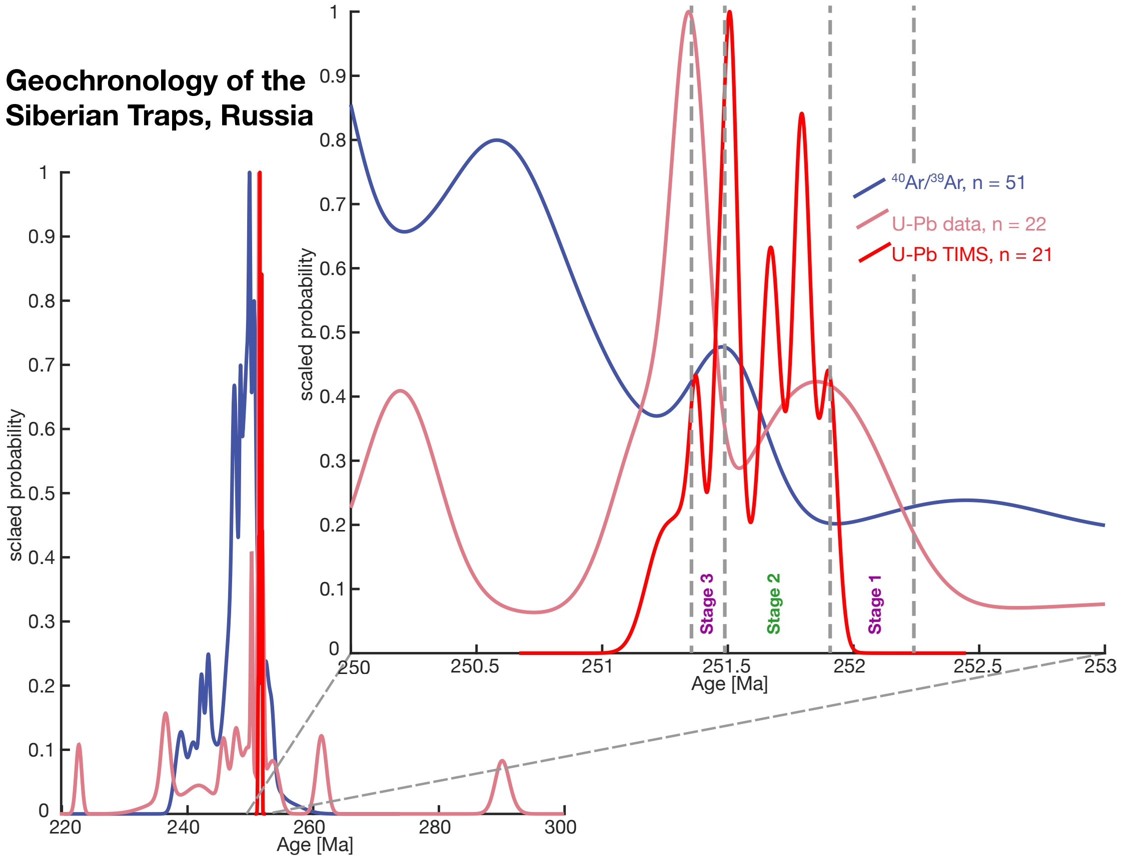

Figure 4: **Siberian Traps geochronology.** Probability density function for ^{40}Ar/^{39}Ar and U-Pb ID-TIMS geochronology obtained for the Siberian Traps. U-Pb TIMS data from Burgess & Bowring (2015); references for other data as follows: Baksi & Farrar, 1991; Basu et al., 1995; Campbell et al., 1992; Dalrymple et al., 1995; Ivanov et al., 2005, 2009, 2013; Kamo et al., 1996, 2003; Malitch et al., 2012, 2010; Paton et al., 2010; Reichow et al., 2002, 2009; Renne, 1995; Renne & Basu, 1991; Svensen et al., 2009; Venkatesan et al., 1997; Vernikovsky et al., 2003; Walderhaug et al., 2005. The different stages of emplacement from Burgess & Bowring (2015) and Burgess et al. (2017) are labeled.

(Mundil et al., 2001, 2004; Reichow et al., 2009). Following the advent and broad adoption of the chemical abrasion protocol to single-grain zircon U-Pb TIMS geochronology, Shen et al., (2011) placed the P-T boundary at 252.17 ± 0.06 Ma, with an extinction duration of less than 200 kyr based on bracketing zircon U-Pb TIMS dates. Subsequent to this work, further advances in zircon U-Pb TIMS analysis and data reduction protocol (see review in supplement to Burgess et al., (2014)) enabled an increase in both accuracy and precision, leading Burgess et al., (2014) to place the Permian-Triassic boundary at 251.902 ± 0.024 Ma, the onset of extinction just after 251.941 ± 0.037 Ma, and cessation prior to 251.880 ± 0.031 Ma, a maximum duration of ~ 60 kyr. This punctuated extinction interval is corroborated by astrochronologic timescales developed for the interval, which suggest extinction over a maximum of ~ 80 ka (Wu et al., 2013) or <40 ka (Li et al., 2016). Employing similar methodology and protocol as Burgess et al., (2014), Baresel et al., (2017a) demonstrate synchrony of the Permian-Triassic boundary within the section dated by Burgess at al., (2014) and at two additional stratigraphic intervals in China, both characterized by much more rapid sediment accumulation rate prior to, and across the extinction interval. This synchrony permits Baresel et al., (2017b) to define a weighted mean Permian-Triassic boundary age of 251.959 ± 0.18 Ma for China, and to suggest that at the resolution of their geochronology (± ~40ka), the extinction interval and timing of the Permian-Triassic boundary cannot be resolved from one-another. Shen et al., (2018) utilize an similar dating protocol to date zircon from one of the two expanded stratigraphic intervals studied by Baresel et al., (2017a). Shen et al, (2018) place the Permian-Triassic boundary at 251.939 ± 0.031 Ma, and more tightly constrain the maximum duration of extinction to ~ 30 kyr.

As the geochronologic, paleontologic, and paleostratigraphic datasets linking emplacement of the Siberian Traps and the end-Permian extinction have become more accurate, comprehensive, and precise, the plausibility of a causal connection has been affirmed (see review in Burgess et al., 2014; 2017), and has moved far beyond broad temporal coincidence and an assumption of causality. The paleophysiologic selectivity of the extinction (see review in Knoll et al., 2007), evidence for widespread ocean anoxiaand geographic selectivity of extinction (e.g., Penn et al., 2018), and evidence for rapid global temperature increase (see Black et al., 2018; Kiehl & Shields, 2005; Sun et al., 2012), all point toward a massive influx of greenhouse gas into the atmosphere system immediately preceding the onset of mass extinction. Currently, general consensus suggests Siberian Traps magmatism likely drove this rapid input of extinction-triggering greenhouse gasses via direct degassing from erupted lavas, and more importantly via metamorphism of sediments contacted by ascending and ponding magmas (e.g., Burgess et al., 2017; Ganino & Arndt, 2009; Svensen et al., 2009). Using this mechanism and the geochronology and emplacement age model of Burgess and Bowring, (2015), Burgess et al. (2017) propose that the initial pulse of Siberian Traps sill emplacement triggered the massive burst of greenhouse gasses necessary to drive extinction. Because the ability of a LIP to drive massive environmental change is likely predicated on the tempo of magmatism, with faster emplacement rates more likely to overwhelm environmental buffering capacity, Burgess et al. (2017) suggest the initial pulse of sill emplacement led to sufficiently rapid gas generation. With conservative eruption rates of ~ 3-4 km^3/yr, emplacement of Siberian Traps lavas may also have played a key role in rapid greenhouse gas generation (Burgess & Bowring, 2015).

Central Atlantic Magmatic Province & End-Triassic Extinction

The Central Atlantic Magmatic Province (CAMP) was erupted and emplaced in association with the initial breakup of Pangea ca. 200 Ma, and has been implicated in the end-Triassic mass extinction event. Due to its association with rifting, the CAMP was highly fragmented and distributed on numerous continents such that its extent and volume have been difficult to estimate (Marzoli et al., 1999; McHone, 2003). The exposed volume of the CAMP is likely $<1\text{x}10^6$ km^3, whereas estimates of the total original volume are $>2\text{-}3 \text{ x } 10^6$ km^3 (Marzoli et al., 2018). Basaltic rocks of the CAMP have been identified in outcrop and drill core from North and South America, west Africa, and southern Europe. The chronology of the CAMP has been the subject of many studies over several decades, but here we focus on studies from the last ~20 years, for which numerous compilations exist. Because of this fragmented record of CAMP emplacement and eruption, it is hard to know how representative the geochronologic record is of the actual eruption and intrusion history, which is important when comparing emplacement timing to the end-Triassic mass extinction. Nonetheless, a combination of geochronological, geochemical and geological work has assembled a framework of global correlations for the magmatic history of the CAMP that serve geologic and biologic events. For example, observations of eruptive stratigraphic sections, where well-exposed, record three main eruptive pulses of lavas separated by sedimentary horizons. These pulses are often unique geochemically, and can be correlated between isolated CAMP sections on different continents (Bertrand, 1991; Blackburn et al., 2013; Deenen et al., 2010; Marzoli et al., 2004, 2019; Olsen et al., 2003; Whiteside et al., 2007).

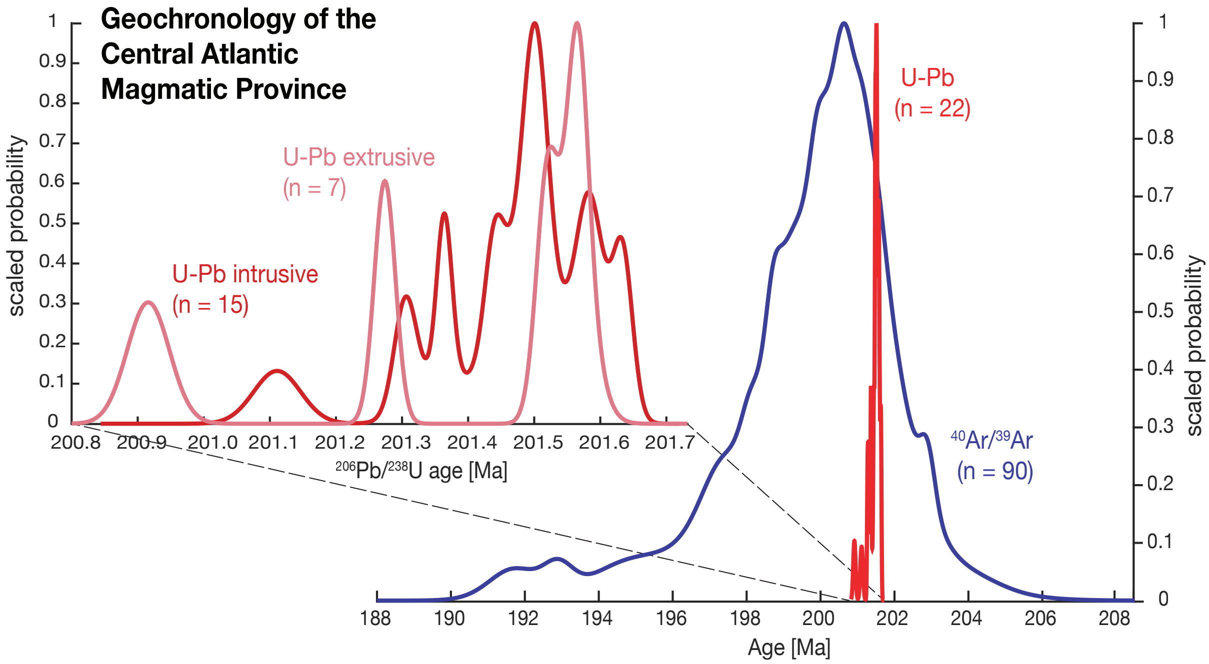

Figure 5: **CAMP geochronology.** Probability density function for ^{40}Ar/^{39}Ar and U-Pb ID-TIMS geochronology obtained for the CAMP, as compiled by (Marzoli et al., 2018, 2019), with some additional data from Heimdal et al. (2018).

Modern geochronology for the CAMP includes both ^{40}Ar/^{39}Ar and U-Pb data. While hundreds of K-Ar and ^{40}Ar/^{39}Ar data exist, recent compilations have focused on the most reliable data, typically comprised of hand-picked plagioclase separates from both intrusive and extrusive units that cover the entirety of known CAMP stratigraphy (Marzoli et al., 2018, 2019). Recent compilations (Marzoli et al., 2018, 2019) contain ~90 step heating plateau dates, each typically with uncertainties of ±1-2 Ma, that when plotted together range over ~10 Ma, from 204-192 Ma (Figure 5). However most analyses fall within a briefer window of about 1-2 Ma centered around 200 Ma, relative to an age for the Fish Canyon Sanidine neutron fluence monitor from Kuiper et al. (2008) of 28.201 Ma (Jourdan et al., 2009; Knight et al., 2004; Marzoli et al., 2011, 2018, 2019; Nomade et al., 2007). These data form an asymmetric distribution with younger tails that generally correspond to lavas high in the stratigraphy in Morocco, but also include some intrusive rocks (Nomade et al., 2007).

U-Pb geochronology on the CAMP has been carried out primarily on sills and dikes that, because of slow cooling rate and internal differentiation, crystallized zircon (Blackburn et al., 2013; Davies et al., 2017; Dunning & Hodych, 1990; Heimdal et al., 2018; Krogh et al., 1987). However, several thick basaltic lava flows in North America that are also zircon-bearing and dated with high precision (Blackburn et al., 2013; Davies et al., 2017; Schoene et al., 2010). A high precision baddeleyite date from the mafic Freetown Layered Complex, Sierra Leone, has been published but these data show large dispersion and are ca. 2 Ma younger than other U-Pb dates, perhaps indicating Pb-loss (Callegaro et al., 2017). Other estimates for the timing of the main eruptions come from CAMP flows in Morocco and North America are derived from correlating dated sills with flows geochemically (Blackburn et al., 2013). The U-Pb data, similarly to the ^{40}Ar/^{39}Ar data, show that the CAMP erupted in <1 Ma. However, all the of the U-Pb dates produced so far fall from 201.6 to 200.9 Ma, with precision of ±20-50 ka. In North American stratigraphic sections, younging upwards is maintained and durations of hiatuses between the three main basalt formations are consistent with predictions from cyclostratigraphic analysis of sedimentary interbeds (Blackburn et al., 2013).

The apparent discrepancy in timescales derived from ^{40}Ar/^{39}Ar versus U-Pb geochronology likely derives from the relatively larger uncertainties associated with the reported ^{40}Ar/^{39}Ar dates. However, excess dispersion in the ^{40}Ar/^{39}Ar dates, demonstrated by high MSWDs on weighted means of culled datasets (Jourdan et al., 2009; Marzoli et al., 2018, 2019; Nomade et al., 2007), suggests that either the ^{40}Ar/^{39}Ar geochronology has dated rocks that have not been sampled by U-Pb geochronology, or that some ^{40}Ar/^{39}Ar dates were affected by open-system behavior, excess Ar, or Ar recoil. Given the larger dataset obtained by ^{40}Ar/^{39}Ar geochronology, it is possible that younger dates represent a more prolonged lifetime of the CAMP than sampled by U-Pb geochronology. Most of the anomalously young dates (i.e. <198 Ma) are from older studies (Baksi & Archibald, 1997; Deckart et al., 1997; Marzoli et al., 1999; Verati et al., 2005) and have not been re-dated by U-Pb or ^{40}Ar/^{39}Ar geochronology for confirmation. Regardless, these younger dates, if accurate, likely represent a volumetrically small portion of the CAMP, so it seems likely that the majority of the magmatism fell within a period of <1 Ma between ca. 201.6-200.9 Ma (Davies et al., 2017; Marzoli et al., 2018).

The CAMP is implicated in the end-Triassic mass extinction event, and geochronology has both supported and refined that assertion (Marzoli et al., 1999; Pálfy et al., 2000b; Schoene et al., 2010). The extinction event is recognized in both the terrestrial and marine biospheres (Tanner et al., 2004), though the position of the extinction interval is defined based on ammonite biostratigraphy (Guex et al., 2004; Von Hillebrandt et al., 2007). The extinction event has been dated by U-Pb zircon ID-TIMS geochronology in three locations: the Queen Charlotte Islands, western Canada; the Pucara Basin, Peru; and New York Canyon, Nevada, USA. The zircon data from the Queen Charlotte Islands location was complicated, and potentially affected by Pb-loss, giving a weighted-mean date of 199.6 ± 0.3 Ma (2σ, [X])(Pálfy et al., 2000b). Data from the Pucara Basin represent the efforts of three studies, with more than a dozen zircon dates spanning the interval from the Norian-Rhaetian boundary to the Haetangian-Sinnemurian boundary (Guex et al., 2012; Schoene et al., 2010; Wotzlaw et al., 2014). The resulting age for the Triassic-Jurassic boundary is 201.36 ± 0.17 Ma, defined as the first occurrence of Jurassic ammonite *Psiloceras Spelae*. The onset of the end-Triassic extinction is represented by the last occurrence of Triassic ammonite *Choristoceras Crickmayi* and the onset of an initial carbon isotope excursion (Guex et al., 2004; Lindström et al., 2017), which is most closely stratigraphically associated with an ashbed dated at 201.51 ± 0.15 Ma (Schoene et al., 2010; Wotzlaw et al., 2014). These dates are corroborated by a single ashbed date from Nevada that occurs near the Triassic-Jurassic boundary (Schoene et al., 2010). Another widely cited date for the Triassic-Jurassic extinction comes from the Newark basin, where a palynological turnover event occurs just below the lowermost CAMP basalt, the Orange Mountain Basalt (Whiteside et al., 2007). Using cyclostratigraphy to generate an age model below the basalt, Blackburn et al., (2013) calculate an age of 201.564 ± 0.015 Ma for the extinction event. However, whether or not the palynological event is representative of the global extinction event remains disputed (Cirilli et al., 2009), so we consider the date from the ammonite extinction record in Peru at 201.51 ± 0.15 Ma to be a more conservative and accurate date for the onset of the end-Triassic extinction.

The oldest high-precision U-Pb date of CAMP magmatism comes from an intrusion in west Africa, and is 201.635 ± 0.029 Ma (Davies et al., 2017), likely older than the date of the extinction event from Peru, and ca. 100 ka older than the date from the Newark Basin.

In the Newark Basin, the oldest high-precision date from extrusive volcanism associated with the CAMP is that of the North Mountain Basalt and Orange Mountain Basalts (correlated geochemically with Palisades Sill), at 201.566±0.031 / 201.481±0.021 Ma (dates from Blackburn et al., 2013; Schoene et al., 2010) and 201.520±0.034 Ma (Blackburn et al., 2013), respectively. The North Mountain Basalt was recently redated in Davies et al. (2017), and they adopt at age that averages existing data to get 201.498 ± 0.028 Ma. A date from the Amelal Sill in the Argana Basin in Morocco is 201.564 ± 0.054 Ma (Blackburn et al., 2013), which was placed within the intermediate lavas stratigraphically. Marzoli et al. (2019) report an additional date from the Amelal Sill of 201.569 ± 0.042 Ma, but correlate their sample with the stratigraphically lower lavas, implying rapid eruption for the lower and intermediate basalts in Morocco. Thus, it has become increasingly clear that the end-Triassic extinction coincides within tens of ka of the onset of extrusive CAMP volcanism in eastern North America and may postdate the beginning of sill emplacement by up to 100 ka. Underlining this observation is that the timescales of intrusive and extrusive magmas may not coincide (Figure 5), though it is difficult to say at this point because high-precision dates on lavas are not very abundant. Understanding this record, and continuing to search for older CAMP magmatic events will help tie down more precisely the timing of the onset of magmatism to the onset of extinction. Furthermore, higher-precision dates that can be tied closely to biostratigraphic and stable isotope data for the extinction interval itself will be key to understanding cause and effect in the end-Triassic biotic crisis.

Karoo-Ferrar LIP & Pliensbachian-Toarcian Boundary Event

The Karoo-Ferrar LIP is comprised primarily of basaltic lavas, sills, and dikes, and was emplaced in the early Jurassic during breakup of Gondwana (e.g., Elliot, 2013; Elliot & Fleming, 2008; Fleming et al., 1997; Pálfy & Smith, 2000; Svensen et al., 2012). At present, the LIP extends over multiple continents, with the two primary portions of the LIP being the Karoo, which is found in South Africa, and the Ferrar, which crops out predominantly in Antarctica, with volumetrically subordinate intrusive rocks found in Australia, Tasmania, and New Zealand (Elliot & Fleming, 2004, 2008). Volume estimates for the entire province are on the order of 2.5 x 10^6 km^3 (Cox, 1988; Encarnación et al., 1996). This LIP has received considerable attention due to emplacement of the province in broad temporal coincidence with global environmental perturbations in the early Jurassic, near the Pliensbachian-Toarcian boundary (Pl-To), and the possibility that LIP magmatism triggered these instabilities (e.g., Burgess et al., 2015; Huang & Hesselbo, 2014; Jourdan et al., 2008; Moulin et al., 2017; Sell et al., 2014; Suan et al., 2008; Svensen et al., 2012).

Early efforts to date Karoo-Ferrar magmatism suggested broad synchrony between emplacement of disparate portions of the LIP, and a total emplacement duration of >10 Ma (see review in Burgess et al., 2015). For the Karoo, initial work was primarily done via the $^{40}Ar/^{39}Ar$ chronometer, with a total duration of sill and lava emplacement eventually constrained to ~3 Ma including uncertainty on dates (Duncan et al., 1997; Encarnación et al., 1996; Jourdan et al., 2005, 2007, 2008; Moulin et al., 2011). The idea of a protracted emplacement interval for the Karoo has subsequently been revised, with zircon U-Pb TIMS dates suggesting a much narrower emplacement interval of < 0.5 Ma starting at ~182.7 Ma (Corfu et al., 2016; Svensen et al., 2012). Further U-Pb TIMS work on zircon and baddeleyite by Sell et al. (2014) indicate that Karoo intrusive magmatism progressed over 2 Ma, however there is some debate as to whether all of these rocks are associated with the main phase of Karoo LIP magmatism, and whether baddeleyite dates were affected by Pb-loss (Corfu et al., 2016; Sell et al., 2016). Similarly, a protracted emplacement interval characterized by multiple, shorter-lived episodes of voluminous eruption is supported by K-Ar and $^{40}Ar/^{39}Ar$ work by Moulin et al. (2017). One U-Pb TIMS zircon date by Burgess et al, (2015) falls within the largest-volume pulse defined by Moulin et al. (2017), and is slightly older than, but within uncertainty of the older sample dated by Sell et al. (2014) and emplacement range defined by Svensen et al. (2014). At present, dates characterized by the highest analytical precision suggest emplacement of the Karoo over less than 1 Ma, while less precise but more stratigraphically inclusive K-Ar and $^{40}Ar/^{39}Ar$ dates suggest Karoo emplacement over nearly 10 Ma (Figure 6).

For the Ferrar, initial dating efforts by U-Pb and $^{40}Ar/^{39}Ar$ chronometers constrained emplacement duration to between ~ 1-2 Ma (e.g., Duncan et al., 1997; Encarnación et al., 1996; Fleming et al., 1997; Foland et al., 1993; Heimann et al., 1994; Minor & Mukasa, 1997). Subsequent CA-ID-TIMS U-Pb zircon dates by Burgess et al. (2015) significantly decreased this range, suggesting emplacement over 349 ± 49 kyr, with magmatism starting by 182.779 ± 0.033 Ma and persisting until at least 182.430 ± 0.036 Ma. This duration is consistent with U-Pb ID-TIMS baddeleyite dating of Ferrar rocks from

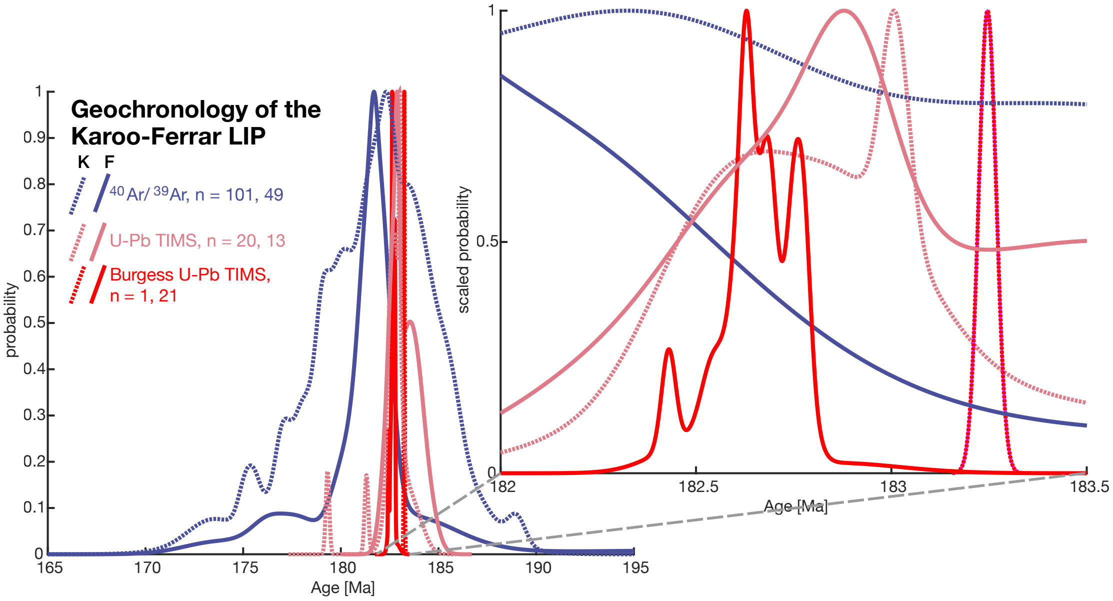

Figure 6: **Karoo-Ferrar LIP geochronology.** Probability density function for ^{40}Ar/^{39}Ar and U-Pb ID-TIMS geochronology obtained for the Karoo-Ferrar LIP, highlighting high-precision U-Pb results of Burgess et al. (2017). References for other age data as follows: Antonini, 1998; Brewer et al., 1996; Duncan et al., 1997; Elliot et al., 1999; Encarnación et al., 1996; Fleming et al., 1997; Foland et al., 1993; Le Gall et al., 2002; Hargraves et al., 1997; Heimann et al., 1994; Ivanov et al., 2017; Jones et al., 2001; Jourdan et al., 2005, 2007, 2008; Minor & Mukasa, 1997; Moulin et al., 2017; Riley et al., 2005; Sell et al., 2014; Svensen et al., 2012; Ware & Jourdan, 2018.

Tasmania by Ivanov et al. (2017), within the bounds of ^{40}Ar-^{39}Ar pyroxene and plagioclase geochronology on Tasmanian dolerites by Ware and Jourdan (2018), and falls within the bounds defined for the Karoo by Sell et al. (2014) and Svensen et al. (2012). Together, these datasets indicate broadly contemporaneous magmatism in what are now two geographically disparate Ferrar provinces. Extending this correlation with the Karoo requires temporal resolution beyond what currently exists for the Karoo. Estimates of average emplacement tempo for the Karoo-Ferrar are similarly precarious due to uncertainty on eruption duration and total province volume, as LIP erosion and concealment by Antarctic ice may bias volume estimates. Based on the range in eruption duration from the Karoo and Ferrar of between 10 Ma and 1 Ma, reasonable estimates for average eruption tempo range from 0.25 – 2.5 km^3/my, with the potential for short-lived (< 100 ka) higher flux pulses within the broader LIP emplacement interval.

Broad coincidence between Karoo-Ferrar LIP emplacement and the Pl-To biotic crises and oceanic anoxic event (OAE) has been recognized for decades (e.g., Sepkoski, 1986). Recent work indicates multiple extinction events at this time, with the two most impactful events occurring coincident with the Pl-To boundary and in the early Toarcian (see review in Moulin et al., 2017). This time period is also characterized by multiple large amplitude excursions in the carbon isotope record, evidence for widespread ocean anoxia, global warming and cooling events, and fluctuations in sea level (e.g., Al-Suwaidi et al., 2010; Boulila et al., 2014; Guex et al., 2012; Huang & Hesselbo, 2014; Pálfy et al., 2002; Suan et al., 2008, 2011, and many others). Determining coincidence between Karoo-Ferrar LIP emplacement and environmental perturbations in the early Jurassic requires not only a stratigraphically comprehensive, accurate, and precise age model for LIP emplacement, but also on the Pl-To boundary date, and the timing and tempo of various environmental perturbations. The absolute temporal record of the LIP is in this instance more thoroughly characterized than geochronology of the environmental crises. Accepting the Pl-To boundary age from Palfy et al. (2000) of 183.6 +1.7/-1.1 Ma, which is consistent within uncertainty with constraints from Sell et al. (2014), Ferrar emplacement occurs within uncertainty of the boundary date and carbon cycle perturbation and is contemporaneous with the onset of the early Jurassic carbon isotope excursion, extinction, and ocean anoxia (Burgess et al., 2015). A more detailed temporal relationship between Ferrar emplacement and Toarcian perturbations is difficult to ascertain due to large uncertainty in the timing and tempo of these events (e.g., Boulila et al., 2014; Hesselbo et al., 2007; Hesselbo & Pienkowski, 2011). Age uncertainty on the timing and, importantly, tempo of Karoo eruption/emplacement is high relative to that on the Ferrar, which further exacerbates efforts to conclusively link emplacement with environmental perturbation. Recent geochronology efforts do not preclude coincidence, but additional high-precision geochronology with age uncertainty smaller than the duration of events being compared is required to make robust comparison.

Cretaceous Oceanic LIPs & Oceanic Anoxic Events

The Cretaceous is marked by the prevalence of oceanic LIP eruptions and Oceanic Anoxic Events, which appear to be broadly correlative. OAEs were brief episodes of disturbance to the carbon cycle, with enhanced organic carbon burial, evidenced by the widespread deposition of black shales, and positive carbon isotope excursions of 1.5–2‰ (Jenkyns, 2010). They are associated with global warming, sea level rise, and the drowning of carbonate platforms (Jenkyns, 2010). OAEs appear to have been concurrent with the eruptions of the Cretaceous oceanic flood basalts, which may have provided excess carbon to the ocean that allowed for greater marine productivity, and pCO_2 to the atmosphere, allowing for global warming that accelerated the hydrological cycle, increasing continental weathering and nutrient discharge to the ocean (Ogg et al., 2012). Greater productivity allowed for an increase in organic matter, which placed a greater demand for oxygen in the water column as it was buried, leading to widespread anoxia (Jenkyns, 2010) as the warm global climate did not allow for cold oxygenated bottom water (Schlanger & Jenkyns, 1976). Here we will focus on two of the largest Cretaceous oceanic LIPs, Ontong Java Plateau and the Caribbean LIP, because they are connected to the two most widespread OAEs, the Early Aptian OAE1a, and the Cenomanian-Turonian OAE2 (the Selli and Bonarelli events, named for their initial recognition in Italy).

Ontong Java Plateau & OAE1a

The Ontong Java Plateau (OJP) is the largest oceanic large igneous province and largest series of volcanic eruptions in the last 250 Ma, with an estimated volume of 60 million km^3 over an area of 2 million km^2 in the southwestern equatorial Pacific (Courtillot & Renne, 2003). The Greater OJP also includes the minor plateaus of Manahiki, Hikurangi, and South Kerguelen, and is exposed above sea level in the Solomon Islands Arc (Kerr, 2014), and the eastern portion of the plateau is thought to have been emplaced near or at sea level (Chambers et al., 2004).

Given its uniform normal polarity and biostratigraphy, the OJP is thought to have formed in the early Aptian, during the Cretaceous normal polarity superchron (Tarduno et al., 1991). All radioistopic geochronology in the OJP has been performed using the ^{40}Ar/^{39}Ar method, primarily on whole-rock samples. Mahoney et al. (1993) report that six whole-rock samples from ODP Site 807 yield eruption ages indistinguishable from one another, with a weighted mean value of 122.3±2.0 Ma (range from 124.7±4.4 Ma to 119.9±5.2 Ma). Ages results from Site 289, which was sampled 500 km away, and from the island of Malaita, over 1600 km away, overlap with this mean value. Further dating from exposed OJP basement on the Solomon Islands yielded ages overlapping with the 122 Ma age group (Tejada et al., 1996, 2002). These early studies also had suggested a second pulse of volcanism at ~90 Ma, given ages obtained from ODP Site 803 (Mahoney et al., 1993) and the island of Sigana (Tejada et al., 1996). However, these younger ages are thought to be affected by argon recoil, given the low potassium content of the rocks and the few plateau heating steps used to obtain the ages, and thus should be interpreted as minimum ages (Chambers et al., 2002). Total fusion ages on plagioclase crystals extracted from OJP basalts sampled at ODP Site 1184, in the eastern salient of the plateau, yield a weighted mean age of 123.5±3.6 Ma, overlapping with the age population obtained elsewhere in the plateau (Chambers et al., 2004).

Though these ages lack the precision of more recent ^{40}Ar/^{39}Ar and U-Pb studies on other LIPs, they do suggest that OJP volcanism was occurring simultaneously across a widespread area at ~122 Ma. It cannot yet be assessed whether volcanism occurred on the short timescale of other LIPs in <1 Ma, or if it occurred in the 9 Ma permitted by the range of dates, which would allow calculated emplacement rates to vary over an order of magnitude (Fitton & Godard, 2004). With the current data, there is no apparent geographic age progression, though this may be obscured by the precision of the ages and by the limitations of sampling over only 9 m – 2 km of stratigraphy at a given sampling site (Tejada et al., 1996, 2002).

OAE1a, also known as the Selli event, is recognized for its apparent concurrence with the emplacement of the OJP in the early Aptian. It is marked by the deposition of organic-rich black shales in all major ocean basins, and a complex geochemical signature in δ^{13}C, with a negative excursion followed by a major positive excursion (Menegatti et al., 1998). The influx of light carbon causing the negative excursion is thought to result from injection of CO_2 from submarine volcanic outgassing (Larson & Erba, 1999; Tejada et al., 2009), or by the dissociation of methane hydrates (Jahren, 2002). The biostratigraphic record of the event is manifested by first, an increased speciation of calcareous nannofossils, followed by a drastic decrease in the calcification of these fossils as well as of planktonic foraminifera, known as the "nannoconid crisis" (Erba, 1994).

While there are no radiometric ages available for OAE1a, two different astronomical tuning models have attempted to constrain the duration of the event, even though the astronomical solution of Laskar et al. (2004) does not apply in the Cretaceous. Li et al. (2008) correlate the carbon isotope records from Italy, Mexico, and the Iberian shelf to estimate a 1.27 Ma duration for OAE1a, with the initial negative $\delta^{13}C$ excursion occurring over 27-41 ka. Meanwhile, Malinverno et al. (2010) suggest a duration of OAE1a of 1.11±0.11 Ma through astronomical tuning of the Cismon APTICORE borehole in Italy. They suggest that the record be tied to the base of polarity chron M0r, formerly estimated at 121 Ma (Channell et al., 1995), making the timing of OAE1a from 120.21 to 119.11 Ma. However, a review of advances in Early Cretaceous geochronology suggest that the base of chron M0r, which is also the Barremian-Aptian boundary, is conservatively between 123.8-121.8 Ma, following U-Pb CA-ID-TIMS and $^{40}Ar/^{39}Ar$ studies (Corfu et al., 2013; He et al., 2008; Midtkandal et al., 2016; Olierook et al., 2019). Thus, the timing of OAE1a is likely to have occurred at least 1 Ma if not a few Ma earlier than previously suggested. This time period would be a fruitful interval to pursue more high-precision age constraints, to better ascertain the timing of this boundary and OAE1a.

The current state of geochronology for OJP and OAE1a allows for correlation of the events, since the ages for OJP overlap with the age assigned to OAE1a at ~120 Ma, though at an order of magnitude lower resolution. Higher-precision ages are required to improve this correlation, and to assess a causal relationship between oceanic LIP volcanism and this global climate event at the same resolution as other events in this chapter. Geochronology of the OJP is hindered by sample availability: there have been only a few ODP cores to drill into OJP basement, and it is exposed above sea level in only a few small islands, inhibiting wide sampling across both area and depth of the province. Furthermore, there is no description of felsic ashbeds or gabbroic intervals in the basalts that may potentially yield zircon. Additionally, the low K content of the basalts has limited the precision of $^{40}Ar/^{39}Ar$ dating (Fitton & Godard, 2004). pCO_2 proxy records suggest that the documented shift to lighter oceanic $^{187}Os/^{186}Os$ isotopes (Bottini et al., 2012; Tejada et al., 2009), reflecting volcanogenic mantle values, was concurrent with the rise in oceanic CO_2, strengthening the connection between OJP emplacement and the carbon cycle perturbation of OAE1a (Naafs et al., 2016).

Caribbean LIP & OAE2

The Caribbean LIP consists of 4.5 million km^3 (Kuroda et al., 2007) of highly faulted basaltic or picritic lavas and sills, layered gabbros, and ultramafic rocks interpreted to be a remnant of an eastern Pacific oceanic plateau that was inserted between North and South America. These rocks were obducted and exposed around the Caribbean margin and the northwestern coast of South America, and exhibit a thickness of 8-20 km (Sinton et al., 1998). With carbonized tree trunks and corals occasionally interbedded with the basalts, parts of the LIP appear to have been emplaced subaerially or in shallow water (Kerr, 2014). The limited presence of interbedded sediments and ash layers in the Caribbean LIP suggest rapid eruptions with few hiatuses (Kerr, 2014).

Like the OJP, most age constraints for the Caribbean LIP are based on whole rock $^{40}Ar/^{39}Ar$ dates, constrained by biostratigraphic ages of surrounding sediments, which indicate that much of the LIP was emplaced before the Coniacian (89.8-86.3 Ma (Ogg et al., 2012)). These dates similarly suffer from low precision as most of the rocks sampled were tholeiitic, with low K_2O content (Sinton et al., 1998; Snow et al., 2005). The primary pulse of Caribbean LIP volcanism seems to have occurred between 92 and 88 Ma (ranging from 92.0±9.6 to 87.9±4.2 Ma), as evidenced by dates from outcrops on Haiti, Colombia, Costa Rica, Curacao, as well as from DSDP cores sampling the Venezuelan basin (Kerr et al., 2003; Sinton et al., 1998). More recent whole rock $^{40}Ar/^{39}Ar$ dating has yielded a weighted mean of four dates of 93.96±0.38 Ma for the Dumisseau Formation in Haiti, and 92.75±0.46 Ma for a sample from Curacao (Snow et al., 2005). These dates suggest that volcanism was broadly synchronous across the region over a short period of time, potentially 1-2 Ma. A second set of ages from basalts in Columbia, a sill in Curacao, volcanics in Haiti, and from DSDP Site 152 reveal a younger phase of volcanism from 76-72 Ma, which is as extensive in area as the first phase, but is likely less voluminous, and may be related to extension as the plateau was emplaced in its current location (Sinton et al., 1998).

OAE2 was first recognized as a 1 m thick package of laminated black shale with total organic carbon content >30% in the Umbria-Marche region of Italy (Schlanger & Jenkyns, 1976). The black shale has been found across the globe, most prominently in pelagic Atlantic settings, Caribbean, and Alpine-Mediterranean areas, and to a lesser extent in north Africa and Asia (Jenkyns, 2010). This global distribution suggests a widespread reducing environment, occurring in the context of a major sea level transgression, higher global temperatures with elevated pCO_2, and a positive carbon isotope excursion of 4-5‰, reflecting increased rates of productivity and organic carbon burial (Jenkyns, 2010). The timing of this event, overlapping the Cenomanian-Turonian boundary, is also coincident with an extinction event in which 26% of known genera were lost, particularly affecting more than half of ammonoid and brachiopod genera (Kerr, 2014). Oceanic LIP volcanism has been implicated as a potential cause of OAE2 because of this loss in deep marine biota, the geochemical signature of black shales resembling oceanic plateau, and the increase in productivity related to a greater flux of nutrients provided by volcanism (Kerr, 2014).

Sedimentary sections containing the records of OAE2 have been astronomically tuned to suggest a range of possible durations of the event: 1.8 Ma for the Bonarelli level in central Italy, with the event beginning at 94.21 or 93.72 Ma (Mitchell et al., 2008), 430-445 ka for the Wunstorf section in northern Germany (Voigt et al., 2008), 600 ka for the Greenhorn Formation in the western USA (Meyers et al., 2001; Sageman et al., 2006). A recent high-precision U-Pb zircon geochronology study of bentonites bracketing OAE2 in the Yezo Group of Japan has refined the timing and duration of the event, which begins at 94.436±0.093/0.14 Ma ([X/Z], MSWD = 0.8, n = 5), and ends at 93.920±0.031/0.11 Ma ([X/Z], MSWD = 2, n = 3) (Du Vivier et al., 2015). This age model yields a duration of 392-640 ka, in broad agreement with prior astrochronological constraints. The age model's timing for OAE2 also overlaps with the Cenomanian-Turonian Boundary age of 93.90+0.07/-0.09 Ma, (±0.15 Ma) [X/Z], which was derived from intercalibrated ^{40}Ar/^{39}Ar, U-Pb, and astrochronology of the Western Interior Seaway (Meyers et al., 2012).

Given its observed temporal coincidence, the Caribbean LIP has frequently been implicated as one of the causes of OAE2, though other LIPs, such as the High Arctic LIP (Polteau et al., 2016) and the flood basalt volcanism from the rifting of Madagascar (Storey et al., 1995; Turgeon & Creaser, 2008) have also been implicated as possible causes. However, high-precision geochronology studies of these LIPs will be required to better understand this connection, now that the occurrence of OAE2 is well-constrained to ~94 Ma (Figure 2). With uncertainty on the order of a few million years, many of the ages used to suggest a first main phase of Caribbean volcanism at 92-88 Ma overlap with the OAE2 zircon ages (Kerr et al., 2003; Sinton et al., 1998; Du Vivier et al., 2015), including the higher-precision ^{40}Ar/^{39}Ar dates from the Dumisseau Formation (Snow et al., 2005). While it is also possible that the main phase of the Caribbean LIP eruption could have postdated OAE2 entirely, and may in fact align better with the Turonian-Coniacian boundary (Ogg et al., 2012), a variety of osmium isotope records suggest that a large magmatic pulse triggered the onset of OAE2 (Turgeon & Creaser, 2008; Du Vivier et al., 2014). While the Caribbean LIP suffers from its fragmentary, fault-bounded nature, complicating sampling across its full vertical stratigraphy and horizontal extent, higher-precision ages would allow for a better understanding of its timing, duration, effusion rate, and connection to OAE2.

Deccan Traps & End-Cretaceous Extinction

In the late Cretaceous at *ca*. 90 Ma the Indian subcontinent rifted from Madagascar, marking the initial drift of India towards Eurasia, an event that culminated in the Himalayan Orogeny (Besse & Courtillot, 1988; Raval & Veeraswamy, 2003). The impingement of the Reunion plume under the western Indian margin occurred ca. 66 Ma, which resulted in the eruption of the Deccan Traps flood basalt province. As outlined below, the timing of the Deccan Traps corresponds well with the end-Cretaceous mass extinction event, though whether it played a role in that disaster remains heavily debated due to the simultaneous occurrence of the Chicxulub bolide impact and the evidence that the impact coincided with the potentially very rapid extinction of marine organisms (Keller et al., 2012; Schulte et al., 2010).

The Deccan Traps covers ~500,000 km^2 of western India, with estimated volumes ranging from 1-2 million km^3 (Jay & Widdowson, 2008; Richards et al., 2015; Self et al., 2008). Large uncertainties in the total volume derive from both the portion of the Deccan that is eroded and also from the amount of basaltic magma that is currently below sea level on the continental shelf off the west coast of India. However, by comparison to other flood basalts, the stratigraphy of the Deccan Traps is well exposed along the western margin of the 1000 m elevation Deccan plateau, called the Western Ghats, where deep erosion down to the coastal plain has resulted in outstanding exposure of the volcanic stratigraphy. As a result, geological, paleomagnetic, and geochemical studies conducted over several decades have generated a very well-characterized stratigraphy of the Deccan Traps relative to many other flood basalt provinces (Beane et al., 1986; Chenet et al., 2007, 2008, 2009; Khadri et al., 1988; Subbarao et al., 2000).

The stratigraphy of the Deccan Traps has been divided into twelve formations within three subgroups that can be well correlated over ~80,000 km^2 surrounding the Western Ghats. The stratigraphy becomes less certain towards the east, south and north, though geochemical and paleomagnetic data have been used to correlate with the Western Ghats (Courtillot et al., 2000; Jay & Widdowson, 2008; Schöbel et al., 2014; Self et al., 2008; Shrivastava & Pattanayak, 2002). As one spectacular example, basalt flows exposed in quarries on the southeast coast of India are thought to have traveled 1000s of km within the Krishna-Godavari paleo river valley from the Western Ghats into the Indian Ocean. Paleomagnetic, geochemical and chronologic data support an affiliation with the Deccan Traps, though exact correlations have yet to be confirmed (Keller et al., 2008; Knight et al., 2003; Self et al., 2008). While these peripheral flows are important for understanding of the overall evolution of the Deccan Traps, they are volumetrically less significant and therefore perhaps less important for understanding the paleoclimatic implications of the Deccan eruptions.

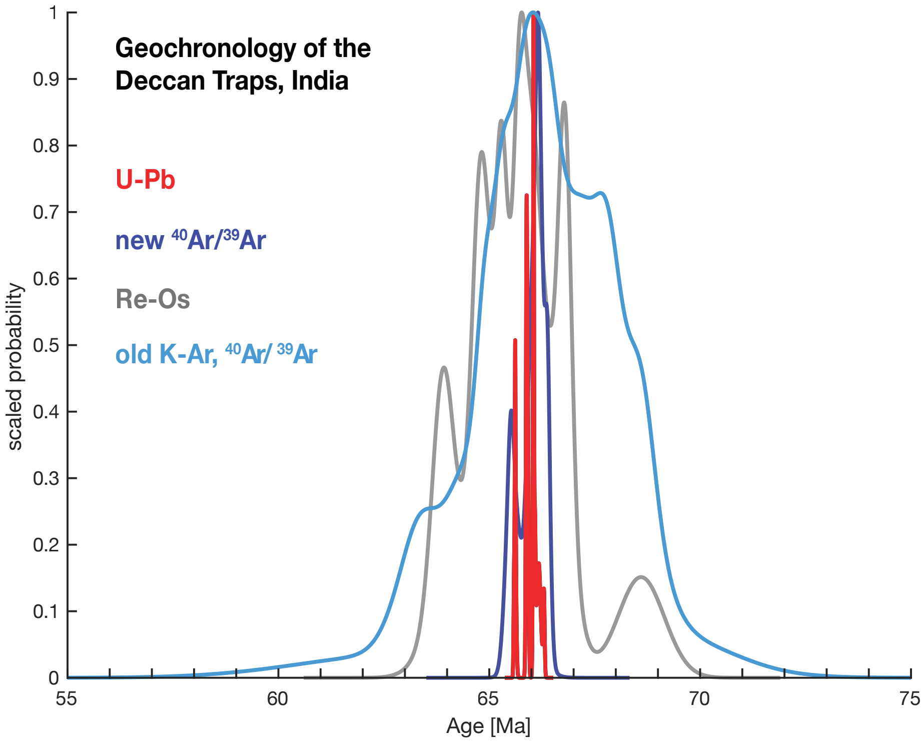

Figure 7: **Deccan Traps geochronology.** Probability density function for Re-Os, ^{40}Ar/^{39}Ar, and U-Pb ID-TIMS geochronology obtained for the Deccan Traps. U-Pb data are from Schoene et al. (2019), new ^{40}Ar/^{39}Ar data are from Sprain et al. (2019), Re-Os data is from Allègre et al., (1999) and old K-Ar and ^{40}Ar/^{39}Ar are from Baksi (1994), Chenet et al. (2007), Courtillot et al. (1986, 1988, 2000), Duncan & Pyle (1988), Hofmann et al. (2000), Hooper et al. (2010), Knight et al. (2003), Pande (2002), Venkatesan et al. (1993).

Because portions of the Deccan Traps are interstratified with sediments containing late Cretaceous flora and fauna, they have been long known to potentially overlap with the end-Cretaceous mass extinction (McLean, 1985). K-Ar, ^{40}Ar/^{39}Ar, Re-Os geochronology and paleomagnetic data were gathered over several decades (Allègre et al., 1999; Baksi, 1994; Chenet et al., 2007; Courtillot et al., 1986, 1988, 2000; Duncan & Pyle, 1988; Hofmann et al., 2000; Hooper et al., 2010; Knight et al., 2003; Pande, 2002; Venkatesan et al., 1993), which confirmed that the majority of the eruptions occurred during chron C29r (now known to be between ca. 66.3 and 65.6 Ma), but beginning and finishing during normal polarity (Chenet et al., 2009; Courtillot et al., 2000) (Figure 7). Chron 29r contains the end-Cretaceous mass extinction and the Cretaceous-Paleogene boundary, which has been defined as the timing of the Chicxulub impact (see review in Smit, 1999). However, uncertainties of ±1-2 Ma or more on the dates for the Deccan Traps prevented a high-resolution correlation of the Deccan Traps with the Chicxulub impact and the biotic crisis. Additionally, the age uncertainties, when combined with paleomagnetic data, led several authors to conclude that an early pulse of volcanism as old as 68 Ma predated the main phase in the western Ghats sections (Chenet et al., 2007), indicating a total duration of volcanism to be several millions of years.

Two recent ongoing efforts using $^{40}Ar/^{39}Ar$ and U-Pb geochronology have established a much higher resolution timeline for the eruption of the Deccan Traps. The $^{40}Ar/^{39}Ar$ geochronology has focused on multi-grain plagioclase separates from Deccan basalt flows (Renne et al., 2015; Sprain et al., 2019), whereas the U-Pb geochronology is based on dating single zircons from volcanic ash interstratified with the basalts (Schoene et al., 2015, 2019). Both datasets show that over 90% of the Deccan Traps erupted between ~66.3 and 65.6 Ma, and therefore do not support a prolonged eruption over millions of years in the Western Ghats. Neither of the studies have dated the C30n portion of the Deccan Traps nor the topmost formations, so the total duration cannot yet be calculated.

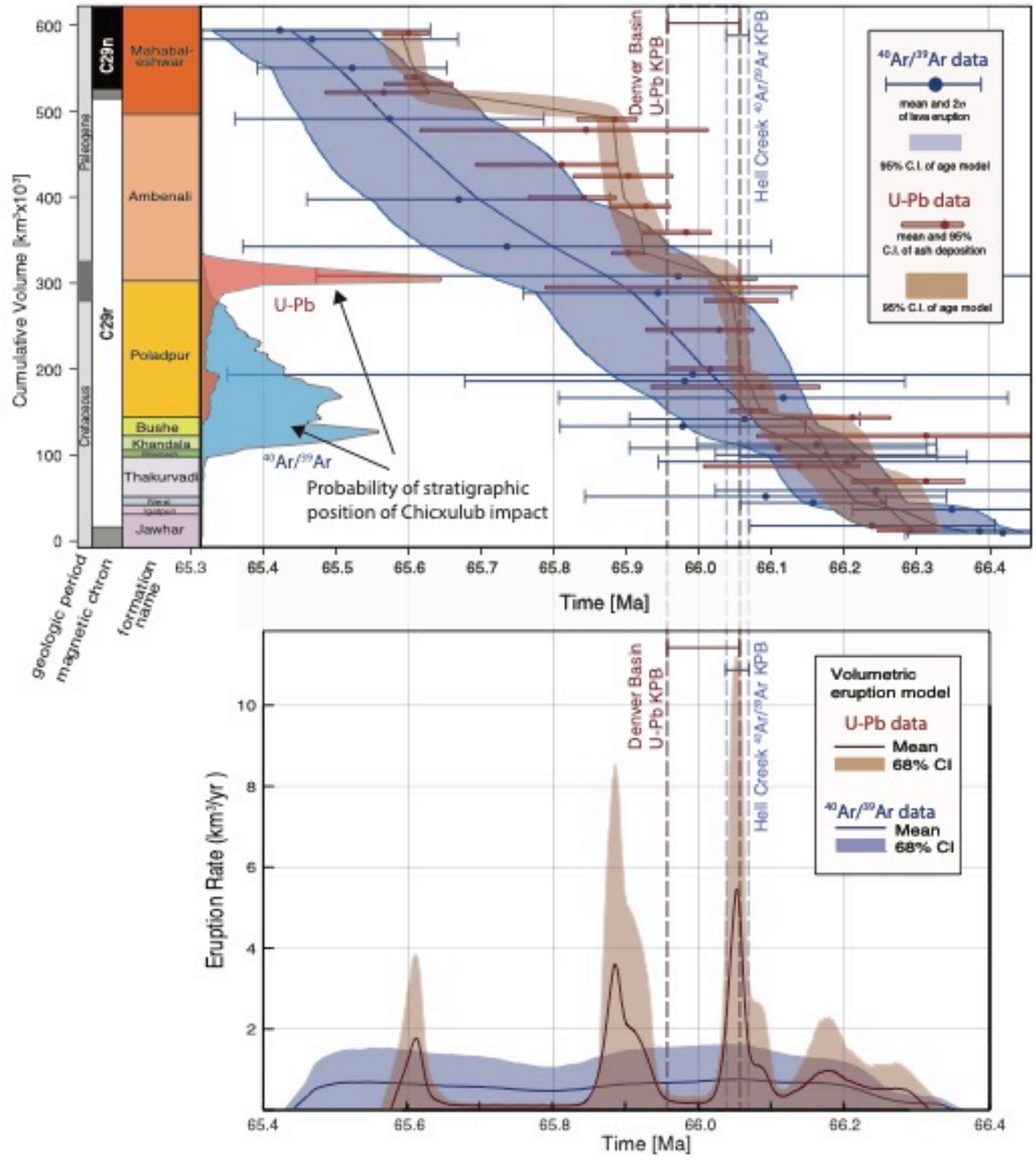

Figure 8: **High-precision geochronology from the Deccan Traps, India.** Compilation of recently published ^{40}Ar/^{39}Ar and U-Pb datasets (Sprain et al., 2019; Schoene et al., 2019), compared using the same Bayesian techniques for generating an eruptive age model from each dataset. Upper plot shows the age of stratigraphic units versus the cumulative volume of basalt, using the volume model of Richards et al., (2015). Lower plot shows the corresponding volumetric eruptive rate. Methods are outlined in Schoene et al., (2019). As an output of the same model, the probabilistic position of the Chicxulub impact within the Deccan Traps for each dataset is shown, using the Chicxulub U-Pb date from Clyde et al. (2016) and the ^{40}Ar/^{39}Ar date from Sprain et al. (2018), compared to the age model derived from each method.

However, U-Pb geochronology of the same outcrop originally reported to be 67-68 Ma (Chenet et al., 2007) and of transitional polarity was shown to represent the C30n-C29r transition at ca. 66.3 Ma (Schoene et al., 2015), supporting a short duration.

Both the recent ^{40}Ar/^{39}Ar and U-Pb datasets (Renne et al., 2015; Schoene et al., 2015, 2019; Sprain et al., 2019) have excellent coverage of the entire Deccan stratigraphy and reveal good agreement between the two methods, but a direct comparison of absolute ages remains difficult. This is because of systematic uncertainties between the ^{40}Ar/^{39}Ar to U-Pb dating methods that arise from the decay constants and physical constants of both the ^{238}U and ^{40}K decay schemes (Min et al., 2000; Renne et al., 1998, 2010; Schoene et al., 2006), which are discussed in the Dating Methods section. Given these uncertainties, we refrain from comparing the ^{40}Ar/^{39}Ar and U-Pb data at better than the 200 kyr level, but instead focus on the datasets and calculated eruption rates internally and compare to geochronology from the same system for assessing their temporal relation to the Chicxulub impact.

Because of the spectacular exposure and preservation of the Deccan Traps in the western Ghats, the ^{40}Ar/^{39}Ar and U-Pb datasets can be combined with models for the relative volumes of each formation (Richards et al., 2015) and used to calculate volumetric eruption rates for the flood basalts. Doing so with the U-Pb dataset reveals that the Deccan Traps erupted in four major pulses, separated by relative lulls in volcanism of up to 100 ka (Figure 8). The ^{40}Ar/^{39}Ar dataset, in contrast, shows roughly constant eruption rates over the entirety of the Deccan Traps.

However, the comparably large uncertainties associated with the $^{40}Ar/^{39}Ar$ dataset make it impossible to test the presence of pulses identified by the U-Pb dataset. A challenge facing both dating methods in calculating eruption rates is the large uncertainties in the volume models for the flood basalt, in addition to the unknown volume or age of basalts located offshore to the west of the Indian margin. Furthermore, the intrusive component of the Deccan Traps is poorly exposed compared to other LIPs, and thus difficult to compare to the eruption record. As a result, estimating volatile release associated with the Deccan Traps remains a challenge.

The end-Cretaceous mass extinction has not been directly dated. Terrestrial records have low stratigraphic resolution, making it difficult to pinpoint an extinction horizon, and no geochronology has been published from marine records. However, ejecta material from the Chicxulub impact has been well dated by both U-Pb and $^{40}Ar/^{39}Ar$ geochronology. Given the stratigraphic correspondence between the impact ejecta and the peak marine extinction, these dates may also calibrate the timing of the extinction. U-Pb dates on impact ejecta come from zircon geochronology of ashbeds bracketing Chicxulub ejecta in the Denver Basin, Colorado (Clyde et al., 2016); the $^{40}Ar/^{39}Ar$ date comes from both sanidine extracted from ashbeds bracketing Chicxulub ejecta in Hells Creek, Montana, and on glassy tektites defining the Cretaceous-Paleogene boundary from both Haiti and Columbia (Renne et al., 2013, 2018; Sprain et al., 2018). Both U-Pb and $^{40}Ar/^{39}Ar$ datasets show that the Deccan Traps began several hundred thousand years before the Chicxulub impact and continued for a similar duration afterwards. It has been hypothesized that seismic energy from the impact itself may have influenced the eruption of the Deccan Traps, for example by leading to an increase in eruption rates (Renne et al., 2015; Richards et al., 2015). While the ^{40}Ar/^{39}Ar dataset cannot rule this model out (Sprain et al., 2019), the U-Pb dataset shows a pulse of eruptions likely beginning before the impact and a decrease afterwards, suggesting the Chicxulub impact and Deccan Traps were completely independent of one another (Schoene et al., 2019).

There remains much to learn about what the effect of the Deccan Traps may have been on the end-Cretaceous mass extinction event. Several datasets have argued for a role for Deccan Traps in late Maastrichtian ecological changes, such as a warming and cooling event evidenced by oxygen isotopes records in foraminifera (Barnet et al., 2017; Li & Keller, 1998; Tobin et al., 2012) and fossil leaf evolution (Wilf et al., 2003), evidence for biologic disturbance in the lead-up to the Chicxulub impact (Henehan et al., 2016; Petersen et al., 2016; Punekar et al., 2014; Wilson, 2014; Wilson et al., 2014), and a significant change in silicate weathering documented by seawater Os isotopes (Ravizza & VonderHaar, 2012; Robinson et al., 2009). The pulse of Deccan volcanism identified in the U-Pb dataset that begins within tens of ka before the Chicxulub impact may hint at a closer temporal link between volcanism and the main extinction event. However, environmental, climate, and biologic records within this timeframe do not paint a clear picture as to what the effect of volcanism was. Some evidence of a hyperthermal event prior to the Chicxulub impact in Elles, Tunisia, has been suggested (Thibault et al., 2016), but corroborating records are scarce. A better understanding of the contribution of the Deccan Traps to the end-Cretaceous mass extinction and recovery period will require continued stratigraphic work generating very high resolution biotic and proxy records, geochronology from marine sections, as well as continued geochronology on the Deccan Traps to test recently established eruptive histories, including the intrusive history.

North Atlantic Igneous Province & Paleocene-Eocene Thermal Maximum

The North Atlantic Igneous Province (NAIP) initiated when the proto-Icelandic plume impinged on the base of Greenland (Larsen et al., 1999; Richards et al., 1989). Magmatism initiated as a result ca. 61-62 Ma in what is now West and East Greenland, Baffin Island, the Faeroe Islands, and throughout the British Isles (Saunders, 2016). Magmatism continued during rifting of east Greenland and Europe, where inferred plume magmatism is superimposed on mid-ocean ridge magmatism of the mid-Atlantic ridge, forming thickened crust ridges leading towards Iceland (Saunders, 2016; Saunders et al., 1997). In addition to the exposed basalt stratigraphy associated with the NAIP, abundant submarine sills have been imaged seismically along the continental margins (so-called "seaward dipping reflectors (White et al., 1987)), some of which have been dated from drill core and shown to be synchronous with the NAIP (Svensen et al., 2010). Given the fragmentary nature of the NAIP and the abundance of submerged intrusive rocks, the volume of the NAIP has been difficult to determine. An estimate of pre-erosion volume for extrusive rocks of ~1.8 milllion km^3 is often cited (Eldholm & Grue, 1994), and estimates for the total magmatic volume including intrusive rocks range between 5-10 million km^3 (Eldholm & Grue, 1994; White et al., 1987). Despite potentially being one of the largest LIPs, there is no mass extinction associated with the NAIP. However, geochronology suggests that peak magma production rates may have coincided with the

Paleocene-Eocene boundary and the associated hyperthermal event (the PETM). Testing this correlation requires high-precision geochronology on both basalts, intrusive rocks, and sedimentary sections that contain the PETM.

Published geochronology for the NAIP includes data from the ^{40}Ar/^{39}Ar, K-Ar, U-Pb, Re-Os, and Rb-Sr methods. In a recent comprehensive review of existing geochronology, (Wilkinson et al., 2017) rejected the vast majority of these dates based on criteria including poor data quality, incomplete data reporting, dubious interpretations, ambiguous data handing, and questionable sample quality. Their resulting database focuses on subaerial sampling localities and includes between ~80 and 120 ^{40}Ar/^{39}Ar and U-Pb dates; the number of acceptable dates depends predominantly on whether groundmass, glass, or whole-rock data were included for ^{40}Ar/^{39}Ar data (Figure 9a). Our summary here focuses on their more restrictive database that contains only pure mineral separates, given that whole-rock, groundmass and glass ^{40}Ar/^{40}Ar dates are too often inaccurate (see other sections of this paper).

The majority of dates within the subset are ^{40}Ar/^{39}Ar dates from a handful of studies on basalts and gabbros from west Greenland, east Greenland, the Faeroe Islands and the British Isles (Figure 9b). Both intrusive and extrusive samples have been dated, and some studies (Larsen et al., 2014, 2016; Storey et al., 2007b) focus on sampling from known stratigraphic sections in order to make regional correlations and estimate volumetric eruption rates. Modern ID-TIMS U-Pb geochronology for the NAIP is sparse. Eight dates have been published, from the British Isles (Chambers et al., 2005; Hamilton et al., 1998) and from submarine cores off the coast of Norway (Svensen et al., 2010). One study of the Skaergaard intrusion in East Greenland was not included on the compilation of (Wilkinson et al., 2017), in which construction of the mafic complex was estimated to be between 56.02 ± 0.02 and 55.84 ± 0.02 Ma (Wotzlaw et al., 2012).

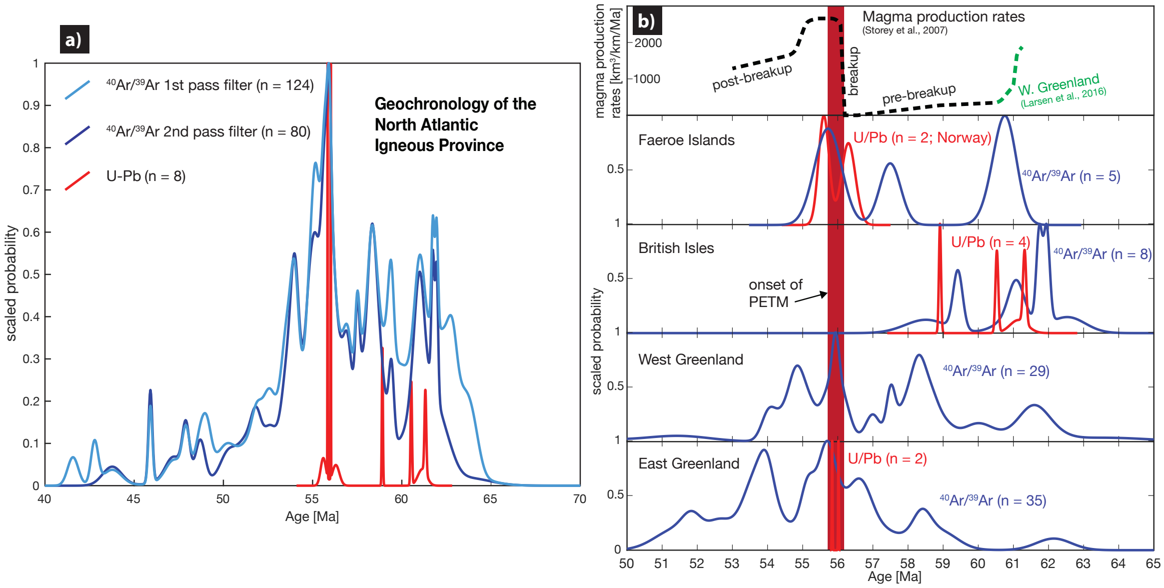

Figure 9: **NAIP geochronology.** Probability density function for ^{40}Ar/^{39}Ar and U-Pb ID-TIMS geochronology obtained for the NAIP, as compiled by Wilkinson et al., (2017). The first pass filter of Wilkinson et al. (2017) eliminated dates in the NAG-TEC database adversely affected by poor data quality, incomplete data reporting, dubious interpretations, ambiguous data-handling, and questionable sample quality. The second pass filter removes whole-rock, groundmass, and glass ^{40}Ar/^{39}Ar dates, leaving only dates from pure mineral separates.

The results show that magmatism began in the early Paleocene and continued well beyond the Paleocene-Eocene boundary. These geochronologic data have led to the hypothesis that the NAIP was erupted and intruded in two main phases, one that predates the initial breakup of Greenland, North America and Europe ca. 63-61 Ma, and a second beginning ca. 56 Ma (Larsen et al., 2014, 2016; Storey et al., 2007a, 2007b). Wilkinson et al., (2017) argue that, given their full compilation of available geochronology, this gap in magmatism is less significant. However, assessing changes in the rates of magmatism that may define different phases requires robust volumetric estimates of eruption rates, which are difficult to calculate given the fragmentary preservation of the NAIP. In an attempt to reconcile this, Storey et al., (2007a, 2007b) combined stratigraphically resolved $^{40}Ar/^{39}Ar$ geochronology from eastern Greenland with estimates of volumes of each formation to calculate an order of magnitude increase in eruption rates that defines the onset of the second phase of magmatism ca. 56 Ma. In a similar effort in western Greenland, (Larsen et al., 2016) also calculate higher eruption rates in the pre-breakup phase prior to ca. 61 Ma.

The most severe hyperthermal event in the Cenozoic, the Paleocene-Eocene Thermal Maximum (PETM), may overlap with the onset of the second phase of NAIP magmatism. The PETM is marked globally in marine and terrestrial stratigraphic records. It is recorded by both a negative $\delta^{13}C$ anomaly of carbonate and organic carbon of several permil, and also a negative $\delta^{18}O$ anomaly in foraminifera that indicates a warming of seawater of 3-4° (Cui et al., 2011; Zachos et al., 2001, 2005). The duration of the PETM has been estimated to be either 170 ka or 220 ka, by cyclostratigraphy on astronomically tuned sediments (Röhl et al., 2007) and extraterrestrial ^{3}He accumulation (Murphy et al., 2010), respectively. The absolute timing of the onset of the PETM has been calibrated through a combination of U-Pb and $^{40}Ar/^{39}Ar$ geochronology on volcanic ashbeds and cyclostratigraphic estimation of the time between the onset and stratigraphic position of the ashbed (Charles et al., 2011; Jaramillo et al., 2010; Storey et al., 2007a; Westerhold et al., 2009). These result in a range of estimates spanning 500 ka between ca. 55.7 and 56.2 Ma, despite reported uncertainties on the geochronology of 100 ka or better. The uncertainties in these estimates derive from both the uncertainties in standard ages used for $^{40}Ar/^{39}Ar$ dates, the interpretation of the U-Pb zircon data, and the assumptions inherent in cyclostratigraphy, for example that observed cyclicity is caused by Milankovitch cycles and that there are no hiatuses.

There is agreement that the PETM was likely driven by delivery of a large amount of isotopically light carbon to the ocean-atmosphere system, but the source and isotopic composition of that carbon remain debated. Possible sources include methane hydrate dissociation (Dickens et al., 1995), organic carbon volatilization through contact with NAIP sills (Svensen et al., 2004, 2010), weathering of exposed organic-rich epicontinental seaways (Higgins & Schrag, 2006), and mantle carbon derived directly from NAIP magmatism (Gutjahr et al., 2017). It is difficult to reconcile the negative carbon isotope shift of the PETM with mantle carbon extracted from the NAIP, thus explaining the attraction to methane hydrate or organic carbon volatilization. However, Gutjahr et al., (2017) argue based on the pH of seawater derived from boron isotope measurements combined with carbon isotope mass balance that volcanic/mantle carbon was an important source of CO_2 for the driving the PETM. In order to resolve this issue, more stratigraphically linked, high-precision geochronology is necessary from the NAIP to calculate eruption rates during the break-up phase of the magmatism. Also, the differences in estimates for the onset of the PETM need to be resolved (Charles et al., 2011), likely through a combination of geochronology and potentially cyclostratigraphy in sections that record the PETM. It is unlikely that cyclostratigraphic estimates for the timing of the PETM alone will have the accuracy to resolve this question (Westerhold et al., 2012).

Columbia River Basalt Group & Miocene Climate Optimum

The Columbia River Basalt Group (CRBG), the youngest, smallest, and best-preserved continental flood basalt, erupted 210,000 km^3 of lava over Washington, Oregon, and Idaho, USA from ~17-6 Ma. Due to its accessibility, it has been the subject of numerous stratigraphic, paleomagnetic, geochemical, mapping, and geochronological studies, providing an unparalleled level of detail for LIP researchers. The province has been divided into five formations (Steens Basalt, 15.3% of total volume; Imnaha Basalt, 5.3%; Grande Ronde Basalt, 72.3%; Wanapum Basalt, 5.9%, and Saddle Mountains Basalt, 1.2%), and each of these has been subdivided into 2-24 stratigraphic members based on mineralogy, geochemistry, and paleomagnetic signature. Volume estimates exist for each member, consisting of 1-20 tholeiitic basalt to basaltic andesite lava flows (Reidel, 2015).

For decades, K-Ar and $^{40}Ar/^{39}Ar$ geochronology techniques have been used in order to assess the timing and duration of CRBG volcanism. However, large uncertainties (>1 Ma) in these analyses, with ages overlapping despite known stratigraphic order, have precluded the development of an unambiguous chronology. The most recent review of $^{40}Ar/^{39}Ar$ dates for the basalts (Figure 10) suggests an age model of Steens Basalt erupting from 16.9-16.7 Ma, the Imnaha Basalt from 16.7-16.0 Ma, the Grande Ronde Basalt from 16.0-15.6 Ma, the Wanapum Basalt from 15.6-15.0 Ma, and the Saddle

Mountains Basalt in small events between 15 and 6 Ma (Barry et al., 2013). This age model yields several inconsistencies with the Geomagnetic Polarity Timescale (GPTS) (Hilgen et al., 2012) – for example, the universally normally magnetized Imnaha Basalt would have erupted during an interval with two complete magnetic field reversals, while the Grande Ronde Basalt, which does exhibit two complete reversals, would have erupted during a reversed chron.

Recent high-precision geochronological studies using both $^{40}Ar/^{39}Ar$ and U-Pb methods have provided a reassessment of the CRBG age model. Since plagioclase phenocrysts extracted from basalt contain low concentrations of K_2O, and basaltic groundmass can be easily altered, Mahood & Benson (2017) performed $^{40}Ar/^{39}Ar$ geochronology on feldspar phenocrysts extracted from rhyolitic and trachytic tuffs intercalated with and below the Steens Basalt. Improving on the precision of prior studies by an order of magnitude, the oldest tuff in their study of the Main Scarp section of the southern Pueblo Mountains is dated at 16.699±0.028 Ma, and the youngest tuff is 16.601±0.048 Ma. Twenty-four lava flows comprising 230 m of section were emplaced between the tuffs, allowing for the calculation of an average eruption rate of 2.4 m/ka (1.3-11 ka at 95% confidence interval). With these constraints, they estimate that the Steens Basalt erupted from ~16.75-16.54 Ma, and that the Steens Mountain geomagnetic reversal occurred at 16.602±0.028 Ma (all dates re-calculated with Fish Canyon Sanidine age of 28.201, (Kuiper et al., 2008), and expressed with 2σ model error).

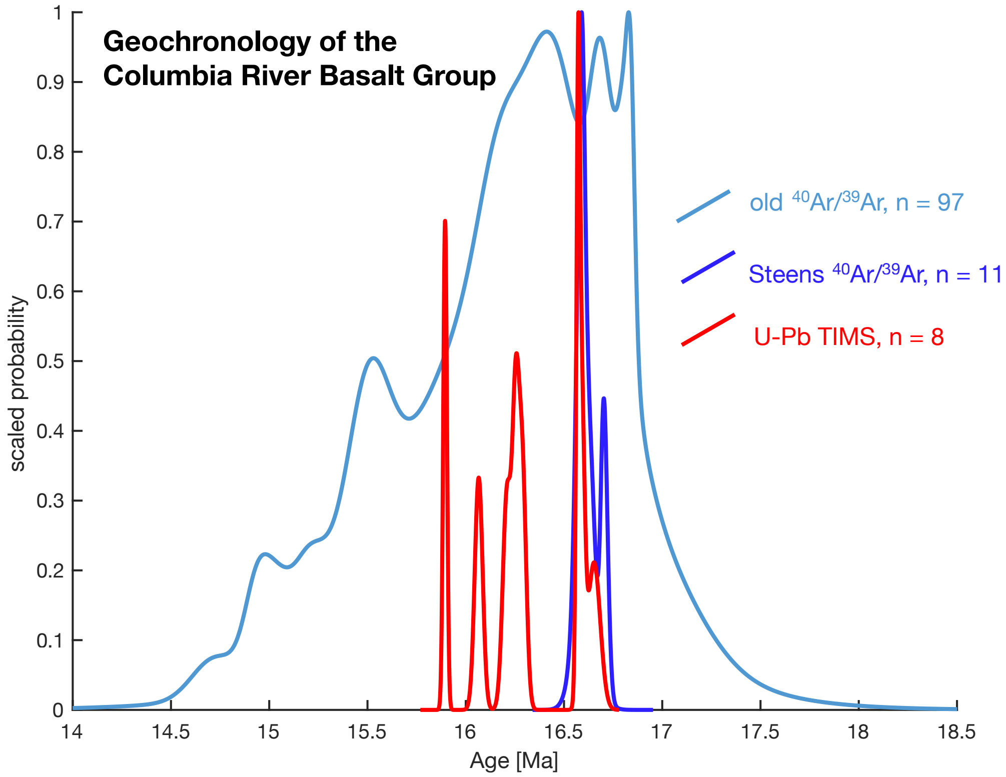

Figure 10: **CRBG geochronology.** Probability density function for ^{40}Ar/^{39}Ar and U-Pb ID-TIMS geochronology obtained for the CRBG, comparing the compilation of ^{40}Ar/^{39}Ar dates by Barry et al. (2013) to age constraints on the Steens Basalt (Mahood & Benson, 2017) and CRBG zircon geochronology (Kasbohm & Schoene, 2018). Dates for Saddle Mountains Basalt are omitted.

A similar approach was undertaken by Kasbohm & Schoene (2018), who extracted zircons from silicic ash beds interbedded throughout the CRBG stratigraphy, and dated them with U-Pb geochronology through CA-ID-TIMS. Zircon ages show that 95% of the eruptive volume was emplaced in 758±66 ka, 2.4 times faster than previous estimates (Camp, 2013), between 16.653±0.063 Ma in the Lower Steens Basalt, and 15.895±0.019 Ma in the upper Wanapum Basalt. Zircon dating in the Steens Basalt gives good agreement with the results of Mahood & Benson (2017). The volume estimates for CRBG stratigraphic members allow the calculation of an average effusion rate of 0.334±0.042 km^3/year for the Steens, Imnaha, and Grande Ronde Basalts; volcanism slows during the emplacement of the Wanapum Basalt, to a rate of 0.055±0.014 km^3/year. The samples also indicate at least one effusive pulse of volcanism; the Wapshilla Ridge Member, which comprises 20% of the total CRBG volume, was emplaced at an average rate of 1.18 km^3/year, though the dates for the top and bottom of the member overlap with ~30 ka precision, permitting extremely rapid eruption.

A connection between the emplacement of the CRBG and the ~17-15 Ma Miocene Climate Optimum (MCO) has long been suggested (Hodell & Woodruff, 1994). This interval was marked by elevated high-latitude sea surface temperatures 4-6°C above background (Shevenell et al., 2004), with a benthic $\delta^{18}O$ minimum, a benthic $\delta^{13}C$ maximum, and an inferred reduction in high-latitude ice sheet extent (Armstrong McKay et al., 2014). Vertebrates migrated poleward as temperatures warmed, with increased species originations (Böhme, 2003). A variety of pCO_2 proxy records, including stomata (Kürschner et al., 2008), alkenone (Zhang et al., 2013), and $\delta^{11}B$ (Foster et al., 2012) proxies indicate a possible doubling of atmospheric CO_2 levels to >400 ppm concurrent with the warming. CRBG volcanism has been suggested as the source of the CO_2 that led to this warming, and the prior age model for volcanism (Barry et al., 2013) offered a reasonable temporal overlap for these events.

However, there are no radiometric dates calibrating the timing and duration of the MCO, inhibiting an assessment of its connection to the CRBG, particularly in light of new high-precision age models for flood volcanism. The early- and middle-Miocene has proven to be the most difficult interval of the Neogene for establishing precise independent chronologies in the marine sediments that exhibit the MCO, due to problems obtaining undisturbed stratigraphic sections that yield reliable magnetostratigraphy, biostratigraphy, astronomical tuning, and radiometric ages (Hilgen et al., 2012). All Miocene time scales depend in some way on correlation with the GPTS, for which there are currently several proposals. The most recent, Geologic Time Scale 2012 (Hilgen et al., 2012), notes that the interval from 17-14 Ma is the only portion of the Neogene GPTS that is not calibrated by astronomical tuning of a core with reliable magnetostratigraphy. Instead, this interval was calibrated by seafloor anomaly profiles of the Antarctic and Australian plates, and assuming a relatively constant spreading rate to give a 23.03 Ma age for the Oligocene-Miocene boundary. Proxy records of the MCO use a variety of age models that yield conflicting accounts of the timing of the event, inhibiting the ability to compare its timing to that of CRBG eruptions (Foster et al., 2012; Holbourn et al., 2007, 2015).

In the absence of radiometric ages for the MCO, one way forward, as suggested by Kasbohm & Schoene (2018), may be to focus on MCO records with reliable magnetostratigraphy. By integrating U-Pb zircon dates into the magnetostratigraphic framework of the CRBG, Kasbohm & Schoene (2018) suggest four absolute age constraints on the ages of magnetic field reversals concurrent with CRBG eruption. These absolute ages differ from all prior calibrations of the GPTS, indicating that prior GPTS age models may be in error. However, isotopic records of the MCO that also yielded magnetostratigraphy may be aligned with the proposed GPTS recalibration, and compared to the zircon-derived age model for CRBG eruptions. At Sites 1090 (Billups et al., 2004; Channell et al., 2003) and U1335 (Kochhann et al., 2016), the decline in benthic $\delta^{18}O$, a proxy for deep-ocean temperature, occur in chron C5Cr, which is the same chron in which CRBG eruptions began with the Lower Steens Basalt, and reach a nadir during chrons C5Cn.3n-C5Cn.1r, during which time the Grande Ronde Basalt was erupting. The astronomically tuned record from U1335 suggests that the decline in $\delta^{18}O$ may have begun 100-200 ka before the onset of Steens eruptions. This offset may be explained by the onset of cryptic degassing of CO_2 as magma migrated through CRBG dike swarms (Armstrong McKay et al., 2014), or it may suggest that these events are unrelated. Further work improving age models for the MCO is required in order to determine its relationship to the CRBG.

Regardless of adjustments to individual proxy records that may occur through refining MCO age models, global proxy data (Zachos et al., 2008) indicate that the MCO continued for ~1 Ma after the termination of all but the smallest CRBG eruptions by 15.895±0.019 Ma (Kasbohm & Schoene, 2018). A continuation of warm temperatures following the cessation of volcanism may be explained by the long response time of the silicate weathering feedback, which may occur on 200-500 ka time scales (Stolper et al., 2016), allowing for volcanogenic CO_2 drawdown over 1 Ma. Alternatively, the CRBG may not be the primary driver for the MCO. Other explanations include changing dynamics of the East Antarctic Ice Sheet (Foster et al., 2012) and changes in global oceanic circulation (Holbourn et al., 2014).

DISCUSSION

Our review of high-precision geochronology of LIPs and their corresponding environmental perturbations permits new insights to be gained toward understanding the temporal overlap of these events (Figure 2), and potential patterns across these LIP/event couplets in three different areas: (1) the duration and dynamics of LIP magmatism; (2) correlation of LIP magmatism with mass extinctions and environmental change; and (3) challenges and future opportunities in geochronology to better assess how LIPs disrupt the Earth system.

Duration and dynamics of LIP magmatism

Continued improvement in the accuracy and precision of both U-Pb and $^{40}Ar/^{39}Ar$ geochronometers, and their widespread application to LIP rocks, have progressively narrowed estimates for the total duration of LIP emplacement in most cases (Figures 3-9). In particular, $^{40}Ar/^{39}Ar$ and K-Ar datasets published before *ca*. 2010 seemed to indicate eruption durations of at least several Ma for most LIPs, whereas recent refinements, predominantly by U-Pb geochronology, have drastically shortened that duration to < 1 Ma. This pattern of decreasing emplacement duration as age accuracy and precision increase applies to the Emeishan LIP, Siberian Traps, CAMP, Karoo-Ferrar, Deccan Traps, and CRBG. Improved LIP age models also agree with magneto- and cyclostratigraphic timescales, as demonstrated by new age models for the CAMP, Deccan Traps, and CRBG (Blackburn et al., 2013; Kasbohm & Schoene, 2018; Schoene et al., 2015), which yield ages for magnetic field reversals in the basalt stratigraphy that are largely concordant with reversal ages suggested by astronomical tuning (Kochhann et al., 2016; Westerhold et al., 2008), and, in the case of the CRBG, yield better agreement with reversal ages proposed by the Geologic Time Scale 2012 (Hilgen et al., 2012) than the most recent ^{40}Ar/^{39}Ar age model (Barry et al., 2013). While these LIPs are sourced from a variety of geodynamic processes (related to mantle plumes, continental rifting, or upwelling related to subduction), they seem to have been emplaced in a characteristically brief timeframe, placing constraints on how long voluminous eruptions can be sustained.

One notable exception to the < 1 Ma emplacement duration is the NAIP (Figure 9), which shows magmatism extending over several million years. The changing geographic locus of emplacement may result from the movement of the North American and Eurasian plates over the hotspot thought to supply magma, and/or a varying contribution of mid-ocean ridge magmatism to erupted volume. Meanwhile, the other LIPs described in this chapter lack sufficient high-precision geochronology to sufficiently resolve emplacement duration at the ~ 1 Ma level

In addition to a better understanding of overall emplacement duration, better dates have led to a more complete knowledge of the relative timing of intrusive and extrusive magmatism. For those LIPs with sufficiently high precision geochronology and comprehensive sample coverage to resolve the timing of intrusion and extrusion (Siberian Traps, CAMP, Ferrar LIP, and NAIP), all permutations are seen, indicating that there is no characteristic pattern for the order of intrusive and extrusive emplacement of LIPs. For example, in the Siberian Traps, “Stage 1” extrusive magmatism is followed by “Stage 2” intrusion, which is followed by contemporaneous intrusion and extrusion in “Stage 3”

(Burgess et al., 2017). For the CAMP, while further sampling may reveal new insights, currently geochronology is consistent with intrusion slightly predating extrusive magmatism, although both are ongoing through most of the LIP's duration (Davies et al., 2017; Figure 5). In the Ferrar, weighted mean ages for sills are mostly older than the dates for lavas, though there is considerable overlap among individual zircon analyses from lavas and sills (Burgess et al., 2015). In the case of the NAIP, the highest-precision dates indicate contemporaneous extrusive and intrusive magmatism throughout the relatively long duration of emplacement. However, U-Pb dates, which have been instrumental in refining the timelines of other LIPs, are still scarce in the NAIP. For the Franklin and Kalkarindji LIPs, high-precision dates have been obtained only from intrusive units (Cox et al., 2015; Jourdan et al., 2014; Macdonald et al., 2010), while in the Deccan Traps and CRBG, high-precision age constraints have been provided only for lava flows (Kasbohm & Schoene, 2018; Mahood & Benson, 2017; Schoene et al., 2015, 2019; Sprain et al., 2019). For the remaining LIPs, both intrusive and extrusive rocks have been dated, but these dates lack the precision necessary to discern the relative order of emplacement style.

Continued improvement in radiometric dating accuracy and precision has also led to hypotheses regarding eruptive pulses within the overall LIP emplacement duration. These pulses are manifested as short periods of high-tempo volcanism punctuating periods of relative quiescence, and have been documented via U-Pb geochronology in the Siberian Traps, CAMP, Deccan Traps, and CRBG. The CAMP age model of Blackburn et al. (2013) suggests CAMP emplacement in three discrete pulses over an ~700 kyr emplacement duration, with the astrochronologically determined timing and duration of hiatuses (totaling ~600 ka) supported by U-Pb zircon dates. Similarly, Schoene et al. (2019) propose Deccan Traps emplacement occurred in four high-output pulses, with durations ranging from 50-200 ka, while Kasbohm & Schoene (2018) suggest that the emplacement of the Wapshilla Ridge Member of the CRBG, which comprises 20% of the total LIP volume, likely occurred over tens of ka. In the Siberian Traps, a study of magnetic secular variation suggests that a large portion of magma was emplaced in as little as ~10 ka, though this estimate does not take into account the length of hiatuses (Pavlov et al., 2019). Models for pulsed eruptions of LIPs need to be tested with additional geochronology from a broader area to test whether the apparent hiatuses are simply changes in depositional locations or eruptive center migration. This is a challenge given the large geographic distribution of LIPs and also variable preservation.

Correlation of LIP magmatism with environmental change and biotic extinctions

While a broad temporal overlap of LIPs and environmental perturbations was once sufficient to hypothesize a causal relationship (e.g., Courtillot & Renne, 2003), progressively higher precision geochronology of LIPs and their corresponding crises has enabled a more detailed interrogation of this hypothesis. In Figure 2, we present the relative timing (zero is set as the age or midpoint timing of environmental event) and total duration of each event, incorporating the most recent geochronology (with 2σ uncertainty). This visualization shows the progress made in assessing the relative timing of these events and the plausibility of a causal connection, as well as fruitful areas to pursue future work. While all of the pairs of events show temporal overlap, for many, uncertain age constraints on at least one of the events hinders the assessment of the possible effects of LIP emplacement. A minority of pairs have high-precision age constraints for both events: Siberian Traps/End-Permian Extinction, CAMP/End-Triassic Extinction, Deccan Traps/End-Cretaceous Extinction, and the CRBG/MCO. The CRBG and MCO show the as-yet unique relationship of the climate event apparently beginning before LIP volcanism, though it is necessary to obtain absolute age constraints on the MCO in addition to its current astronomical calibration. If the MCO were shown to begin before CRBG emplacement, it would suggest that either other processes, such as changing ocean circulation patterns and fluctuations in the East Antarctic Ice Sheet, were more important in driving the MCO (Foster et al., 2012; Holbourn et al., 2014), or that cryptic degassing of the CRBG affected climate prior to the start of extrusive volcanism (Kasbohm & Schoene, 2018). Efforts to find evidence for cryptic degassing in other LIPs are described in the following section, and could be applied to the CRBG.

For the other three couplets (Siberian Traps, CAMP, and Deccan), geochronology suggests emplacement beginning ~100-300 ka prior to the onset of corresponding extinction. For the Siberian Traps, Svensen et al. (2009) propose that the most lethal aspect of the LIP was widespread sill emplacement into an organic-rich sedimentary basin, and Burgess et al. (2017) observe that the end-Permian extinction coincides with the beginning of emplacement Stage 2, dominated by sill emplacement. For the CAMP, the timing of the first intrusive emplacement in western Africa and sill emplacement into an organic-rich basin in Brazil also overlaps with the End-Triassic Extinction (Davies et al., 2017; Heimdal et al., 2018). In the Deccan Traps, Schoene et al. (2019) resolve the largest pulse of Deccan volcanism immediately before the end-Cretaceous mass extinction, suggesting that the LIP may have played a role, along with the Chicxulub impact, in creating catastrophic conditions for the biosphere. The Deccan Traps emplacement and the K-Pg event do not adhere to the model of Burgess et al. (2017), which argues that the emplacement of sills into a volatile-rich sedimentary basin makes a LIP deadly, rather than voluminous extrusive volcanism or dyke emplacement. A significant volume of intrusive rocks have not been described, and the rocks through which the Deccan was emplaced are not obviously volatile-rich relative to those of the Siberian Traps, leading Burgess et al. (2017) to suggest that the Chicxulub impact would have played an equal if not greater role in causing the extinction as Deccan emplacement. Alternatively, the pronounced increase in Deccan effusion rate just prior to extinction (Schoene et al., 2019) would have been accompanied by more rapid loading of deadly gases into the atmosphere, potentially creating high-stress conditions immediately prior to the Chicxulub impact.

Broadly, Figure 2 and the information reviewed above allow LIP – environmental crisis couplets to be divided into three groups: (1) LIPs connected to mass extinctions (Kalkarindji, Yakutsk-Vilyui, Emeishan, Siberian, CAMP, Deccan), (2) LIPs associated with oceanic anoxic events (Karoo-Ferrar, OJP, Caribbean LIP), and (3) LIPs related to global climate perturbations without mass extinction or oceanic anoxic events (Franklin, NAIP, CRBG). With existing datasets, it is premature to develop a single general model describing why certain LIPs drive specific environmental feedbacks. For example, LIP size doesn’t seem a uniquely deadly trait, as the largest LIP, OJP, was not the most deadly to the biosphere, though its underwater emplacement seems to have disrupted ocean chemistry (Naafs et al., 2016). Nor is duration a unique indicator of deadliness, as the CRBG is of comparable lifespan to the Siberian Traps, CAMP, and Deccan Traps, but is not related to a mass extinction, though it is disputed whether the Deccan Traps played a role in the end-Cretaceous extinction. In every case, the duration of LIP volcanism continues beyond the age of the extinction, indicating that the simple presence of magmatic activity is insufficient to create lasting climatic distress; other aspects of LIP emplacement, such as effusion rate or emplacement style, are likely to drive the short-lived perturbations. While the Franklin LIP’s original location in the tropics is hypothesized to be a necessary condition for the onset of the Sturtian Snowball Earth through CO_2 drawdown via silicate weathering (Goddéris et al., 2003; Macdonald et al., 2010), this mechanism does not explain why larger LIPs that were emplaced at the equator (Kalkarindji LIP, CAMP, Caribbean LIP, Deccan Traps) did not also cause similarly dramatic global cooling events. It is likely that the effect a LIP had on the climate and biosphere is at least partly a reflection of the weaknesses inherited in that particular climate or ecosystem state, which have yet to be fully characterized. Further high-precision geochronology in conjunction with development of paleoclimate and biostratigraphic records, and a better understanding of the causes, isotopic composition, and quantity of volatile release will be necessary to improve our understanding of the temporal connection between LIPs and their corresponding environmental catastrophes.

Challenges and Future Opportunities

Geological limitations to improving LIP geochronology occur on macroscopic and microscopic scales. At the macroscopic scale, there is a limit to stratigraphically comprehensive sample collection due to access (particularly for oceanic LIPs), and in some cases, to erosive or depositional processes, which may eliminate much of the LIP stratigraphy from the rock record. At the microscopic scale, obtaining precise geochronology depends on finding the necessary minerals. ^{40}Ar/^{39}Ar studies require unaltered minerals, and even when ideal minerals are isolated, can still be hindered by a lack of radiogenic parent isotope and therefore low precision. While U-Pb ID-TIMS zircon studies yield ages with greater precision, they can only be applied to LIPs from which zircons can be extracted from gabbroic segregations or interbedded ashes. A promising approach to improving the precision of ^{40}Ar/^{39}Ar geochronology of LIPs may also lie in targeting interbedded ash deposits that contain K-feldspar, which can yield much higher precision than plagioclase (Mahood & Benson, 2017), though it may be prone to similar issues of pre-eruptive residence time as seen in zircon geochronology of ashes (Andersen et al., 2017).

For many LIPs, these geological limitations have impeded the calculation of magmatic volumes and the creation of a detailed timeline for eruptions across the original horizontal extent of the LIP and the vertical stratigraphy of eruptions. For example, the limited exposure and relatively low-precision ages of the Kalkarindji LIP make it difficult to ascertain the overall duration of volcanism and the total volume emplaced; current geochronology permits this LIP to have erupted rapidly or over ~ 10 Ma (Figure 2). Well-established volcanostratigraphies based on geochemistry and magnetic polarity of the basalts have been constructed for only a minority of LIPs (e.g., Siberian Traps, CAMP, Deccan Traps, CRBG), as both widespread exposure and somewhat complete vertical sections remain for these events. Without this detail, however, it is difficult to assess volumetric eruptive rates, which may be as important as overall emplacement volume to the environmental impact of LIPs.

Geological limitations may also affect the age calibration of environmental events, as radiometric dating of these events would require volcanic ash deposition in the middle of the sedimentary successions in which they are recorded, which is rarely the case. Future geochronological studies of environmental crises would also benefit from a horizontal approach, which would assess the synchroneity of an event across different geographic locations (e.g., Baresel et al., 2017a, 2017b; Schoene et al., 2010), as well as a vertical approach, which would provide a greater number of dates constraining not only an extinction horizon, but also any biogeochemical or paleoecological changes that occur before or after that horizon (e.g., Maclennan et al., 2018; Shen et al., 2018; Du Vivier et al., 2015). When radiometric dating cannot be used to constrain the timing of environmental events, astronomical tuning methods may be effectively used to obtain age models, specifically in the Cenozoic for events like the MCO (Kochhann et al., 2016). Improving assessments of the timing, duration, and synchrony of these events at a global scale will not only yield greater insights into their connection to LIP emplacement, but also will provide better temporal constraints to calibrate future versions of the Geologic Time Scale.

Overcoming analytical limitations will also be necessary to provide more detailed assessments of the timescales of LIP eruption and environmental change. Even with methodological advances yielding U-Pb zircon ages with precision to better than ±0.1%, this resolution is inadequate to address the relative order of LIPs and climatic perturbations that are several hundred Ma old. For younger LIPs, such as the Deccan Traps and CRBG, with geochronological uncertainty on the order of 10-30 ka, a more nuanced account of LIP eruptions can be generated, which indicates rapid pulses of voluminous eruptions and periods of relatively slow, or quiescent eruptions (Kasbohm & Schoene, 2018; Schoene et al., 2019). If analytical limits to absolute precision for eruption and emplacement dates can be overcome, it might be possible to observe such pulsed volcanism in older LIPs.

With new high-precision geochronology improving age constraints on both LIP emplacement and environmental perturbations, demonstrating a simple age overlap for event couplets is insufficient to assess whether or not LIPs play a causative role in these events. Instead, it becomes essential to consider the timing and timescales of different climatic effects of LIPs that may not be recorded in the rock record, such as volatile, aerosol, and particulate release, acid rain, and ozone depletion, and how these are temporally related to intrusive and extrusive LIP emplacement. The effects of ozone depletion from Cl_2, acid rain, and cooling due to sulfate aerosols occur on the timescales of months to years (Wignall, 2001), far below both the analytical precision of today’s most precise radiometric ages and the typical temporal resolution of the rock record. The environmental effects of CO_2 release, evident on 10 ka–100 ka timescales (Wignall, 2001) may be more easily captured by pCO_2 proxy records, and compared to LIP emplacement age models with 10 ka–100 ka resolution. With this resolution already obtained, these age models provide crucial temporal constraints for researchers seeking to model the environmental effects of LIP volcanism.

To constrain the timing of CO_2 liberation from LIPs, it may be possible to date rocks that show geological evidence for degassing. For example, Svensen et al. (2010) performed U-Pb zircon geochronology on NAIP sills sampled in drill core offshore Norway, which contain contact aureoles indicative of violent gas release from organic-rich host sediments, as well as a connection to hydrothermal vent complexes; these ages thereby constrain the timing of degassing. Obtaining ages for other intrusive units in contact with metamorphosed organic-rich sediments, for which studies have modeled the amount of CO_2 and methane released (Aarnes et al., 2011; Ganino & Arndt, 2009), would be a fruitful target for future geochronology. Stratigraphic proxy records, such as Hg concentration in sediments and osmium isotope records (Bottini et al., 2012; Tejada et al., 2009; Turgeon & Creaser, 2008; Du Vivier et al., 2014), are proving to be promising for identifying volcanic episodes in sedimentary basins that are distant from LIPs .

The goal of this review was to show how high-precision geochronology has progressively reinforced and refined temporal correlations between LIP emplacement and global environmental perturbations, and to seek out patterns in LIP eruption that may suggest when and how LIPs directly trigger these perturbations. The relative efficacy of various

LIP characteristics (area, volume, effusion rate, host rock composition) in driving situational change is dependent on a number of factors, paramount of which is accurately knowing the timing and duration of both events to a level of precision on par or better than the durations of the events themselves. As discussed, this has been and continues to be a main goal of the broader geochronologic community. Without accurate and precise dates and rates, the detailed role of LIPs in driving environmental change, and why some LIPs are more deadly than others, will remain frustratingly opaque.

ACKNOWLEDGMENTS

We thank Richard Ernst for inviting our participation in this volume and for great editorial support and extreme patience as we prepared this manuscript. Constructive reviews by Lawrence Percival, Josh Davies, and Mark Stelten improved the quality of the manuscript. We would also like to thank Sam Bowring, who as a leader in the field of geochronology worked tirelessly to push the accuracy and precision of geochronometers to new levels. His work, embraced by the LIP and mass extinction research communities, has led to unprecedented clarity on when and how volcanism and environmental change are linked, and has, as a result, begged questions of incredible detail and nuance that future workers endeavor to answer. We owe Sam a great debt of gratitude for the leadership and mentorship he has shown us, and the benefits of his work to the broader community striving to understand links between the geosphere and biosphere are immeasurable.

SUPPLEMENTAL TABLES (following References)

Table 1: High-Precision Geochronology of LIPs. This table compiles individual high-precision ages of LIPs, with stratigraphic and geographic context, the method by which an age was obtained, statistical information required to report the appropriate uncertainty, and references to the original studies in which these ages were presented. For comprehensive summaries of high-quality ^{40}Ar/^{39}Ar geochronology from the CAMP and NAIP, readers are directed to Marzoli et al. (2018, 2019) and Wilkinson et al. (2017). All U-Pb studies included are U-Pb CA-ID-TIMS. Abbreviations for Mineral: a = anorthoclase, b = baddeleyite, pl = plagioclase, ps = perovskite, s = sanidine, z = zircon. Abbreviations for Age interpretation: WMA = weighted mean age; WMA-YF = weighted mean age of youngest few zircons; YZ = youngest zircon; TPB = triangular prior in Bayesian age model. Abbreviations for Tracer/Standard used: ET = EARTHTIME; FCs = Fish Canyon Sanidine; BGC = Berkeley Geochronology Center tracer.

Table 2: High-Precision Geochronology of Environmental Events. This table compiles individual high-precision ages of global change events, with stratigraphic and geographic context, the method by which an age was obtained, statistical information required to report the appropriate uncertainty, and references to the original studies in which these ages were presented. All U-Pb studies included are U-Pb CA-ID-TIMS. Abbreviations for Mineral: a = anorthoclase, af = alkali feldspar, z = zircon. Abbreviations for Age interpretation: MCMC = Markov Chain Monte Carlo; WMA = weighted mean age; WMA-YF = weighted mean age of youngest few zircons; YZ = youngest zircon. Abbreviations for Tracer/Standard used: ET = EARTHTIME; FCs = Fish Canyon Sanidine.

REFERENCES

Aarnes, I., Svensen, H. H., Polteau, S., & Planke, S. (2011). Contact metamorphic devolatilization of shales in the Karoo Basin, South Africa, and the effects of multiple sill intrusions. *Chemical Geology*. https://doi.org/10.1016/j.chemgeo.2010.12.007

Al-Suwaidi, A. H., Angelozzi, G. N., Baudin, F., Damborenea, S. E., Hesselbo, S. P., Jenkyns, H. C., et al. (2010). First record of the Early Toarcian Oceanic Anoxic Event from the Southern Hemisphere, Neuquén Basin, Argentina. *Journal of the Geological Society*, *167*(4), 633–636. https://doi.org/10.1144/0016-76492010-025

Algeo, T. J., & Scheckler, S. E. (1998). Terrestrial-marine teleconnections in the Devonian: links between the evolution of land plants, weathering processes, and marine anoxic events. *Philosophical Transactions of the Royal Society of London. Series B: Biological Sciences*, *353*(1365), 113–130. https://doi.org/10.1098/rstb.1998.0195

Ali, J. R., Thompson, G. M., Song, X., & Wang, Y. (2002). Emeishan Basalts (SW China) and the 'end-Guadalupian' crisis: magnetobiostratigraphic constraints. *Journal of the Geological Society*. https://doi.org/10.1144/0016-764901086

Allègre, C. J., Birck, J. L., Capmas, F., & Courtillot, V. E. (1999). Age of the Deccan traps using ^{187}Re–^{187}Os systematics. *Earth and Planetary Science Letters*, *170*(3), 197–204. https://doi.org/10.1016/S0012-821X(99)00110-7

Andersen, N. L., Jicha, B. R., Singer, B. S., & Hildreth, W. (2017). Incremental heating of Bishop Tuff sanidine reveals preeruptive radiogenic Ar and rapid remobilization from cold storage. *Proceedings of the National Academy of Sciences of the United States of America*, *114*(47), 12407–12412. https://doi.org/10.1073/pnas.1709581114

Armstrong McKay, D. I., Tyrrell, T., Wilson, P. A., & Foster, G. L. (2014). Estimating the impact of the cryptic degassing of Large Igneous Provinces: A mid-Miocene case-study. *Earth and Planetary Science Letters*, *403*, 254–262. https://doi.org/10.1016/j.epsl.2014.06.040

Baksi, A. K. (1994). Geochronological studies on whole-rock basalts, Deccan Traps, India: evaluation of the timing of volcanism relative to the K-T boundary. *Earth and Planetary Science Letters*, *121*(1–2), 43–56. https://doi.org/10.1016/0012-821X(94)90030-2

Baksi, A. K. (2014). ^{40}Ar/^{39}Ar ages of flood basalt provinces in Russia and China and their possible link to global faunal extinction events: A cautionary tale regarding alteration and loss of ^{40}Ar*. *Journal of Asian Earth Sciences*. https://doi.org/10.1016/j.jseaes.2013.07.029

Baksi, A. K., & Archibald, D. A. (1997). Mesozoic igneous activity in the Maranhão province, northern Brazil: ^{40}Ar/^{39}Ar evidence for separate episodes of basaltic magmatism. *Earth and Planetary Science Letters*, *151*(3–4), 139–153.

Baksi, A. K., & Farrar, E. (1991). 40Ar/39Ar dating of the Siberian Traps, USSR: evaluation of the ages of the two major extinction events relative to episodes of flood-basalt volcanism in the USSR and the Deccan Traps, India. *Geology*, *19*(5), 461–464. https://doi.org/10.1130/0091-7613(1991)019<0461:ADOTST>2.3.CO

Baresel, B., D'Abzac, F. X., Bucher, H., & Schaltegger, U. (2017a). High-precision time-space correlation through coupled apatite and zircon tephrochronology: An example from the Permian-Triassic boundary in South China. *Geology*, *45*(1), 83–86. https://doi.org/10.1130/G38181.1

Baresel, B., Bucher, H., Bagherpour, B., Brosse, M., Guodun, K., & Schaltegger, U. (2017b). Timing of global regression and microbial bloom linked with the Permian-Triassic boundary mass extinction: Implications for driving mechanisms. *Scientific Reports*, *7*(43630), 1–8. https://doi.org/10.1038/srep43630

Barnet, J. S. K., Littler, K., Kroon, D., Leng, M. J., Westerhold, T., Röhl, U., & Zachos, J. C. (2017). A new high-resolution chronology for the late Maastrichtian warming event: Establishing robust temporal links with the onset of Deccan volcanism. *Geology*, *46*(2), 147–150. https://doi.org/10.1130/G39771.1

Barry, T. L., Kelley, S. P., Camp, V. E., Self, S., Jarboe, N. A., & Duncan, R. A. (2013). Eruption chronology of the Columbia River Basalt Group. *Geological Society of America Special Paper*, *497*, 45–66. https://doi.org/10.1130/2013.2497(02).

Basu, A. R., Poreda, R. J., Renne, P. R., Teichmann, F., Vasiliev, Y. R., Sobolev, N. V, & Turrin, B. D. (1995). High-3He plume origin and temporal-spatial evolution of the Siberian flood basalts. *Science*, *269*(5225), 822–825. https://doi.org/10.1126/science.269.5225.822

Beane, J. E., Turner, C. A., Hooper, P. R., Subbarao, K. V., & Walsh, J. N. (1986). Stratigraphy, composition and form of the Deccan Basalts, Western Ghats, India. *Bulletin of Volcanology*, *48*(1), 61–83. https://doi.org/10.1007/BF01073513

Becker, T. R., Gradstein, F. M., & Hammer, Ø. (2012). The Devonian Period. In *The*

Geologic Time Scale 2012. https://doi.org/10.1016/B978-0-444-59425-9.00022-6

Bertrand, H. (1991). The Mesozoic Tholeiitic Province of Northwest Africa: A Volcano-Tectonic Record of the Early Opening of Central Atlantic. In *Magmatism in Extensional Structural Settings* (pp. 147–188). Berlin, Heidelberg: Springer Berlin Heidelberg. https://doi.org/10.1007/978-3-642-73966-8_7

Besse, J., & Courtillot, V. E. (1988). Paleogeographic maps of the continents bordering the Indian Ocean since the Early Jurassic. *Journal of Geophysical Research: Solid Earth*, *93*(B10), 11791–11808. https://doi.org/10.1029/JB093iB10p11791

Billups, K., Pälike, H., Channell, J. E. T., Zachos, J. C., & Shackleton, N. J. (2004). Astronomic calibration of the late Oligocene through early Miocene geomagnetic polarity time scale. *Earth and Planetary Science Letters*, *224*(1–2), 33–44. https://doi.org/10.1016/j.epsl.2004.05.004

Black, B. A., Neely, R. R., Lamarque, J. F., Elkins-Tanton, L. T., Kiehl, J. T., Shields, C. A., et al. (2018). Systemic swings in end-Permian climate from Siberian Traps carbon and sulfur outgassing. *Nature Geoscience*. https://doi.org/10.1038/s41561-018-0261-y

Blackburn, T. J., Olsen, P. E., Bowring, S. A., McLean, N. M., Kent, D. V., Puffer, J. H., et al. (2013). Zircon U-Pb geochronology links the end-Triassic extinction with the Central Atlantic magmatic Province. *Science*. https://doi.org/10.1126/science.1234204

Böhme, M. (2003). The Miocene Climatic Optimum: Evidence from ectothermic vertebrates of Central Europe. *Palaeogeography, Palaeoclimatology, Palaeoecology*, *195*(3–4), 389–401. https://doi.org/10.1016/S0031-0182(03)00367-5

Bottini, C., Cohen, A. S., Erba, E., Jenkyns, H. C., & Coe, A. L. (2012). Osmium-isotope evidence for volcanism, weathering, and ocean mixing during the early Aptian OAE 1a. *Geology*, *40*(7), 583–586. https://doi.org/10.1130/G33140.1

Boulila, S., Galbrun, B., Huret, E., Hinnov, L. A., Rouget, I., Gardin, S., & Bartolini, A. (2014). Astronomical calibration of the Toarcian Stage: Implications for sequence stratigraphy and duration of the early Toarcian OAE. *Earth and Planetary Science Letters*, *386*, 98–111. https://doi.org/10.1016/j.epsl.2013.10.047

Bowring, S. A., Erwin, D. H., Jin, Y. G., Martin, M. W., Davidek, K. L., & Wang, W. (1998). U/Pb zircon geochronology and tempo of the end-Permian mass extinction. *Science*. https://doi.org/10.1126/science.280.5366.1039

Bryan, S. E., & Ferrari, L. (2013). Large igneous provinces and silicic large igneous provinces: Progress in our understanding over the last 25 years. *Bulletin of the Geological Society of America*. https://doi.org/10.1130/B30820.1

Burgess, S. D., & Bowring, S. A. (2015). High-precision geochronology confirms voluminous magmatism before, during, and after Earth's most severe extinction. *Science Advances*, *1*(7), e1500470–e1500470. https://doi.org/10.1126/sciadv.1500470

Burgess, S. D., Bowring, S. A., & Shen, S. (2014). High-precision timeline for Earth's most severe extinction. *Proceedings of the National Academy of Sciences of the United States of America*, *111*(9), 3316–21. https://doi.org/10.1073/pnas.1317692111

Burgess, S. D., Bowring, S. A., Fleming, T. H., & Elliot, D. H. (2015). High-precision geochronology links the Ferrar large igneous province with early-Jurassic ocean anoxia and biotic crisis. *Earth and Planetary Science Letters*, *415*, 90–99. https://doi.org/10.1016/j.epsl.2015.01.037

Burgess, S. D., Muirhead, J. D., & Bowring, S. A. (2017). Initial pulse of Siberian Traps sills as the trigger of the end-Permian mass extinction. *Nature Communications*, *8*(1), 164. https://doi.org/10.1038/s41467-017-00083-9

Callegaro, S., Marzoli, A., Bertrand, H., Blichert-Toft, J., Reisberg, L., Cavazzini, G., et al. (2017). Geochemical constraints provided by the Freetown Layered Complex (Sierra Leone) on the origin of high-ti tholeiitic CAMP magmas. *Journal of Petrology*, *58*(9), 1811–1840. https://doi.org/10.1093/petrology/egx073

Camp, V. E. (2013). Origin of Columbia River Basalt: Passive rise of shallow mantle, or active upwelling of a deep-mantle plume? *Geological Society of America Special Paper*, *497*, 181–199. https://doi.org/10.1130/2013.2497(07).

Campbell, I. H., Czamanske, G. K., Fedorenko, V. A., Hill, R. I., & Stepanov, V. (1992). Synchronism of the Siberian Traps and the Permian-Triassic Boundary. *Science*, *258*(5089), 1760–3. https://doi.org/10.1126/science.258.5089.1760

Chambers, L. M., Pringle, M. S., & Fitton, J. G. (2002). Age and duration of magmatism on the Ontong Java Plateau: ^{40}Ar-^{39}Ar results from ODP Leg 192. In *American Geophysical Union Fall Meeting Abstracts* (pp. V71B-1271).

Chambers, L. M., Pringle, M. S., & Fitton, J. G. (2004). Phreatomagmatic eruptions on the Ontong Java Plateau: An Aptian ^{40}Ar/^{39}Ar age for volcaniclastic rocks at ODP Site 1184. *Geological Society Special Publication*, *229*, 325–331. https://doi.org/10.1144/GSL.SP.2004.229.01.18

Chambers, L. M., Pringle, M. S., & Parrish, R. R. (2005). Rapid formation of the Small Isles Tertiary centre constrained by precise ^{40}Ar/^{39}Ar and U-Pb ages. *Lithos*, *79*, 367–384.

Channell, J. E. T., Erba, E., Nakanishi, M., & Tamaki, K. (1995). Late Jurassic-early Cretaceous time scales and oceanic magnetic anomaly block models. *Geochronology, Time Scales and Global Stratigraphic Correlation*.

Channell, J. E. T., Galeotti, S., Martin, E. E., Billups, K., Scher, H. D., & Stoner, J. S. (2003). Eocene to Miocene magnetostratigraphy, biostratigraphy, and chemostratigraphy at ODP site 1090 (sub-Antarctic South Atlantic). *Bulletin of the Geological Society of America*, *115*(5), 607–623. https://doi.org/10.1130/0016-7606(2003)115<0607:ETMMBA>2.0.CO;2

Charles, A. J., Condon, D. J., Harding, I. C., Pälike, H., Marshall, J. E. A., Cui, Y., et al. (2011). Constraints on the numerical age of the Paleocene-Eocene boundary. *Geochemistry, Geophysics, Geosystems*, *12*(6). https://doi.org/10.1029/2010GC003426

Chen, B., Joachimski, M. M., Sun, Y., Shen, S., & Lai, X. (2011). Carbon and conodont apatite oxygen isotope records of Guadalupian-Lopingian boundary sections: Climatic or sea-level signal? *Palaeogeography, Palaeoclimatology, Palaeoecology*, *311*(3–4), 145–153. https://doi.org/10.1016/j.palaeo.2011.08.016

Chenet, A.-L., Quidelleur, X., Fluteau, F. F., Courtillot, V. E., & Bajpai, S. (2007). ^{40}K-^{40}Ar dating of the Main Deccan large igneous province: Further evidence of KTB age and short duration. *Earth and Planetary Science Letters*, *263*(1–2), 1–15. https://doi.org/10.1016/j.epsl.2007.07.011

Chenet, A.-L., Fluteau, F. F., Courtillot, V. E., Gérard, M., & Subbarao, K. V. (2008).

Determination of rapid Deccan eruptions across the Cretaceous-Tertiary boundary using paleomagnetic secular variation: Results from a 1200-m-thick section in the Mahabaleshwar escarpment. *Journal of Geophysical Research*, *113*(B4). https://doi.org/10.1029/2006jb004635

Chenet, A.-L., Courtillot, V. E., Fluteau, F. F., Gérard, M., Quidelleur, X., Khadri, S. F. R., et al. (2009). Determination of rapid Deccan eruptions across the Cretaceous-Tertiary boundary using paleomagnetic secular variation: 2. Constraints from analysis of eight new sections and synthesis for a 3500-m-thick composite section. *Journal of Geophysical Research: Solid Earth*, *114*(6). https://doi.org/10.1029/2008JB005644

Cirilli, S., Marzoli, A., Tanner, L. H., Bertrand, H., Buratti, N., Jourdan, F., et al. (2009). Latest Triassic onset of the Central Atlantic Magmatic Province (CAMP) volcanism in the Fundy Basin (Nova Scotia): New stratigraphic constraints. *Earth and Planetary Science Letters*, *286*(3–4), 514–525. https://doi.org/10.1016/j.epsl.2009.07.021

Clyde, W. C., Ramezani, J., Johnson, K. R., Bowring, S. A., & Jones, M. M. (2016). Direct high-precision U–Pb geochronology of the end-Cretaceous extinction and calibration of Paleocene astronomical timescales. *Earth and Planetary Science Letters*, *452*, 272–280. https://doi.org/10.1016/j.epsl.2016.07.041

Condon, D. J., Schoene, B., McLean, N. M., Bowring, S. A., & Parrish, R. R. (2015). Metrology and traceability of U-Pb isotope dilution geochronology (EARTHTIME Tracer Calibration Part I). *Geochimica et Cosmochimica Acta*, *164*, 464–480. https://doi.org/10.1016/j.gca.2015.05.026

Corfu, F., Polteau, S., Planke, S., Faleide, J. I., Svensen, H. H., Zayoncheck, A., & Stolbov, N. (2013). U–Pb geochronology of Cretaceous magmatism on Svalbard and Franz Josef Land, Barents Sea Large Igneous Province. *Geological Magazine*, *150*(6), 1127–1135. https://doi.org/10.1017/S0016756813000162

Corfu, F., Svensen, H. H., & Mazzini, A. (2016). Comment to paper: Evaluating the temporal link between the Karoo LIP and climatic–biologic events of the Toarcian Stage with high-precision U–Pb geochronology by Bryan Sell, Maria Ovtcharova, Jean Guex, Annachiara Bartolini, Fred Jourdan, Jorge E. Spangen. *Earth and Planetary Science Letters*, *434*, 349–352. https://doi.org/10.1016/j.epsl.2015.07.010

Courtillot, V. E., & Renne, P. R. (2003). On the ages of flood basalt events. *Comptes Rendus - Geoscience*, *335*(1), 113–140. https://doi.org/10.1016/S1631-0713(03)00006-3

Courtillot, V. E., Besse, J., Vandamme, D., Montigny, R., Jaeger, J.-J., & Cappetta, H. (1986). Deccan flood basalts at the Cretaceous/Tertiary boundary? *Earth and Planetary Science Letters*, *80*(3–4), 361–374. https://doi.org/http://dx.doi.org/10.1016/0012-821X(86)90118-4

Courtillot, V. E., Feraud, G., Maluski, H., Vandamme, D., Moreau, M. G., & Besse, J. (1988). Deccan flood basalts and the Cretaceous/Tertiary boundary. *Nature*, *333*(6176), 843–846. Retrieved from http://dx.doi.org/10.1038/333843a0

Courtillot, V. E., Gallet, Y., Rocchia, R., Féraud, G., Robin, E., Hofmann, C., et al. (2000). Cosmic markers, 40Ar/39Ar dating and paleomagnetism of the KT sections in the Anjar Area of the Deccan large igneous province. *Earth and Planetary Science Letters*, *182*(2), 137–156. https://doi.org/10.1016/S0012-821X(00)00238-7

Courtillot, V. E., Kravchinsky, V. A., Quidelleur, X., Renne, P. R., & Gladkochub, D. P. (2010). Preliminary dating of the Viluy traps (Eastern Siberia): Eruption at the time of Late Devonian extinction events? *Earth and Planetary Science Letters*, *300*(3–4), 239–245. https://doi.org/10.1016/j.epsl.2010.09.045

Cox, G. M., Strauss, J. V., Halverson, G. P., Schmitz, M. D., McClelland, W. C., Stevenson, R. S., & Macdonald, F. A. (2015). Kikiktat volcanics of Arctic Alaska—Melting of harzburgitic mantle associated with the Franklin large igneous province. *Lithosphere*. https://doi.org/10.1130/L435.1

Cox, K. G. (1988). The Karoo Province (pp. 239–271). Springer, Dordrecht. https://doi.org/10.1007/978-94-015-7805-9_7

Cui, Y., Kump, L. R., Ridgwell, A. J., Charles, A. J., Junium, C. K., Diefendorf, A. F., et al. (2011). Slow release of fossil carbon during the Palaeocene–Eocene Thermal Maximum. *Nature Geoscience*, *4*(7), 481–485. https://doi.org/10.1038/ngeo1179

Dalrymple, G. B., Czamanske, G. K., Fedorenko, V. A., Simonov, O. N., Lanphere, M. A., & Likhachev, A. P. (1995a). A reconnaissance ^{40}Ar^{39}Ar geochronologic study of ore-bearing and related rocks, Siberian Russia. *Geochimica et Cosmochimica Acta*, *59*(10), 2071–2083. https://doi.org/10.1016/0016-7037(95)00127-1

Dalrymple, G. B., Czamanske, G. K., Fedorenko, V. A., Simonov, O. N., Lanphere, M. A., & Likhachev, A. P. (1995b). A reconnaissance 40Ar39Ar geochronologic study of ore-bearing and related rocks, Siberian Russia. *Geochimica et Cosmochimica Acta*, *59*(10), 2071–2083. https://doi.org/10.1016/0016-7037(95)00127-1

Davies, J. H. F. L., Marzoli, A., Bertrand, H., Youbi, N., Ernesto, M., & Schaltegger, U. (2017). End-Triassic mass extinction started by intrusive CAMP activity. *Nature Communications*, *8*, 15596. https://doi.org/10.1038/ncomms15596

Day, M. O., Ramezani, J., Bowring, S. A., Sadler, P. M., Erwin, D. H., Abdala, F., & Rubidge, B. S. (2015). When and how did the terrestrial mid-Permian mass extinction occur? Evidence from the tetrapod record of the Karoo Basin, South Africa. *Proceedings of the Royal Society B: Biological Sciences*. https://doi.org/10.1098/rspb.2015.0834

Deckart, K., Féraud, G., & Bertrand, H. (1997). Age of Jurassic continental tholeiites of French Guyana, Surinam and Guinea: implications for the initial opening of the Central Atlantic Ocean. *Earth and Planetary Science Letters*, *150*(3–4), 205–220. https://doi.org/10.1016/S0012-821X(97)00102-7

Deenen, M. H. L., Ruhl, M., Bonis, N. R., Krijgsman, W., Kürschner, W. M., Reitsma, M., & van Bergen, M. J. (2010). A new chronology for the end-Triassic mass extinction. *Earth and Planetary Science Letters*. https://doi.org/10.1016/j.epsl.2010.01.003

Denyszyn, S. W., Halls, H. C., Davis, D. W., & Evans, D. A. D. (2009). Paleomagnetism and U-Pb geochronology of Franklin dykes in High Arctic Canada and Greenland: a revised age and paleomagnetic pole constraining block rotations in the Nares Strait region. *Canadian Journal of Earth Sciences*. https://doi.org/10.1139/E09-042

Dickens, G. R., O'Neil, J. R., Rea, D. K., & Owen, R. M. (1995). Dissociation of oceanic methane hydrate as a cause of the carbon isotope excursion at the end of the Paleocene. *Paleoceanography and Paleoclimatology*, *10*(6), 965–971. https://doi.org/10.1029/95PA02087

Duncan, R. A., & Pyle, D. G. (1988). Rapid eruption of the Deccan flood basalts at the

Cretaceous/Tertiary boundary. *Nature*, *333*(6176), 841–843. Retrieved from http://dx.doi.org/10.1038/333841a0

Duncan, R. A., Hooper, P. R., Rehacek, J., Marsh, J. S., & Duncan, A. R. (1997). The timing and duration of the Karoo igneous event, southern Gondwana. *Journal of Geophysical Research: Solid Earth*, *102*(B8), 18127–18138. https://doi.org/10.1029/97JB00972

Dunning, G. R., & Hodych, J. P. (1990). U/Pb zircon and baddeleyite ages for the Palisades and Gettysburg sills of the northeastern United States: implications for the age of the Triassic/Jurassic boundary. *Geology*, *18*(8), 795–798. https://doi.org/10.1130/0091-7613(1990)018<0795:UPZABA>2.3.CO;2

Eldholm, O., & Grue, K. (1994). North Atlantic volcanic margins: dimensions and production rates. *Journal of Geophysical Research: Solid Earth*, *99*(B2), 2955–2968. https://doi.org/10.1029/93JB02879

Elliot, D. H. (2013). The geological and tectonic evolution of the Transantarctic Mountains: a review. *Geological Society, London, Special Publications*, *381*(1), 7–35. https://doi.org/10.1144/SP381.14

Elliot, D. H., & Fleming, T. H. (2004). Occurrence and dispersal of magmas in the Jurassic Ferrar large igneous province, Antarctica. *Gondwana Research*, *7*(1), 223–227. https://doi.org/10.1016/S1342-937X(05)70322-1

Elliot, D. H., & Fleming, T. H. (2008). Physical volcanology and geological relationships of the Jurassic Ferrar Large Igneous Province, Antarctica. *Journal of Volcanology and Geothermal Research*, *172*(1–2), 20–37. https://doi.org/10.1016/j.jvolgeores.2006.02.016

Encarnación, J., Fleming, T. H., Elliot, D. H., & Eales, H. V. (1996). Synchronous emplacement of Ferrar and Karoo dolerites and the early breakup of Gondwana. *Geology*, *24*(6), 535. https://doi.org/10.1130/0091-7613(1996)024<0535:SEOFAK>2.3.CO;2

Erba, E. (1994). Nannofossils and superplumes: The Early Aptian "nannoconid crisis." *Paleoceanography*, *9*(3), 483–501. https://doi.org/10.1029/94PA00258

Evins, L. Z., Jourdan, F., & Phillips, D. (2009). The Cambrian Kalkarindji Large Igneous Province: Extent and characteristics based on new ^{40}Ar/^{39}Ar and geochemical data. *Lithos*. https://doi.org/10.1016/j.lithos.2009.01.014

Fitton, J. G., & Godard, M. (2004). Origin and evolution of magmas on the Ontong Java Plateau. *Geological Society, London, Special Publications*, *229*(1), 151–178. https://doi.org/10.1144/GSL.SP.2004.229.01.10

Fleming, T. H., Heimann, A., Foland, K. A., & Elliot, D. H. (1997). 40Ar/39Ar geochronology of Ferrar Dolerite sills from the Transantarctic Mountains, Antarctica: Implications for the age and origin of the Ferrar magmatic province. *Geological Society of America Bulletin*, *109*. https://doi.org/10.1130/0016-7606(1997)109<0533:AAGOFD>2.3.CO;2

Foland, K. A., Fleming, T. H., Heimann, A., & Elliot, D. H. (1993). Potassium-argon dating of fine-grained basalts with massive Ar loss: Application of the 40Ar39Ar technique to plagioclase and glass from the Kirkpatrick Basalt, Antarctica. *Chemical Geology*, *107*(1–2), 173–190. https://doi.org/10.1016/0009-2541(93)90109-V

Foster, G. L., Lear, C. H., & Rae, J. W. B. (2012). The evolution of pCO_2, ice volume and climate during the middle Miocene. *Earth and Planetary Science Letters*, *341–*

344, 243–254. https://doi.org/10.1016/j.epsl.2012.06.007

Ganino, C., & Arndt, N. T. (2009). Climate changes caused by degassing of sediments during the emplacement of large igneous provinces. *Geology*. https://doi.org/10.1130/G25325A.1

Glass, L. M., & Phillips, D. (2006). The Kalkarindji continental flood basalt province: A new Cambrian large igneous province in Australia with possible links to faunal extinctions. *Geology*. https://doi.org/10.1130/G22122.1

Goddéris, Y., Donnadieu, Y., Nédélec, A., Dupré, B., Dessert, C., Grard, A., et al. (2003). The Sturtian "snowball" glaciation: Fire and ice. *Earth and Planetary Science Letters*. https://doi.org/10.1016/S0012-821X(03)00197-3

Gozalo, R., Álvarez, M. E. D., Vintaned, J. A. G., Zhuravlev, A. Y., Bauluz, B., Subías, I., et al. (2013). Proposal of a reference section and point for the Cambrian Series 2-3 boundary in the Mediterranean subprovince in Murero (NE Spain) and its intercontinental correlation. *Geological Journal*. https://doi.org/10.1002/gj.1330

Guex, J., Bartolini, A., Atudorei, V., & Taylor, D. (2004). High-resolution ammonite and carbon isotope stratigraphy across the Triassic-Jurassic boundary at New York Canyon (Nevada). *Earth Planet. Sci. Lett.*, *225*(1–2), 29–41. https://doi.org/10.1016/j.epsl.2004.06.006

Guex, J., Schoene, B., Bartolini, A., Spangenberg, J. E., Schaltegger, U., O'Dogherty, L., et al. (2012). Geochronological constraints on post-extinction recovery of the ammonoids and carbon cycle perturbations during the Early Jurassic. *Palaeogeography, Palaeoclimatology, Palaeoecology*, *346–347*(0), 1–11.

Gutjahr, M., Ridgwell, A. J., Sexton, P. F., Anagnostou, E., Pearson, P. N., Pälike, H., et al. (2017). Very large release of mostly volcanic carbon during the Palaeocene–Eocene Thermal Maximum. *Nature*, *548*(7669), 573. https://doi.org/10.1038/nature23646

Hamilton, M. A., Pearson, D. G., Thompson, R. N., Kelley, S. P., & Emeleus, C. H. (1998). Rapid eruption of Skye lavas inferred from precise U–Pb and Ar–Ar dating of the Rum and Cuillin plutonic complexes. *Nature*, *394*(6690), 260–263. https://doi.org/10.1038/28361

Harvey, T. H. P., Williams, M., Condon, D. J., Wilby, P. R., Siveter, D. J., Rushton, A. W. A., et al. (2011). A refined chronology for the Cambrian succession of southern Britain. *Journal of the Geological Society*. https://doi.org/10.1144/0016-76492010-031

He, H., Pan, Y., Tauxe, L., Qin, H., & Zhu, R. (2008). Toward age determination of the M0r (Barremian–Aptian boundary) of the Early Cretaceous. *Physics of the Earth and Planetary Interiors*, *169*(1–4), 41–48. https://doi.org/10.1016/J.PEPI.2008.07.014

Heimann, A., Fleming, T. H., Elliot, D. H., & Foland, K. A. (1994). A short interval of Jurassic continental flood basalt volcanism in Antarctica as demonstrated by 40Ar39Ar geochronology. *Earth and Planetary Science Letters*, *121*, 19–41. https://doi.org/10.1016/0012-821X(94)90029-9

Heimdal, T. H., Svensen, H. H., Ramezani, J., Iyer, K., Pereira, E., Rodrigues, R., et al. (2018). Large-scale sill emplacement in Brazil as a trigger for the end-Triassic crisis. *Scientific Reports*, *8*(1), 141. https://doi.org/10.1038/s41598-017-18629-8

Henderson, C. M., Davydov, V. I., Wardlaw, B. R., Gradstein, F. M., & Hammer, Ø.

(2012). *Chapter 24 - The Permian Period. The Geologic Time Scale*. https://doi.org/10.1016/B978-0-444-59425-9.00024-X

Henehan, M. J., Hull, P. M., Penman, D. E., Rae, J. W. B., & Schmidt, D. N. (2016). Biogeochemical significance of pelagic ecosystem function: an end-Cretaceous case study. *Phil. Trans. R. Soc. B*, *371*(1694), 20150510. https://doi.org/10.1098/rstb.2015.0510

Hesselbo, S. P., & Pienkowski, G. (2011). Stepwise atmospheric carbon-isotope excursion during the Toarcian Oceanic Anoxic Event (Early Jurassic, Polish Basin). *Earth and Planetary Science Letters*, *301*(1–2), 365–372. https://doi.org/10.1016/j.epsl.2010.11.021

Hesselbo, S. P., Jenkyns, H. C., Duarte, L. V., & Oliveira, L. C. V. (2007). Carbon-isotope record of the Early Jurassic (Toarcian) Oceanic Anoxic Event from fossil wood and marine carbonate (Lusitanian Basin, Portugal). *Earth and Planetary Science Letters*, *253*(3–4), 455–470. https://doi.org/10.1016/j.epsl.2006.11.009

Higgins, J. A., & Schrag, D. P. (2006). Beyond methane: towards a theory for the Paleocene–Eocene thermal maximum. *Earth and Planetary Science Letters*, *245*(3–4), 523–537. https://doi.org/10.1016/j.epsl.2006.03.009

Hilgen, F. J., Lourens, L. J., Van Dam, J. A., Beu, A. G., Boyes, A. F., Cooper, R. A., et al. (2012). *Chapter 29 - The Neogene Period. The Geologic Time Scale 2012 2-Volume Set*. https://doi.org/10.1016/B978-0-444-59425-9.00029-9

Von Hillebrandt, A. V, Krystyn, L., & Kürschner, W. M. (2007). A candidate GSSP for the base of the Jurassic in the Northern Calcareous Alps (Kuhjoch section, Karwendel Mountains, Tyrol, Austria). *International Subcommission on Jurassic Stratigraphy Newsletter*, *34*(1), 2–20.

Hodell, D. A., & Woodruff, F. (1994). Variations in the strontium isotopic ratio of seawater during the Miocene: Stratigraphic and geochemical implications. *Paleoceanography*, *9*(3), 405–426. https://doi.org/10.1029/94PA00292

Hofmann, C., Féraud, G., & Courtillot, V. E. (2000). ^{40}Ar/^{39}Ar dating of mineral separates and whole rocks from the Western Ghats lava pile: further constraints on duration and age of the Deccan traps. *Earth and Planetary Science Letters*, *180*(1–2), 13–27. https://doi.org/http://dx.doi.org/10.1016/S0012-821X(00)00159-X

Holbourn, A., Kuhnt, W., Schulz, M., Flores, J. A., & Andersen, N. (2007). Orbitally-paced climate evolution during the middle Miocene "Monterey" carbon-isotope excursion. *Earth and Planetary Science Letters*. https://doi.org/10.1016/j.epsl.2007.07.026

Holbourn, A., Kuhnt, W., Lyle, M., Schneider, L., Romero, O., & Andersen, N. (2014). Middle Miocene climate cooling linked to intensification of eastern equatorial Pacific upwelling. *Geology*, *42*(1), 19–22. https://doi.org/10.1130/G34890.1

Holbourn, A., Kuhnt, W., Kochhann, K. G. D., Andersen, N., & Sebastian Meier, K. J. (2015). Global perturbation of the carbon cycle at the onset of the Miocene Climatic Optimum. *Geology*, *43*(2), 123–126. https://doi.org/10.1130/G36317.1

Hooper, P. R., Widdowson, M., & Kelley, S. P. (2010). Tectonic setting and timing of the final Deccan flood basalt eruptions. *Geology*, *38*(9), 839–842. https://doi.org/10.1130/g31072.1

Hough, M. L., Shields, G. A., Evins, L. Z., Strauss, H., Henderson, R. A., & Mackenzie, S. (2006). A major sulphur isotope event at c. 510 Ma: A possible anoxia-extinction-volcanism connection during the Early-Middle Cambrian transition? *Terra Nova*. https://doi.org/10.1111/j.1365-3121.2006.00687.x

Huang, C., & Hesselbo, S. P. (2014). Pacing of the Toarcian Oceanic Anoxic Event (Early Jurassic) from astronomical correlation of marine sections. *Gondwana Research*, *25*(4), 1348–1356. https://doi.org/10.1016/j.gr.2013.06.023

Ivanov, A. V, Rasskazov, S. V, Feoktistov, G. D., He, H., & Boven, A. (2005). 40Ar/39Ar dating of Usol'skii sill in the south-eastern Siberian Traps Large Igneous Province: Evidence for long-lived magmatism. *Terra Nova*, *17*(3), 203–208. https://doi.org/10.1111/j.1365-3121.2004.00588.x

Ivanov, A. V, He, H., Yang, L., Nikolaeva, I. V, & Palesskii, S. V. (2009). 40Ar/39Ar dating of intrusive magmatism in the Angara-Taseevskaya syncline and its implication for duration of magmatism of the Siberian traps. *Journal of Asian Earth Sciences*, *35*(1), 1–12. https://doi.org/10.1016/j.jseaes.2008.11.006

Ivanov, A. V, He, H., Yan, L., Ryabov, V. V, Shevko, A. Y., Palesskii, S. V, & Nikolaeva, I. V. (2013). Siberian Traps large igneous province: Evidence for two flood basalt pulses around the Permo-Triassic boundary and in the Middle Triassic, and contemporaneous granitic magmatism. *Earth-Science Reviews*. https://doi.org/10.1016/j.earscirev.2013.04.001

Ivanov, A. V, Meffre, S., Thompson, J., Corfu, F., Kamenetsky, V. S., Kamenetsky, M. B., & Demonterova, E. I. (2017). Timing and genesis of the Karoo-Ferrar large igneous province: New high precision U-Pb data for Tasmania confirm short duration of the major magmatic pulse. *Chemical Geology*, *455*, 32–43. https://doi.org/10.1016/j.chemgeo.2016.10.008

Jahren, A. H. (2002). The biogeochemical consequences of the mid-Cretaceous superplume. *Journal of Geodynamics*. https://doi.org/10.1016/S0264-3707(02)00020-0

Jaramillo, C., Ochoa, D., Contreras, L., Pagani, M., Carvajal-Ortiz, H., Pratt, L. M., et al. (2010). Effects of Rapid Global Warming at the Paleocene-Eocene Boundary on Neotropical Vegetation. *Science*, *330*(6006), 957. https://doi.org/10.1126/science.1193833

Jay, A. E., & Widdowson, M. (2008). Stratigraphy, structure and volcanology of the SE Deccan continental flood basalt province: implications for eruptive extent and volumes. *Journal of the Geological Society*, *165*(1), 177–188. https://doi.org/10.1144/0016-76492006-062

Jenkyns, H. C. (2010). Geochemistry of oceanic anoxic events. *Geochemistry, Geophysics, Geosystems*, *11*(3). https://doi.org/10.1029/2009GC002788

Joachimski, M. M., & Buggisch, W. (1993). Anoxic events in the late Frasnian - causes of the Frasnian- Famennian faunal crisis? *Geology*, *21*(8), 675–678. https://doi.org/10.1130/0091-7613(1993)021<0675:AEITLF>2.3.CO;2

Joachimski, M. M., Pancost, R. D., Freeman, K. H., Ostertag-Henning, C., & Buggisch, W. (2002). Carbon isotope geochemistry of the Frasnian-Famennian transition. *Palaeogeography, Palaeoclimatology, Palaeoecology*, *181*(1–3), 91–109. https://doi.org/10.1016/S0031-0182(01)00474-6

Jost, A. B., Mundil, R., He, B., Brown, S. T., Altiner, D., Sun, Y., et al. (2014). Constraining the cause of the end-Guadalupian extinction with coupled records of carbon and calcium isotopes. *Earth and Planetary Science Letters*.

https://doi.org/10.1016/j.epsl.2014.04.014

Jourdan, F., Féraud, G., Bertrand, H., Kampunzu, A. B., Tshoso, G., Watkeys, M. K., & Le Gall, B. (2005). Karoo large igneous province: Brevity, origin, and relation to mass extinction questioned by new ^{40}Ar/^{39}Ar age data. *Geology*, *33*(9), 745. https://doi.org/10.1130/G21632.1

Jourdan, F., Féraud, G., Bertrand, H., Watkeys, M. K., & Renne, P. R. (2007). Distinct brief major events in the Karoo large igneous province clarified by new ^{40}Ar/^{39}Ar ages on the Lesotho basalts. *Lithos*, *98*(1–4), 195–209. https://doi.org/10.1016/j.lithos.2007.03.002

Jourdan, F., Féraud, G., Bertrand, H., Watkeys, M. K., & Renne, P. R. (2008). The ^{40}Ar/^{39}Ar ages of the sill complex of the Karoo large igneous province: Implications for the Pliensbachian-Toarcian climate change. *Geochemistry, Geophysics, Geosystems*, *9*(6). https://doi.org/10.1029/2008GC001994

Jourdan, F., Marzoli, A., Bertrand, H., Cirilli, S., Tanner, L. H., Kontak, D. J., et al. (2009). ^{40}Ar/^{39}Ar ages of CAMP in North America: implications for the Triassic–Jurassic boundary and the ^{40}K decay constant bias. *Lithos*, *110*(1–4), 167–180. https://doi.org/10.1016/j.lithos.2008.12.011

Jourdan, F., Hodges, K., Sell, B., Schaltegger, U., Wingate, M. T. D., Evins, L. Z., et al. (2014). High-precision dating of the Kalkarindji large igneous province, Australia, and synchrony with the Early-Middle Cambrian (Stage 4-5) extinction. *Geology*. https://doi.org/10.1130/G35434.1

Kamo, S. L., Czamanske, G. K., & Krogh, T. E. (1996). A minimum U-Pb age for Siberian flood-basalt volcanism. *Geochimica et Cosmochimica Acta*, *60*(18), 3505–3511. https://doi.org/10.1016/0016-7037(96)00173-1

Kamo, S. L., Czamanske, G. K., Amelin, Y., Fedorenko, V. A., Davis, D. W., & Trofimov, V. R. (2003). Rapid eruption of Siberian flood-volcanic rocks and evidence for coincidence with the Permian-Triassic boundary and mass extinction at 251 Ma. *Earth and Planetary Science Letters*, *214*(1–2), 75–91. https://doi.org/10.1016/S0012-821X(03)00347-9

Kasbohm, J. J., & Schoene, B. (2018). Rapid eruption of the Columbia River flood basalt and correlation with the mid-Miocene climate optimum. *Science Advances*, *4*(9), 1–8. https://doi.org/10.1126/sciadv.aat8223

Kaufmann, B., Trapp, E., & Mezger, K. (2004). The Numerical Age of the Upper Frasnian (Upper Devonian) Kellwasser Horizons: A New U-Pb Zircon Date from Steinbruch Schmidt (Kellerwald, Germany). *The Journal of Geology*. https://doi.org/10.1086/421077

Keller, G., Adatte, T., Gardin, S., Bartolini, A., & Bajpai, S. (2008). Main Deccan volcanism phase ends near the K–T boundary: Evidence from the Krishna–Godavari Basin, SE India. *Earth and Planetary Science Letters*, *268*(3–4), 293–311. https://doi.org/10.1016/j.epsl.2008.01.015

Keller, G., Adatte, T., Bhowmick, P. K., Upadhyay, H., Dave, A., Reddy, A. N., & Jaiprakash, B. C. (2012). Nature and timing of extinctions in Cretaceous-Tertiary planktic foraminifera preserved in Deccan intertrappean sediments of the Krishna–Godavari Basin, India. *Earth and Planetary Science Letters*, *341–344*, 211–221. https://doi.org/10.1016/j.epsl.2012.06.021

Kerr, A. C. (2014). *Oceanic Plateaus*. *Treatise on Geochemistry* (2nd ed.). Elsevier Ltd.

https://doi.org/10.1016/B978-0-08-095975-7.00320-X

Kerr, A. C., White, R. V., Thompson, P. M. E., Tarney, J., & Saunders, A. D. (2003). No Oceanic plateau - No caribbean plate? The seminal role of an oceanic plateau in Caribbean plate evolution. *AAPG Memoir*, (79), 23–26.

Khadri, S. F. R., Subbarao, K. V., Hooper, P. R., & Walsh, J. N. (1988). Stratigraphy of Thakurvadi formation, western Deccan basalt province, India. *Deccan Flood Basalts. Geol Soc Ind Mem*, *10*, 281–304.

Kiehl, J. T., & Shields, C. A. (2005). Climate simulation of the latest Permian: Implications for mass extinction. *Geology*. https://doi.org/10.1130/G21654.1

Knight, K. B., Renne, P. R., Halkett, A., & White, N. (2003). ^{40}Ar/^{39}Ar dating of the Rajahmundry Traps, Eastern India and their relationship to the Deccan Traps. *Earth and Planetary Science Letters*, *208*(1–2), 85–99. https://doi.org/10.1016/s0012-821x(02)01154-8

Knight, K. B., Nomade, S., Renne, P. R., Marzoli, A., Bertrand, H., & Youbi, N. (2004). The Central Atlantic Magmatic Province at the Triassic-Jurassic boundary: paleomagnetic and ^{40}Ar/^{39}Ar evidence from Morocco for brief, episodic volcanism. *Earth Planet. Sci. Lett.*, *228*(1–2), 143–160. https://doi.org/10.1016/j.epsl.2004.09.022

Knoll, A. H., Bambach, R. K., Payne, J. L., Pruss, S., & Fischer, W. W. (2007). Paleophysiology and end-Permian mass extinction. *Earth and Planetary Science Letters*. https://doi.org/10.1016/j.epsl.2007.02.018

Kochhann, K. G. D., Holbourn, A., Kuhnt, W., Channell, J. E. T., Lyle, M., Shackford, J. K., et al. (2016). Eccentricity pacing of eastern equatorial Pacific carbonate dissolution cycles during the Miocene Climatic Optimum. *Paleoceanography*, *31*(9), 1176–1192. https://doi.org/10.1002/2016PA002988

Krogh, T. E., Corfu, F., Davis, D. W., Dunning, G. R., Heaman, L. M., Kamo, S. L., et al. (1987). Precise U–Pb isotopic ages of diabase dykes and mafic to ultramafic rocks using trace amounts of baddeleyite and zircon. In H. C. Halls & W. F. Fahrig (Eds.), *Mafic Dike Swarms* (Vol. 34, pp. 147–152). Geological Association of Canada, Special Paper.

Kuiper, K. F., Deino, A. L., Hilgen, F. J., Krijgsman, W., Renne, P. R., & Wijbrans, J. R. (2008). Synchronizing rock clocks of earth history. *Science*, *320*(5875), 500–504. https://doi.org/10.1126/science.1154339

Kuroda, J., Ogawa, N. O., Tanimizu, M., Coffin, M. F., Tokuyama, H., Kitazato, H., & Ohkouchi, N. (2007). Contemporaneous massive subaerial volcanism and late Cretaceous Oceanic Anoxic Event 2. *Earth and Planetary Science Letters*, *256*(1–2), 211–223. https://doi.org/10.1016/J.EPSL.2007.01.027

Kürschner, W. M., Kvacek, Z., & Dilcher, D. L. (2008). The impact of Miocene atmospheric carbon dioxide fluctuations on climate and the evolution of terrestrial ecosystems. *Proceedings of the National Academy of Sciences*, *105*(2), 449–453. https://doi.org/10.1073/pnas.0708588105

Landing, E., Bowring, S. A., Davidek, K. L., Westrop, S. R., Geyer, G., & Heldmaier, W. (1998). Duration of the Early Cambrian: U-Pb ages of volcanic ashes from Avalon and Gondwana. *Canadian Journal of Earth Sciences*. https://doi.org/10.1139/e97-107

Larsen, L. M., Pedersen, A. K., Tegner, C., & Duncan, R. A. (2014). Eocene to Miocene igneous activity in NE Greenland: northward younging of magmatism along the East Greenland margin. *Journal of the Geological Society*, *171*(4), 539–553. https://doi.org/10.1144/jgs2013-118

Larsen, L. M., Pedersen, A. K., Tegner, C., Duncan, R. A., Hald, N., & Larsen, J. G. (2016). Age of Tertiary volcanic rocks on the West Greenland continental margin: volcanic evolution and event correlation to other parts of the North Atlantic Igneous Province. *Geological Magazine*, *153*(3), 487–511. https://doi.org/10.1017/S0016756815000515

Larsen, T. B., Yuen, D. A., & Storey, M. (1999). Ultrafast mantle plumes and implications for flood basalt volcanism in the Northern Atlantic Region. *Tectonophysics*, *311*(1–4), 31–43. https://doi.org/10.1016/S0040-1951(99)00163-8

Larson, R. L., & Erba, E. (1999). Onset of the mid-Cretaceous greenhouse in the Barremian-Aptian: Igneous events and the biological, sedimentary, and geochemical responses. *Paleoceanography*, *14*(6), 663–678. https://doi.org/10.1029/1999PA900040

Laskar, J., Robutel, P., Joutel, F., Gastineau, M., Correia, A. C. M., & Levrard, B. (2004). A long-term numerical solution for the insolation quantities of the Earth. *Astronomy and Astrophysics*, *428*(1), 261–285. https://doi.org/10.1051/0004-6361:20041335

Li, L., & Keller, G. (1998). Abrupt deep-sea warming at the end of the Cretaceous. *Geology*, *26*(11), 995–998. https://doi.org/10.1130/0091-7613(1998)026<0995:ADSWAT>2.3.CO;2

Li, M., Ogg, J. G., Zhang, Y., Huang, C., Hinnov, L. A., Chen, Z. Q., & Zou, Z. (2016). Astronomical tuning of the end-Permian extinction and the Early Triassic Epoch of South China and Germany. *Earth and Planetary Science Letters*, *441*, 10–25. https://doi.org/10.1016/j.epsl.2016.02.017

Li, Y. X., Bralower, T. J., Montañez, I. P., Osleger, D. A., Arthur, M. A., Bice, D. M., et al. (2008). Toward an orbital chronology for the early Aptian Oceanic Anoxic Event (OAE1a, ~ 120 Ma). *Earth and Planetary Science Letters*. https://doi.org/10.1016/j.epsl.2008.03.055

Lindström, S., van de Schootbrugge, B., Hansen, K. H., Pedersen, G. K., Alsen, P., Thibault, N., et al. (2017). A new correlation of Triassic–Jurassic boundary successions in NW Europe, Nevada and Peru, and the Central Atlantic Magmatic Province: A time-line for the end-Triassic mass extinction. *Palaeogeography, Palaeoclimatology, Palaeoecology*, *478*, 80–102. https://doi.org/10.1016/j.palaeo.2016.12.025

Macdonald, F. A., & Wordsworth, R. (2017). Initiation of Snowball Earth with volcanic sulfur aerosol emissions. *Geophysical Research Letters*. https://doi.org/10.1002/2016GL072335

Macdonald, F. A., Schmitz, M. D., Crowley, J. L., Roots, C. F., Jones, D. S., Maloof, A. C., et al. (2010). Calibrating the Cryogenian. *Science*. https://doi.org/10.1126/science.1183325

Macdonald, F. A., Schmitz, M. D., Strauss, J. V., Halverson, G. P., Gibson, T. M., Eyster, A., et al. (2017). Cryogenian of Yukon. *Precambrian Research*. https://doi.org/10.1016/j.precamres.2017.08.015

Maclennan, S., Park, Y., Swanson-Hysell, N., Maloof, A. C., Schoene, B., Gebreslassie, M., et al. (2018). The arc of the Snowball: U-Pb dates constrain the Islay anomaly and the initiation of the Sturtian glaciation. *Geology*. https://doi.org/10.1130/G40171.1

Mahoney, J. J., Storey, M., Duncan, R. A., Spencer, K. J., & Pringle, M. S. (1993). Geochemistry and geochronology of Leg 130 basement lavas: nature and origin of the Ontong Java Plateau. *Proc., Scientific Results, ODP, Leg 130, Ontong Java Plateau*, *130*, 3–22.

Mahood, G. A., & Benson, T. R. (2017). Using ^{40}Ar/^{39}Ar ages of intercalated silicic tuffs to date flood basalts: Precise ages for Steens Basalt Member of the Columbia River Basalt Group. *Earth and Planetary Science Letters*, *459*, 340–351. https://doi.org/10.1016/j.epsl.2016.11.038

Malitch, K. N., Belousova, E. A., Griffin, W. L., Badanina, I. Y., Pearson, N. J., Presnyakov, S. L., & Tuganova, E. V. (2010). Magmatic evolution of the ultramafic-mafic Kharaelakh intrusion (Siberian Craton, Russia): Insights from trace-element, U-Pb and Hf-isotope data on zircon. *Contributions to Mineralogy and Petrology*, *159*(6), 753–768. https://doi.org/10.1007/s00410-009-0452-z

Malitch, K. N., Badanina, I. Y., Belousova, E. A., & Tuganova, E. V. (2012). Results of U-Pb dating of zircon and baddeleyite from the Noril'sk-1 ultramafic-mafic intrusion (Russia). *Russian Geology and Geophysics*, *53*(2), 123–130. https://doi.org/10.1016/j.rgg.2011.12.010

Marzoli, A., Renne, P. R., Piccirillo, E. M., Ernesto, M., Bellieni, G., & De Min, A. (1999). Extensive 200-million-year-old Continental Flood Basalts of the Central Atlantic Magmatic Province. *Science*, *284*, 616–618. https://doi.org/10.1126/science.284.5414.616

Marzoli, A., Bertrand, H., Knight, K. B., Cirilli, S., Buratti, N., Vérati, C., et al. (2004). Synchrony of the Central Atlantic magmatic province and the Triassic-Jurassic boundary climatic and biotic crisis. *Geology*. https://doi.org/10.1130/G20652.1

Marzoli, A., Jourdan, F., Puffer, J. H., Cuppone, T., Tanner, L. H., Weems, R. E., et al. (2011). Timing and duration of the Central Atlantic magmatic province in the Newark and Culpeper basins, eastern USA. *Lithos*, *122*(3–4), 175–188. https://doi.org/10.1016/j.lithos.2010.12.013

Marzoli, A., Callegaro, S., Dal Corso, J., Davies, J. H. F. L., Chiaradia, M., Youbi, N., et al. (2018). The Central Atlantic Magmatic Province (CAMP): a review. In *The Late Triassic World* (pp. 91–125). Springer.

Marzoli, A., Bertrand, H., Youbi, N., Callegaro, S., Merle, R. E., Reisberg, L., et al. (2019). The Central Atlantic Magmatic Province (CAMP) in Morocco. *Journal of Petrology*, *60*(5), 945–996. https://doi.org/10.1093/petrology/egz021

Mattinson, J. M. (2005). Zircon U-Pb chemical abrasion ("CA-TIMS") method: Combined annealing and multi-step partial dissolution analysis for improved precision and accuracy of zircon ages. *Chemical Geology*, *220*(1–2), 47–66. https://doi.org/10.1016/j.chemgeo.2005.03.011

McGhee, G. R. (2013). The First Catastrophe and Retreat. In *When the Invasion of Land Failed: The Legacy of the Devonian Extinctions* (pp. 99–158). Columbia University Press. https://doi.org/10.7312/mcgh16056

McHone, J. G. (2003). Volatile emissions from Central Atlantic Magmatic Province basalts; mass assumptions and environmental consequences. In W. E. Hames, J. G. McHone, P. R. Renne, & C. R. Ruppel (Eds.), *the Central Atlantic Magmatic*

Province; Insights from Fragments of Pangea: Geophysical monograph (Vol. 136, pp. 241–254). Washington: American Geophyiscal Union.

McLean, D. M. (1985). Deccan Traps mantle degassing in the terminal Cretaceous marine extinctions. *Cretaceous Research*, *6*(3), 235–259.

Menegatti, A. P., Weissert, H., Brown, R. S., Tyson, R. V., Farrimond, P., Strasser, A., & Caron, M. (1998). High-resolution δ ^{13} C stratigraphy through the Early Aptian "Livello selli" of the Alpine tethys. *Paleoceanography*, *13*(5), 530–545. https://doi.org/10.1029/98PA01793

Meyers, S. R., Sageman, B. B., & Hinnov, L. A. (2001). Integrated Quantitative Stratigraphy of the Cenomanian-Turonian Bridge Creek Limestone Member Using Evolutive Harmonic Analysis and Stratigraphic Modeling. *Journal of Sedimentary Research*. https://doi.org/10.1306/012401710628

Meyers, S. R., Siewert, S. E., Singer, B. S., Sageman, B. B., Condon, D. J., Obradovich, J. D., et al. (2012). Intercalibration of radioisotopic and astrochronologic time scales for the Cenomanian-Turonian boundary interval, Western Interior Basin, USA. *Geology*, *40*(1), 7–10. https://doi.org/10.1130/G32261.1

Midtkandal, I., Svensen, H. H., Planke, S., Corfu, F., Polteau, S., Torsvik, T. H., et al. (2016). The Aptian (Early Cretaceous) oceanic anoxic event (OAE1a) in Svalbard, Barents Sea, and the absolute age of the Barremian-Aptian boundary. *Palaeogeography, Palaeoclimatology, Palaeoecology*, *463*, 126–135. https://doi.org/10.1016/J.PALAEO.2016.09.023

Min, K., Mundil, R., Renne, P. R., & Ludwig, K. R. (2000). A test for systematic errors in ^{40}Ar/^{39}Ar geochronology through comparison with U-Pb analysis of a 1.1 Ga rhyolite. *Geochim. Cosmochim. Acta*, *64*, 73–98. https://doi.org/10.1016/S0016-7037(99)00204-5

Minor, D. R., & Mukasa, S. B. (1997). Zircon U-Pb and hornblende ^{40}Ar-^{39}Ar ages for the Dufek layered mafic intrusion, Antarctica: Implications for the age of the Ferrar large igneous province. *Geochimica et Cosmochimica Acta*, *61*(12), 2497–2504. https://doi.org/10.1016/S0016-7037(97)00098-7

Mitchell, R. N., Bice, D. M., Montanari, A., Cleaveland, L. C., Christianson, K. T., Coccioni, R., & Hinnov, L. A. (2008). Oceanic anoxic cycles? Orbital prelude to the Bonarelli Level (OAE 2). *Earth and Planetary Science Letters*. https://doi.org/10.1016/j.epsl.2007.11.026

Moulin, M., Fluteau, F. F., Courtillot, V. E., Marsh, J. S., Delpech, G., Quidelleur, X., et al. (2011). An attempt to constrain the age, duration, and eruptive history of the Karoo flood basalt: Naude's Nek section (South Africa). *Journal of Geophysical Research: Solid Earth*, *116*(B7), 2300–2327. https://doi.org/10.1029/2011JB008210

Moulin, M., Fluteau, F. F., Courtillot, V. E., Marsh, J. S., Delpech, G., Quidelleur, X., & Gérard, M. (2017). Eruptive history of the Karoo lava flows and their impact on early Jurassic environmental change. *Journal of Geophysical Research: Solid Earth*, *122*(2), 738–772. https://doi.org/10.1002/2016JB013354

Mundil, R., Metcalfe, I., Ludwig, K. R., Renne, P. R., Oberli, F., & Nicoll, R. S. (2001). Timing of the Permian-Triassic biotic crisis: Implications from new zircon U/Pb age data (and their limitations). *Earth and Planetary Science Letters*. https://doi.org/10.1016/S0012-821X(01)00274-6

Mundil, R., Ludwig, K. R., Metcalfe, I., & Renne, P. R. (2004). Age and timing of the

Permian mass extinctions: U/Pb dating of closed-system zircons. *Science*. https://doi.org/10.1126/science.1101012

Murphy, B. H., Farley, K. A., & Zachos, J. C. (2010). An extraterrestrial ^{3}He-based timescale for the Paleocene–Eocene thermal maximum (PETM) from Walvis Ridge, IODP Site 1266. *Geochimica et Cosmochimica Acta*, *74*(17), 5098–5108. https://doi.org/10.1016/j.gca.2010.03.039

Naafs, B. D. A., Castro, J. M., De Gea, G. A., Quijano, M. L., Schmidt, D. N., & Pancost, R. D. (2016). Gradual and sustained carbon dioxide release during Aptian Oceanic Anoxic Event 1a. *Nature Geoscience*, *9*(2), 135–139. https://doi.org/10.1038/ngeo2627

Nomade, S., Knight, K. B., Beutel, E., Renne, P. R., Verati, C., Féraud, G., et al. (2007). Chronology of the Central Atlantic Magmatic Province: Implications for the Central Atlantic rifting processes and the Triassic-Jurassic biotic crisis. *Palaeogeography, Palaeoclimatology, Palaeoecology*, *244*(1–4), 326–344. https://doi.org/10.1016/j.palaeo.2006.06.034

Ogg, J. G., Hinnov, L. A., & Huang, C. (2012). *Chapter 27 – Cretaceous*. *The Geologic Time Scale*. https://doi.org/10.1016/B978-0-444-59425-9.00027-5

Olierook, H. K. H., Jourdan, F., & Merle, R. E. (2019). Age of the Barremian–Aptian boundary and onset of the Cretaceous Normal Superchron. *Earth-Science Reviews*, *197*(102906), 1–22. https://doi.org/10.1016/j.earscirev.2019.102906

Olsen, P. E., Kent, D. V., Et-Touhami, M., & Puffer, J. H. (2003). Cyclo-, magneto-, and bio-stratigraphic constraints on the duration of the CAMP event and its relationship to the Triassic-Jurassic boundary. In W. E. Hames, J. G. McHone, P. R. Renne, & C. R. Ruppel (Eds.), *The Central Atlantic Magmatic Province; Insights from Fragments of Pangea: Geophysical monograph*. https://doi.org/10.1029/136GM02

Pálfy, J., & Smith, P. L. (2000). Synchrony between Early Jurassic extinction, oceanic anoxic event, and the Karoo-Ferrar flood basalt volcanism. *Geology*, *28*(8), 745–747. https://doi.org/10.1130/0091-7613(2000)28%3C747:SBEJEO%3E2.0.CO

Pálfy, J., Smith, P. L., & Mortensen, J. K. (2000a). A U–Pb and ^{40}Ar/^{39}Ar time scale for the Jurassic. *Canadian Journal of Earth Sciences*, *37*, 923–944. https://doi.org/10.1139/e00-002

Pálfy, J., Mortensen, J. K., Carter, E. S., Smith, P. L., Friedman, R. M., & Tipper, H. W. (2000b). Timing the end-Triassic mass extinction: First on land, then in the sea? *Geology*, *28*(1), 39–42. https://doi.org/10.1130/0091-7613(2000)28<39:TTEMEF>2.0.CO;2

Pálfy, J., Smith, P. L., & Mortensen, J. K. (2002). Dating the end-Triassic and Early Jurassic mass extinctions, correlative large igneous provinces, and isotopic events. In *Special Paper 356: Catastrophic events and mass extinctions: impacts and beyond* (pp. 523–532). Geological Society of America. https://doi.org/10.1130/0-8137-2356-6.523

Pande, K. (2002). Age and duration of the Deccan Traps, India: a review of radiometric and paleomagnetic constraints. *Proceedings-Indian Academy of Sciences Earth and Planetary Sciences*, *111*(2), 115–124.

Paton, M. T., Ivanov, A. V, Fiorentini, M. L., McNaughton, N. J., Mudrovska, I., Reznitskii, L. Z., & Demonterova, E. I. (2010). Late Permian and Early Triassic magmatic pulses in the Angara-Taseeva syncline, Southern Siberian Traps and their possible influence on the environment. *Russian Geology and Geophysics*, *51*(9), 1012–1020. https://doi.org/10.1016/j.rgg.2010.08.009

Pavlov, V. E., Fluteau, F. F., Latyshev, A. V, Fetisova, A. M., Elkins-Tanton, L. T., Black, B. A., et al. (2019). Geomagnetic Secular Variations at the Permian-Triassic Boundary and Pulsed Magmatism During Eruption of the Siberian Traps. *Geochemistry, Geophysics, Geosystems*, *20*(2). https://doi.org/10.1029/2018GC007950

Penn, J. L., Deutsch, C., Payne, J. L., & Sperling, E. A. (2018). Temperature-dependent hypoxia explains biogeography and severity of end-Permian marine mass extinction. *Science*. https://doi.org/10.1126/science.aat1327

Percival, L. M. E., Davies, J. H. F. L., Schaltegger, U., De Vleeschouwer, D., Da Silva, A. C., & Föllmi, K. B. (2018). Precisely dating the Frasnian-Famennian boundary: Implications for the cause of the Late Devonian mass extinction. *Scientific Reports*. https://doi.org/10.1038/s41598-018-27847-7

Petersen, S. V, Dutton, A., & Lohmann, K. C. (2016). End-Cretaceous extinction in Antarctica linked to both Deccan volcanism and meteorite impact via climate change. *Nat. Commun.*, *7:12079*. https://doi.org/10.1038/ncomms12079

Polteau, S., Hendriks, B. W. H., Planke, S., Ganerød, M., Corfu, F., Faleide, J. I., et al. (2016). The Early Cretaceous Barents Sea Sill Complex: Distribution, ^{40}Ar/^{39}Ar geochronology, and implications for carbon gas formation. *Palaeogeography, Palaeoclimatology, Palaeoecology*, *441*, 83–95. https://doi.org/10.1016/j.palaeo.2015.07.007

Polyansky, O. P., Prokopiev, A. V., Koroleva, O. V., Tomshin, M. D., Reverdatto, V. V., Selyatitsky, A. Y., et al. (2017). Temporal correlation between dyke swarms and crustal extension in the middle Palaeozoic Vilyui rift basin, Siberian platform. *Lithos*, *282–283*, 45–64. https://doi.org/10.1016/j.lithos.2017.02.020

Punekar, J., Mateo, P., & Keller, G. (2014). Effects of Deccan volcanism on paleoenvironment and planktic foraminifera: A global survey. *Geol. Soc. Am. Spec. Pap.*, *505*, 91. https://doi.org/10.1130/2014.2505(04)

Racki, G. (1998). Frasnian-Famennian biotic crisis: Undervalued tectonic control? *Palaeogeography, Palaeoclimatology, Palaeoecology*. https://doi.org/10.1016/S0031-0182(98)00059-5

Racki, G., Rakociński, M., Marynowski, L., & Wignall, P. B. (2018). Mercury enrichments and the Frasnian-Famennian biotic crisis: A volcanic trigger proved? *Geology*, *46*(6), 543–546. https://doi.org/10.1130/G40233.1

Ramezani, J., & Bowring, S. A. (2017). Advances in numerical calibration of the Permian timescale based on radioisotopic geochronology. *Geological Society, London, Special Publications*. https://doi.org/10.1144/sp450.17

Rampino, M. R., & Stothers, R. B. (1988). Flood basalt volcanism during the past 250 million years. *Science*. https://doi.org/10.1126/science.241.4866.663

Raval, U., & Veeraswamy, K. (2003). India-Madagascar separation: breakup along a pre-existing mobile belt and chipping of the craton. *Gondwana Research*, *6*(3), 467–485. https://doi.org/10.1016/S1342-937X(05)70999-0

Ravizza, G., & VonderHaar, D. (2012). A geochemical clock in earliest Paleogene pelagic carbonates based on the impact-induced Os isotope excursion at the Cretaceous-Paleogene boundary. *Paleoceanography and Paleoclimatology*, *27*(3).

https://doi.org/10.1029/2012PA002301

Reichow, M. K., Saunders, A. D., White, R. V., Pringle, M. S., Al'Mukhamedov, A. I., Medvedev, A. I., & Kirda, N. P. (2002). 40Ar/39Ar dates from the West Siberian Basin: Siberian flood basalt province doubled. *Science*, *296*(5574), 1846–1849. https://doi.org/10.1126/science.1071671

Reichow, M. K., Pringle, M. S., Al'Mukhamedov, A. I., Allen, M. B., Andreichev, V. L., Buslov, M. M., et al. (2009). The timing and extent of the eruption of the Siberian Traps large igneous province: Implications for the end-Permian environmental crisis. *Earth and Planetary Science Letters*, *277*(1–2), 9–20. https://doi.org/10.1016/j.epsl.2008.09.030

Reichow, M. K., Saunders, A. D., Scott, R. A., Millar, I. L., Barfod, D., Pringle, M. S., et al. (2016). Petrogenesis and timing of mafic magmatism, South Taimyr, Arctic Siberia: A northerly continuation of the Siberian Traps? *Lithos*. https://doi.org/10.1016/j.lithos.2016.01.018

Reidel, S. P. (2015). The Columbia River Basalt Group: a flood basalt province in the Pacific Northwest, USA. *Geoscience Canada*, *42*, 151–168. https://doi.org/10.1007/s13398-014-0173-7.2

Reimold, W. U., Kelley, S. P., Sherlock, S. C., Henkel, H., & Koeberl, C. (2005). Laser argon dating of melt breccias from the Siljan impact structure, Sweden: Implications for a possible relationship to Late Devonian extinction events. *Meteoritics and Planetary Science*. https://doi.org/10.1111/j.1945-5100.2005.tb00965.x

Renne, P. R. (1995). Excess 40Ar in biotite and hornblende from the Noril'sk 1 intrusion, Siberia: implications for the age of the Siberian Traps. *Earth and Planetary Science Letters*, *131*(3–4), 165–176. https://doi.org/10.1016/0012-821X(95)00015-5

Renne, P. R., & Basu, A. R. (1991). Rapid Eruption of the Siberian Traps Flood Basalts at the Permo-Triassic Boundary. *Science*, *253*(5016), 176–179. https://doi.org/10.1126/science.253.5016.176

Renne, P. R., Zichao, Z., Richards, M. A., Black, M. T., & Basu, A. R. (1995). Synchrony and causal relations between Permian-Triassic boundary crises and siberian flood volcanism. *Science*. https://doi.org/10.1126/science.269.5229.1413

Renne, P. R., Karner, D. B., & Ludwig, K. R. (1998). Absolute ages aren't exactly. *Science*, *282*, 1840–1841. https://doi.org/10.1126/science.282.5395.1840

Renne, P. R., Mundil, R., Balco, G., Min, K., & Ludwig, K. R. (2010). Joint determination of ^{40}K decay constants and ^{40}Ar/^{40}K for the Fish Canyon sanidine standard, and improved accuracy for ^{40}Ar/^{39}Ar geochronology. *Geochimica et Cosmochimica Acta*, *74*(18), 5349–5367. https://doi.org/10.1016/j.gca.2010.06.017

Renne, P. R., Deino, A. L., Hilgen, F. J., Kuiper, K. F., Mark, D. F., Mitchell 3rd, W. S., et al. (2013). Time scales of critical events around the Cretaceous-Paleogene boundary. *Science*, *339*(6120), 684–687. https://doi.org/10.1126/science.1230492

Renne, P. R., Sprain, C. J., Richards, M. A., Self, S., Vanderkluysen, L., & Pande, K. (2015). State shift in Deccan volcanism at the Cretaceous-Paleogene boundary, possibly induced by impact. *Science*. https://doi.org/10.1126/science.aac7549

Renne, P. R., Arenillas, I., Arz, J. A., Vajda, V., Gilabert, V., & Bermúdez, H. D. (2018). Multi-proxy record of the Chicxulub impact at the Cretaceous-Paleogene boundary from Gorgonilla Island, Colombia. *Geology*, *46*(6), 547–550. https://doi.org/10.1130/G40224.1

Ricci, J., Quidelleur, X., Pavlov, V. E., Orlov, S., Shatsillo, A., & Courtillot, V. E. (2013). New ^{40}Ar/^{39}Ar and K-Ar ages of the Viluy traps (Eastern Siberia): Further evidence for a relationship with the Frasnian-Famennian mass extinction. *Palaeogeography, Palaeoclimatology, Palaeoecology*. https://doi.org/10.1016/j.palaeo.2013.06.020

Richards, M. A., Duncan, R. A., & Courtillot, V. E. (1989). Flood basalts and hot-spot tracks: plume heads and tails. *Science*, *246*(4926), 103–107. https://doi.org/10.1126/science.246.4926.103

Richards, M. A., Alvarez, W., Self, S., Karlstrom, L., Renne, P. R., Manga, M., et al. (2015). Triggering of the largest Deccan eruptions by the Chicxulub impact. *Geological Society of America Bulletin*, *127*(11–12), 1507–1520. https://doi.org/10.1130/B31167.1

Robinson, N., Ravizza, G., Coccioni, R., Peucker-Ehrenbrink, B., & Norris, R. D. (2009). A high-resolution marine ^{187}Os/^{188}Os record for the late Maastrichtian: Distinguishing the chemical fingerprints of Deccan volcanism and the KP impact event. *Earth and Planetary Science Letters*, *281*(3–4), 159–168. https://doi.org/10.1016/j.epsl.2009.02.019

Röhl, U., Westerhold, T., Bralower, T. J., & Zachos, J. C. (2007). On the duration of the Paleocene-Eocene thermal maximum (PETM). *Geochemistry, Geophysics, Geosystems*, *8*(12). https://doi.org/10.1029/2007GC001784

Sageman, B. B., Meyers, S. R., & Arthur, M. A. (2006). Orbital time scale and new C-isotope record for Cenomanian-Turonian boundary stratotype. *Geology*. https://doi.org/10.1130/G22074.1

Saunders, A. D. (2016). Two LIPs and two Earth-system crises: the impact of the North Atlantic Igneous Province and the Siberian Traps on the Earth-surface carbon cycle. *Geological Magazine*, *153*(2), 201–222. https://doi.org/10.1017/S0016756815000175

Saunders, A. D., Fitton, J. G., Kerr, A. C., Norry, M. J., & Kent, R. W. (1997). The North Atlantic Igneous Province. *Large Igneous Provinces: Continental, Oceanic, and Planetary Flood Volcanism*, 45–93.

Schlanger, S. O., & Jenkyns, H. C. (1976). Cretaceous Oceanic Anoxic Events: Causes and Consequences. *Geologie En Mijnbouw*, *55*(3–4), 179–184.

Schöbel, S., de Wall, H., Ganerød, M., Pandit, M. K., & Rolf, C. (2014). Magnetostratigraphy and ^{40}Ar–^{39}Ar geochronology of the Malwa Plateau region (Northern Deccan Traps), central western India: Significance and correlation with the main Deccan Large Igneous Province sequences. *Journal of Asian Earth Sciences*, *89*(0), 28–45. https://doi.org/http://dx.doi.org/10.1016/j.jseaes.2014.03.022

Schoene, B. (2014). U-Th-Pb Geochronology. *Treatise on Geochemistry: Second Edition*, *4*, 341–378. https://doi.org/10.1016/B978-0-08-095975-7.00310-7

Schoene, B., Crowley, J. L., Condon, D. J., Schmitz, M. D., & Bowring, S. A. (2006). Reassessing the uranium decay constants for geochronology using ID-TIMS U-Pb data. *Geochimica et Cosmochimica Acta*, *70*(2), 426–445. https://doi.org/10.1016/j.gca.2005.09.007

Schoene, B., Guex, J., Bartolini, A., Schaltegger, U., & Blackburn, T. J. (2010). Correlating the end-Triassic mass extinction and flood basalt volcanism at the 100 ka level. *Geology*, *38*(5), 387–390. https://doi.org/10.1130/G30683.1

Schoene, B., Samperton, K. M., Eddy, M. P., Keller, G., Adatte, T., Bowring, S. A., et al. (2015). U-Pb geochronology of the Deccan Traps and relation to the end-Cretaceous mass extinction. *Science*, *347*(6218), 182–184. https://doi.org/10.1126/science.aaa0118

Schoene, B., Eddy, M. P., Samperton, K. M., Keller, C. B., Keller, G., Adatte, T., & Khadri, S. F. R. (2019). U-Pb constraints on pulsed eruption of the Deccan Traps across the end-Cretaceous mass extinction. *Science*, *363*(6429), 862–866. https://doi.org/10.1126/science.aau2422

Schulte, P., Alegret, L., Arenillas, I., Arz, J. A., Barton, P. J., Bown, P. R., et al. (2010). The Chicxulub asteroid impact and mass extinction at the Cretaceous-Paleogene boundary. *Science*, *327*(5970), 1214–1218. https://doi.org/10.1126/science.1177265

Self, S., Jay, A. E., Widdowson, M., & Keszthelyi, L. P. (2008). Correlation of the Deccan and Rajahmundry Trap lavas: Are these the longest and largest lava flows on Earth? *Journal of Volcanology and Geothermal Research*, *172*(1–2), 3–19. https://doi.org/10.1016/j.jvolgeores.2006.11.012

Sell, B., Ovtcharova, M., Guex, J., Bartolini, A., Jourdan, F., Spangenberg, J. E., et al. (2014). Evaluating the temporal link between the Karoo LIP and climatic-biologic events of the Toarcian Stage with high-precision U-Pb geochronology. *Earth and Planetary Science Letters*, *408*, 48–56. https://doi.org/10.1016/j.epsl.2014.10.008

Sell, B., Ovtcharova, M., Guex, J., Bartolini, A., Jourdan, F., Spangenberg, J. E., et al. (2016). Response to comment on “Evaluating the temporal link between the Karoo LIP and climatic–biologic events of the Toarcian Stage with high-precision U–Pb geochronology.” *Earth and Planetary Science Letters*, *434*, 353–354. https://doi.org/10.1016/j.epsl.2015.07.016

Sepkoski, J. J. (1986). Phanerozoic overview of mass extinction. *Patterns and Processes in the History of Life. Report of the Dahlem Workshop, Berlin 1985*, 277–295.

Sheldon, N. D., Chakrabarti, R., Retallack, G. J., & Smith, R. M. H. (2014). Contrasting geochemical signatures on land from the Middle and Late Permian extinction events. *Sedimentology*. https://doi.org/10.1111/sed.12117

Shellnutt, J. G. (2014). The Emeishan large igneous province: A synthesis. *Geoscience Frontiers*. https://doi.org/10.1016/j.gsf.2013.07.003

Shellnutt, J. G., Denyszyn, S. W., & Mundil, R. (2012). Precise age determination of mafic and felsic intrusive rocks from the Permian Emeishan large igneous province (SW China). *Gondwana Research*. https://doi.org/10.1016/j.gr.2011.10.009

Shen, S.-Z., Ramezani, J., Chen, J., Cao, C.-Q., Erwin, D. H., Zhang, H., et al. (2018). A sudden end-Permian mass extinction in South China. *GSA Bulletin*, *131*(1–2), 205–223. https://doi.org/10.1130/B31909.1

Shen, S., Crowley, J. L., Wang, Y., Bowring, S. A., Erwin, D. H., Sadler, P. M., et al. (2011). Calibrating the end-Permian mass extinction. *Science*. https://doi.org/10.1126/science.1213454

Shevenell, A. E., Kennett, J. P., & Lea, D. W. (2004). Middle Miocene Southern Ocean Cooling and Antarctic Cryosphere Expansion. *Science*, *305*, 1766–1770. https://doi.org/10.1126/science.1100061

Shrivastava, J. P., & Pattanayak, S. K. (2002). Basalts of the Eastern Deccan Volcanic Province, India. *Gondwana Research*, *5*(3), 649–665. https://doi.org/10.1016/S1342-937X(05)70636-5

Sinton, C. W., Duncan, R. A., Storey, M., Lewis, J., & Estrada, J. J. (1998). An oceanic flood basalt province within the Caribbean plate. *Earth and Planetary Science Letters*. https://doi.org/10.1016/S0012-821X(97)00214-8

Smit, J. (1999). The Global Stratigraphy of the Cretaceous-Tertiary Boundary Impact Ejecta. *Annual Review of Earth and Planetary Sciences*, *27*(1), 75–113. https://doi.org/10.1146/annurev.earth.27.1.75

Snow, L. J., Duncan, R. A., & Bralower, T. J. (2005). Trace element abundances in the Rock Canyon Anticline, Pueblo, Colorado, marine sedimentary section and their relationship to Caribbean plateau construction and ocean anoxic event 2. *Paleoceanography*, *20*(3), 1–14. https://doi.org/10.1029/2004PA001093

Sprain, C. J., Renne, P. R., Clemens, W. A., & Wilson, G. P. (2018). Calibration of chron C29r: New high-precision geochronologic and paleomagnetic constraints from the Hell Creek region, Montana. *Geological Society of America Bulletin*. https://doi.org/10.1130/B31890.1

Sprain, C. J., Renne, P. R., Vanderkluysen, L., Pande, K., Self, S., & Mittal, T. (2019). The eruptive tempo of Deccan volcanism in relation to the Cretaceous-Paleogene boundary. *Science*, *363*(6429), 866–870. https://doi.org/10.1126/science.aav1446

Stolper, D. A., Bender, M. L., Dreyfus, G. B., Yan, Y., & Higgins, J. A. (2016). A Pleistocene ice core record of atmospheric O_2 concentrations. *Science*, *353*(6306), 1427–1430. https://doi.org/10.1126/science.aaf5445

Storey, M., Mahoney, J. J., Saunders, A. D., Duncan, R. A., Kelley, S. P., & Coffin, M. F. (1995). Timing of hot spot-related volcanism and the breakup of Madagascar and India. *Science*, *267*(5199), 852–855. https://doi.org/10.1126/science.267.5199.852

Storey, M., Duncan, R. A., & Swisher, C. C. (2007a). Paleocene-Eocene thermal maximum and the opening of the northeast Atlantic. *Science*, *316*(5824), 587–589. https://doi.org/10.1126/science.1135274

Storey, M., Duncan, R. A., & Tegner, C. (2007b). Timing and duration of volcanism in the North Atlantic Igneous Province: Implications for geodynamics and links to the Iceland hotspot. *Chemical Geology*, *241*(3–4), 264–281. https://doi.org/10.1016/j.chemgeo.2007.01.016

Suan, G., Pittet, B., Bour, I., Mattioli, E., Duarte, L. V., & Mailliot, S. (2008). Duration of the Early Toarcian carbon isotope excursion deduced from spectral analysis: Consequence for its possible causes. *Earth and Planetary Science Letters*, *267*(3–4), 666–679. https://doi.org/10.1016/j.epsl.2007.12.017

Suan, G., Nikitenko, B. L., Rogov, M. A., Baudin, F., Spangenberg, J. E., Knyazev, V. G., et al. (2011). Polar record of Early Jurassic massive carbon injection. *Earth and Planetary Science Letters*, *312*(1–2), 102–113. https://doi.org/10.1016/j.epsl.2011.09.050

Subbarao, K. V., Bodas, M. S., Khadri, S. F. R., & Beane, J. E. (2000). Penrose Deccan 2000, Field Excursion Guide to the Western Deccan Basalt Province. *Penrose Field Guides, B. Geological Society of India, Ed.*

Sun, Y., Joachimski, M. M., Wignall, P. B., Yan, C., Chen, Y., Jiang, H., et al. (2012). Lethally hot temperatures during the early Triassic greenhouse. *Science*. https://doi.org/10.1126/science.1224126

Svensen, H. H., Planke, S., Malthe-Sørenssen, A., Jamtveit, B., Myklebust, R., Eidem, T. R., & Rey, S. S. (2004). Release of methane from a volcanic basin as a mechanism for initial Eocene global warming. *Nature*, *429*(6991), 542. https://doi.org/10.1038/nature02566

Svensen, H. H., Planke, S., Polozov, A. G., Schmidbauer, N., Corfu, F., Podladchikov, Y. Y., & Jamtveit, B. (2009). Siberian gas venting and the end-Permian environmental crisis. *Earth and Planetary Science Letters*, *277*(3–4), 490–500. https://doi.org/10.1016/j.epsl.2008.11.015

Svensen, H. H., Planke, S., & Corfu, F. (2010). Zircon dating ties NE Atlantic sill emplacement to initial Eocene global warming. *Journal of the Geological Society*, *167*(3), 433–436. https://doi.org/10.1144/0016-76492009-125

Svensen, H. H., Corfu, F., Polteau, S., Hammer, Ø., & Planke, S. (2012). Rapid magma emplacement in the Karoo Large Igneous Province. *Earth and Planetary Science Letters*, *325–326*, 1–9. https://doi.org/10.1016/j.epsl.2012.01.015

Svensen, H. H., Polteau, S., Cawthorn, G., & Planke, S. (2015). Sub-volcanic Intrusions in the Karoo Basin, South Africa. In *Physical Geology of Shallow Magmatic Systems* (pp. 349–362). Springer, Cham. https://doi.org/10.1007/11157_2014_7

Tanner, L. H., Lucas, S. G., & Chapman, M. G. (2004). Assessing the record and causes of Late triassic extinctions. *Earth-Science Reviews*, *65*, 15–103. https://doi.org/10.1016/S0012-8252(03)00082-5

Tarduno, J. A., Sliter, W. V., Kroenke, L., Leckie, R. M., Mayer, H., Mahoney, J. J., et al. (1991). Rapid formation of Ontong Java Plateau by Aptian mantle plume volcanism. *Science*. https://doi.org/10.1126/science.254.5030.399

Tejada, M. L. G., Mahoney, J. J., Duncan, R. A., & Hawkins, M. P. (1996). Age and geochemistry of basement and Alkalic rocks of Malaita and Santa Isabel, Solomon Islands, Southern Margin of Ontong Java Plateau. *Journal of Petrology*, *37*(2), 361–394. https://doi.org/10.1093/petrology/37.2.361

Tejada, M. L. G., Mahoney, J. J., Neal, C. R., Duncan, R. A., & Petterson, M. G. (2002). Basement Geochemistry and Geochronology of Central Malaita, Solomon Islands, with Implications for the Origin and Evolution of the Ontong Java Plateau. *Journal of Petrology*, *43*(3), 449–484. https://doi.org/10.1093/petrology/43.3.449

Tejada, M. L. G., Suzuki, K., Kuroda, J., Coccioni, R., Mahoney, J. J., Ohkouchi, N., et al. (2009). Ontong Java Plateau eruption as a trigger for the early Aptian oceanic anoxic event. *Geology*, *37*(9), 855–858. https://doi.org/10.1130/G25763A.1

Thibault, N., Galbrun, B., Gardin, S., Minoletti, F., & Le Callonnec, L. (2016). The end-Cretaceous in the southwestern Tethys (Elles, Tunisia): orbital calibration of paleoenvironmental events before the mass extinction. *International Journal of Earth Sciences*. https://doi.org/10.1007/s00531-015-1192-0

Tobin, T. S., Ward, P. D., Steig, E. J., Olivero, E. B., Hilburn, I. A., Mitchell, R. N., et al. (2012). Extinction patterns, δ^{18}O trends, and magnetostratigraphy from a southern high-latitude Cretaceous–Paleogene section: Links with Deccan volcanism. *Palaeogeography, Palaeoclimatology, Palaeoecology*, *350–352*(0), 180–188. https://doi.org/http://dx.doi.org/10.1016/j.palaeo.2012.06.029

Turgeon, S. C., & Creaser, R. A. (2008). Cretaceous oceanic anoxic event 2 triggered by a massive magmatic episode. *Nature*, *454*(7202), 323–326. https://doi.org/10.1038/nature07076

Turgeon, S. C., Creaser, R. A., & Algeo, T. J. (2007). Re-Os depositional ages and seawater Os estimates for the Frasnian-Famennian boundary: Implications for weathering rates, land plant evolution, and extinction mechanisms. *Earth and Planetary Science Letters*. https://doi.org/10.1016/j.epsl.2007.07.031

Venkatesan, T. R., Pande, K., & Gopalan, K. (1993). Did Deccan volcanism pre-date the Cretaceous/Tertiary transition? *Earth and Planetary Science Letters*, *119*(1–2), 181–189. https://doi.org/10.1016/0012-821X(93)90015-2

Venkatesan, T. R., Kumar, A., Gopalan, K., & Al'Mukhamedov, A. I. (1997). ^{40}Ar-^{39}Ar age of Siberian basaltic volcanism. *Chemical Geology*. https://doi.org/10.1016/S0009-2541(97)00006-5

Verati, C., Bertrand, H., & Féraud, G. (2005). The farthest record of the Central Atlantic Magmatic Province into West Africa craton: Precise ^{40}Ar/^{39}Ar dating and geochemistry of Taoudenni basin intrusives (northern Mali). *Earth and Planetary Science Letters*, *235*(1–2), 391–407. https://doi.org/10.1016/j.epsl.2005.04.012

Vernikovsky, V. A., Vernikovskaya, A. E., Kotov, A. B., Sal'nikova, E. B., & Kovach, V. P. (2003). Neoproterozoic accretionary and collisional events on the western margin of the Siberian craton: New geological and geochronological evidence from the Yenisey Ridge. *Tectonophysics*, *375*(1–4), 147–168. https://doi.org/10.1016/S0040-1951(03)00337-8

Du Vivier, A. D. C., Selby, D., Sageman, B. B., Jarvis, I., Gröcke, D. R., & Voigt, S. (2014). Marine ^{187}Os/^{188}Os isotope stratigraphy reveals the interaction of volcanism and ocean circulation during Oceanic Anoxic Event 2. *Earth and Planetary Science Letters*, *389*, 23–33. https://doi.org/10.1016/j.epsl.2013.12.024

Du Vivier, A. D. C., Selby, D., Condon, D. J., Takashima, R., & Nishi, H. (2015). Pacific 187Os/188Os isotope chemistry and U-Pb geochronology: Synchroneity of global Os isotope change across OAE 2. *Earth and Planetary Science Letters*. https://doi.org/10.1016/j.epsl.2015.07.020

De Vleeschouwer, D., Da Silva, A. C., Sinnesael, M., Chen, D., Day, J. E., Whalen, M. T., et al. (2017). Timing and pacing of the Late Devonian mass extinction event regulated by eccentricity and obliquity. *Nature Communications*. https://doi.org/10.1038/s41467-017-02407-1

Voigt, S., Erbacher, J., Mutterlose, J., Weiss, W., Westerhold, T., Wiese, F., et al. (2008). The Cenomanian - Turonian of the Wunstorf section - (North Germany): Global stratigraphic reference section and new orbital time scale for Oceanic Anoxic Event 2. *Newsletters on Stratigraphy*, *43*(1), 65–89. https://doi.org/10.1127/0078-0421/2008/0043-0065

Walderhaug, H. J., Eide, E. A., Scott, R. A., Inger, S., & Golionko, E. G. (2005). Palaeomagnetism and 40Ar/39Ar geochronology from the South Taimyr igneous complex. Arctic Russia: A Middle-Late Triassic magmatic pulse after Siberian flood-basalt volcanism. *Geophysical Journal International*, *163*(2), 501–517. https://doi.org/10.1111/j.1365-246X.2005.02741.x

Ware, B., & Jourdan, F. (2018). ^{40}Ar/^{39}Ar geochronology of terrestrial pyroxene. *Geochimica et Cosmochimica Acta*, *230*, 112–136. https://doi.org/10.1016/j.gca.2018.04.002

Westerhold, T., Röhl, U., Raffi, I., Fornaciari, E., Monechi, S., Reale, V., et al. (2008). Astronomical calibration of the Paleocene time. *Palaeogeography, Palaeoclimatology, Palaeoecology*, *257*(4), 377–403. https://doi.org/10.1016/J.PALAEO.2007.09.016

Westerhold, T., Röhl, U., McCarren, H. K., & Zachos, J. C. (2009). Latest on the absolute age of the Paleocene–Eocene Thermal Maximum (PETM): New insights from exact stratigraphic position of key ash layers +19 and −17. *Earth and Planetary Science Letters*, *287*(3–4), 412–419. https://doi.org/10.1016/j.epsl.2009.08.027

Westerhold, T., Röhl, U., & Laskar, J. (2012). Time scale controversy: Accurate orbital calibration of the early Paleogene. *Geochemistry, Geophysics, Geosystems*, *13*(6). https://doi.org/10.1029/2012GC004096

White, R. S., Spence, G. D., Fowler, S. R., McKenzie, D. P., Westbrook, G. K., & Bowen, A. N. (1987). Magmatism at rifted continental margins. *Nature*, *330*(6147), 439. https://doi.org/10.1038/330439a0

Whiteside, J. H., Olsen, P. E., Kent, D. V., Fowell, S. J., & Et-Touhami, M. (2007). Synchrony between the Central Atlantic magmatic province and the Triassic-Jurassic mass-extinction event? *Palaeogeography, Palaeoclimatology, Palaeoecology*, *244*(1–4), 345–367. https://doi.org/10.1016/j.palaeo.2006.06.035

Wignall, P. B. (2001). Large igneous provinces and mass extinctions. *Earth Science Reviews*, *53*(1–2), 1–33. https://doi.org/10.1016/S0012-8252(00)00037-4

Wignall, P. B., Sun, Y., Bond, D. P. G., Izon, G., Newton, R. J., Védrine, S., et al. (2009). Volcanism, mass extinction, and carbon isotope fluctuations in the Middle Permian of China. *Science (New York, N.Y.)*, *324*(5931), 1179–82. https://doi.org/10.1126/science.1171956

Wilf, P., Johnson, K. R., & Huber, B. T. (2003). Correlated terrestrial and marine evidence for global climate changes before mass extinction at the Cretaceous–Paleogene boundary. *Proceedings of the National Academy of Sciences*, *100*(2), 599–604. https://doi.org/10.1073/pnas.0234701100

Wilkinson, C. M., Ganerød, M., Hendriks, B. W. H., & Eide, E. A. (2017). Compilation and appraisal of geochronological data from the North Atlantic Igneous Province (NAIP). *Geological Society, London, Special Publications*, *447*(1), 69–103. https://doi.org/10.1144/SP447.10

Williams, G. E., & Gostin, V. A. (2000). Mantle plume uplift in the sedimentary record: Origin of kilometre-deep canyons within late Neoproterozoic successions, south Australia. *Journal of the Geological Society, London*. https://doi.org/10.1144/jgs.157.4.759

Wilson, G. P. (2014). Mammalian extinction, survival, and recovery dynamics across the Cretaceous-Paleogene boundary in northeastern Montana, USA. *Geological Society of America Special Papers*, *503*, 365–392. https://doi.org/10.1130/2014.2503(15)

Wilson, G. P., DeMar, D. G., & Carter, G. (2014). Extinction and survival of salamander and salamander-like amphibians across the Cretaceous-Paleogene boundary in northeastern Montana, USA. *Geological Society of America Special Papers*, *503*, 271–297. https://doi.org/10.1130/2014.2503(10)

Wotzlaw, J.-F., Bindeman, I. N., Schaltegger, U., Brooks, C. K., & Naslund, H. R. (2012). High-resolution insights into episodes of crystallization, hydrothermal alteration and remelting in the Skaergaard intrusive complex. *Earth and Planetary Science Letters*, *355–356*, 199–212. https://doi.org/10.1016/j.epsl.2012.08.043

Wotzlaw, J.-F., Guex, J., Bartolini, A., Gallet, Y., Krystyn, L., McRoberts, C. A., et al. (2014). Towards accurate numerical calibration of the Late Triassic: High-precision

U-Pb geochronology constraints on the duration of the Rhaetian. *Geology*, *42*(7), 571–574. https://doi.org/10.1130/G35612.1

Wu, H., Zhang, S., Hinnov, L. A., Jiang, G., Feng, Q., Li, H., & Yang, T. (2013). Time-calibrated Milankovitch cycles for the late Permian. *Nature Communications*, *4*. https://doi.org/10.1038/ncomms3452

Zachos, J. C., Pagani, M., Sloan, L., Thomas, E., & Billups, K. (2001). Trends, rhythms, and aberrations in global climate 65 Ma to present. *Science*, *292*(5517), 686–693. https://doi.org/10.1126/science.1059412

Zachos, J. C., Röhl, U., Schellenberg, S. A., Sluijs, A., Hodell, D. A., Kelly, D. C., et al. (2005). Rapid acidification of the ocean during the Paleocene-Eocene thermal maximum. *Science*, *308*(5728), 1611–1615. https://doi.org/10.1126/science.1109004

Zachos, J. C., Dickens, G. R., & Zeebe, R. E. (2008). An early Cenozoic perspective on greenhouse warming and carbon-cycle dynamics. *Nature*, *451*, 279–283. https://doi.org/10.1038/nature06588

Zhang, Y. G., Pagani, M., Liu, Z., Bohaty, S. M., & Deconto, R. (2013). A 40-million-year history of atmospheric CO_2. *Philosophical Transactions of the Royal Society of London.*, (September). https://doi.org/10.1098/rsta.2013.0096

Zheng, L., Yang, Z., Tong, Y., & Yuan, W. (2010). Magnetostratigraphic constraints on two-stage eruptions of the Emeishan continental flood basalts. *Geochemistry, Geophysics, Geosystems*. https://doi.org/10.1029/2010GC003267

Zhong, Y. T., He, B., Mundil, R., & Xu, Y. G. (2014). CA-TIMS zircon U-Pb dating of felsic ignimbrite from the Binchuan section: Implications for the termination age of Emeishan large igneous province. *Lithos*. https://doi.org/10.1016/j.lithos.2014.03.005

Zhuravlev, A. Y., & Wood, R. A. (1996). Anoxia as the cause of the mid-Early Cambrian (Botomian) extinction event. *Geology*. https://doi.org/10.1130/0091-7613(1996)024<0311:AATCOT>2.3.CO;2

Table 1: High-Precision Geochronology of Large Igneous Provinces

LIP	Formation(: Member) and/or Location	Lithology	Method	Mineral	Sample	Age	[X]	[Y]	[Z]	MSWD	n	Age interp.	Tracer/ Standard	Reference
Franklin LIP	intruding Wynniatt Formation	diabase sill	U-Pb	b	S8	716.33	0.54			0.6	5	WMA		Macdonald et al., 2010
Franklin LIP	Kikiktat Volcanics, Alaska	volcaniclastic	U-Pb	z	F624B	719.47	0.29			0.57		WMA	ET535	Cox et al., 2015
Kalkarindji LIP	Milliwindi	dolerite dike	U-Pb	z	Z01	510.67	0.17	0.30	0.62	2.0	5	WMA	ET2535	Jourdan et al., 2014
Emeishan LIP	Daheishan syenite	syenitic pluton	U-Pb	z	DHS-1	259.1	0.5			0.5	5	WMA	BGC	Shellnutt et al., 2012
Emeishan LIP	Woshui syenite	metaluminous syenite	U-Pb	z	GS05-067	259.6	0.5			1.5	6	WMA	BGC	Shellnutt et al., 2012
Emeishan LIP	Huangcao syenite	fayalite+quartz bearing syenite	U-Pb	z	GS05-059	258.9	0.7			0.7	5	WMA	BGC	Shellnutt et al., 2012
Emeishan LIP	Cida granite	granite	U-Pb	z	GS04-143	258.4	0.6			1.8	5	WMA	BGC	Shellnutt et al., 2012
Emeishan LIP	Dyke intruding Baima peralkaline syenite	mafic dyke	U-Pb	z	GS05-005	259.2	0.4			1.9	8	WMA	BGC	Shellnutt et al., 2012
Emeishan LIP	Dyke intruding Baima peralkaline syenite	mafic dyke	U-Pb	z	GS03-105	259.4	0.8			0.2	7	WMA	BGC	Shellnutt et al., 2012
Emeishan LIP	Dyke intruding Woshui syenite	mafic dyke	U-Pb	z	GS03-111	257.6	0.5			0.5	6	WMA	BGC	Shellnutt et al., 2012
Emeishan LIP	Binchuan section, subunit P2-5	felsic ignimbrite	U-Pb	z	JW-1	259.1	0.5			0.7	6	WMA	BGC	Zhong et al., 2014
Siberian Traps	Bratsk/Padunskii	sill	U-Pb	z	A10-23-1	251.681	0.063	0.091	0.28	1.2	8	WMA	ET2535	Burgess & Bowring, 2015
Siberian Traps	Bratsk/Padunskii	sill	U-Pb	z	A10-23-2	251.539	0.056	0.086	0.28	1.2	11	WMA	ET2535	Burgess & Bowring, 2015
Siberian Traps	Bratsk/Padunskii	sill	U-Pb	z	A10-23-3	251.460	0.051	0.083	0.28	1	12	WMA	ET2535	Burgess & Bowring, 2015
Siberian Traps	Nepa/lower sill/ Scholokhovskoie pipe	sill	U-Pb	z	194/35/860	251.354	0.088	0.110	0.29	0.4	4	WMA	ET2535	Burgess & Bowring, 2015
Siberian Traps	Nepa/Scholokhovskoie pipe	sill	U-Pb	z	SHI-3085	251.501	0.071	0.097	0.29	0.34	10	WMA	ET2535	Burgess & Bowring, 2015
Siberian Traps	Lower Tungusskaya	sill	U-Pb	z	LT10-1-1	251.786	0.054	0.085	0.28	0.69	8	WMA	ET2535	Burgess & Bowring, 2015
Siberian Traps	Lower Tunguska	sill	U-Pb	z	LT10-2-2	251.795	0.070	0.096	0.29	1.3	14	WMA	ET2535	Burgess & Bowring, 2015

Table 1: High-Precision Geochronology of LIPs

Siberian Traps	Lower Tunguska	sill	U-Pb	z	NT12-5-4	251.74	0.18	0.19	0.33	0.65	2	WMA	ET2535	Burgess & Bowring, 2015
Siberian Traps	Bratsk/Oktybroskoe deposit	sill	U-Pb	z	S68-700	251.509	0.044	0.079	0.28	1.4	13	WMA	ET2535	Burgess & Bowring, 2015
Siberian Traps	Bratsk/Oktybroskoe deposit	sill	U-Pb	z	O-6832	251.504	0.059	0.088	0.28	0.36	8	WMA	ET2535	Burgess & Bowring, 2015
Siberian Traps	Noril'sk/Kharaelakh	sill	U-Pb	z	KZ1818-1691	251.71	0.14	0.16	0.31	0.13	3	WMA	ET2535	Burgess & Bowring, 2015
Siberian Traps	Noril'sk/Talnakh	sill	U-Pb	z	KZ1799-1195	251.801	0.088	0.110	0.29	0.45	10	WMA	ET2535	Burgess & Bowring, 2015
Siberian Traps	Noril'sk/Chernogorsky	sill	U-Pb	z	R06-05	251.660	0.064	0.092	0.28	0.7	9	WMA	ET2535	Burgess & Bowring, 2015
Siberian Traps	Noril'sk/Noril'sk 1	sill	U-Pb	z	G22-105-2	251.64	0.10	0.12	0.30	0.48	11	WMA	ET2535	Burgess & Bowring, 2015
Siberian Traps	Noril'sk/Noril'sk 1	sill	U-Pb	z	G22-63-5	251.907	0.067	0.094	0.29	0.7	2	WMA	ET2535	Burgess & Bowring, 2015
Siberian Traps	Noril'sk/Noril'sk 1	sill	U-Pb	z	G22-65-0	251.813	0.065	0.092	0.28	1	5	WMA	ET2535	Burgess & Bowring, 2015
Siberian Traps	Daldykansky	sill	U-Pb	z	N12-3-2	251.376	0.050	0.082	0.28	1.1	7	WMA	ET2535	Burgess & Bowring, 2015
Siberian Traps	Maymecha-Kotuy	lava	U-Pb	ps	K08-14-3	252.20	0.12	0.16	0.31	1.1	15	WMA	ET2535	Burgess & Bowring, 2015
Siberian Traps	Maymecha-Kotuy	lava	U-Pb	ps	K09-6-1	252.27	0.11	0.15	0.31	1.1	12	WMA	ET2535	Burgess & Bowring, 2015
Siberian Traps	Maymecha-Kotuy	welded tuff	U-Pb	z	M09-11-1	251.901	0.061	0.089	0.28	1.6	21	WMA	ET2535	Burgess & Bowring, 2015
Siberian Traps	Maymecha-Kotuy	welded tuff	U-Pb	z	M09-12-1	251.483	0.088	0.110	0.29	1.1	7	WMA	ET2535	Burgess & Bowring, 2015
Siberian Traps	Angara river	pyroclastic breccia	U-Pb	z	A10-13-3	256.56	0.46	0.51	0.58		1	WMA	ET2535	Burgess & Bowring, 2015
Siberian Traps	Noril'sk	pyroclastic breccia	U-Pb	z	SG2610.4	255.58	0.38	0.43	0.51		1	YZ	ET2535	Burgess & Bowring, 2015
CAMP	North Mountain Basalt	Lava	U-Pb	z	NMB-03-1	201.38	0.02	0.22	0.31	1.2	20	WMA	ET535 or ET2535	Schoene et al., 2010
CAMP	North Mountain Basalt, Canada	Lava	U-Pb	z	AVC-1-2	201.522	0.064	1.4	1.4	0.71	8	WMA	ET2535	Blackburn et al., 2013
CAMP	North Mountain Basalt, Canada	pegmatite lens in lava	U-Pb	z	NMB_03	201.523	0.028	0.059	0.22	1.5	10	WMA	ET2535	Davies et al., 2017
CAMP	North Mountain Basalt, Canada	Lava (base of flow)	U-Pb	z	SU1201	201.440	0.047	0.71	0.23	3.5	13	WMA	ET2535	Davies et al., 2017

Table 1: High-Precision Geochronology of LIPs

CAMP	Amelal Sill (Argana Basalt correlate), Morocco	Sill correlated as lava	U-Pb	z	MOR	201.564	0.054	0.075	0.23	0.93	10	WMA	ET2535	Blackburn et al., 2013
CAMP	Palisades Sill, New Jersey, USA	Sill correlated as lava	U-Pb	z	NB08-13	201.515	0.033	0.02	0.22	1.7	10	WMA	ET2535	Blackburn et al., 2013
CAMP	Butner Diabase, North Carolina, USA	Sill correlated as lava	U-Pb	z	Butner Diabase	200.916	0.064	0.075	0.23	1.5	14	WMA	ET2535	Blackburn et al., 2013
CAMP	Preakness Basalt, New Jersey, USA	Lava	U-Pb	z	NB08-12	201.274	0.032	0.062	0.22	0.71	15	WMA	ET2535	Blackburn et al., 2013
CAMP	York Haven Diabase, Pennsylvania, USA	Sill	U-Pb	z	YORK	201.509	0.035	0.063	0.22	0.77	6	WMA	ET2535	Blackburn et al., 2013
CAMP	Rapidan Sheet, Virgina, USA	Sill	U-Pb	z	030507-2	201.498	0.033	0.062	0.22	0.44	5	WMA	ET2535	Blackburn et al., 2013
CAMP	Rossville Diabase, Pennsylvania, USA	Sill	U-Pb	z	ROSSGPH	201.305	0.034	0.063	0.22	1.4	6	WMA	ET2535	Blackburn et al., 2013
CAMP	Messejana dyke, Spain	dyke	U-Pb	z	MD48	201.585	0.034	0.063	0.22	2	8	WMA	ET2535	Davies et al., 2017
CAMP	Shelborne dyke, Canada	dyke	U-Pb	z	SD1_2	201.364	0.084	0.099	0.24	0.01	2	WMA	ET2535	Davies et al., 2017
CAMP	Foum Zguid dyke, Morocco	dyke	U-Pb	z	AN731	201.111	0.071	0.089	0.23	1.7	3	WMA	ET2535	Davies et al., 2017
CAMP	Hodh Sill, Mauritania	gabbro sill	U-Pb	z	HD38	201.440	0.031	0.061	0.22	4	7	WMA	ET2535	Davies et al., 2017
CAMP	Foura Djalon sill, Guinea	Sill	U-Pb	z	GUI22-26	201.493	0.051	0.073	0.23	1.5	8	WMA	ET2535	Davies et al., 2017
CAMP	Kakoulima intrusion, Guinea	Sill (layered ultramafic intrusion)	U-Pb	z	GUI126	201.635	0.029	0.06	0.22	1.8	16	WMA	ET2535	Davies et al., 2017
CAMP	Amazonia sill high Ti, Brazil	gabbro sill	U-Pb	z	RP113	201.364	0.023	0.057	0.22	1.88	9	WMA	ET2535	Davies et al., 2017
CAMP	Amazonia sill low Ti, Brazil	gabbro sill	U-Pb	z	RP126	201.525	0.065	0.076	0.23	1.2	9	WMA	ET2535	Davies et al., 2017
CAMP	Tarabuco sill, Bolivia	Sill	U-Pb	z	Bol	201.612	0.046	0.07	0.23	1.2	5	WMA	ET2535	Davies et al., 2017
CAMP	Amelal sill, Morocco	Sill	U-Pb	z	LV34	201.569	0.042			1.1	4	WMA	ET2535	Marzoli et al., 2019
CAMP	Solimões Basin, Brazil	Sill	U-Pb	z	Amostra 8	201.470	0.089	0.13	0.25	0.16	3	WMA-YF	ET535	Heimdal et al., 2018
CAMP	Amazonas Basin, Brazil	Sill	U-Pb	z	1-MA-1-PA-2883.18	201.477	0.062	0.11	0.24	1.7	5	WMA	ET535	Heimdal et al., 2018

Table 1: High-Precision Geochronology of LIPs

Ferrar LIP	Storm Peak, Central Transantarctic Mountains (CTM)	uppermost lava	U-Pb	z	85-76-63	182.43	0.04	0.06	0.20	1.6	7	WMA	ET535 or ET2535	Burgess et al., 2015
Ferrar LIP	Mt. Bumstead, CTM	lowermost lava	U-Pb	z	96-55-2	182.48	0.20	0.21	0.28	0.81	3	WMA	ET535 or ET2535	Burgess et al., 2015
Ferrar LIP	Mt. Bumstead, CTM	uppermost lava	U-Pb	z	96-52-1	182.54	0.20	0.21	0.28	1	4	WMA	ET535 or ET2535	Burgess et al., 2015
Ferrar LIP	Nilsen Plateau, CTM	sill	U-Pb	z	96-65-11	182.59	0.08	0.093	0.22	0.94	6	WMA	ET535 or ET2535	Burgess et al., 2015
Ferrar LIP	Mt. Picciotto, CTM	sill A	U-Pb	z	85-4-18	182.633	0.049	0.069	0.21	1.3	9	WMA	ET535 or ET2535	Burgess et al., 2015
Ferrar LIP	Mt. Picciotto, CTM	sill B	U-Pb	z	85-4-4	182.616	0.049	0.068	0.21	0.47	4	WMA	ET535 or ET2535	Burgess et al., 2015
Ferrar LIP	Dawson Peak, CTM	sill	U-Pb	z	85-5-6	182.635	0.068	0.100	0.22	1.4	6	WMA	ET535 or ET2535	Burgess et al., 2015
Ferrar LIP	Wahl Glacier, CTM	sill	U-Pb	z	85-6-16	182.643	0.055	0.073	0.21	0.2	6	WMA	ET535 or ET2535	Burgess et al., 2015
Ferrar LIP	Roberts Massif, CTM	sill	U-Pb	z	96-74-6	182.746	0.054	0.072	0.21	0.7	7	WMA	ET535 or ET2535	Burgess et al., 2015
Ferrar LIP	Rougier Hill, CTM	sill	U-Pb	z	96-51-67	182.753	0.037	0.060	0.20	0.9	10	WMA	ET535 or ET2535	Burgess et al., 2015
Ferrar LIP	Mt. Falla, CTM	sill	U-Pb	z	90-63-6	182.779	0.033	0.061	0.20	0.98	14	WMA	ET535 or ET2535	Burgess et al., 2015
Ferrar LIP	Dawson Peak, CTM	sill	U-Pb	z	90-3-12	182.85	0.34	0.35	0.40	0.23	2	WMA	ET535 or ET2535	Burgess et al., 2015
Ferrar LIP	Brimstone Pea, South Victoria Land (SVL)	uppermost lava	U-Pb	z	97-55-1	182.635	0.077	0.090		0.9	4	WMA	ET535 or ET2535	Burgess et al., 2015
Ferrar LIP	Bull Pass, SVL	basement sill	U-Pb	z	05-06-01	182.680	0.038	0.061	0.20	0.84	8	WMA	ET535 or ET2535	Burgess et al., 2015
Ferrar LIP	Pandora Spire, SVL	Peneplain sill	U-Pb	z	A-236-A	182.689	0.038	0.061	0.20	0.87	6	WMA	ET535 or ET2535	Burgess et al., 2015
Ferrar LIP	Labyrinth Intrusion, SVL	intrusion	U-Pb	z	04-03-04	182.750	0.048	0.067	0.21	0.74	7	WMA	ET535 or ET2535	Burgess et al., 2015
Ferrar LIP	Pearse Valley, SVL	basement sill	U-Pb	z	90-76-13	182.776	0.059	0.098	0.22	0.78	6	WMA	ET535 or ET2535	Burgess et al., 2015
Ferrar LIP	Red Hill, Tasmania	sill	U-Pb	z	97-17	182.540	0.059	0.075	0.21	1.1	6	WMA	ET535 or ET2535	Burgess et al., 2015
Ferrar LIP	Forrestal granophyre, Dufek intrusion	Granophyre	U-Pb	z	PRR-8633	182.700	0.050	0.066	0.21	0.85	7	WMA	ET535 or ET2535	Burgess et al., 2015
Ferrar LIP	Lexington granophyre, Dufek intrusion	Granophyre	U-Pb	z	PRR-09305	182.629	0.029	0.056	0.20	1.3	11	WMA	ET535 or ET2535	Burgess et al., 2015

Table 1: High-Precision Geochronology of LIPs

Karoo LIP	New Amalfi Sheet, South Africa	intrusion	U-Pb	z	I-247	182.246	0.045	0.066	0.21	0.74	5	WMA	ET535 or ET2535	Burgess et al., 2015
Deccan Traps	Jawhar Fm (lower)	coarse grained gabbro veinlets	U-Pb	z	DEC13-30	66.296	+0.037 /-0.030	+0.042 /-0.038	+0.081 /-0.080			TPB	ET2535	Schoene et al., 2019
Deccan Traps	Thakurvadi Fm (lower-middle)	redbole	U-Pb	z	RBAB	66.225	+0.077 /-0.071	+0.078 /-0.075	+0.104 /-0.104			TPB	ET2535	Schoene et al., 2019
Deccan Traps	Thakurvadi Fm (middle)	redbole	U-Pb	z	RBAG	66.185	+0.061 /-0.056	+0.068 /-0.060	+0.094 /-0.093			TPB	ET2535	Schoene et al., 2019
Deccan Traps	Khandala Fm (uppermost)	redbole	U-Pb	z	RBBQ	66.161	+0.066 /-0.069	+0.070 /-0.073	+0.099 /-0.101			TPB	ET2535	Schoene et al., 2019
Deccan Traps	Bushe Fm (2m below Poladpur Fm)	redbole	U-Pb	z	RBBL	66.132	+0.069 /-0.058	+0.071 /-0.064	+0.100 /-0.096			TPB	ET2535	Schoene et al., 2019
Deccan Traps	Poladpur Fm (10 m above Bushe contact)	breccia fill redbole	U-Pb	z	RBBI	66.088	+0.032 /-0.026	+0.043 /-0.034	+0.081 /-0.077			TPB	ET2535	Schoene et al., 2019
Deccan Traps	Poladpur Fm (middle)	breccia fill redbole	U-Pb	z	RBBM	66.07	+0.031 /-0.028	+0.036 /-0.032	+0.077 /-0.078			TPB	ET2535	Schoene et al., 2019
Deccan Traps	Poladpur Fm (middle)	breccia fill redbole	U-Pb	z	RBBR	66.055	+0.017 /-0.018	+0.026 /-0.024	+0.074 /-0.073			TPB	ET2535	Schoene et al., 2019
Deccan Traps	Poladpur Fm (middle)	redbole	U-Pb	z	RBBJ	66.052	+0.015 /-0.018	+0.023 /-0.023	+0.073 /-0.072			TPB	ET2535	Schoene et al., 2019
Deccan Traps	Poladpur Fm (upper)	redbole	U-Pb	z	RBBS	66.047	+0.017 /-0.020	+0.025 /-0.027	+0.073 /-0.073			TPB	ET2535	Schoene et al., 2019
Deccan Traps	Poladpur Fm (uppermost)	redbole	U-Pb	z	RBAW	66.044	+0.019 /-0.022	+0.026 /-0.028	+0.073 /-0.073			TPB	ET2535	Schoene et al., 2019
Deccan Traps	Poladpur Fm (uppermost)	redbole	U-Pb	z	RBX	66.039	+0.022 /-0.030	+0.027 /-0.029	+0.074 /-0.075			TPB	ET2535	Schoene et al., 2019
Deccan Traps	Ambenali Fm (lower)	breccia fill redbole	U-Pb	z	RBBH	65.926	+0.035 /-0.028	+0.045 /-0.036	+0.081 /-0.079			TPB	ET2535	Schoene et al., 2019
Deccan Traps	Ambenali Fm	breccia fill redbole	U-Pb	z	RBBF	65.92	+0.032 /-0.031	+0.039 /-0.040	+0.080 /-0.079			TPB	ET2535	Schoene et al., 2019
Deccan Traps	Ambenali Fm (middle)	redbole	U-Pb	z	RBB2	65.905	+0.033 /-0.033	+0.042 /-0.045	+0.082 /-0.082			TPB	ET2535	Schoene et al., 2019
Deccan Traps	Ambenali Fm (middle)	breccia fill redbole	U-Pb	z	RBAY	65.895	+0.032 /-0.030	+0.042 /-0.041	+0.082 /-0.081			TPB	ET2535	Schoene et al., 2019
Deccan Traps	Ambenali Fm (middle)	redbole	U-Pb	z	RBAO	65.889	+0.029 /-0.028	+0.041 /-0.043	+0.081 /-0.080			TPB	ET2535	Schoene et al., 2019
Deccan Traps	Ambenali Fm (middle)	redbole	U-Pb	z	RBAN	65.885	+0.027 /-0.029	+0.042 /-0.044	+0.081 /-0.082			TPB	ET2535	Schoene et al., 2019
Deccan Traps	Ambenali Fm (middle-upper)	redbole	U-Pb	z	RBP	65.879	+0.024 /-0.029	+0.045 /-0.053	+0.084 /-0.086			TPB	ET2535	Schoene et al., 2019

Table 1: High-Precision Geochronology of LIPs

Deccan Traps	Ambenali Fm (upper)	redbole	U-Pb	z	RBO	65.875	+0.022 /-0.042	+0.047 /-0.057	+0.085 /-0.088		TPB	ET2535	Schoene et al., 2019
Deccan Traps	Mahableshwar Fm	redbole	U-Pb	z	RBE	65.631	+0.053 /-0.030	+0.059 /-0.037	+0.088 /-0.080		TPB	ET2535	Schoene et al., 2019
Deccan Traps	Mahableshwar Fm	redbole	U-Pb	z	RBF	65.62	+0.028 /-0.021	+0.033 /-0.029	+0.075 /-0.075		TPB	ET2535	Schoene et al., 2019
Deccan Traps	Mahableshwar Fm	greenbole	U-Pb	z	DEC13-09	65.614	+0.015 /-0.017	+0.024 /-0.025	+0.073 /-0.073		TPB	ET2535	Schoene et al., 2019
Deccan Traps	Mahableshwar Fm (middle-upper)	redbole	U-Pb	z	RBG	65.59	+0.026 /-0.027	+0.032 /-0.033	+0.077 /-0.075		TPB	ET2535	Schoene et al., 2019
Deccan Traps	Jawhar Fm	lava	^{40}Ar/^{39}Ar	pl	KAS15-2	66.234	0.168		0.186	38	WMA	FCs = 28.294; Renne et al.,	Sprain et al., 2019
Deccan Traps	Jawhar Fm	lava	^{40}Ar/^{39}Ar	pl	KAS15-3	66.413	0.134		0.158	45	WMA	FCs = 28.294; Renne et al.,	Sprain et al., 2019
Deccan Traps	Neral Fm	lava	^{40}Ar/^{39}Ar	pl	MG7	66.153	0.100		0.132	36	WMA	FCs = 28.294; Renne et al.,	Sprain et al., 2019
Deccan Traps	Thakurvadi Fm	lava	^{40}Ar/^{39}Ar	pl	BOR14-1	65.912	0.136		0.158	38	WMA	FCs = 28.294; Renne et al.,	Sprain et al., 2019
Deccan Traps	Bhimashankar Fm	lava	^{40}Ar/^{39}Ar	pl	KHK15-1	66.171	0.152		0.176	36	WMA	FCs = 28.294; Renne et al.,	Sprain et al., 2019
Deccan Traps	Khandala Fm	lava	^{40}Ar/^{39}Ar	pl	MAT14-6	66.105	0.204		0.224	53	WMA	FCs = 28.294; Renne et al.,	Sprain et al., 2019
Deccan Traps	Khandala Fm	lava	^{40}Ar/^{39}Ar	pl	MAT14-7	66.158	0.164		0.186	57	WMA	FCs = 28.294; Renne et al.,	Sprain et al., 2019
Deccan Traps	Bushe Fm	lava	^{40}Ar/^{39}Ar	pl	VER14-3 (pooled)	65.974	0.168		0.186	86	WMA	FCs = 28.294; Renne et al.,	Sprain et al., 2019
Deccan Traps	Bushe Fm	lava	^{40}Ar/^{39}Ar	pl	POL15-2	66.059	0.158		0.180	43	WMA	FCs = 28.294; Renne et al.,	Sprain et al., 2019
Deccan Traps	Poladpur Fm	lava	^{40}Ar/^{39}Ar	pl	KJA14-1	65.977	0.302		0.316	##	WMA	FCs = 28.294; Renne et al.,	Sprain et al., 2019
Deccan Traps	Poladpur Fm	lava	^{40}Ar/^{39}Ar	pl	KJA15-1 (pooled)	65.988	0.638		0.658	44	WMA	FCs = 28.294; Renne et al.,	Sprain et al., 2019
Deccan Traps	Poladpur Fm	lava	^{40}Ar/^{39}Ar	pl	KJA14-2 (pooled)	65.94	0.184		0.202	91	WMA	FCs = 28.294; Renne et al.,	Sprain et al., 2019
Deccan Traps	Poladpur Fm	lava	^{40}Ar/^{39}Ar	pl	POL15-1 (pooled)	66.112	0.308		0.324	72	WMA	FCs = 28.294; Renne et al.,	Sprain et al., 2019
Deccan Traps	Ambenali Fm	lava	^{40}Ar/^{39}Ar	pl	AMB14-4	65.968	0.496		0.508	28	WMA	FCs = 28.294; Renne et al.,	Sprain et al., 2019

Table 1: High-Precision Geochronology of LIPs

Deccan Traps	Ambenali Fm	lava	^{40}Ar/^{39}Ar	pl	AMB14-5	65.733	0.362		0.376		50	WMA	FCs = 28.294; Renne et al.,	Sprain et al., 2019
Deccan Traps	Ambenali Fm	lava	^{40}Ar/^{39}Ar	pl	AMB15-1 (pooled)	65.667	0.208		0.228		50	WMA	FCs = 28.294; Renne et al.,	Sprain et al., 2019
Deccan Traps	Mahableshwar Fm	lava	^{40}Ar/^{39}Ar	pl	AMB14-13	65.521	0.130		0.156		65	WMA	FCs = 28.294; Renne et al.,	Sprain et al., 2019
Deccan Traps	Mahableshwar Fm	lava	^{40}Ar/^{39}Ar	pl	AMB14-14	65.466	0.200		0.220		40	WMA	FCs = 28.294; Renne et al.,	Sprain et al., 2019
Deccan Traps	Mahableshwar Fm	lava	^{40}Ar/^{39}Ar	pl	PAN15-3	65.422	0.206		0.224		51	WMA	FCs = 28.294; Renne et al.,	Sprain et al., 2019
NAIP	Tardree Rhyolite (between Antrim Plateau Volcanics), UK	Rhyolite	U-Pb	z	Tardree forest	61.32	0.09			1.1	6	WMA	Oslo 205Pb-235U tracer	Ganerød et al., 2011
NAIP	Vøring margin sill, offshore Norway	Sill	U-Pb	z	Utgard Upper Sill	55.6	0.3	0.4			4	WMA	Oslo 235U-205Pb-202Pb tracer	Svensen et al., 2010
NAIP	Vøring margin sill, offshore Norway	Sill	U-Pb	z	Utgard Lower Sill	56.3	0.4	0.5			1	YZ	Oslo 235U-205Pb-202Pb tracer	Svensen et al., 2010
NAIP	Skaergaard Intrusion, lower zone b, East Greenland	gabbroic pegmatite sill	U-Pb	z	SK-218	55.960	0.018	0.031	0.064	1.4	7	WMA	ET535 or ET2535	Wotzlaw et al., 2012
NAIP	Skaergaard Intrusion, Basistoppen Sill, East Greenland	tholeiitic sill	U-Pb	z	BZN	55.895	0.018	0.031	0.064	0.51	8	WMA	ET535 or ET2535	Wotzlaw et al., 2012
NAIP	Skaergaard Intrusion, Sandwich Horizon, East Greenland	ferrodiorite sill	U-Pb	z	SH-428	55.838	0.019	0.032	0.064	0.1	5	WMA	ET535 or ET2535	Wotzlaw et al., 2012
CRBG	Steens Basalt	Tuff 1 in Main Scarp	^{40}Ar/^{39}Ar	a	TB-124	16.592		0.028				WMA	FCs = 28.02; Renne et al.,	Mahood & Benson, 2017
CRBG	Steens Basalt	Tuff 2 in Main Scarp	^{40}Ar/^{39}Ar	a	TB-125	16.606		0.034				WMA	FCs = 28.02; Renne et al.,	Mahood & Benson, 2017
CRBG	Steens Basalt	Tuff 3 in Main Scarp	^{40}Ar/^{39}Ar	pl	TB-128A	16.499		0.104				WMA	FCs = 28.02; Renne et al.,	Mahood & Benson, 2017
CRBG	Steens Basalt	Tuff 4 in Main Scarp	^{40}Ar/^{39}Ar	pl	TB-128B	16.490		0.090				WMA	FCs = 28.02; Renne et al.,	Mahood & Benson, 2017
CRBG	Steens Basalt	Ignimbrite in East Creek	^{40}Ar/^{39}Ar	pl	ML-316	16.513		0.120				WMA	FCs = 28.02; Renne et al.,	Mahood & Benson, 2017
CRBG	Steens Basalt	Tuff 5 in Main Scarp	^{40}Ar/^{39}Ar	pl	TB-129	16.495		0.048				WMA	FCs = 28.02; Renne et al.,	Mahood & Benson, 2017

Table 1: High-Precision Geochronology of LIPs

CRBG	Steens Basalt	Tuff in Rosebriar Creek	^{40}Ar/^{39}Ar	pl	TB-382	16.532		0.046			WMA	FCs = 28.02; Renne et al., 1998	Mahood & Benson, 2017
CRBG	above Steens Basalt	Alkali rhyolite lava capping Main Scarp	^{40}Ar/^{39}Ar	s	TB-130	16.485		0.028			WMA	FCs = 28.02; Renne et al., 1998	Mahood & Benson, 2017
CRBG	above Steens Basalt	Tuff capping Steens Basalt in East Creek	^{40}Ar/^{39}Ar	pl	TB-397	16.474		0.042			WMA	FCs = 28.02; Renne et al., 1998	Mahood & Benson, 2017
CRBG	above Steens Basalt	Tuff in Cottonwood Creek	^{40}Ar/^{39}Ar	s	TB-103A	16.475		0.054			WMA	FCs = 28.02; Renne et al., 1998	Mahood & Benson, 2017
CRBG	above Steens Basalt	Tuff of Monument Basin	^{40}Ar/^{39}Ar	s	TB-101	16.479		0.042			WMA	FCs = 28.02; Renne et al., 1998	Mahood & Benson, 2017
CRBG	Steens Basalt: Lower Steens	Redbole	U-Pb	z	CRB1625	16.653	0.063	0.071	0.073	1	YZ	ET535	Kasbohm & Schoene, 2018
CRBG	Steens Basalt: Upper Steens	Redbole	U-Pb	z	CRB1624	16.589	0.031	0.032	0.037	1	YZ	ET535	Kasbohm & Schoene, 2018
CRBG	Imnaha Basalt	Lapilli tuff	U-Pb	z	CRB1586	16.572	0.018	0.018	0.026	1	YZ	ET2535	Kasbohm & Schoene, 2018
CRBG	Grande Ronde Basalt: Wapshilla Ridge (lower)	Redbole	U-Pb	z	CRB1634	16.288	0.039	0.043	0.046	1	YZ	ET535	Kasbohm & Schoene, 2018
CRBG	Grande Ronde Basalt: Meyer Ridge / Wapshilla Ridge (upper)	Redbole	U-Pb	z	CRB1556	16.254	0.034	0.037	0.041	1	YZ	ET535	Kasbohm & Schoene, 2018
CRBG	Grande Ronde Basalt: Meyer Ridge / Wapshilla Ridge (upper)	Redbole	U-Pb	z	CRB1519	16.210	0.043	0.044	0.047	1	YZ	ET2535	Kasbohm & Schoene, 2018
CRBG	Wanapum Basalt: Frenchman Springs / Grande Ronde Basalt: Sentinel Bluffs (Vantage Interbed)	Pumice clasts	U-Pb	z	CRB1533	16.066	0.040	0.040	0.043	1	YZ	ET2535	Kasbohm & Schoene, 2018
CRBG	Wanapum Basalt: Priest Rapids (Basalt of Rosalia) / Roza	Ash	U-Pb	z	CRB1506	15.895	0.019	0.020	0.026	1	YZ	ET535	Kasbohm & Schoene, 2018

Table 2: High-Precision Geochronology of Environmental Events

Event	Location	Formation	Lithology	Method	Mineral	Sample	Age	[X]	[Y]	[Z]	MSWD	n	Age interp.	Tracer/ Standard	Reference
Sturtian Glaciation	Tambien Group, Ethiopia	Upper Mariam Bohkahko Formation	tuffaceous siltstone	U-Pb	z	SAM-ET-03	719.68	0.56	0.64	1.0	0.54	3	WMA	ET535 or ET2535	Maclennan et al., 2018
Sturtian Glaciation	Tambien Group, Ethiopia	Upper Mariam Bohkahko Formation	tuffaceous siltstone	U-Pb	z	SAM-ET-04	719.68	0.46	0.54	0.94	1.3	8	WMA	ET535 or ET2535	Maclennan et al., 2018
Sturtian Glaciation	Tambien Group, Ethiopia	over contact betw Didikama & Matheos	crystal-rich tuff	U-Pb	z	T46-102_2Z	735.25	0.25	0.39	0.88	0.36	5	WMA	ET535 or ET2535	Maclennan et al., 2018
Sturtian Glaciation	Bald Hill, Coal Creek Inlier, Canada	Mount Harper Volcanic Complex	quartz-phyric rhyolite	U-Pb	z	F837B	717.43	0.14			0.8	7	WMA	ET535	Macdonald et al., 2010
Sturtian Glaciation	Tango Tarn, Coal Creek Inlier, Canada	Eagle Creek Fm	green/pink brecciated tuff	U-Pb	z	F840A	716.47	0.24			1.1	6	WMA	ET535	Macdonald et al., 2010
Sturtian Glaciation	SW inlier, Coal Creek Inlier, Canada	Mount Harper Volcanic Complex	welded rhyolitic tuff	U-Pb	z	15PM06	718.1	0.3	0.5	0.9	0.42	4	WMA	ET535	Macdonald et al., 2017
Sturtian Glaciation	SW inlier, Coal Creek Inlier, Canada	Mount Harper Volcanic Complex	welded rhyolitic tuff	U-Pb	z	15PM08	718.1	0.2	0.4	0.8	0.98	6	WMA	ET535	Macdonald et al., 2017
Sturtian Glaciation	Bald Hill, Coal Creek Inlier, Canada	Mount Harper Volcanic Complex	rhyolite flow	U-Pb	z	F837A	717.8	0.2	0.4	0.8	0.64	4	WMA	ET535	Macdonald et al., 2017
Sturtian Glaciation	Bald Hill, Coal Creek Inlier, Canada	Mount Harper Volcanic Complex	rhyolite flow	U-Pb	z	F837C	717.7	0.3	0.5	0.9	0.29	3	WMA	ET535	Macdonald et al., 2017
Sturtian Glaciation	Tango Tarn, Coal Creek Inlier, Canada	Eagle Creek Fm	green tuff in diamictite	U-Pb	z	F917-1	716.9	0.4	0.5	0.9	1.5	5	WMA	ET535	Macdonald et al., 2017
Sturtian Glaciation	Jabal Akhdar region, Oman Mtns	Ghubrah Formation	tuffaceous sandstone	U-Pb	z	WM 54	711.52	0.20	0.31	1.09	0.18	5	WMA	ET535?	Bowring et al., 2007
Early-Middle Cambrian Extinction	Shropshire, England	Upper Comley Sandstone Formation	bentonite	U-Pb	z	Comley ub	509.1	0.22	0.56	0.77	0.51	7	WMA	ET535	Harvey et al., 2011

Table 2: High-Precision Geochronology of Environmental Events

Frasnian-Famennian bounday	Steinbruch Schmidt Quarry, Germany	Bed 36	bentonite	U-Pb	z	Bed 36 bentonite	372.36	0.053	0.11	0.41	1.47	8	WMA	ET2535	Percival et al., 2018
end-Guadalupian Extinction	Sutherland, Northern Cape Province, South Africa	Poortjie Member, Tekloof Formation, Beaufort Group	white tuff 3.5 m above basal sstn	U-Pb	z	K1202-B1	260.259	0.081	0.14	0.31	1.5	4	WMA-YF	ET535	Day et al., 2015
End-Permian Extinction	Meishan, China	Changhsing Formation, Bed 25; extinction onset	ash	U-Pb	z	Bed 25-MBE0203	251.941	0.037		0.28	1.3	16	WMA	ET2535	Burgess et al., 2014
End-Permian Extinction	Meishan, China	Yinkeng Formation, Bed 28; extinction	ash	U-Pb	z	Bed 28-MBE0205	251.880	0.031		0.28	0.76	13	WMA	ET2535	Burgess et al., 2014
End-Triassic Extinction	Pucara Basin, North Peru	onset of δ13C excursion	ash	U-Pb	z	LM4-86	201.510	0.15				1	YZ; MCMC	ET2535	Schoene et al., 2010; Wotzlaw et al.. 2014
OAE2 (beginning)	Yezo Group, Hokkaido, Japan	Saku Formation, Hakkin Member	bentonite (felsic tuff)	U-Pb	z	HK017	94.436	0.093		0.14	0.8	5	WMA-YF	ET2535	Du Vivier et al., 2015
OAE2 (next; beginning)	Yezo Group, Hokkaido, Japan	Saku Formation, Hakkin Member	bentonite (felsic tuff)	U-Pb	z	CT103	94.536	0.170		0.21	0.4	6	WMA-YF	ET2535	Du Vivier et al., 2015
OAE2 (end)	Yezo Group, Hokkaido, Japan	Saku Formation, Hakkin Member	bentonite (felsic tuff)	U-Pb	z	HK018	93.92	0.031		0.11	2	3	WMA-YF	ET2535	Du Vivier et al., 2015
K-Pg boundary	Kiowa Core, Denver Basin, USA	D1 sequence; 1 ft above boundary	ash	U-Pb	z	KJ10-04	66.019	0.024	0.038	0.08	0.94	5	WMA	ET535	Clyde et al., 2016
K-Pg boundary	Bowring Pit, Denver Basin, USA	D1 sequence; 1.5 ft below boundary	ash	U-Pb	z	KJ08-157	66.082	0.022	0.037	0.08	0.78	12	WMA	ET535	Clyde et al., 2016
K-Pg boundary	Bowring Pit, Denver Basin, USA	D1 sequence; 3.2 ft above boundary	ash	U-Pb	z	KJ04-70	65.889	0.027	0.044	0.083	1.1	11	WMA	ET535	Clyde et al., 2016
K-Pg boundary	Denver Basin, USA	D1 sequence	K-Pg boundary	U-Pb	z		66.021	0.024	0.039	0.081			interpolated age		Clyde et al., 2016
K-Pg boundary	Hell Creek, Montana, USA	Hell Creek Fm / Fort Union Formation	Iridium Coal layer	^{40}Ar/^{39}Ar	af	IrZ	66.052	0.016		0.086		730	pooled WMA	FCs = 28.294; Renne et al., 2011	Sprain et al., 2018
PETM	Longyearben, Spitsbergen, Norway	Frysjaodden Fm, mid-excursion	bentonite	U-Pb	z	SB01-1	55.785	0.034	0.066	0.086	0.88	5	WMA-YF	ET535	Charles et al., 2011